

Alma Mater Studiorum – Università di Bologna

DOTTORATO DI RICERCA IN

**Dottorato di Ricerca in  
Scienze Biotecnologiche e Farmaceutiche**

Ciclo XXXII

**Settore Concorsuale: 03/D1**

**Settore Scientifico Disciplinare: CHIM/08**

TITOLO TESI

**Synthesis and Characterization of Novel Selective NKCC1  
Inhibitors for the Treatment of Down Syndrome and Brain  
Disorders Characterized by Depolarizing GABAergic  
Transmission.**

**Presentata da: Marco Borgogno**

**Coordinatore Dottorato**

**Prof.ssa Maria Laura Bolognesi**

**Supervisore**

**Dott. Marco De Vivo**

**Co-supervisore**

**Dott.ssa Laura Cancedda**

**Esame finale anno 2020**

## Index

<b>Abstract</b> .....	<b>3</b>
<b>Chapter 1. NKCC1 function, structure and pathological relevance</b> .....	<b>5</b>
1.1 Cation-chloride cotransporters. ....	5
1.1.2 NKCC1 and KCC2 are crucial for brain development, cellular proliferation and secreting epithelia. ....	6
1.2 NKCC1 structure. ....	8
1.2.1 Ion transport pathway and K <sup>+</sup> , Na <sup>+</sup> , Cl <sup>-</sup> binding sites. ....	10
1.3 Expression and role of other NKCCs and KCCs.....	12
1.4 Chloride transporters in neurodevelopmental disorders. ....	13
1.4.1 Inhibition of NKCC1 by bumetanide for the treatment of neurological diseases. ....	15
1.4.2 Epilepsy.....	15
1.4.3 Autism spectrum disorders.....	16
1.4.4 Rett syndrome.....	17
1.4.5 Fragile X syndrome.....	17
1.4.6 Schizophrenia.....	18
1.4.7 Tuberous Sclerosis Complex.....	18
1.4.8 Traumatic brain injury.....	19
1.4.9 Glioma.....	19
1.4.10 Down syndrome.....	20
1.5 GABAergic transmission in DS.....	21
1.5.1. NKCC1 dysregulation drives depolarizing GABA <sub>R</sub> signalling in Down syndrome.....	21
1.5.2 Bumetanide treatment rescues the altered GABAergic transmission, synaptic plasticity and cognitive deficits in Ts65Dn Mice.....	22
1.6 Bumetanide repurposing: issues and pitfalls.....	23
1.6.1 Bumetanide analogues and prodrugs.....	25
<b>Aim of the project</b> .....	<b>28</b>
<b>Chapter 2. Design, synthesis and characterization of novel bumetanide analogues</b> .....	<b>29</b>
2.1 Rationale.....	29
2.2 Synthesis of a small library of bumetanide analogs.....	30
2.3 Results and discussion.....	34
2.4 Experimental section.....	38

<b>Chapter 3. Discovery and characterization of novel selective NKCC1 inhibitors.....</b>	<b>51</b>
3.1 Ligand based identification of new molecular scaffolds.....	51
3.2 Synthesis of 2-amino-5-nitro-benzene-sulfonamide derivatives (Series A).....	54
3.2.1 Testing of 2-amino-5-nitro-benzene-sulfonamide derivatives (Series A).....	55
3.3 Synthesis of 4-amino-3-sulfamoyl-benzoic acid derivatives (Series B).....	57
3.3.1 Testing of 4-amino-3-sulfamoyl-benzoic acid derivatives (series B).....	60
3.4 Evaluation of the most promising compounds in calcium kinetic assay in neuronal cultures.....	64
3.5 Experimental section.....	67
<b>Chapter 4. Characterization of lead compound ARN23746.....</b>	<b>94</b>
4.1 <i>In vitro</i> characterization of ARN23746.....	94
4.1.1 ARN23746 is able to restore the physiological chloride concentration in Ts65Dn neurons.....	94
4.1.2 ARN23746 does not inhibit significantly NKCC2 and KCC2.....	95
4.1.3 <i>In vitro</i> assessment of AR23746 drug-like properties.....	97
4.2 <i>In vivo</i> characterization of ARN23746.....	98
4.2.1 ARN23746 displays higher brain penetration compared to bumetanide.....	98
4.2.3 ARN23746 does not exert significant diuretic effect <i>in vivo</i> .....	100
4.2.2 ARN23746 is able to rescue memory deficits in Down syndrome mice.....	101
4.2.4 Toxicity assessment of ARN23746 after chronic treatment.....	104
4.2.5 ARN23746 is able to rescue social deficits and the repetitive behaviors in the valproic acid mouse model of autism with no diuretic effect.....	106
4.3 Discussion.....	108
4.4 Experimental section.....	110
<b>Chapter 5. Design, synthesis and characterization of ARN23746 derivatives.....</b>	<b>118</b>
5.1 Rationale.....	118
5.1.1 Synthesis of bioisosteric analogues of the carboxylic moiety of ARN23746.....	119
5.1.2 Synthesis of substituted sulfonamide derivatives.....	121
5.1.3 Synthesis of R <sup>2</sup> substituted analogues.....	121
5.2 Results and discussion.....	126
5.3 Experimental section.....	131
<b>Chapter 6. Concluding Remarks.....</b>	<b>148</b>
References.....	153
Appendix.....	166

## Abstract.

Proper GABAergic transmission through Cl<sup>-</sup>-permeable GABA<sub>A</sub> receptors is fundamental for physiological brain development and function. Indeed, defective GABAergic signaling – due to a high NKCC1/KCC2 expression ratio – has been implicated in several neurodevelopmental disorders (e.g., Down syndrome, DS, Autism spectrum disorders, ASD). Interestingly, NKCC1 inhibition by the FDA-approved diuretic drug bumetanide reverts cognitive deficits in the TS65Dn mouse models of DS and core symptoms in other models of brain disorders. However, the required chronic treatment with bumetanide is burdened by its diuretic side effects caused by the antagonization of the kidney Cl<sup>-</sup> importer NKCC2. This may lead to hypokalemia, while jeopardizing drug compliance. Crucially, these issues would be solved by selective NKCC1 inhibitors, thus devoid of the diuretic effect of bumetanide. To this aim, starting from bumetanide's structure, we applied a ligand-based computational approach to design new molecular entities that we tested *in vitro* for their capacity to selectively block NKCC1. Extensive synthetic efforts and structure-activity relationships analyses allowed us to improve *in vitro* potency and overall drug-like properties of the initially identified chemical hits. As a result, we identified a new highly potent NKCC1 inhibitor (ARN23746) that displayed excellent solubility, metabolic stability, and no significant effect on NKCC2 *in vitro*. Moreover, this novel and selective NKCC1 inhibitor was able to rescue cognitive deficits in DS mice and social/repetitive behaviors in ASD mice, with no diuretic effect and no overt toxicity upon chronic treatment in adult animals. Thus, ARN23746 a selective NKCC1 inhibitor devoid of the diuretic effect – represents a suitable and solid therapeutic strategy for the treatment of Down syndrome and all the brain neurological disorders characterized by depolarizing GABAergic transmission.

## Contribution statement

The medicinal chemistry work exposed in this thesis illustrates part of an extensive drug discovery project conducted in collaboration with the laboratory of Brain Development and Disease led by Dr. Laura Cancedda at IIT. This drug discovery effort aimed at the individuation of novel specific NKCC1 inhibitors for the treatment of neurodevelopmental disorders. In this thesis, I mostly focus on my contributions to the project during my PhD. In particular, I will emphasize and discuss my contributions in the design, synthesis, optimization and physicochemical characterization of the molecules that have been discovered and realized during the drug discovery project. The *in vitro* and *in vivo* experiments presented in the thesis, on the other hand, have been designed and performed by our collaborators. In specific, most of the *in vitro* and *in vivo* studies were mainly carried out by Dr. Annalisa Savardi, Dr. Roberto Narducci and Dr. Andrea Contestabile, which are all members of Dr. Cancedda's laboratory.

## Chapter 1. NKCC1 function, structure and pathological relevance.

### 1.1 Cation-chloride cotransporters.

GABA ( $\gamma$ -aminobutyric acid) is the main inhibitory neurotransmitter in the brain and the first to be functional in developing neuronal networks during brain development. At inhibitory synapses, the neurotransmitter GABA activates the ionotropic GABA<sub>A</sub> receptor (GABA<sub>A</sub>R). GABA<sub>A</sub>Rs are ligand-gated ion channels that respond to binding of GABA released at inhibitory synapses. GABA<sub>A</sub>Rs open and regulate neuronal excitability in the central nervous system by increasing neuronal permeability to chloride (Cl<sup>-</sup>). Neuronal chloride regulation is an essential factor for the regulation of GABAergic signalling. Depending on its concentration gradient across the cell membrane and the membrane resting potential of the neuron, Cl<sup>-</sup> can flow through the GABA<sub>A</sub>R in both the directions. In the mature brain the intracellular Cl<sup>-</sup> concentration ([Cl<sup>-</sup>]<sub>i</sub>) is generally low, directing Cl<sup>-</sup> influx into the cell leading to hyperpolarizing and inhibitory actions of GABA. However, during early neurodevelopment and certain pathophysiological conditions<sup>1</sup>, there is a high Cl<sup>-</sup> concentration inside the cell. Thus, opening of the GABA<sub>A</sub>R causes a Cl<sup>-</sup> efflux from the cell and consequently GABA activation results in a depolarization of the membrane<sup>2</sup>. This depolarization leads to activation of voltage-gated calcium channels and removal of the Mg<sup>2+</sup> block from NMDA receptors, causing further membrane depolarization and calcium influx into the cell. These sequences of events are vital for the activation of second messengers that participate in neuronal migration, differentiation, synaptogenesis and physiological brain development<sup>3-6</sup>. Most mature neurons in the central nervous system (CNS) actively extrude Cl<sup>-</sup> and thus exhibit a low intracellular Cl<sup>-</sup> concentration<sup>7</sup> ([Cl<sup>-</sup>]<sub>i</sub>). This is a necessary condition for the generation of hyperpolarizing inhibitory potentials by GABA<sub>A</sub>R receptors. The main regulators of Cl<sup>-</sup> homeostasis in neurons are the Cation-chloride cotransporter<sup>8,9</sup> (CCCs), especially the sodium-potassium-chloride cotransporter isoform 1 (NKCC1) and the potassium-chloride symporter isoform 2 (KCC2). NKCC1 is highly expressed in immature neurons and is the principal transport mechanism responsible for Cl<sup>-</sup> uptake, leading to high [Cl<sup>-</sup>]<sub>i</sub> ( $\approx$  30mM), and for the depolarizing and mostly excitatory GABA<sub>A</sub>R responses<sup>10,11</sup>. KCC2 is highly expressed in mature neurons, where it keeps the

intracellular  $\text{Cl}^-$  level at low values (4-6 mM)<sup>12</sup>, thereby determining the hyperpolarizing and inhibitory GABA action<sup>3,13-15</sup>.

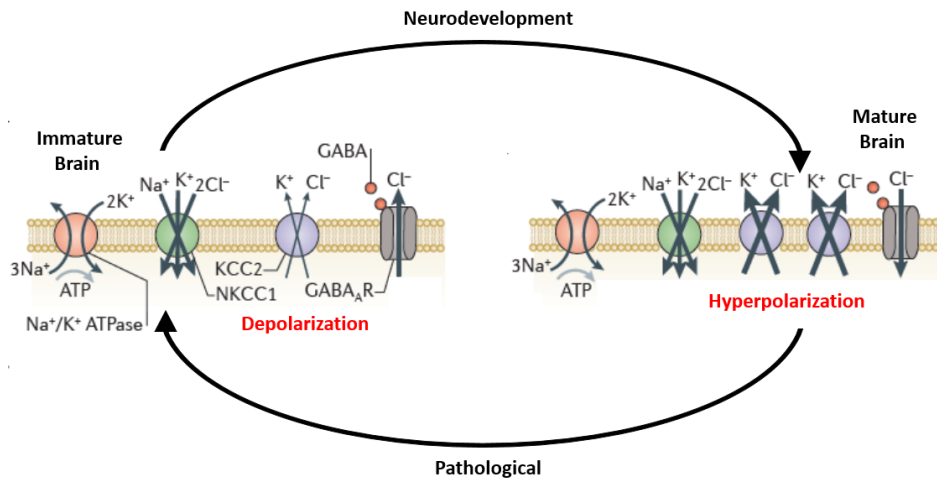


**Figure 1.1.** Schematic representation of the control mechanism of intracellular  $\text{Cl}^-$  concentration ( $[\text{Cl}^-]_i$ ) by NKCC1 and KCC2 in neurons. CCCs use the  $\text{K}^+$  and  $\text{Na}^+$  gradients generated by the Na-K/ATPase. In immature neurons, NKCC1 drives cellular uptake of  $\text{Cl}^-$  via NKCC1 and KCC2 has a minor role. This generates a depolarizing  $\text{Cl}^-$  current upon  $\text{GABA}_A\text{Rs}$  opening. During neuronal maturation, functional KCC2 attains a high level of expression and the  $\text{Cl}^-$  current becomes hyperpolarizing.  $\text{Cl}^-$  extrusion by KCC2 is favoured by the Na-K/ATPase  $\text{K}^+$  generated gradient. The NKCC1/KCC2 ratio can be dysregulated in pathological development. Adapted from Kaila et al., 2014.

### 1.1.2 NKCC1 and KCC2 are crucial for brain development, cellular proliferation and secreting epithelia.

NKCC1 and KCC2 have a pivotal role in physiological brain development. The high levels of NKCC1 in early developmental phases, before the maturation of sensory inputs, induce endogenous network activity, which contributes to the construction of neuronal connections. The high  $\text{Cl}^-$  concentration maintained by the high expression of NKCC1 and the low expression of KCC2 is fundamental for neuronal morphological maturation. Indeed, knockdown of NKCC1 *in vivo* disrupts the dendritic maturation of mouse cortical neurons<sup>16,17</sup>.

NKCC1 is also present on the tips of growing neurites and its blockade by RNA interference<sup>18-20</sup> or pharmacological inhibition by treatment with bumetanide<sup>21</sup> abolishes neurite outgrowth *in vitro*.

After the first synaptic connection among developing neurons are built, depolarizing GABA also controls spontaneous neuronal activity in the form of network action potential bursts of different shapes across brain areas and species.

Upregulation of KCC2 during development ends the trophic effect of depolarizing GABA by lowering the neuronal Cl<sup>-</sup> levels. This shift in regulation occurs during the second postnatal weeks in rodents. In rat hippocampi, an increased KCC2 mRNA expression is observed after postnatal week 2<sup>22</sup>, whereas a decrease of NKCC1 expression is observed between P14 and P21<sup>22</sup>. In comparison, in humans, KCC2 expression increases around postconceptional week (PCW) 40, whereas NKCC1 expression reaches adult levels around PCW 50<sup>22</sup>. Aside from being species-specific, the developmental upregulation of KCC2 is also brain region-specific. Indeed, the developmental gradient in the onset of KCC2 expression proceeds from caudal-to-rostral regions of the CNS<sup>9,23</sup>. In addition, evolutionarily older brain structures (e.g, spinal cord, brainstem, and hypothalamus) develop earlier the mature pattern of NKCC1 and KCC2 expression<sup>24</sup>.

NKCC1 play also a key role in cellular proliferation and apoptosis. NKCC1 knockdown mice have defects in the proliferation of neural precursor cells of the subventricular zone<sup>17</sup>. Moreover, inhibition of NKCC1 with the drug bumetanide inhibits cell proliferation in neuronal precursors of the subventricular zone in mice<sup>25</sup>. Several evidence suggest also that NKCC1 plays a fundamental role in apoptosis during development. In particular, NKCC1 is implicated in the activity-regulated cell death in Cajal-Retzius neurons, a population that mostly disappears from apoptosis early in life in the mouse-developing cortex<sup>26</sup>. Accordingly, NKCC1 blockade by bumetanide *in vitro* or genetic deletion of the cotransporter *in vivo* (NKCC1<sup>-/-</sup> mice) rescued the population of Cajal-Retzius neurons from apoptosis<sup>26</sup>.

NKCC1 is also highly expressed in the choroid plexus of mice and rats, during both development and adulthood<sup>9,27</sup>. In this district, NKCC1 is located on the apical membrane of epithelial cells and it plays a key role in the formation of the cerebrospinal fluid (CSF). Conversely, KCC2 is not expressed in the choroid plexus epithelial cells in mice<sup>28</sup>.

Finally, NKCC1 is also expressed in the inner ear, where its knockdown leads to a defect in the production of endolymph in the ear secreting epithelia leading to deafness and imbalance<sup>29</sup>.



## 1.2 NKCC1 structure.

NKCC1 is a glycoprotein encoded by the gene *Slc12a2* consisting in 12 transmembrane segments and intracellular C-terminal domain (CTD) and N-terminal domain (NTD). The full-length protein has a core molecular weight of ~ 121 kDa. Two splice variants can result from *Slc12a2* post translational modification, NKCC1a and NKCC1b. In the adult human brain, the expression of NKCC1b is significantly higher than NKCC1a<sup>30</sup>. Nevertheless, function of the two variants role and their expression pattern in brain function and pathology is still unclear<sup>31</sup>.

Recently, Chew *et al.* reported the cryo-electron microscopy (cryo-EM) structure of NKCC1 of *Danio rerio*<sup>32</sup>. Consistently with previous knowledge<sup>33,34</sup>, the authors found that NKCC1 presents a dimeric structure (Figure 1.2a) constituted by the C-terminal domain (CTD) of one subunit close to the transmembrane domain (TMD) of the opposing subunit, which form a swapped configuration (Figure 1.2a). All the domains contribute to the function of the protein. The TMD contains the ion-translocation pathway, while the cytosolic N- terminal (NTD) and the CTD domains regulate transport and trafficking.

Cation-chloride cotransporters belong to the amino-acid-polyamineorganocation (APC) superfamily. The transporters share indeed a common structural scaffold that results then in permeability to different ions. Accordingly, the NKCC1 TMD adopts an APC superfamily fold, with an inverted repeat architecture formed by transmembrane segment (TM)1–TM5 and TM6–TM10 (Fig. 1.2c). Two TMDs interact through an interface formed by TM11, TM12 and the TM10 CTD end. The two TMDs are favoured in their association by the presence of three lipid molecules in the inner membrane leaflet at level of the dimer interface.

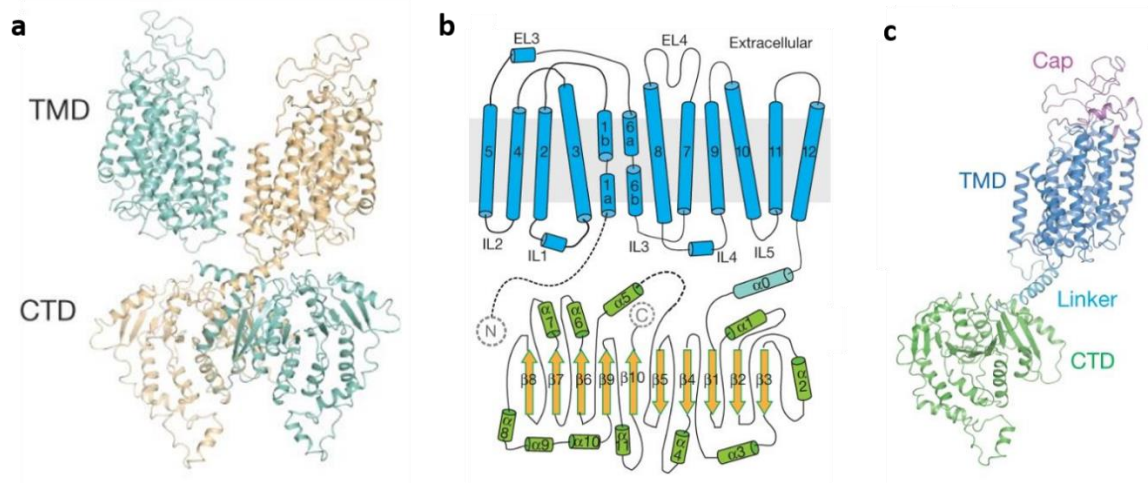


**Figure 1.2.** (a), Overall structure of the NKCC1 dimer. (b), Topology diagram of NKCC1. c, NKCC1 monomer coloured by structural element.. Adapted from Chew et al. 2019.

NKCC1 presents also an extracellular element called cap domain (Figure 1.2b,c), which is important for surface expression and transport regulation in human NKCC1. The cap domain is formed by an extended ordered loop between TM7 and TM8 (EL4) stabilized by a conserved disulphide bond and a structured element between TM5 and TM6 (EL3).

The NKCC1 NTD structure and interactions have not been understood in detail. However, the NTD apparently does not make direct contacts with the TMD or CTD. This data prompts for further investigations of the NTD role and structure. Instead, the CTD core adopts a mixed  $\alpha/\beta$  fold with two structurally related subdomains. Previous literature<sup>35-37</sup> highlighted the importance of the CTD in NKCC1 folding, in particular for protein homodimerization, and proper membrane trafficking. In addition, substantial movement of the CTD accompanies NKCC1 activation. Consistently, the authors found that the two protomers CTDs directly interact suggesting a pivotal role for dimerization. Finally, the CTD is connected by an  $\alpha$ -helix with a linker to the TMD. This helix crosses below the TMD-dimer interface, bringing the CTD of one protomer under the TMD of its neighbouring protomer, producing a domain swapped architecture.

### 1.2.1 Ion transport pathway and K<sup>+</sup>, Na<sup>+</sup>, Cl<sup>-</sup> binding sites.

The ion transport pathway is located in the TMD into a solvent-accessible cavity surrounded by four transmembrane segments that extend from the intracellular surface into the TMD. This cavity widens half-way approaching the intracellular side and presents a marked electrostatic sidedness as an indication of selectivity towards anion or cations. The potassium cation (K<sup>+</sup>) binding site is located in the typical APC substrate-binding pocket. In this vestibule, K<sup>+</sup> is coordinated by the backbone carbonyl of Asn220, Ile221, Pro417 and Thr420 (Figure 1.3a) and directly interacts with the hydroxyl group of Tyr305. Interestingly, Tyr305 is rigorously conserved (Figure 1.3c) in K<sup>+</sup>-transporting NKCC and KCC but not in K<sup>+</sup>-independent sodium-chloride symporter (NCC), which contains histidine instead<sup>38</sup>. A Na<sup>+</sup> binding site similar to the Na2 coordination site conserved across many APC transporters has been observed in NKCC1. The authors found in this site two consecutive serines (Ser538 and Ser539), that are strictly conserved in Na<sup>+</sup>-transporting NKCCs and NCC, whereas cysteine and glycine are typically found in Na<sup>+</sup>-independent KCCs<sup>38</sup>. These residues are sustained in their function by the backbone carbonyls of two TM1 residues (Leu219 and Trp222), one TM8 residue (Ala535) in direct Na<sup>+</sup> coordination (Figure 1.3b). Superimposition of this site with the Na2 of the SiaT (Figure 1.3b) transporter revealed nearly identical spatial disposition of the coordinating elements, corroborating the Na<sup>+</sup> binding function of this region.

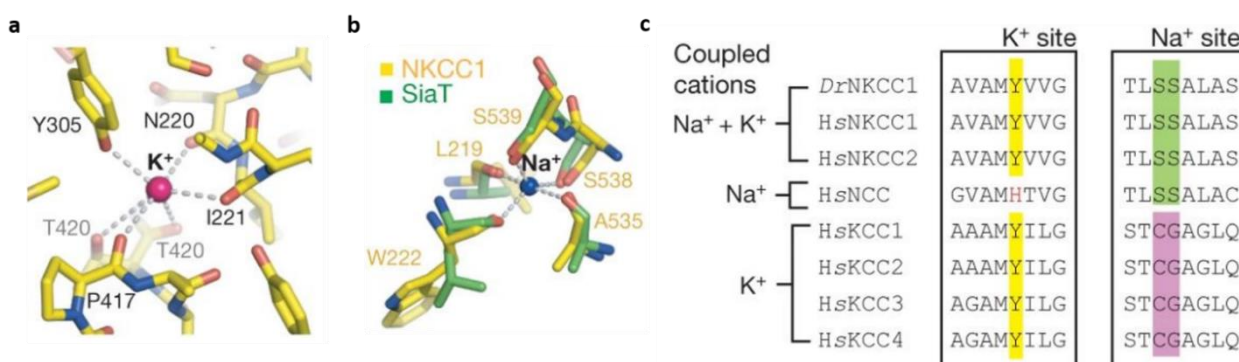


**Figure 1.3.** Representation of the K<sup>+</sup> and Na<sup>+</sup>-binding sites. (a), K<sup>+</sup>-binding site. Dashed lines denote possible coordination. (b), Na<sup>+</sup>-binding site. Superimposition of the Na<sup>+</sup>-binding site (yellow) of NKCC1 onto the Na2 site of (green) SiaT. Dashed lines denote the Na<sup>+</sup> coordination in SiaT. (c), Sequence alignment around K<sup>+</sup>- or Na<sup>+</sup>-coordinating residues of human and zebrafish CCCs. Highlighted positions show Y305 (K<sup>+</sup>-coordinating), S538 and S539 (Na<sup>+</sup>-coordinating). Adapted from Chew et al. 2019.

Chew and collaborators also studied the Cl<sup>-</sup>-binding sites via molecular dynamics (MD) simulations. The calculations indicated three potential Cl<sup>-</sup>-binding sites with two chloride ions bound in any of these three regions at once. Among the three potential Cl<sup>-</sup>-binding sites, two are deep in the translocation pathway and resemble Cl<sup>-</sup>-coordinating sites in other transporters with adjacent main-chain amide coordination (Figure 1.4a, left and middle), leading to stable binding in simulations. By contrast, the site closest to the intracellular bulk solvent (Figure 1.4a, right) coordinated Cl<sup>-</sup> less tightly through side-chain interactions, indicating probably a transient Cl<sup>-</sup> binding function.

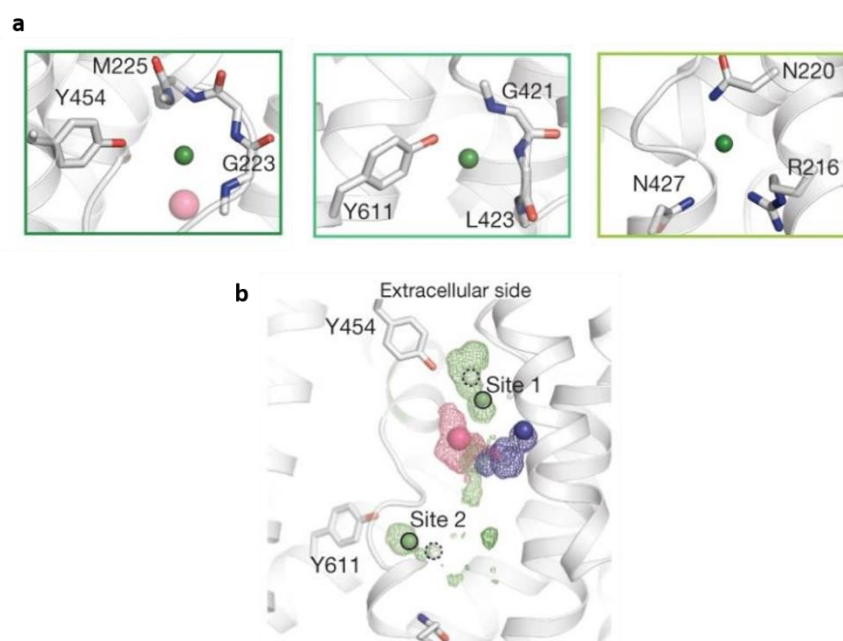


**Figure 1.4.** Cl<sup>-</sup> binding sites. (a), Regions of Cl<sup>-</sup> binding identified via molecular dynamics. (b), Ion probability densities, as shown in a, for a simulation initiated with all four ions bound. Pink, blue and green (with dashed boundaries) spheres indicate the initial position of K<sup>+</sup>, Na<sup>+</sup> and Cl<sup>-</sup>, respectively. Green spheres with solid boundaries indicate the positions of Cl<sup>-</sup>, based on the cryo-EM map. Adapted from Chew et al. 2019.

Further MD simulations with both cations bound and with chloride ions bound at the two stable Cl<sup>-</sup>-binding regions (Figure. 1.4a, left and middle) ended with the Cl<sup>-</sup> shifted away from Tyr454 to form an electrostatic interaction with K<sup>+</sup> (Fig. 1.4c). Additional calculations suggested that one Cl<sup>-</sup> binds primarily to K<sup>+</sup> and the main chain amides of Val224 and Met225 (site1), while the second Cl<sup>-</sup> shifts to coordinate with main-chain amides at positions 421-423 and the side chain of Tyr611 (site 2, Figure 1. 4b). Then, simulations initiated with K<sup>+</sup> and Na<sup>+</sup> bound - but not with only either K<sup>+</sup> or Na<sup>+</sup> bound showed frequent Cl<sup>-</sup> binding to the more intracellular Cl<sup>-</sup> site (site 2), suggesting that both cations are needed to facilitate Cl<sup>-</sup> binding. The authors performed mutagenesis studies to confirm this

computational data. Consistently, replacing of Tyr611 diminished Cl<sup>-</sup> transport activity, while mutating Tyr454 completely abolished Cl<sup>-</sup> uptake highlighting the importance of this residue for ion transport.

### 1.3 Expression and role of other NKCCs and KCCs.

Besides NKCC1, another NKCC1 isoform is expressed in the kidney. The NKCC2 isoform (encoded by Slc12a1) is mainly expressed in the apical membrane of the epithelial cells of the thick ascending limb (TAL) of the loop of Henle and the macula densa cells (specialized sensor cells detecting changes in the fluid composition of the distal tubule). In these districts, NKCC2 mediates the reabsorption of Na<sup>+</sup> and Cl<sup>-</sup> into the blood contributing to the maintenance of blood pressure<sup>39,40</sup> NKCC2 is the target of loop diuretics (e.g. bumetanide, furosemide, azosemide, torasemide, ethacrynic acid). Blockade of NKCC2 by these drugs lead to a substantial natriuresis, hyponatraemia, kaliuresis, hypokalemia and diuresis. NKCC2 gene's loss of function mutations cause Bartter's syndrome, the clinical features of which are hypotension, hypokalaemia, hypercalciuria and metabolic alkalosis<sup>41</sup>. Finally, NKCC2 is strongly expressed also in the epithelial layer of the endolymphatic sac in humans, a part of the vestibular system<sup>42</sup>.

The KCC family is composed by three other isoforms, namely KCC1, KCC3 and KCC4. Although these isoforms are less studied, it is believed that they play an important role in physiological brain development. In the embryonic mouse brain, KCC1 mRNA is exclusively present in the choroid plexus<sup>9</sup>, but KCC1 transcripts have been found in neuronal and glial cells in the olfactory bulb, hippocampus, choroid plexus, and posterior hypothalamic nucleus of the adult rat CNS *in vivo*<sup>27</sup>. KCC3 mRNA expression is generally weak in embryonic rodent brain<sup>9</sup>, but KCC3 was detected in all adult CNS regions, mainly located in myelinated tracts of the spinal cord and brain, although cells in the choroid plexus, pyramidal neurons in the hippocampus and cortex, and cerebellar Purkinje cells were also labelled<sup>43</sup>. Moreover, KCC3 protein is expressed in white matter-rich structures in the rodent brain, spinal cord and peripheral nerves, indicating a role of KCC3 in myelination<sup>43</sup>. Nevertheless, the physiological roles of KCC3 in neurons remain largely unknown<sup>44-46</sup>, its importance in CNS function is strongly underlined by the fact that peripheral neuropathy associated with agenesis of the corpus

callosum (ACCPN; also known as Andermann syndrome) is caused by a loss of function mutation of KCC3<sup>47</sup>. Interestingly, neuron-specific knockout of KCC3 in mice recapitulate most of the neuropathic features of ACCPN 119 as locomotor abnormalities and areflexia as well as axonal swelling, hypomyelination and demyelination in sciatic nerves<sup>48</sup>. KCC4 is highly expressed in the embryonic mouse brain, including choroid plexus, peripheral ganglia, ventricular zones and the nucleus of the trigeminal nerve<sup>9</sup>. KCC4 is involved along NKCC1 in cochlear development, as KCC4 KO mice exhibit deafness. KCC4 loss possibly exerts that effect by causing the death of hair cells by osmotic perturbation or membrane depolarization<sup>49</sup>.

Spatiotemporal expression of the KCC transporters has been studied also in humans. In particular, KCC1 mRNA was first observed in the cortex of the cerebellum at embryonal stages (between PCW 10-13) and found in other brain regions (hippocampus, striatum and thalamus between PCW 21 and birth)<sup>50</sup>. KCC3 mRNA was described in the cortex, cerebellum, hippocampus, amygdala, striatum and thalamus in all the stages of development and adulthood (age range: 5 PCW–82 years)<sup>50</sup>. KCC4 mRNA was detected at low levels in the cortex both at prenatal and postnatal ages<sup>7</sup>, but not detected in a subsequent study in any brain region<sup>50</sup>. NKCC2 mRNA was not detected in any brain region<sup>50</sup>.

#### **1.4 Chloride transporters in neurodevelopmental disorders.**

The term neurodevelopmental disorders (NDs) encompasses a wide range of chronic neurological/psychiatric diseases that affect 4-5% of the population<sup>51</sup>. Such pathological conditions are mostly caused by impaired nervous system development, induced by both genetic and environmental factors, leading to abnormal brain function.

The complex plot of spatiotemporal events needed for proper nervous system development opens to many potential causes of neurodevelopmental disorders that may affect different areas of the nervous system at different times and ages. Although most of the NDs share a number of features (e.g., impairments in learning, memory, emotional regulation, sociality, and self-control) and some comorbidity (e.g., increased seizure susceptibility and sleep disorders). Strikingly, high  $[Cl^-]_i$  levels and

excitatory GABA actions attributable to an altered NKCC1/KCC2 ratio were observed in a wide range NDs including epilepsy, autism spectrum disorders, Asperger syndrome, Rett syndrome, Fragile X syndrome, schizophrenia, tuberous sclerosis complex, traumatic brain injury, glioma and Down syndrome<sup>1,52-55</sup>.

Interestingly, pharmacological approaches aimed at restoring  $[Cl^-]_i$  by modulating of NKCC1/KCC2 activity proved to have a beneficial effect in rodent models and patient with this conditions. In order to restore physiological  $[Cl^-]_i$ , it is possible to inhibit NKCC1 importer activity or to enhance KCC2 exporter activity<sup>1,52-54,56</sup>. In the last years, a growing body of studies used bumetanide, which has been used over decades as a potent loop diuretic, as NKCC1 inhibitor in the brain. Bumetanide is able to restore at low doses physiological  $[Cl^-]_i$  levels and to enhance GABAergic inhibitory function and has no effects on GABAergic activity in NKCC1 knockouts<sup>10</sup>, suggesting that antagonizing NKCC1 is the most likely underlying mechanism of action<sup>1</sup>. Another suitable option has recently proved to be KCC2 activity enhancement by pharmacological modulation. Gagnon et al. identified the small molecule CLP257<sup>57</sup>, able to effectively enhance  $Cl^-$  extrusion *in vitro* in cultured cell lines and in spinal cord slices obtained from rats with peripheral nerve injury, characterized by reduced KCC2 function<sup>57</sup>. Interestingly, CLP257 exerted antinociceptive effect *in vivo* in peripheral nerve injury rats<sup>57</sup>. Nevertheless, another group was unable to reproduce CLP257 activity *in vitro* on KCC2 in the same cultured cell line used in this study, opening the possibility that CLP257 do not target KCC2 *in vivo*<sup>58</sup>. Gagnon and colleague replied to Cardarelli and co-workers objection confirming their previous findings<sup>59</sup>, thus indicating the need for further investigation.

Recently, another study achieved to rescue electrophysiological activity by pharmacological enhancement of KCC2 gene expression<sup>60</sup>. The authors identified a number of hit compounds acting on different pathways: inhibitors of the fms-like tyrosine kinase 3 (FLT3) or glycogen synthase kinase 3 (GSK3 $\beta$ ) pathways and activators of the sirtuin 1 (SIRT1) and transient receptor potential cation channel subfamily V member 1 (TRPV1) pathways. These compounds were able to rescue proper GABAergic transmission, excitatory synapses, and neuronal morphological development in Rett syndrome neurons *in vitro* by increasing KCC2 expression<sup>60</sup>. Notably, *in vivo* administration of the

FLT3 inhibitor KW-2449 or TRPV1 agonist piperine in Rett syndrome mutant mice ameliorated disease-associated respiratory and locomotion phenotypes<sup>60</sup>.

#### **1.4.1 Inhibition of NKCC1 by bumetanide for the treatment of neurological diseases.**

Although the above-mentioned approaches demonstrated to be promising therapeutic approaches, a growing body of literature describes the positive outcomes of direct NKCC1 inhibition by bumetanide in a number of neurological conditions including neurodevelopmental disorders, psychiatric disorders, and CNS traumatic injuries. These studies opened the way to the proof of concept that NKCC1 pharmacological inhibition is a sustainable therapeutic approach with a high translational potential. In the following paragraphs, the pathologies in which NKCC1 is involved and bumetanide has been evaluated are briefly discussed, with particular attention to Down syndrome and autism spectrum disorders.

#### **1.4.2 Epilepsy**

Epilepsy is characterized by recurrent, usually unprovoked epileptic seizures, and there is a wide spectrum of cognitive, psychosocial, and social consequences of this condition<sup>61</sup>. Varieties of genetic and developmental abnormalities as well as brain insults have the potential to induce epileptogenesis in humans and rodent disease models. Between these, there is a wide range of alterations that are responsible for disrupted excitatory/inhibitory balance. Imbalance in NKCC1 and KCC2 activity together with depolarizing GABAergic action have been observed in several animal models of epilepsy<sup>1,62</sup> including amygdala-kindled rats<sup>63</sup>, pilocarpine-induced status epilepticus<sup>64</sup> post-traumatic seizures, trauma and neuronal hyperactivity<sup>64,65</sup>. Moreover, mice deficient in KCC2 show recurrent seizure episodes<sup>66</sup>. A number of studies also confirmed positive outcomes upon bumetanide treatment<sup>61,64,65,67-86</sup>.

In addition, several human studies indicate that an imbalance in NKCC1/KCC2 ratio is also present in epileptic patients. Downregulation of KCC2 and/or upregulation of NKCC1 was observed in



hippocampal brain slices from adult patients with temporal lobe epilepsy<sup>87-91</sup>. Then, other studies found improper NKCC1/KCC2 ratio in several other clinical conditions characterized by epileptic events like hypothalamic hamartoma<sup>92</sup>, infantile epilepsy<sup>93</sup>, peritumoral epilepsy<sup>94,95</sup> and, more recently, Dravet syndrome<sup>96</sup>. Importantly, treatment with bumetanide was able to ameliorate seizure frequency in temporal lobe epilepsy<sup>71</sup>. Moreover, bumetanide was able to reduce seizure duration and frequency in a child affected by intractable multifocal seizures<sup>97</sup>. In addition, a phase I/II trial (NEMO trial) assessing the efficacy and safety and optimal dose of bumetanide for the treatment of acute neonatal encephalopathy seizures has been performed<sup>98</sup>, but was recently halted due to poor bumetanide antiepileptic action and ototoxicity<sup>99</sup>.

#### **1.4.3 Autism spectrum disorders.**

Autism spectrum disorders (ASDs) are a group of NDs characterized by an impressive clinical and pathogenic heterogeneity with early onset in life, sharing autism as a common feature, but caused by separate processes<sup>100</sup>. It is characterized by two core symptoms: (1) persistent deficits in social communication and social interaction, (2) restricted, repetitive patterns of behavior, interests, and activities. Moreover, ASD can be comorbid with other neurodevelopmental syndromes such as epilepsy<sup>101</sup>, Rett syndrome<sup>102</sup>, Fragile X<sup>103</sup> syndrome<sup>104</sup>, or Down syndrome<sup>105</sup>. Several lines of evidence suggest that an impairment of GABAergic transmission contributes to the development of ASDs, both in rodent models and humans<sup>4</sup>. Interestingly, two rare, functional impairing variants in the KCC2 C-terminal regulatory domain are observed more frequently in families with ASD<sup>106</sup>. Moreover, autistic children show paradoxical response (eg. anxiety and aggression) to GABA-enforcing agents such as benzodiazepines, suggesting an involvement of depolarizing GABAergic action in ASDs<sup>107,108</sup>. These evidences prompted to the evaluation of the efficacy of bumetanide in ASD patients. A pilot trial performed on five children led to amelioration of behavioural symptom severity<sup>109</sup>. Based on these results a larger clinical trial for 54 autistic patients was designed<sup>110</sup> and consequently a phase II clinical study<sup>111</sup>. Moreover, treatment with bumetanide of a young girl with Asperger syndrome, a neurodevelopmental disorder belonging to ASD, led to an improvement of sensory behaviours<sup>112</sup>.

#### **1.4.4 Rett syndrome.**

Rett syndrome (RTT) is a neurodevelopmental disorder that arises from loss-of-function mutations in the X-linked methyl-CpG binding protein 2 gene (*Mecp2*). MeCP2 plays a critical role in brain development and adult neural function regulating the transcription of a number of genes by promoter methylation. Individuals affected by RTT display normal growth until the age of 6-18 months but then develop various symptoms (e.g., cognitive impairment, seizures, altered motor function and stereotype behaviours)<sup>113</sup>. As for other NDs, several studies relate RTT pathophysiology in rodent models and humans with possible alterations in the GABAergic signalling<sup>4</sup>. A first study detected decreased levels of KCC2 expression on CSF obtained from RTT patients<sup>114</sup>. More recently, a lowering in KCC2 expression has been found in human progenitor cells from RTT patients<sup>115</sup> as well as in a *Mecp2* gKO mouse model of RTT<sup>116</sup>. Accordingly, treatment with bumetanide restored GABA polarity and reversal potential in *Mecp2* gKO mice<sup>116</sup>.

#### **1.4.5 Fragile X syndrome.**

Fragile X syndrome (FXS) is a genetic disorder caused by mutations in the X-linked FMR1 gene encoding for Fragile X mental retardation protein (FRMP). FXS individuals show cognitive deficits, autistic behavior, hypersensitivity to sensory stimuli and comorbidity with epilepsy<sup>117</sup>. There are some indications that the excitatory/inhibitory balance is disturbed in FRX<sup>1</sup>. Interestingly, a study on FXS mice showed that increased expression of NKCC1 caused a delay in the developmental switch of GABA polarity from depolarizing to hyperpolarizing<sup>118</sup>. Importantly, another study in rodents found that foetal treatment with bumetanide right before birth was able to recover the intracellular Cl<sup>-</sup> concentration, GABAergic transmission and autistic like behaviours<sup>71,119</sup>. The positive outcome of earlier human study on autistic patients<sup>110</sup>, led also to a pilot study in a FRX child with bumetanide<sup>103</sup>. Importantly, treatment with bumetanide was able to attenuate the severity of autistic core symptoms, opening the way to larger clinical investigations.

#### **1.4.6 Schizophrenia.**

Schizophrenia is a neurodevelopmental disorder characterized by psychosis and cognitive impairments, leading to disability and premature mortality. Schizophrenia is characterised by diverse psychopathology: the core features are positive symptoms (e.g., delusions and hallucinations), negative symptoms (e.g., depression and apathy), and cognitive impairment<sup>120</sup>. The aetiology of schizophrenia is linked either to genetic and environmental factors. Between all these factors, a number of studies indicate that GABAergic transmission seems to play an important role in the pathogenesis of this disease. NKCC1 expression was found to be increased in the prefrontal cortex and hippocampus of schizophrenic patients<sup>121,122</sup>. Furthermore, increased expression of the NKCC1 and KCC2 regulatory kinases, OXRS1 and WNK3 was observed in the prefrontal cortex of schizophrenic subjects<sup>123</sup>. These evidences are further corroborated by animal studies, as two different schizophrenia mouse models bear abnormalities in NKCC1/KCC2 ratio<sup>124,125</sup>. Finally, human studies in schizophrenic patients with bumetanide showed a significant reduction in the severity of symptoms, in particular hallucinations<sup>126-128</sup>. Notably, these recurred when treatment was interrupted<sup>126</sup>.

#### **1.4.7 Tuberous Sclerosis Complex**

Tuberous sclerosis complex (TSC) is a multiorgan genetic disorder caused by loss of function mutations of the TSC1 or TSC2 genes<sup>129</sup>. A characteristic feature of TSC is the presence of cortical tubers (i.e., dysplastic lesions), source of focal epilepsy, autistic behaviors and intellectual disability. The previous findings about NKCC1/KCC2 ratio in epilepsy<sup>54</sup> prompted to the hypothesis of an involvement of altered GABAergic signaling also in TSC. Notably, extracts from cortical tubers of TSC patients present an increased NKCC1/KCC2 ratio<sup>128,129</sup>. In addition, altered GABA reversal potential was also described in the cortical tissues<sup>77</sup>. Altogether, these studies suggest a possible involvement of NKCC1/KCC2 imbalance in the pathogenesis of TSC. However further investigation of the pathological mechanism of TSC are needed in order to be able to deliver new therapies targeting dysregulated GABAergic signalling.

#### **1.4.8 Traumatic brain injury.**

Traumatic brain injury (TBI) occurs when external objects or forces cause an injury to the brain. Injuries occurring in childhood can lead to altered neurodevelopment causing cognitive defects persisting for the lifetime of the individual. The pathology of TBI is impacted by both immediate and delayed response mechanisms. The latter are indicated as secondary brain injuries and include damage of the blood-brain barrier, inflammation, excitotoxicity, edema, ischemia and neuronal damage (e.g., excitotoxicity, aberrant ionic homeostasis, axonal disconnection and death<sup>130,131</sup>). Among these factors, excitatory shift of GABAergic transmission may play a major role. Indeed different studies found an increase in NKCC1 expression in the hippocampus and choroid plexus of TBI rat models and that bumetanide administration decreased the inflammatory response and neuronal damage<sup>132-135</sup>. Moreover, treatment with bumetanide attenuated BBB disruption in a mouse model of traumatic brain injury<sup>86</sup>.

#### **1.4.9 Glioma.**

Glioma is a form of brain tumor originating from glial cells and is the most recurring pediatric brain tumor. Pediatric gliomas have unique properties in comparison to those affecting the adults, thus they can be considered neurodevelopmental disorders<sup>136</sup>. Among pediatric gliomas, there is wide heterogeneity from histopathological and therapeutic standpoints. The severity level, and the transition from low-grade to high-grade of morbidity, of gliomas is generally related to the ability of the tumor to migrate and invade other areas. Thus, the invasion phenomena have been widely studied in recent years. Among the mechanisms involved, NKCC1 and other transporters and channels play a role in tumor metastasis<sup>137</sup>. Accordingly, bumetanide administration reduced glioma invasion in mice<sup>138</sup>. Further studies both in primary patient-derived glioblastoma cells *in vitro*, and in mice *in vivo*, found that the involvement of NKCC1 in glioma cell migration was mediated by modulation of the cytoskeleton and regulation of cell volume<sup>139,140</sup>, opening the possibility of NKCC1 as a specific therapeutic target to decrease cell invasion in pediatric glioma patients.

#### **1.4.10 Down syndrome.**

Down Syndrome (DS) is the most common genetic form of intellectual disability, estimated to be 1/750–800 live born<sup>141</sup>, caused by the presence of all, or of part, of a third copy of chromosome 21 (Hsa21). A wide range of typical traits and symptoms can be recognized in DS population, but the most striking clinical features of DS are intellectual disabilities, characterized by low Intelligence Quotient (IQ), learning deficits, and memory impairment, particularly in hippocampus-related functions<sup>142</sup>.

The complex pathophysiological alterations in the DS brain are studied through mouse models that recapitulate many of the phenotypic features of the human syndrome. Ts65Dn mouse is the most widely used DS animal model given that it recapitulates the main phenotypic feature of DS<sup>143</sup>. This model possesses a major portion of mouse chromosome 16 (MMU16) carrying some of Hsa21 orthologues at its distal end translocated to the centromeric region of mouse chromosome 17 (MMU17)<sup>141</sup>. In particular, these mice show impaired neuronal development<sup>144-148</sup> and synaptic plasticity defects<sup>149-151</sup>. Finally, Ts65Dn mice exhibit severe behavioural deficits in different learning and memory tasks due to impaired hippocampus-dependent memory functions<sup>143,149,152,153</sup>, hyperactivity<sup>143,154,155</sup> and sleep disorders<sup>156-158</sup>.

Several pharmacological treatments for DS were proposed for clinical trials on DS individuals based on studies in DS Ts65Dn mice. The FDA-approved drugs fluoxetine, memantine, donepezil and a green tea extract rich in epigallocatechin gallate have been proposed for repositioning to treat cognitive impairment in DS patients<sup>159-161</sup>. However, the mechanism of action in DS is poorly established for these compounds. Epigallocatechin gallate lacks of strong clinical evidence<sup>162</sup> for its activity and many adverse effects have been reported following long-term treatment with fluoxetine<sup>163</sup>. Regarding memantine and donepezil, no significant differences between the treated and placebo groups in two respective double blind clinical trials were registered<sup>164,165</sup>. Interestingly, 2014 Roche started a Phase II clinical trial with is a newly synthesized alpha5 GABA<sub>A</sub> inverse agonist (NCT02024789, basmisanil). Although this specific subunit of the GABA<sub>A</sub> receptor (alpha5 subunit) has been demonstrated to be a promising target for treating cognitive impairment in Ts65Dn mice<sup>166</sup>, the clinical

evaluation of basmisanil did not obtain any significant outcomes to ameliorate cognitive disabilities in DS population<sup>167</sup>.

In this scenario, there are still no approved drugs to ameliorate the cognitive symptoms of Down syndrome and specific educational methods represent the only possible intervention to mitigate cognitive decline in DS in childhood<sup>168,169</sup>. However, adults with DS have a high risk for progressive cognitive decline and loss of acquired abilities<sup>170</sup>. Thus, new pharmacological lifelong treatments are urgently needed, in parallel with further investigations on the still poorly understood mechanism behind cognitive impairment in DS.

## **1.5 GABAergic transmission in DS**

Several lines of evidence indicate that altered GABAergic transmission is responsible for synaptic deficit and memory impairment in DS mouse models and DS individuals<sup>171</sup>. A first main observation that the number of GABAergic interneurons is increased in both the cortex and the hippocampus of adult and adolescent Ts65Dn mice, respectively<sup>145,172</sup>. These alterations were also accompanied by an increase in spontaneous GABAergic postsynaptic events in CA1 pyramidal neurons of adult Ts65Dn mice<sup>145</sup>. In contrast, analyses of autaptic brain samples from DS individuals and analysis of cortical neuronal progenitors showed a general reduction in the GABAergic system at various levels<sup>173,174</sup>. Interestingly, further studies demonstrated that the altered GABAergic transmission affected synaptic plasticity in DS mice, experimentally measured with the long-term potentiation (LTP) protocols in acute brain slices of adult Ts65Dn mice<sup>151,153,175</sup>.

### **1.5.1. NKCC1 dysregulation drives depolarizing GABA<sub>R</sub> signalling in Down syndrome.**

In 2015, our collaborators in this project, with the work of Deidda and colleagues described the dysregulation of the expression of NKCC1 as major cause of altered GABAergic signalling in DS. Strikingly, they found that that GABA<sub>A</sub>R signalling was mostly excitatory rather than inhibitory in adult Ts65Dn mice. The authors found increased [Cl<sup>-</sup>]<sub>i</sub> in hippocampal CA1 pyramidal neurons from

Ts65Dn mice when compared to WT neurons<sup>176</sup>. As a result,  $E_{Cl}$  was less negative than  $V_{REST}$  leading to depolarizing currents upon GABA<sub>A</sub>R activation. Accordingly, they observed an increased mean of firing frequency in individual CA1 neurons upon exogenous GABA application, whereas it was decreased by blockade of GABA<sub>A</sub>R-mediated transmission with GABA<sub>A</sub>R antagonist bicuculline.

Importantly, Deidda and colleagues found that NKCC1 transporter is upregulated the brain of both Ts65Dn mice (Figure 1.5) and individuals with DS, in a consistent manner with excitatory GABAergic signalling<sup>176</sup>. In particular, the authors found increased NKCC1 expression in the entire hippocampus, the CA3-CA1 subregion and cortices of adult Ts65Dn mice compared to WT littermates<sup>176</sup>. Interestingly, Deidda and co-workers found increased NKCC1 expression also in hippocampi from DS individuals, providing a translational link between the animal model and DS individuals. Conversely, levels of KCC2 protein expression in both Ts65Dn mice and DS individuals did not show any considerable alteration. Notably, the authors did not find a significant increase in NKCC1 mRNA in adult Ts65Dn mice.

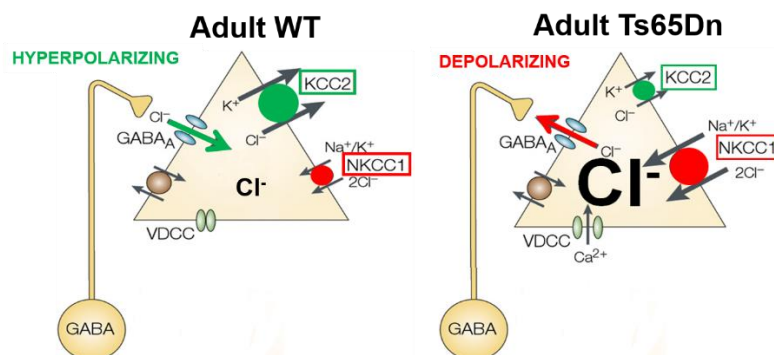


**Figure 1.5.** Representation of the different CCCs expression in WT adult (left) and in Ts65Dn adult (right) neurons. Left: In the adulthood, the high KCC2 expression determines a low  $Cl^-$  concentration inside the cell. When GABA<sub>A</sub>R opens, the  $Cl^-$  influx in the cell determine neuron hyperpolarization. Right: The upregulation of NKCC1 in Ts65Dn neurons leads to a high  $Cl^-$  concentration inside the cells, thus determining a  $Cl^-$  efflux when GABA<sub>A</sub>R opens and the cell depolarization.

### 1.5.2 Bumetanide treatment rescues the altered GABAergic transmission, synaptic plasticity and cognitive deficits in Ts65Dn Mice.

The finding that NKCC1 increased expression could be at the origin of the impaired GABAergic signalling prompted Deidda and colleagues to evaluate NKCC1 inhibition by bumetanide as a possible pharmacological approach.

Bumetanide bath application to acute hippocampal brain slices of adult Ts65Dn mice was able to rescue  $E_{Cl}$ , reducing spontaneous spiking activity and decreasing GABA-induced spike frequency and to recover the hippocampal CA1-CA3 LTP to WT levels. Conversely, Bumetanide did not show any significant effect upon application in WT mice either on  $E_{Cl}$  or on LTP.

Finally, Deidda and colleagues tested Ts65Dn mice and their WT littermates in three independent behavioral tasks to assess hippocampus-dependent long-term explicit memory after either an acute (1 time only), subchronic (1 week) or a chronic (4 weeks) systemic (intraperitoneal) treatment with bumetanide. Interestingly, they proved that all three treatments with bumetanide were able to fully recover the poor associative memory of Ts65Dn mice in the contextual fear-conditioning test. Moreover, bumetanide was able to rescue the performance of Ts65Dn mice to the level of WT mice in the object-location test, showing a full recovery of spatial-memory performance. Finally, bumetanide administration was also able to rescue the novel-discrimination memory of Ts65Dn mice in the novel object recognition test<sup>176</sup>.

Notably, bumetanide exerted acute activity on NKCC1 and it did not provide long-lasting effects. Indeed, a drug withdrawal experimental protocol (i.e., a week of bumetanide washout after a four-week treatment) completely abolished the rescue observed in both LTP and behavioral tasks, indicating the requirement for chronic treatment<sup>176</sup>. These results indicate that bumetanide act by direct  $E_{Cl}$  modulation via NKCC1 inhibition, rather than inducing neuronal-circuit rearrangements<sup>171,176</sup>.

## **1.6 Bumetanide repurposing: issues and pitfalls.**

Bumetanide (3-(butylamino)-4-phenoxy-5-sulfamoylbenzoic acid, Figure 1.6) is a TAL diuretic, which acts by inhibiting the NKCC2 transporter in the kidney. Bumetanide reached the clinic in the seventies and nowadays it is indicated only for the treatment of edemas and swelling caused by congestive heart failure, acute pulmonary congestion, hepatic disease and renal disease<sup>177,178</sup> due to its diuretic effect. As discussed above, several evidences indicate that treatment with bumetanide has beneficial effects on a number of NDs in both rodent model and humans.



However, the highly promising repurposing potential of bumetanide is burdened by a number of issues that seriously hamper its future use as a solid therapeutic option for brain disorders in the clinic.

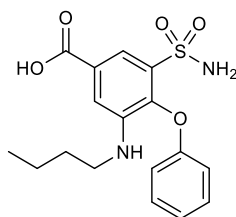


**Figure 1.6.** Structure of bumetanide.

The main drawback of bumetanide is its diuretic activity. Bumetanide administration causes hypokalaemia, hypochloremia, metabolic alkalosis, hyperuricemia, and prerenal azotaemia<sup>177</sup>. Moreover, these side effects could lead to encephalopathy and may promote seizures due to severe ionic imbalance<sup>61,179</sup>. Such potent diuretic effect is irreconcilable with the likely required lifelong-treatment of patients with severe behavioural impairment and seriously jeopardises drug compliance. As another limitation, bumetanide proved to have ototoxic effect in infants. Indeed, the repurposing NEMO trial for the treatment of acute neonatal seizures was halted due to hearing loss observed in a significant group of treated children<sup>99</sup>. Moreover, NKCC2 is also expressed in vasopressinergic and oxytocinergic neurons in the hypothalamo-neurohypophyseal system and in the vestibular system, increasing the potential side effects of a chronic bumetanide treatment. Furthermore, bumetanide display very poor brain penetration. The drug is highly ionized at physiological pH, which restricts passive diffusion across the blood-brain barrier (BBB). In addition, multiple studies found bumetanide to be a substrate of the active efflux transporters Oat3, Oatp1-4 and MRP4<sup>180-183</sup>. For this reason, recent investigations considered bumetanide's low levels in the brain after systemic administration as incompatible with NKCC1 inhibition, thus questioning the brain expressed NKCC1 as the target of bumetanide in NDS<sup>182,184</sup>.

Thus, to be able to take advantage of the therapeutic strategy defined by the studies performed with bumetanide in various neurological disorders further investigations are needed.

First, the mechanism of action of bumetanide needs to be further established as well as investigation of the possible off-targets. These would be fundamental pre-requisites for any drug discovery effort aimed at finding new NKCC1 inhibitors devoid of all of the bumetanide's shortcomings.

### 1.6.1 Bumetanide analogues and prodrugs.

In recent years, in order to improve bumetanide's brain accessibility and overcome its diuretic effect due to NKCC2 inhibition, several prodrugs and analogues of bumetanide have been evaluated. Prodrugs bear uncharged groups (amide, ester, alcohol) and convert to bumetanide after penetrating in the brain. In particular, Töllner and colleagues described compounds BUM 1 (pivaloyloxymethyl ester, Figure 1.7) and BUM 5 (*N,N*-dimethylaminoethyl ester, Figure 1.7) to have significantly higher brain penetration than bumetanide after intravenous (i.v) administration (10 mg/kg)<sup>185</sup>.

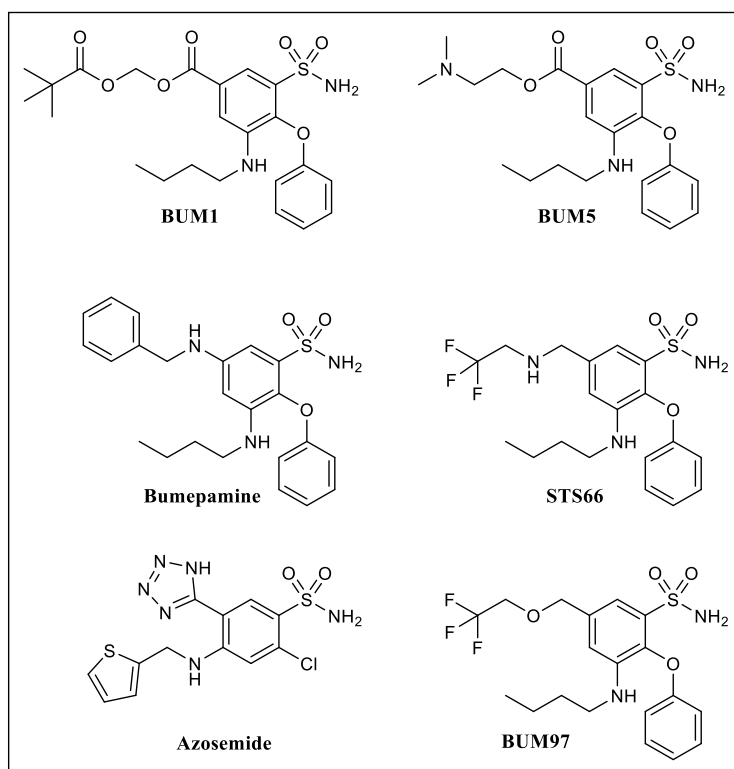


**Figure 1.7.** Structures of bumetanide analogues and prodrugs developed in recent years.

BUM5 was also able to increase brain levels of bumetanide threefold when compared to the only administration of bumetanide. BUM5 was exerted also a lower diuretic activity and showed better brain access when compared to BUM1<sup>185</sup>. Interestingly, BUM1 showed a quantitatively similar diuretic effect in comparison to bumetanide in mice treated at the same i.v dose (10 mg/kg), suggesting that removal of the ionisable carboxylic group may not be sufficient to avert activity on NKCC2. Importantly, BUM5 was shown to potentiate the anticonvulsant effect of phenobarbital markedly better than bumetanide in adult models of epileptic post status epilepticus and post-kindling<sup>185,186</sup>. Nevertheless, brain levels of bumetanide following administration of BUM5 moderately exceeded the levels needed to effectively inhibit neuronal NKCC1, indeed administration of the sole BUM5 was unable to alter focal seizure threshold in fully kindled rats<sup>185</sup>.

Recently, the same authors designed bumetanide derivatives that are only minimally ionized at physiological pH, more lipophilic than bumetanide, and therefore are predicted to better penetrate into the brain. As a first example, the benzylamine derivative bumepamine (Figure 1.7) has been evaluated in preclinical models. The studies performed at Leo Pharma in the 1970s that led to the discovery of bumetanide evaluated these benzylamine derivative lacking the carboxylic group. This analogues displayed a much lower diuretic activity in dogs<sup>187</sup>, prompting the authors to evaluate their effect in epilepsy models. Bumepamine proved to be more effective than bumetanide in potentiating the anticonvulsant effects of phenobarbital in rodent models of epilepsy at 10 mg/kg dose<sup>188</sup>. Strikingly, bumepamine had no effect on NKCC1 *in vitro* in both suppressing giant depolarizing potentials and GABA induced Ca<sup>2+</sup> transient in hippocampal neonatal slices. Consistently, bumepamine did not inhibit NKCC1 or NKCC2 mediated transport in *Xenopus laevis* oocytes, suggesting that bumepamine effect could be related to other targets than NKCC1. Additionally, another study by the same group showed that the diuretic azosemide (Figure 1.7) was 4-times more potent in inhibiting of NKCC1 than bumetanide, opening to potentially new options for the design of BBB penetrating uncharged bumetanide derivatives<sup>189</sup>.

Recently, another bumetanide derivative STS66 (Figure 1.7), which bears a methylamino trifluoroethyl group instead of the carboxylic acid, was evaluated in rodent models of ischemic stroke. STS66 was

superior in comparison to bumetanide at a dose of 2 mg/kg in reducing ischemic infarction, swelling, and neurological deficits in large-vessel transient ischemic stroke, and in permanent focal ischemic stroke with hypertension comorbidity<sup>190</sup>. Strikingly, no mortality was observed in the STS66 treated animals compared to vehicle treated animal<sup>190</sup>. The authors concluded that this effect is due to by higher brain penetration of STS66; however, the diuretic potential of this compound is not mentioned.

Finally, a new uncharged bumetanide analogue has been recently proposed for the treatment of epilepsy by Auer *et al.* The authors designed the 5-trifluoroethoxymethyl derivative BUM97 (Figure 1.7) as new brain penetrant analogue. Treatment with BUM97 was effective in suppressing dose-dependently (1 mg/kg, 3 mg/kg, 10 mg/kg) hippocampal paroxysmal discharges as well as spike trains in a kainic acid model of temporary lobe epilepsy<sup>191</sup>. Moreover, BUM97 was able to enhance the anticonvulsant effect of PB synergistically<sup>191</sup>. Moreover, at higher doses BUM97 achieved long-lasting reduction of spike trains. Strikingly, treatment at 10 mg/kg with this compound did not exert any diuretic effect *in vivo*<sup>191</sup>.

Although these brain accessible derivatives showed to be promising alternatives to bumetanide, they still not completely solved the pitfalls of bumetanide, in particular prodrugs, which are cleaved to bumetanide in significant manner in the blood. In addition, no *in vitro* or *in vivo* data underlies the factual targeting of NKCC1 by these derivatives in the brain. This opens avenues for potential off-target activity in the CNS (i.e. bumepamine) and even greater safety issues in respect to bumetanide. Thus, deeper characterization of the molecular targets and systemic effects of these new compounds is still needed, in particular regarding safety following chronic administration and chronic diuresis induced.

### **Aim of the project.**

There is solid evidence suggesting that impaired Cl<sup>-</sup> homeostasis regulation in the CNS may be at the basis of several neurodevelopmental disorders (NDs). In addition, a number of preclinical and clinical studies have underlined the promising therapeutic effect of NKCC1 modulation in a wide panel of neurological conditions. Those studies have enforced the importance of the diuretic bumetanide as a “direct to patient” pharmacological tool that allowed understanding the positive effects of blocking NKCC1 activity. However, lifelong treatment with bumetanide in patients is burdened by its uncompliant diuretic side effect due to inhibition of the kidney specific NKCC2 and possible ototoxicity in infants. In addition, the pharmacokinetic limitations of bumetanide, especially poor brain penetration, strongly hamper its use as a CNS directed drug. In this scenario, new potent and safer NKCC1 inhibitors have to be developed in order to exploit in the clinic the highly promising therapeutic potential of Cl<sup>-</sup> homeostasis modulation in the brain.

This project aims at the design, synthesis and characterization of new *selective* NKCC1 inhibitors. This work will attempt to elucidate bumetanide’s key structural features necessary for selective NKCC1 vs NKCC2 inhibition, while also generating novel, selective, and possibly safer compounds that will open new possibilities toward potentially effective and sustainable pharmacological therapies for the treatment DS, ASD and in the many other neuro-pathologies characterized by NKCC1/KCC2 defective ratio.

## Chapter 2. Design, synthesis and characterization of novel bumetanide analogues.

### 2.1 Rationale.

To develop novel selective NKCC1 inhibitors, we initially focused on decoding which features of the chemical structure of bumetanide can generate selective inhibition of NKCC1 vs NKCC2 in order to detect those structural features responsible for selective NKCC1 inhibition. For this reason, we performed a structure-activity relationship on a set of novel bumetanide analogues. The compounds were designed by adding small systematic modifications on the different anchor points of the 3-amino-4-phenoxy-5-sulfamoyl-benzoic acid core of bumetanide by exploring the implication of the substituents in positions R<sup>1</sup>, R<sup>3</sup> and R<sup>5</sup> (Figure 2.1). In particular, position R<sup>1</sup> has been modified by insertion of an ester moiety to evaluate the importance of the ionizable acidic group and position R<sup>3</sup> has been manipulated via the introduction of alkyl chain of various length and bulkiness compared to the *n*-butyl chain of bumetanide. Finally, to investigate the role of the sulfonamide in R<sup>5</sup>, we synthesized dimethylamino derivatives to evaluate different H-bond donor (HBD) / H-bond acceptor (HBA) behavior between the primary sulfonamide of bumetanide and tertiary dialkylated sulfonamide.

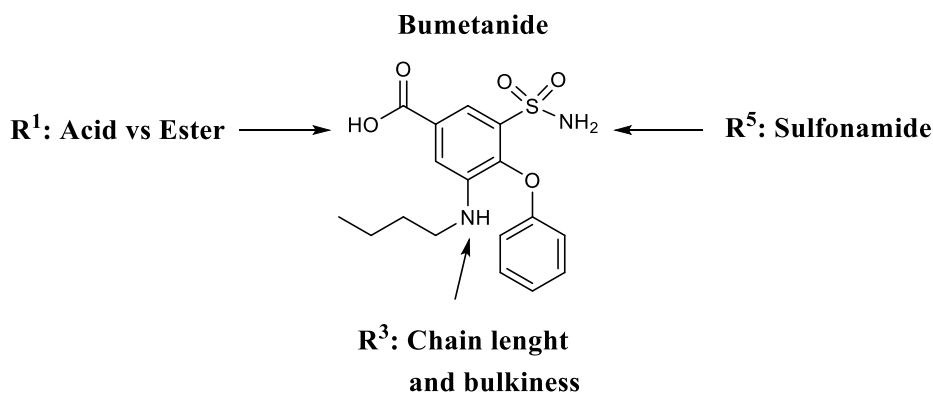
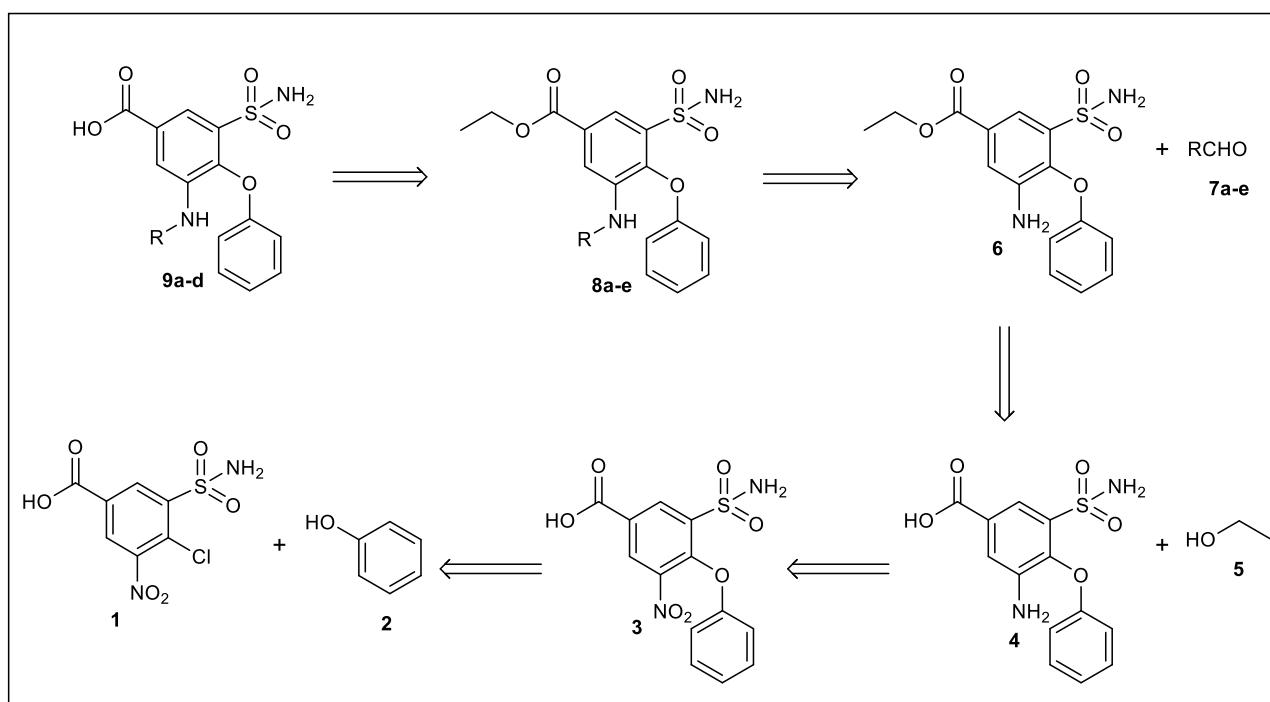


**Figure 2.1.** Schematic representation of the points subject to modification in the bumetanide structure to synthesize novel bumetanide analogues.

## 2.2 Synthesis of a small library of bumetanide analogs.

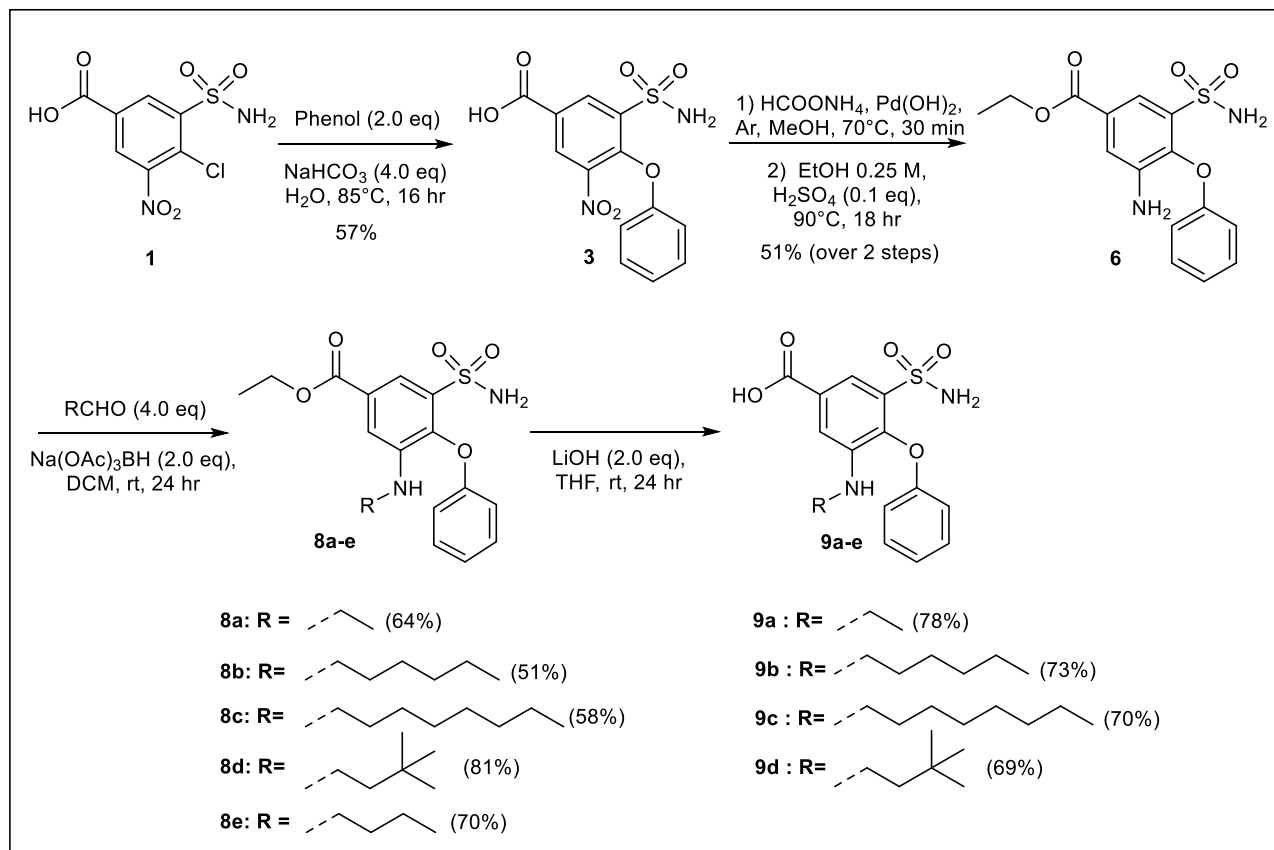
Retrosynthetically, we envisioned construction of the R<sup>3</sup> modified bumetanide analogues **9a-d** from basic hydrolysis of ester **8** (Scheme 2.1). Intermediates **8a-e** could be obtained by reductive amination reaction of aniline **6** with various commercial aldehydes **7a-e** and sodium triacetoxyborohydride. The key intermediate **6** could be obtained from reduction of nitrobenzene **3** followed by esterification with ethanol, which in turn could be achieved from nucleophilic aromatic substitution of intermediate **1** with phenol **2**.



**Scheme 2.1.** Retrosynthetic analysis of R<sup>3</sup> substituted bumetanide analogues.

As depicted in Scheme 2.2, synthesis started from commercially available 4-chloro-3-nitro-5-sulfamoylbenzoic acid **1** that was subjected to nucleophilic aromatic substitution with phenol to afford diaryl ether **3** in a good 57% yield. Nitro group of **3** was then reduced via palladium-catalyzed reduction with ammonium formate, which subsequently reacted with ethanol in Fisher conditions to yield ethyl ester **6**. Suppression of the acidic moiety via esterification proved to be essential for the subsequent step of reductive amination, as a free benzoic acid substrate led to the formation of the dialkylated product also on the sulfonamide position. *N*-alkylation of **6** via reductive amination with the suitable commercial aldehydes **7a-e** using sodium triacetoxyborohydride yielded compounds **8a-e**. Notably,

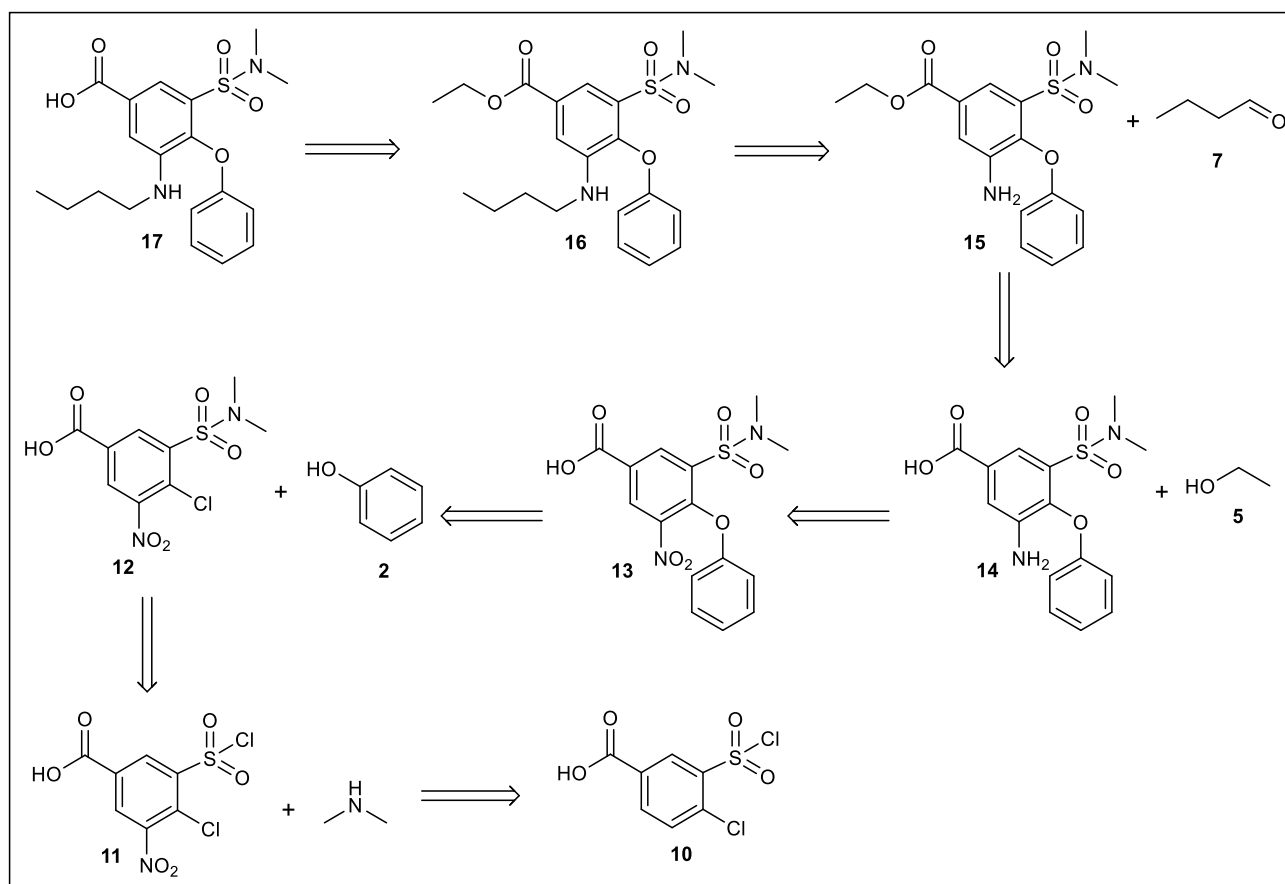
intermediates **8a-e** represented a panel of ethyl ester derivatives combined with different *N*-alkyl chains that were isolated, and have been evaluated for SAR analysis. Finally, basic hydrolysis of esters **8a-d** with lithium hydroxide in THF afforded the target benzoic acids **9a-d** in good yields.



**Scheme 2.2.** Synthesis of  $\text{R}^3$  substituted and  $\text{R}^1$  esters bumetanide analogues.

The *N,N*-dimethylsulfamoyl derivative of bumetanide **17** was approached retrosynthetically exploiting the same sequence of deprotection, reductive amination, esterification, reduction and nucleophilic aromatic substitution (Scheme 2.3). As described in Scheme 2.3, key intermediate **12** could be generated by substitution of the chlorosulfonyl group of **11** with dimethylamine. In turn, 4-chloro-3-(chlorosulfonyl)-5-nitrobenzoic acid **11** could be obtained by nitration of commercial **10** taking advantage of the directing groups on the aromatic ring.

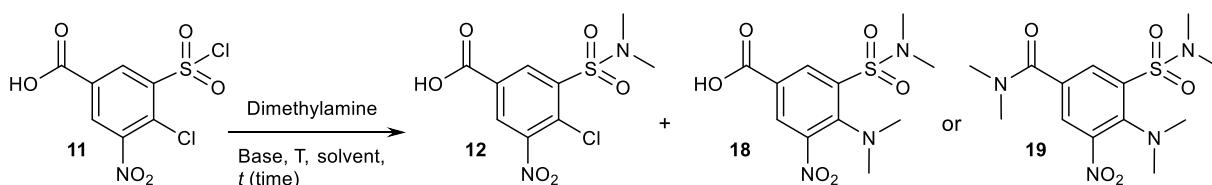




**Scheme 2.3.** Retrosynthetic analysis of R<sup>5</sup> substituted bumetanide analogue.

As shown in Scheme 2.4, synthesis was performed firstly by electrophilic nitration of commercial available 4-chloro-3-(chlorosulfonyl)benzoic acid **10** in a good 72% yield. We then moved on, trying substitution of the chlorosulfonyl group of **11** with dimethylamine to obtain **12**: a step that proved to be more troublesome than expected. Initially the use of four equivalents of dimethylamine (Table 2.1, entry 1) gave a 28:72 mixture of desired **12** and byproduct **18**, where nucleophilic substitution occurred also on the highly activated position 4 in a significant manner. Given the low conversion to the desired product and complicated purification, other reaction conditions were screened to access **12** (Table 2.1). To avoid disubstitution we started by diminishing the equivalents of dimethylamine from 4 to 1.3 equivalent in reaction mixture (Table 2.1, entry 2). Strikingly, we obtained a complex mixture mainly composed of **19** (Table 2.1, entry 2) as the low amount of dimethylamine was probably insufficient to neutralize the chloride generated from the substitution, favoring, in combination with longer reaction time, collateral formation of the amide. For this reason, we decided to add a different base in combination with dimethylamine. Addition of 1.2 equivalents of triethylamine (TEA) was not effective

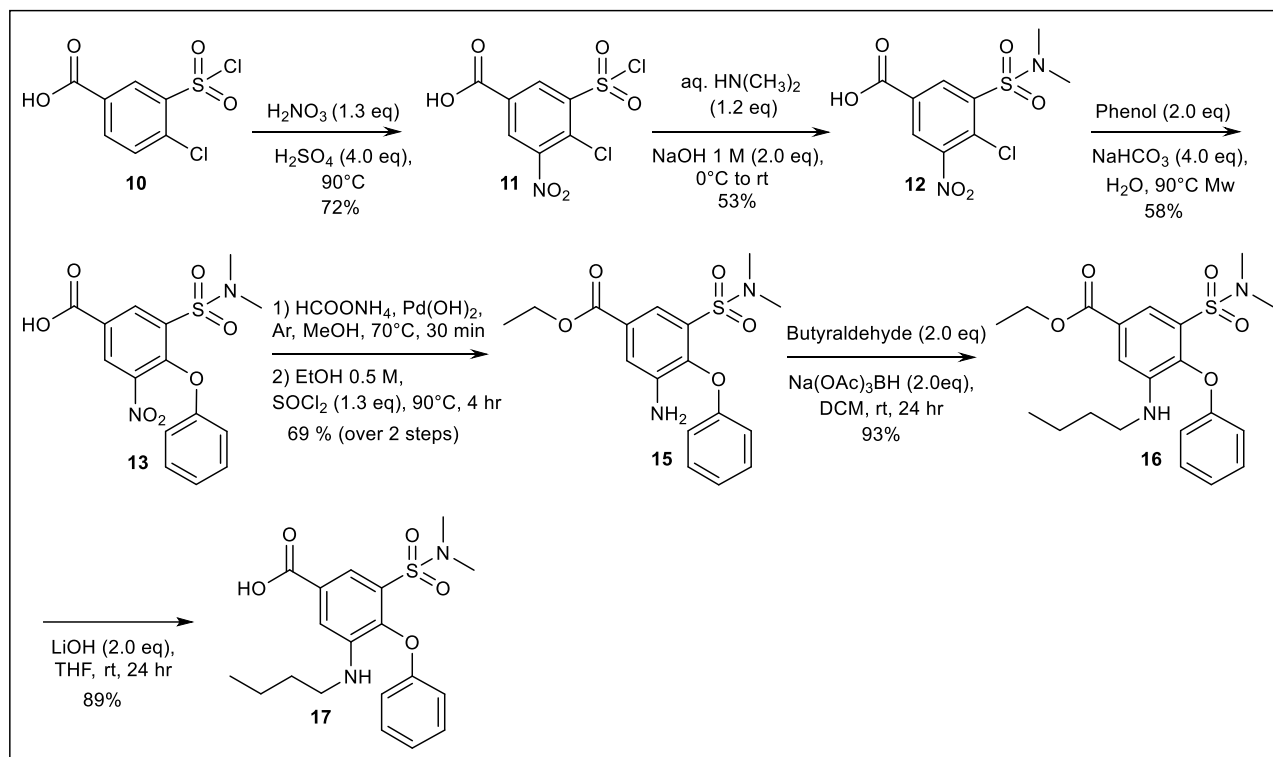
in avoiding formation of **19** (Table 2.1, entry 3), while we observed the generation of the single **12** using *N,N*-diisopropylethylamine (DIPEA), although in a very modest conversion rate (Table 2.1, entry 4). In this latter attempt, the formation of the product seemed to be favored by the short reaction time rather than the effect of the base. Strikingly, when we used aqueous sodium hydroxide as the additive base we observed the exclusive generation of product **12** after 20 minutes of reaction (Table 2.1, entry 5), which was obtained pure in an appreciable yield after recrystallization from aqueous ethanol. Basicity of the base rather than its nucleophilicity seemed to be pivotal to afford the desired product. The presence of excess sodium hydroxide allowed to completely deprotonate the acid and direct the substitution on the chlorosulfonyl group while neutralizing properly the chloride generated. These conditions turned out to be the best for the preparation of intermediate **12** and allowed its preparation in an 800 mg scale.



Entry	Dimethylamine	Base	Solvent	Temperature	<i>t</i>	Conversion ratio ( <b>12/18/19</b> ) <sup>c</sup>
<b>1</b>	4.0 eq <sup>a</sup>	-	THF	0°C to rt	30 min	28/72/0
<b>2</b>	1.3 eq <sup>a</sup>	-	THF	0°C to rt	2:00 hr	21/0/79
<b>3</b>	1.3 eq <sup>a</sup>	TEA (1.2 eq)	THF	0°C to rt	2:30 hr	18/0/72
<b>4</b>	1.2 eq <sup>a</sup>	DIPEA (1.2 eq)	THF	0°C	30 min	13/0/0 <sup>d</sup>
<b>5</b>	1.2 eq <sup>b</sup>	NaOH (2.0 eq)	H <sub>2</sub> O	0°C to rt	20 min	64/0/0 <sup>d</sup>

**Table 2.1.** Conditions screened for the synthesis of intermediate **12**. *a*, 1 M THF solution. *b*, 1 M aqueous solution. *c*, Conversion ratio determined by <sup>1</sup>H NMR from reaction crude. *d*, incomplete starting material conversion observed.

Subsequent nucleophilic aromatic substitution of **12** with phenol under microwave irradiation afforded phenoxy derivative **13**. Palladium-catalyzed reduction with ammonium formate gave access to aniline **14** that was reacted with thionyl chloride and refluxed in ethanol to yield ester **15**. Finally, aniline **15** was *N*-alkylated via reductive amination, followed by basic hydrolysis to afford compound **17** (Scheme 2.4).

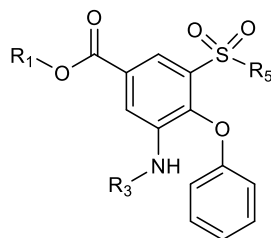


**Scheme 2.4.** Synthesis of  $R^5$  substituted bumetanide analogue.

### 2.3 Results and discussion.

The inhibitory activity of the new analogues was evaluated at two concentrations (10  $\mu\text{M}$  and 100  $\mu\text{M}$ ) and compared to that of bumetanide using a fluorescent chloride assay ( $\text{Cl}^-$ -flux assay) in HEK293 cells. This assay relies on the detection of variations of  $[\text{Cl}^-]_i$  through a  $\text{Cl}^-$ -sensitive, membrane-tagged yellow fluorescent protein (mbYFPQS). mbYFPQS fluorescence is quenched by  $\text{Cl}^-$ . As a result, upon application of a source of  $\text{Cl}^-$  in the bath ( $\text{NaCl}$ ),  $\text{Cl}^-$  ions thus permeate into cells by NKCC1 or NKCC2 transport and bind to mbYFPQS determining a fluorescence decrease. If a NKCC1 inhibitor (i.e. bumetanide) is applied to the medium, it interferes with fluorescence decrease. Thus, in this way, we

could indirectly estimate Cl<sup>-</sup> transporter activity by mbYFPQS fluorescence variations upon treatment with our novel inhibitors. Results are summarized in Table 2.2.



Entry	R <sup>1</sup>	R <sup>3</sup>	R <sup>5</sup>	10 μM NKCC1	100 μM NKCC1	10 μM NKCC2	100 μM NKCC2
<b>Bume</b>	H		NH <sub>2</sub>	58.8 ± 5.6 %	71.7 ± 7 %	82.7 ± 20.4 %	80.5 ± 9 %
<b>8a</b>			NH <sub>2</sub>	No inhibition	No inhibition	No inhibition	No inhibition
<b>8b</b>			NH <sub>2</sub>	No inhibition	No inhibition	No inhibition	No inhibition
<b>8c</b>			NH <sub>2</sub>	No inhibition	No inhibition	No inhibition	No inhibition
<b>8d</b>			NH <sub>2</sub>	No inhibition	No inhibition	No inhibition	No inhibition
<b>8e</b>			NH <sub>2</sub>	No inhibition	No inhibition	No inhibition	No inhibition
<b>9a</b>	H		NH <sub>2</sub>	No inhibition	No inhibition	No inhibition	No inhibition
<b>9b</b>	H		NH <sub>2</sub>	No inhibition	90 ± 9.7 %	No inhibition	61.9 ± 9.1 %
<b>9c</b>	H		NH <sub>2</sub>	No inhibition	22.4 ± 4.8 %	No inhibition	32.9 ± 11.5 %
<b>9d</b>	H		NH <sub>2</sub>	No inhibition	98 ± 6.9 %	48.4 ± 8.3 %	80.5 ± 9 %
<b>17</b>	H		N(CH <sub>3</sub> ) <sub>2</sub>	No inhibition	22.4 ± 6.7 %	No inhibition	No inhibition

**Table 2. 2.** Inhibitory potency of synthesized bumetanide analogues.

The bumetanide ethyl ester **8e**, displayed a complete loss in activity against both NKCC1 and NKCC2. Also the other ethyl ester derivatives **8a-d** with different chain lengths on the amine did not display any activity in both transfected cell lines, indicating that the carboxylic acid in R<sup>1</sup> is fundamental to maintain activity against the two cation-chloride cotransporters. Similarly, the shortening of the chain in R<sup>3</sup> to an ethyl group of compound **9a** was detrimental for activity on both transporters. Conversely, R<sup>3</sup> amino group chain elongation determined a gain in selectivity toward NKCC1 compared to bumetanide. Indeed, both **9b** (*n*-hexyl chain) and **9c** (*n*-octyl chain) did not inhibit NKCC2 at 10 μM and inhibit NKCC2 at 61.9 ± 9.1 % (**9b**) and 32.9 ± 11.6 % (**9c**) at 100 μM, compared to bumetanide's 80.5 ± 9 % inhibition. Nevertheless, these compounds displayed a decrease in potency against NKCC1 at 10 μM when compared to the 58.8 ± 5.6 % of inhibition of bumetanide, but maintained a good inhibition of NKCC1 at 100 μM of 90 ± 9.7 % (**9b**) and ~ 22.4 ± 4.8 % (**9c**), when compared to the 82.7 ± 20.4 % of inhibition of bumetanide. Conversely, insertion of terminal bulky 3,3-dimethylbutyl element in R<sup>3</sup> (**9d**) resulted in a loss of activity against NKCC1 at 10 μM, but maintained a 126 ± 6.9 % inhibition at 100 μM. When tested against NKCC2 **9d** exhibited a good inhibition both at 10 μM (48.4 ± 8.3 %) and at 100 μM (81.7 ± 7.1%), when compared to bumetanide's activity (82.7 ± 20.4 % at 10 μM; 80.5 ± 9 % at 100 μM). Strikingly, the switch from H-bond donor (HBD) / H-bond acceptor (HBA) of bumetanide to HBA of the sulfonamide **17** determined a complete loss of activity against NKCC2, still maintaining inhibition of NKCC1 at 100 μM (22.4 ± 6.7 %). Nevertheless, also in this case, a decrease in potency was observed when compared to bumetanide (80.5 ± 9 %).

The evaluation of this small panel of bumetanide analogues allowed us to interpret some structural motifs, which could decrease the activity against NKCC2. We found that elongation of the carbon chain proved able to slightly direct the inhibitory activity towards NKCC1, while the benzoic acid moiety was crucial for inhibition of both NKCC1 and NKCC2. Nevertheless, none of the compounds exerted a markedly higher ratio in NKCC2/NKCC1 selectivity, confirming data from the literature on other bumetanide analogues<sup>192</sup>, indicating a large difficulty to develop bumetanide derivatives with higher selectivity for NKCC1 vs NKCC2 than bumetanide<sup>192</sup>. In addition, all the modifications that induced low to absent activity toward NKCC2 always coincided with a significant loss of potency also on NKCC1. Thus, we decided to seek new molecular entities, structurally unrelated to bumetanide.

This strategy could open better avenues towards selectivity for the development of novel selective NKCC1 inhibitors without the unwanted effect on NKCC2. In directing our search, we nevertheless took advantage of the knowledge acquired from the experiments on these bumetanide's analogues.

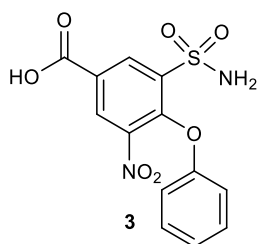
## 2.4 Experimental section.

### Chemistry:

**General consideration.** All chemicals were purchased from Acros, Aldrich, Merck, Fluorochem, TCI or Alfa Aesar and used as such unless stated otherwise. All the commercial available reagents and solvents were used as purchased from vendors without further purification. Dry solvents were purchased from Sigma-Aldrich. Automated column chromatography purifications were done using a Teledyne ISCO apparatus (CombiFlash® Rf) with pre-packed silica gel or basic alumina columns of different sizes (from 4 g up to 120 g) and mixtures of increasing polarity of cyclohexane and ethyl acetate (EtOAc), cyclohexane or dichloromethane (DCM) and methanol (MeOH). NMR experiments were run on a Bruker Avance III 400 system (400.13 MHz for  $^1\text{H}$ , and 100.62 MHz for  $^{13}\text{C}$ ), equipped with a BBI probe and Z-gradients. Spectra were acquired at 300 K, using deuterated dimethylsulfoxide ( $\text{DMSO}-d_6$ ) or deuterated chloroform ( $\text{CDCl}_3$ ) as solvents. For  $^1\text{H}$ -NMR, data are reported as follows: chemical shift, multiplicity (s= singlet, d= doublet, dd= double of doublets, t= triplet, q= quartet, h= sextet, m= multiplet), coupling constants (Hz) and integration. UPLC/MS analyses were run on a Waters ACQUITY UPLC/MS system consisting of a SQD (single quadrupole detector) mass spectrometer equipped with an electrospray ionization interface and a photodiode array detector. The PDA range was 210–400 nm. Analyses were performed on an ACQUITY UPLC BEH C18 column (100x2.1mmID, particle size 1.7  $\mu\text{m}$ ) with a VanGuard BEH C18 pre-column (5x2.1 mmID, particle size 1.7  $\mu\text{m}$ ). Mobile phase was 10 mM  $\text{NH}_4\text{OAc}$  in  $\text{H}_2\text{O}$  at pH 5 adjusted with  $\text{CH}_3\text{COOH}$  (A) and 10 mM  $\text{NH}_4\text{OAc}$  in  $\text{CH}_3\text{CN}-\text{H}_2\text{O}$  (95:5) at pH 5.0. Two types of gradients were applied depending on the analysis, gradient 1 (5 % to 95 % mobile phase B in 3 min) or gradient 2 (50 % to 100 % mobile phase B in 3 min). Electrospray ionization in positive and negative mode was applied. Electrospray ionization in positive and negative mode was applied. ESI was applied in positive and negative mode. All final compounds displayed  $\geq 95\%$  purity by UPLC/MS analysis.

**General reductive amination procedure A for the synthesis of compounds 8a-e, 16 (Scheme 2.2, 2.4).** To a suspension of ethyl benzoate **6** or **15** (1.0 mmol) in dry dichloromethane (15 mL) was added the proper aldehyde (4.0 mmol). After 30 min of stirring, sodium triacetoxyborohydride was added (2.0 mmol) and the mixture was stirred at room temperature for 18 hr. At reaction completion, the crude was portioned between DCM (25 ml) and NaHCO<sub>3</sub> saturated solution (40 ml) and the layers separated. The organic layer was dried over Na<sub>2</sub>SO<sub>4</sub> and concentrated to dryness at low pressure. Purification by silica gel flash chromatography with cyclohexane/EtOAc finally afforded the pure titled compounds.

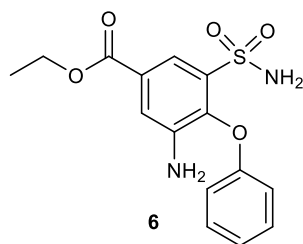
**General ester hydrolysis procedure B for the synthesis of compounds 9a-d, 17 (Scheme 2.2, 2.4).** To a suspension of the proper ester (1.0 mmol) in tetrahydrofuran (10 mL) was added a 0.5 M LiOH aqueous solution (2.0 mmol) and the mixture was stirred at room temperature for 16 hr. At reaction completion, the crude was portioned between EtOAc (25 ml) and an NH<sub>4</sub>Cl saturated solution (25 ml) and the layers separated. The organic layer was dried over Na<sub>2</sub>SO<sub>4</sub> and concentrated to dryness at low pressure. Finally, trituration with cyclohexane afforded the pure titled compounds.



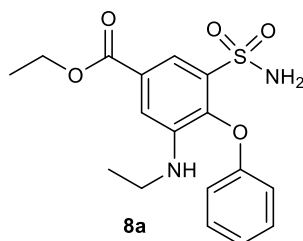
**3-nitro-4-phenoxy-5-sulfamoyl-benzoic acid (3).** To a suspension of commercial 4-Chloro-3-nitro-5-sulfamoylbenzoic acid **1** (4 g, 14.11 mmol) and NaHCO<sub>3</sub> (4.79 g, 56.45 mmol) in water (31.4 mL) was added phenol **2** (2.82 g, 29.64 mmol) and the mixture was stirred at 85°C for 24 hours. At reaction completion, the reaction mixture was cooled in an ice bath and acidified with concentrated HCl until pH 3. The precipitated solid was filtrated and washed twice with cold water (2 x 8 mL) to afford pure benzoic acid **3** (2.71 g, 57 % yield) as a yellow solid.: UPLC/MS: Rt = 1.31 min (gradient 1); MS (ESI) m/z: 337.1 [M-H]<sup>-</sup>, [M-H]<sup>-</sup> calculated: 337.02. <sup>1</sup>H NMR (400 MHz, DMSO-d<sub>6</sub>) δ 8.70 (d, J = 2.1 Hz,



1H), 8.63 (d,  $J = 2.2$  Hz, 1H), 7.87 (s, 2H), 7.42 – 7.24 (m, 2H), 7.14 – 7.03 (m, 1H), 6.92 (d,  $J = 7.7$  Hz, 2 H).

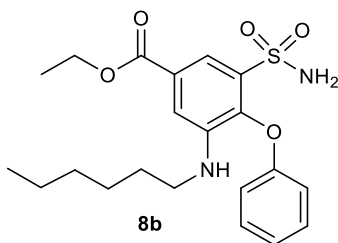


**Ethyl 3-amino-4-phenoxy-5-sulfamoylbenzoate (6).** Under argon atmosphere, to a suspension of benzoic acid **3** (2.71 g, 8.00 mmol) and Pd(OH)<sub>2</sub>/C (541 mg) in anhydrous methanol (159.9 mL) was added ammonium formate (2.61 g, 39.98 mmol) and the reaction crude was stirred at reflux temperature for 30 minutes. At completion, the reaction crude was filtered through a celite coarse patch and the filtrate concentrated to dryness at low pressure. This crude material (3.1 g) was solved in absolute ethanol (40 mL) and the solution degassed with nitrogen. Then, concentrated sulphuric acid was added (54  $\mu$ L, 1.0 mmol) and the reaction mixture was stirred at reflux temperature for 16 hours. At completion, the reaction crude was evaporated to dryness at low pressure. The dry residue was treated with 30 mL of a saturated NaHCO<sub>3</sub> solution and extracted twice with DCM (2 x 30 mL). The combined organic layers were dried over anhydrous Na<sub>2</sub>SO<sub>4</sub>, filtered and concentrated under reduced pressure to afford pure benzoate **6** (1.86 g, 69 % yield over two steps) as a white solid. UPLCS/MS: Rt = 1.84 min (gradient 1); MS (ESI) m/z: 335.1 [M-H]<sup>-</sup>, [M-H]<sup>-</sup> calculated: 335.1. <sup>1</sup>H NMR (400 MHz, DMSO-*d*<sub>6</sub>)  $\delta$  7.69 – 7.61 (m, 2H), 7.32 – 7.24 (m, 4H), 7.01 (t,  $J = 7.4$  Hz, 1H), 6.88 – 6.80 (m, 2H), 5.34 (s, 2H), 4.33 (q,  $J = 7.1$  Hz, 2H), 1.33 (t,  $J = 7.1$  Hz, 3H).

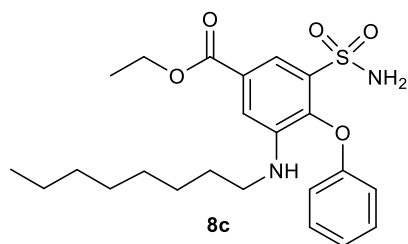


**Ethyl 3-(ethylamino)-4-phenoxy-5-sulfamoylbenzoate (8a).** Compound **8a** was synthesized following the general procedure **A** previously described using ethyl benzoate **6** (120 mg, 0.35 mmol)

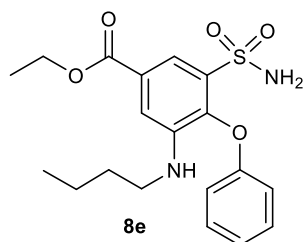
and acetaldehyde (79  $\mu\text{L}$ , 1.41 mmol). Purification by typical silica gel flash chromatography (cyclohexane/EtOAc from 100:0 to 80:20) finally afforded the pure **8a** (81.4 mg, 64% yield) as a white solid. UPLCS/MS:  $R_t = 0.96$  min (gradient 2); MS (ESI)  $m/z$ : 365.2  $[\text{M}+\text{H}]^+$ ,  $[\text{M}+\text{H}]^+$  calculated: 365.1.  $^1\text{H}$  NMR (400 MHz,  $\text{DMSO-}d_6$ )  $\delta$  7.70 (d,  $J = 2.0$  Hz, 1H), 7.43 (d,  $J = 2.0$  Hz, 1H), 7.33 (s, 2H), 7.29 – 7.23 (m, 2H), 7.05 – 6.96 (m, 1H), 6.87 – 6.79 (m, 2H), 5.16 (t,  $J = 5.8$  Hz, 1H), 4.35 (q,  $J = 7.1$  Hz, 2H), 3.12 (p,  $J = 7.0$  Hz, 2H), 1.34 (t,  $J = 7.1$  Hz, 3H), 1.00 (t,  $J = 7.0$  Hz, 3H).  $^{13}\text{C}$  NMR (101 MHz,  $\text{DMSO-}d_6$ )  $\delta$  164.99 (CO), 156.27 (C), 142.59 (C), 139.86 (C), 137.78 (C), 129.09 (CH), 127.23 (C), 122.20 (CH), 115.49 (CH), 114.97 (CH), 114.62 (CH), 61.09 ( $\text{CH}_2$ ), 37.13 ( $\text{CH}_2$ ), 14.19 ( $\text{CH}_3$ ), 13.83 ( $\text{CH}_3$ ).



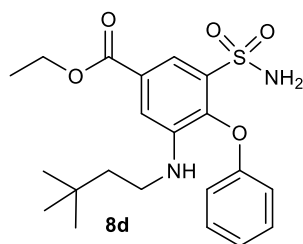
**Ethyl 3-(hexylamino)-4-phenoxy-5-sulfamoylbenzoate (8b).** Compound **8b** was synthesized following the general procedure previously described using ethyl benzoate **6** (100 mg, 0.29 mmol) and hexanal (145  $\mu\text{L}$ , 0.42 mmol). Purification by typical silica gel flash chromatography (cyclohexane/EtOAc from 100:0 to 80:20) finally afforded the pure **8b** (62.6 mg, 51% yield) as a white solid. UPLCS/MS:  $R_t = 1.84$  min (gradient 2); MS (ESI)  $m/z$ : 421.2  $[\text{M}+\text{H}]^+$ ,  $[\text{M}+\text{H}]^+$  calculated: 420.2.  $^1\text{H}$  NMR (400 MHz,  $\text{DMSO-}d_6$ )  $\delta$  7.66 (d,  $J = 2.0$  Hz, 2H), 7.40 (d,  $J = 2.0$  Hz, 1H), 7.27 – 7.21 (m, 2H), 7.00 (t,  $J = 7.3$  Hz, 1H), 6.81 (d,  $J = 8.1$  Hz, 2H), 4.32 (q,  $J = 7.1$  Hz, 2H), 3.02 (t,  $J = 6.7$  Hz, 2H), 1.38 – 1.27 (m, 5H), 1.17 – 0.97 (m, 6H), 0.76 (t,  $J = 6.8$  Hz, 3H).



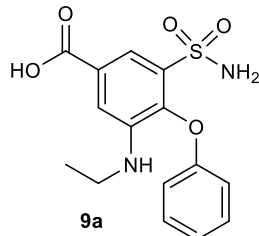
**Ethyl 3-(octylamino)-4-phenoxy-5-sulfamoylbenzoate (8c).** Compound **8c** was synthesized following the general procedure A previously described using ethyl benzoate **6** (80 mg, 0.24 mmol) and octanal (147  $\mu$ L, 0.94 mmol). Purification by typical silica gel flash chromatography (cyclohexane/EtOAc from 100:0 to 85:15) finally afforded the pure **8c** (62.9 mg, 58% yield) as a white solid. UPLCS/MS: Rt = 2.20 min (gradient 2); MS (ESI) m/z: 449.5 [M+H]<sup>+</sup>, [M+H]<sup>+</sup> calculated: 448.2. <sup>1</sup>H NMR (400 MHz, DMSO-*d*<sub>6</sub>)  $\delta$  7.69 (d, *J* = 2.0 Hz, 1H), 7.41 (d, *J* = 2.0 Hz, 1H), 7.34 (s, 2H), 7.30 – 7.21 (m, 2H), 7.05 – 6.97 (m, 1H), 6.87 – 6.81 (m, 2H), 5.08 (t, *J* = 5.7 Hz, 1H), 4.34 (q, *J* = 7.1 Hz, 2H), 3.05 (q, *J* = 6.5 Hz, 2H), 1.35 (m, 5H), 1.27 – 1.01 (m, 10H), 0.84 (t, *J* = 7.1 Hz, 3H).



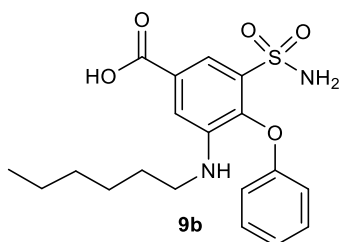
**Ethyl 3-(butylamino)-4-phenoxy-5-sulfamoylbenzoate (8e).** Compound **8e** was synthesized following the general procedure A previously described using ethyl benzoate **6** (100 mg, 0.29 mmol) and butyraldehyde (106  $\mu$ L, 1.18 mmol). Purification by typical silica gel flash chromatography (cyclohexane/EtOAc from 100:0 to 75:25) finally afforded the pure **8e** (79.6 mg, 70% yield) as a white solid. UPLCS/MS: Rt = 1.36 min (gradient 2); MS (ESI) m/z: 393.2 [M+H]<sup>+</sup>, [M+H]<sup>+</sup> calculated: 393.1. <sup>1</sup>H NMR (400 MHz, DMSO-*d*<sub>6</sub>)  $\delta$  7.70 (d, *J* = 1.9 Hz, 1H), 7.42 (d, *J* = 2.0 Hz, 1H), 7.32 (s, 2H), 7.31 – 7.21 (m, 2H), 7.06 – 6.97 (m, 1H), 6.85 (d, *J* = 6.5 Hz, 2H), 5.06 (t, *J* = 5.7 Hz, 1H), 4.35 (q, *J* = 7.1 Hz, 2H), 3.07 (q, *J* = 6.6 Hz, 2H), 1.41 – 1.31 (m, 5H), 1.11 (h, *J* = 7.4 Hz, 2H), 0.78 (t, *J* = 7.3 Hz, 3H). <sup>13</sup>C NMR (101 MHz, DMSO-*d*<sub>6</sub>)  $\delta$  164.96 (CO), 156.22 (C), 142.49 (C), 139.83 (C), 137.75 (C), 129.07 (C), 127.15 (C), 122.25 (CH), 115.53 (CH), 114.83 (CH), 114.48 (CH), 61.04 (CH<sub>2</sub>), 41.95 (CH<sub>2</sub>), 30.07 (CH<sub>2</sub>), 19.23 (CH<sub>2</sub>), 14.15 (CH<sub>3</sub>), 13.52 (CH<sub>3</sub>).



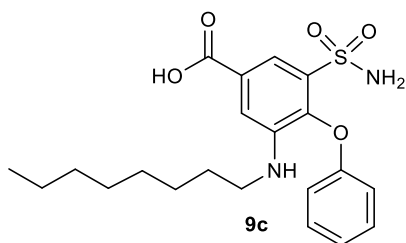
**Ethyl 3-((3,3-dimethylbutyl)amino)-4-phenoxy-5-sulfamoylbenzoate (8d).** Compound **8d** was synthesized following the general procedure A previously described using ethyl benzoate **6** (80 mg, 0.24 mmol) and 3,3-dimethylbutyraldehyde (118  $\mu$ L, 0.94 mmol). Purification by typical silica gel flash chromatography (cyclohexane/EtOAc from 100:0 to 80:20) finally afforded the pure **8d** (82.2 mg, 81% yield) as a white solid. UPLCS/MS: Rt = 1.70 min (gradient 2); MS (ESI) m/z: 421.5 [M+H]<sup>+</sup>, [M+H]<sup>+</sup> calculated: 421.2. <sup>1</sup>H NMR (400 MHz, DMSO-*d*<sub>6</sub>)  $\delta$  7.69 (d, *J* = 2.0 Hz, 1H), 7.44 (d, *J* = 2.1 Hz, 1H), 7.33 (s, 2H), 7.28 – 7.23 (m, 2H), 7.05 – 6.96 (m, 1H), 6.86 – 6.78 (m, 2H), 5.16 (t, *J* = 5.8 Hz, 1H), 4.34 (q, *J* = 7.1 Hz, 2H), 3.13 – 3.05 (m, 2H), 1.33 (t, *J* = 7.1 Hz, 3H), 1.31 – 1.25 (m, 2H), 0.86 (s, 9H).



**3-(ethylamino)-4-phenoxy-5-sulfamoylbenzoic acid (9a).** Compound **9a** was synthesized following the general procedure B previously described using ethyl ester **8a** (70.5 mg, 0.19 mmol). Final trituration in cyclohexane twice (2  $\times$  1 mL) afforded the pure **9a** (49.8 mg, 78% yield) as a white solid. UPLCS/MS: Rt = 1.38 min (gradient 1); MS (ESI) m/z: 335.1 [M-H]<sup>-</sup>, [M-H]<sup>-</sup> calculated: 336.1. <sup>1</sup>H NMR (400 MHz, DMSO-*d*<sub>6</sub>)  $\delta$  7.71 (s, 1H), 7.44 (s, 1H), 7.32 (s, 2H), 7.27 (t, *J* = 7.8 Hz, 2H), 7.01 (t, *J* = 7.4 Hz, 1H), 6.84 (d, *J* = 8.0 Hz, 2H), 5.11 (t, *J* = 5.9 Hz, 1H), 3.12 (p, *J* = 6.8 Hz, 2H), 1.00 (t, *J* = 7.0 Hz, 3H). <sup>13</sup>C NMR (101 MHz, DMSO-*d*<sub>6</sub>)  $\delta$  166.55 (CO), 156.33 (C), 142.43 (C), 139.60 (C), 137.66 (C), 129.08 (CH), 128.12 (C), 122.15 (CH), 115.49 (CH), 115.29 (CH), 114.93 (CH), 37.12 (CH<sub>2</sub>), 13.87 (CH<sub>3</sub>).

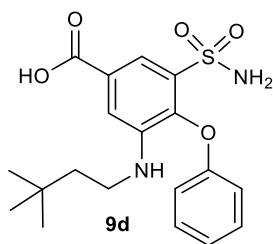


**3-(hexylamino)-4-phenoxy-5-sulfamoylbenzoic acid (9b).** Compound **9b** was synthesized following the general procedure **B** previously described using ethyl ester **8c** (61 mg, 0.14 mmol). Final trituration in cyclohexane twice ( $2 \times 1$  mL) afforded the pure **9b** (40.4 mg, 73% yield) as a white solid. UPLCS/MS: Rt = 0.50 min (gradient 2); MS (ESI) m/z: 391.2 [M-H]<sup>-</sup>, [M-H]<sup>-</sup> calculated: 392.1. <sup>1</sup>H NMR (400 MHz, DMSO-*d*<sub>6</sub>) δ 7.69 (d, *J* = 1.9 Hz, 1H), 7.41 (d, *J* = 2.0 Hz, 1H), 7.32 (s, 2H), 7.29 – 7.24 (m, 2H), 7.01 (t, *J* = 7.3 Hz, 2H), 6.84 (d, *J* = 7.8 Hz, 2H), 3.05 (t, *J* = 6.8 Hz, 2H), 1.42 – 1.32 (m, 2H), 1.25 – 1.02 (m, 6H), 0.80 (t, *J* = 6.9 Hz, 3H). <sup>13</sup>C NMR (101 MHz, DMSO-*d*<sub>6</sub>) δ 166.55 (CO), 156.30 (C), 142.35 (C), 139.57 (C), 137.65 (C), 129.10 (CH), 128.06 (C), 122.24 (CH), 115.56 (CH), 115.14 (CH), 114.76 (CH), 42.29 (CH<sub>2</sub>), 30.86 (CH<sub>2</sub>), 27.96 (CH<sub>2</sub>), 25.78 (CH<sub>2</sub>), 22.00 (CH<sub>2</sub>), 13.85 (CH<sub>3</sub>).

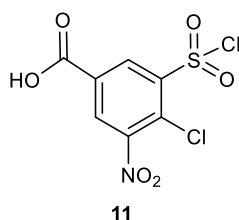


**3-(octylamino)-4-phenoxy-5-sulfamoylbenzoic acid (9c).** Compound **9c** was synthesized following the general procedure **B** previously described using ethyl ester **8d** (63 mg, 0.14 mmol). Final trituration in cyclohexane twice ( $2 \times 1$  mL) afforded the pure **9c** (42.9 mg, 70% yield) as a white solid. UPLCS/MS: Rt = 0.87 min (gradient 2); MS (ESI) m/z: 419.5 [M-H]<sup>-</sup>, [M-H]<sup>-</sup> calculated: 420.2. <sup>1</sup>H NMR (400 MHz, DMSO-*d*<sub>6</sub>) δ 7.69 (d, *J* = 1.9 Hz, 1H), 7.41 (d, *J* = 1.9 Hz, 1H), 7.34 (s, 2H), 7.26 (t, *J* = 7.8 Hz, 2H), 7.00 (t, *J* = 7.3 Hz, 1H), 6.84 (d, *J* = 8.1 Hz, 2H), 5.04 (t, *J* = 5.7 Hz, 1H), 3.05 (q, *J* = 6.5 Hz, 2H), 1.37 (p, *J* = 7.0 Hz, 2H), 1.27 – 1.02 (m, 10H), 0.84 (t, *J* = 7.0 Hz, 3H). <sup>13</sup>C NMR (101 MHz, DMSO-*d*<sub>6</sub>) δ 166.53 (CO), 156.28 (C), 142.31 (C), 139.52 (C), 137.63 (C), 129.06 (CH), 128.10

(C), 122.19 (CH), 115.54 (CH), 115.12 (CH), 114.73 (CH), 42.25 (CH<sub>2</sub>), 31.14 (CH<sub>2</sub>), 28.58 (CH<sub>2</sub>), 27.98 (CH<sub>2</sub>), 26.15 (CH<sub>2</sub>), 26.08 (CH<sub>2</sub>), 22.05 (CH<sub>2</sub>), 13.92 (CH<sub>3</sub>).

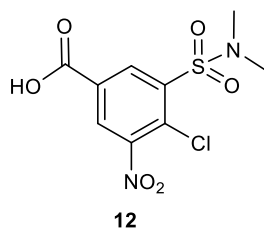


**3-((3,3-dimethylbutyl)amino)-4-phenoxy-5-sulfamoylbenzoic acid (9d).** Compound **9d** was synthesized following the general procedure **B** previously described using ethyl ester **8e** (82.2 mg, 0.2 mmol). Final trituration in cyclohexane twice (2 × 1 mL) afforded the pure **9d** (54.9 mg, 69% yield) as a white solid. UPLCS/MS: Rt = 1.84 min (gradient 1); MS (ESI) m/z: 391.5 [M-H]<sup>-</sup>, [M-H]<sup>-</sup> calculated: 392.1. <sup>1</sup>H NMR (400 MHz, DMSO-*d*<sub>6</sub>) δ 7.69 (d, *J* = 1.9 Hz, 1H), 7.43 (d, *J* = 2.0 Hz, 1H), 7.33 (s, 2H), 7.26 (t, *J* = 8.0 Hz, 2H), 7.00 (t, *J* = 7.3 Hz, 1H), 6.82 (d, *J* = 8.0 Hz, 2H), 5.06 (t, *J* = 5.8 Hz, 1H), 3.12 – 3.04 (m, 2H), 1.32 – 1.25 (m, 2H), 0.85 (s, 9H). <sup>13</sup>C NMR (101 MHz, DMSO-*d*<sub>6</sub>) δ 166.54 (CO), 156.33 (C), 142.46 (C), 139.52 (C), 137.64 (C), 129.07 (C), 128.16 (CH), 122.15 (CH), 115.50 (CH), 115.18 (CH), 114.78 (CH), 41.64 (CH<sub>2</sub>), 39.02 (CH<sub>2</sub>), 29.56 (C), 29.17 (CH<sub>3</sub>).

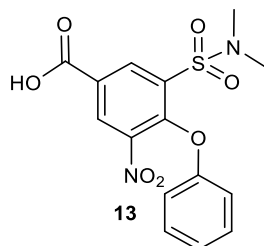


**4-chloro-3-(chlorosulfonyl)-5-nitrobenzoic acid (11).** Under argon atmosphere, to an ice cold solution of nitric Acid (591 μL 15.52 mmol) and sulfuric acid (2.53 mL, 46.57 mmol) was added 4-chloro-3-chlorosulfonyl-benzoic acid **10** (1.0 g, 3.88 mmol) and the reaction mixture was stirred at 90° for 4 hours. At completion, the reaction mixture was quenched dropwise into 50 mL of ice-cold water and extracted twice with EtOAc (2 x 50 ml). The combined organic layers were dried over Na<sub>2</sub>SO<sub>4</sub> filtered, and concentrated to dryness at low pressure to afford pure nitrobenzoic acid **11** (839.8 mg, 72% yield) as a yellow solid. UPLCS/MS: Rt = 1.51 min (gradient 1); MS (ESI) m/z: 298.2 [M-H]<sup>-</sup>,

[M-H]<sup>-</sup> calculated: 298.9. <sup>1</sup>H NMR (400 MHz, DMSO-*d*<sub>6</sub>) δ 8.62 (d, *J* = 2.1 Hz, 1H), 8.37 (d, *J* = 2.1 Hz, 1H).

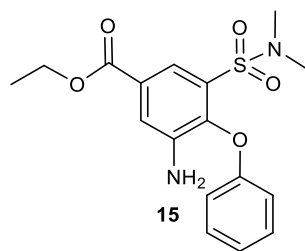


**4-chloro-3-(*N,N*-dimethylsulfamoyl)-5-nitrobenzoic acid (12).** To a an ice cold mixture of 1N sodium hydroxide (5.54 mL) and aqueous 40% methylamine solution (0.5 mL, 3.32 mmol) nitrobenzoic acid **11** (839.8 mg, 2.77 mmol) was added in portions, while stirring. Then the resulting solution was left standing until it had reached room temperature and stirred for additional 5 minutes. Then the reaction mixture was slowly acidified with 2N hydrochloric acid until pH 3. The resulting precipitate was collected by suction and recrystallized from aqueous ethanol to afford pure **12** (427.5 mg, 53% yield) as a brownish solid. UPLCS/MS: Rt = 1.27 min (gradient 1); MS (ESI) *m/z*: 307.3 [M-H]<sup>-</sup>, [M-H]<sup>-</sup> calculated: 307.9. <sup>1</sup>H NMR (400 MHz, DMSO-*d*<sub>6</sub>) δ 8.71 (d, *J* = 2.0 Hz, 1H), 8.57 (d, *J* = 2.0 Hz, 1H), 2.88 (s, 6H).



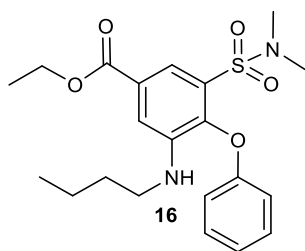
**3-(*N,N*-dimethylsulfamoyl)-5-nitro-4-phenoxybenzoic acid (13).** To a suspension of intermediate **12** (427.5 mg, 1.37 mmol) and NaHCO<sub>3</sub> (465.3 mg, 5.48 mmol) in water (7 mL) was added phenol (237.7 mg, 2.88 mmol) and the mixture was stirred at 90°C for 8 hours under microwave irradiation (CEM Explorer 48 SP apparatus, power 200 W). At reaction completion, the reaction mixture was cooled in an ice bath and acidified with concentrated HCl until pH 3. The resulting precipitate was filtrated and recrystallized from aqueous ethanol to afford pure intermediate **13** (291.1 mg, 58% yield) as a brownish solid. UPLCS/MS: Rt = 1.51 min (gradient 1); MS (ESI) *m/z*: 365.4 [M-H]<sup>-</sup>, [M-H]<sup>-</sup>

calculated: 366.05.  $^1\text{H}$  NMR (400 MHz,  $\text{DMSO-}d_6$ )  $\delta$  8.69 (d,  $J = 2.2$  Hz, 1H), 8.65 (d,  $J = 2.2$  Hz, 1H), 7.37 – 7.30 (m, 2H), 7.14 – 7.08 (m, 1H), 6.96 – 6.90 (m, 2H), 2.79 (s, 6H).

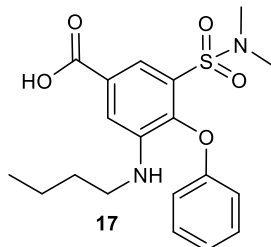


**Ethyl 3-amino-5-(*N,N*-dimethylsulfamoyl)-4-phenoxybenzoate (15).** Under argon atmosphere, to a suspension of benzoic acid **13** (291.1 mg, 0.79 mmol) and  $\text{Pd}(\text{OH})_2/\text{C}$  (58.0 mg) in anhydrous methanol (15.9 mL) was added ammonium formate (258.0 mg, 3.97 mmol) and the reaction crude was stirred at reflux temperature for 30 minutes. At completion, the reaction crude was filtered through a celite coarse patch and the filtrate concentrated to dryness at low pressure. This crude material (380 mg) was dissolved in absolute ethanol (2.2 mL) and the solution was cooled at  $0^\circ\text{C}$  and degassed with nitrogen. Then, thionyl chloride was added (110  $\mu\text{L}$ , 1.45 mmol) and the reaction mixture was stirred at reflux temperature for 4 hours. At completion, the reaction crude was evaporated to dryness at low pressure. The dry residue was treated with 20 mL of a saturated  $\text{NaHCO}_3$  solution and extracted twice with DCM (2 x 20 mL). The combined organic layers were dried over anhydrous  $\text{Na}_2\text{SO}_4$ , filtered and concentrated under reduced pressure. Purification by typical silica gel flash chromatography (cyclohexane/EtOAc from 85:15) finally afforded pure benzoate **15** (198.6 mg, 69% yield over two steps) as a brownish solid. UPLCS/MS:  $R_t = 2.13$  min (gradient 1); MS (ESI)  $m/z$ : 365.4  $[\text{M}+\text{H}]^+$ ,  $[\text{M}+\text{H}]^+$  calculated: 364.1.  $^1\text{H}$  NMR (400 MHz,  $\text{DMSO-}d_6$ )  $\delta$  7.71 (d,  $J = 2.1$  Hz, 1H), 7.61 (d,  $J = 2.1$  Hz, 1H), 7.29 (t,  $J = 7.9$  Hz, 2H), 7.03 (t,  $J = 7.3$  Hz, 1H), 6.77 (d,  $J = 8.1$  Hz, 2H), 5.45 (s, 2H), 4.34 (q,  $J = 7.1$  Hz, 2H), 2.69 (s, 6H), 1.33 (t,  $J = 7.1$  Hz, 3H).





**Ethyl 3-(butylamino)-5-(*N,N*-dimethylsulfamoyl)-4-phenoxybenzoate (16).** Compound **16** was synthesized following the general procedure **A** previously described using ethyl benzoate **15** (75 mg, 0.20 mmol) and butyraldehyde (73  $\mu$ L, 0.81 mmol). Purification by typical silica gel flash chromatography (cyclohexane/EtOAc from 100:0 to 90:10) finally afforded the pure **16** (78.1 mg, 93% yield) as a white solid. UPLCS/MS:  $R_t$  = 1.86 min (gradient 2); MS (ESI)  $m/z$ : 419.5  $[M-H]^-$ ,  $[M-H]^-$  calculated: 420.2.  $^1H$  NMR (400 MHz, DMSO- $d_6$ )  $\delta$  7.62 (d,  $J$  = 2.0 Hz, 1H), 7.48 (d,  $J$  = 2.0 Hz, 1H), 7.31 – 7.24 (m, 2H), 7.06 – 7.00 (m, 1H), 6.79 – 6.74 (m, 2H), 5.21 (t,  $J$  = 5.7 Hz, 1H), 4.35 (q,  $J$  = 7.1 Hz, 2H), 3.07 (q,  $J$  = 6.6 Hz, 2H), 2.69 (s, 6H), 1.42 – 1.31 (m, 5H), 1.14 – 1.05 (m, 2H), 0.77 (t,  $J$  = 7.3 Hz, 3H).



**3-(butylamino)-5-(*N,N*-dimethylsulfamoyl)-4-phenoxybenzoic acid (17).** Compound **17** was synthesized following the general procedure **B** previously described using ethyl ester **16** (78.9 mg, 0.14 mmol). Final trituration in cyclohexane twice ( $2 \times 1$  mL) afforded the pure **17** (48.9 mg, 89% yield) as a white solid. UPLCS/MS:  $R_t$  = 1.87 min (gradient 1); MS (ESI)  $m/z$ : 391.5  $[M-H]^-$ ,  $[M-H]^-$  calculated: 392.1.  $^1H$  NMR (400 MHz, DMSO- $d_6$ )  $\delta$  7.63 (d,  $J$  = 1.9 Hz, 1H), 7.49 (d,  $J$  = 2.0 Hz, 1H), 7.33 – 7.26 (m, 2H), 7.04 (t,  $J$  = 7.4 Hz, 1H), 6.80 – 6.75 (m, 2H), 5.15 (t,  $J$  = 5.7 Hz, 1H), 3.07 (q,  $J$  = 6.6 Hz, 2H), 2.70 (s, 6H), 1.42 – 1.33 (m, 2H), 1.17 – 1.06 (m, 2H), 0.78 (t,  $J$  = 7.3 Hz, 3H).  $^{13}C$  NMR (101 MHz, DMSO- $d_6$ )  $\delta$  166.41 (CO), 156.14 (C), 142.80 (C), 139.60 (C), 130.92 (C), 129.34 (CH), 122.29 (CH), 117.48 (CH), 115.66 (CH), 115.07 (CH), 42.01 (CH<sub>2</sub>), 37.12 (CH<sub>3</sub>), 30.13 (CH<sub>2</sub>), 19.31 (CH<sub>2</sub>), 13.58 (CH<sub>3</sub>).

## **Biology:**

**HEK cell culture and transfection.** HEK293 cells were cultured in Dulbecco's MEM (DMEM) supplemented with 10% fetal bovine serum, 1% L-glutamine, 100 U/ml penicillin, and 100 µg/ml streptomycin, and maintained at 37 °C in a 5% CO<sub>2</sub> humidified atmosphere. To assess NKCC1 and NKCC2 activity (Cl<sup>-</sup>-influx assay), 3 million HEK cells were plated in a 10 cm cell-culture dish and transfected with a transfection mixture comprising 5 ml of DMEM (Dulbecco's Modified Eagle Medium), 4 ml Opti-MEM, 8 µg of DNA plasmid coding for NKCC1 (PRK-NKCC1 obtained from Medical Research Council and the University of Dundee), NKCC2 (OriGene plasmid #RC216145) subcloned in PRK5 plasmid, or mock control (empty vector), together with 8 µg of a plasmid coding for the Cl<sup>-</sup>-sensitive variant of the membrane-targeted fluorescent protein YFP, mbYFPQS (Addgene plasmid #80742)<sup>193</sup>, and 32 µl of Lipofectamin 2000. To assess KCC2 activity (Thallium influx assay), cells were transfected with 16 µg of KCC2<sup>194</sup> subcloned in PRK5 plasmid or mock control (empty vector) and 32 µl of Lipofectamin 2000. After 4 h, the cells were collected and plated in 96-well black-walled, clear-bottomed plates at a density of 2.5x10<sup>4</sup>. After 48 h, cells were used for the Cl<sup>-</sup> or Thallium influx assays. All reagents were purchased from Life Technologies, unless otherwise specified.

**Cl<sup>-</sup>-influx assay in HEK cells.** Transfected cells were treated with 10µM or 100 µM bumetanide and (as positive control), DMSO (se negative control), or with each of our compounds in 100 µl/well of a Cl<sup>-</sup>-free hypotonic solution (67.5 mM Na<sup>+</sup> Gluconate, 2.5mM K<sup>+</sup> Gluconate, 15mM HEPES pH 7.4, 50 mM Glucose, 1mM Na<sub>2</sub>HPO<sub>4</sub>, 1 mM NaH<sub>2</sub>PO<sub>4</sub>, 1 mM MgSO<sub>4</sub>, 1 mM CaSO<sub>4</sub>). After 30 min of incubation, plates were loaded into a Victor 3V (Perkin Elmer) multiplate reader equipped with an automatic liquid in/jector system, and fluorescence of Cl<sup>-</sup>-sensitive mbYFPQS was recorded with excitation at 485 nm and emission at 535 nm. For each well, fluorescence was first recorded for 20 s of baseline and for 60s after delivery of an NaCl concentrated solution (74 mM final concentration in assay well). Florescence of Cl<sup>-</sup>-sensitive mbYFPQS is inversely correlated to the intracellular Cl<sup>-</sup> concentration<sup>193</sup>, therefore chloride influx into the cells determined a decrease of mbYFPQS fluorescence. To represent the fluorescent traces in time, we normalized the fluorescence value for each time point to the average of the fluorescence value of the first 20 s of baseline ( $\Delta F/F_0$ ). To quantify

the average effects as represented by the bar plots, we expressed the decrease in fluorescence upon NaCl application as the average of the last 10 s of  $\Delta F/F_0$  normalized traces. Moreover, for each experiment, to account for the contribution of  $\text{Cl}^-$  changes that were dependent on transporters/exchangers other than NKCC1 or NKCC2, we subtracted the value of the last 10 s of  $\Delta F/F_0$  normalized traces obtained from mock-transfected cells (either control or treated) from the respective  $\Delta F/F_0$  value obtained from the cells transfected with NKCC1 or NKCC2. We then presented in the figures all the data as a percentage of the fluorescence decrease vs the value of the control DMSO.

## Chapter 3. Discovery and characterization of novel selective NKCC1 inhibitors.

### 3.1 Ligand based identification of new molecular scaffolds.

To find novel hit compounds able to inhibit NKCC1, we employed a ligand-based computational strategy. Notably, the NKCC1 structure was not known yet, when this project and hit compound search started. Thus, ligand-based drug design allowed us to perform a virtual screening of the IIT compound library, as well as of virtual libraries from external vendors.

As a starting point, we generated a pharmacophoric model of bumetanide. To this aim, we first performed a force field-based conformational analysis on bumetanide's structure. This approach returned the preferred spatial arrangement of the pharmacophoric features of bumetanide, such as H-bond donor and acceptor, lipophilic and aromatic groups. As a result, the bumetanide generated pharmacophore (Figure 3.1) consisted of four HBA features (red spheres), three HBD interactions (blue spheres) and one lipophilic feature (green sphere). We then implemented ligand disposition by superimposing this template pharmacophore with other unspecific NKCC1 inhibitors (i.e. furosemide, azosemide, piretanide, bendroflumethiazide, benzthiazide, chlorothiazide, metolazone and quinethazone) revealing shared features and different dihedral dispositions of the substituents around the central aromatic core. We then used this refined model as a filter for the virtual screening of the internal chemical collection available in the D3 department at IIT, which contains a diverse and non-redundant set of ~15,000 molecules readily available for experimental testing. A first screening round allowed us to select 167 new compounds from the IIT library, which were individually tested for their ability to inhibit NKCC1 in the Cl<sup>-</sup>-flux assay. Among these compounds, 20% showed a NKCC1 inhibition ranging between 5%-10% at 10  $\mu$ M, while the other 80% did not show any activity (not shown). Then, we took advantage of the data generated in this first round and refine our initial pharmacophore model. In this way, we could perform a refined second screening of the D3's chemical collection, and chemical libraries from commercial vendors (Life chemicals and ZINC). The libraries were filtered to retain only molecules that obey to the Lipinski rules and that do not bear reactive functional groups, amounting to ~ 135,000 compounds. By performing the second run of virtual screening, we selected 86 compounds. Among these compounds, which were tested in the Cl<sup>-</sup>-flux

assay, two structurally related 2-amino-5-nitro-benzenesulfonamide derivatives ARN22392 and ARN22394 (Table 3.1) diversified for the substituent on the amino group, displayed significant (although moderate) inhibitory activity against NKCC1. These compounds thus emerged as promising hit compounds.

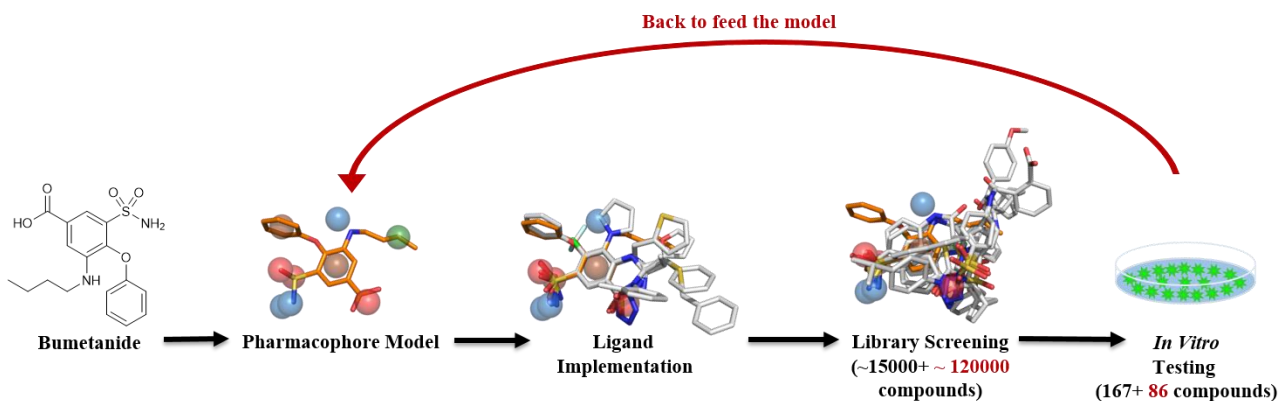
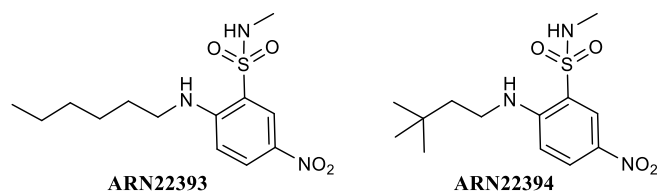


**Figure 3.1.** Schematic representation of the ligand-based computational strategy towards the discovery of novel molecular scaffolds that inhibit NKCC1. Using the structure of bumetanide and several close analogues, we generated a pharmacophore model indicating 3D disposition and physicochemical features needed for key interactions. This model was used for the preliminary screening of the D3 internal library of small molecules. After the first screening of 167 compounds, we refined the pharmacophore to screen chemical libraries from commercial vendors, from which we selected 86 compounds to be tested *in vitro*.

ARN22393 (Table 3.1), with a *n*-hexyl chain on amino group and a methylated sulfonamide, showed a significant inhibition of NKCC1 of  $29.4 \pm 2.8$  % at 100  $\mu$ M. ARN22394 (Table 3.1), bearing a 3,3-dimethylbutyl chain on the amino group and a methylated sulfonamide, also showed a significant inhibition of NKCC1 of  $17.7 \pm 3.9$  % at 10  $\mu$ M and of  $28.6 \pm 4.3$  % at 100  $\mu$ M. Although promising, these two compounds still showed low potency in NKCC1 inhibition compared to bumetanide. Thus, ARN22393 and ARN22394 were selected as a starting point for the design and synthesis of new derivatives.



Entry	10 $\mu$ M NKCC1 inhibition	100 $\mu$ M NKCC1 inhibition
ARN22393	No inhibition	29.4 $\pm$ 2.8 %
ARN22394	17.7 $\pm$ 3.9 %	28.6 $\pm$ 4.3 %

**Table 3.1.** Structure and activity in Cl<sup>-</sup>-flux assay of hit compounds ARN22393 and ARN22394.

Based on the chemical core of ARN22393 and ARN22394, we decided to synthesize new compounds by evaluating two series of analogues based on the substituents in position 1 of the aromatic ring: a 2-amino-5-nitro-benzene-sulfonamide series (**Series A**, Figure 3.2) and a 4-amino-3-sulfamoyl-benzoic acid series (**Series B**, Figure 3.2). In particular, we compared the nitro group with the more drug-like carboxylic acid, aware of its fundamental function for the inhibition of the CCCs, and predicted to confer a favourable balance between potency and solubility to the new compounds. To enhance compounds potency and enrich our SAR, we decided to proceed by inserting the structural motifs that we studied for the bumetanide analogues. This allowed us to understand their effect on this different core, taking advantage of the different disposition of the substituents in respect to bumetanide. The amino group was manipulated with alkyl sidechains of different lengths, and the sulfonamide methylation was compared to dimethylation, as well as the primary sulfonamide effect on activity.

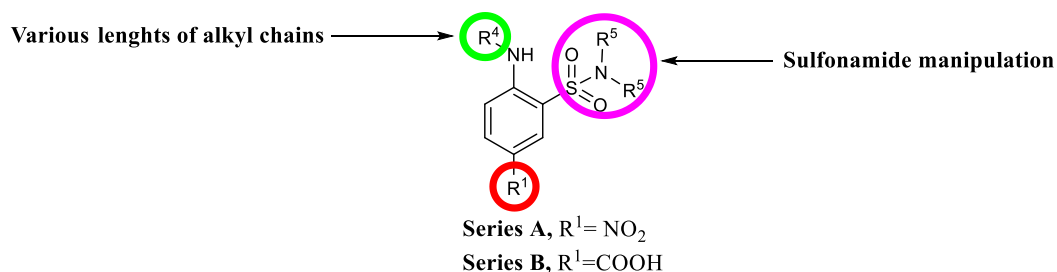
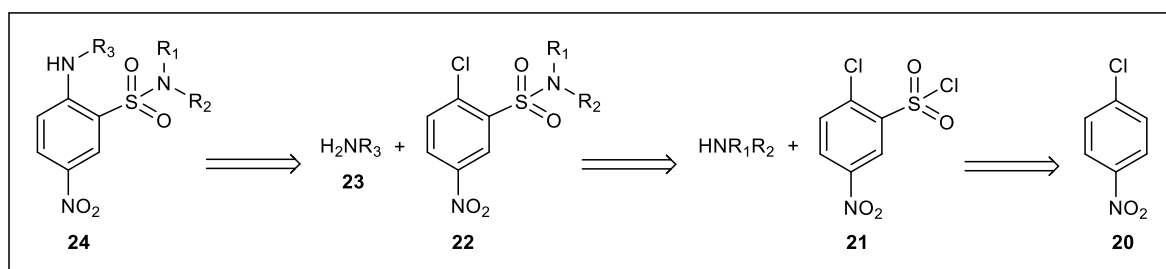


**Figure 3.2.** Representation of the points of subject to modification based in the ARN22393 and ARN22394 common scaffold.

### 3.2 Synthesis of 2-amino-5-nitro-benzene-sulfonamide derivatives (Series A).

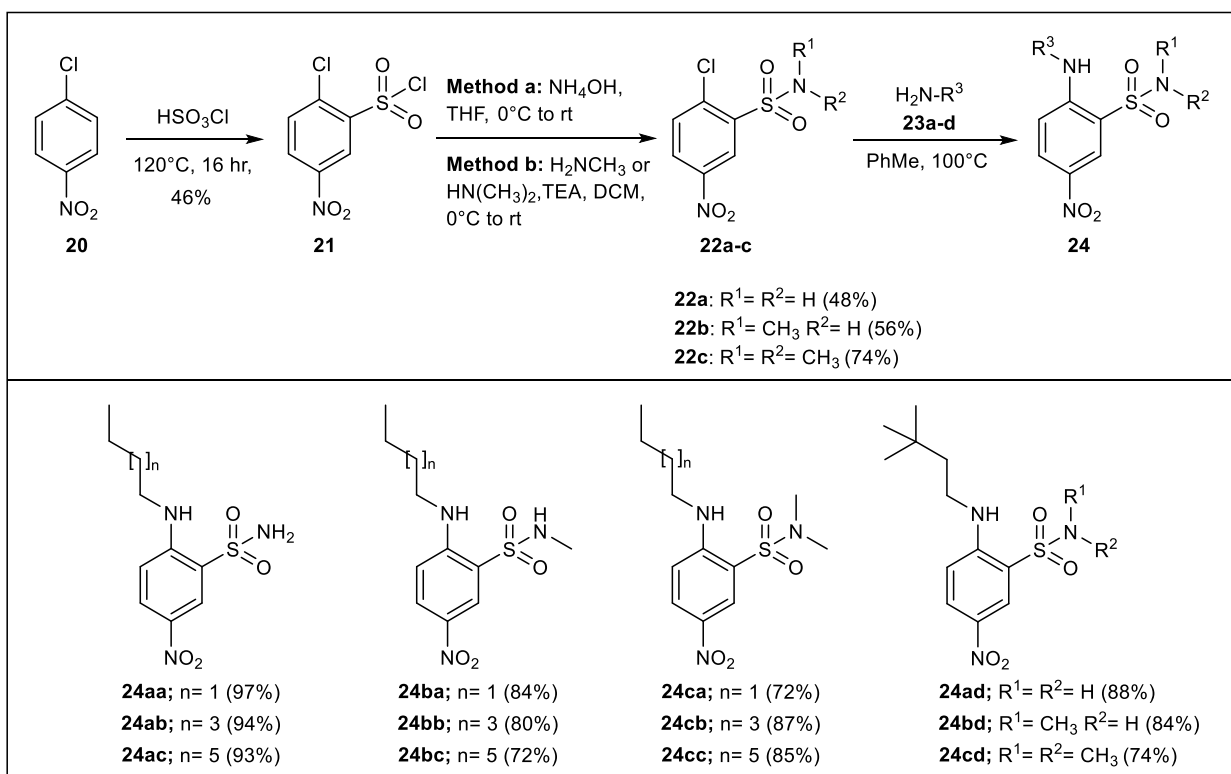
Retrosynthetically, we approached the construction of the 2-amino-5-nitro-benzene-sulfonamide derivative **24** from nucleophilic aromatic substitution of **22** (Scheme 3.1). 2-chloro-5-nitro-benzenesulfonamide **22** could be obtained by substitution of the chlorosulfonyl group of **21** with a suitable amine of type **23**, which in turn could be achieved from electrophilic aromatic substitution of commercial starting material **20** with chlorosulfonic acid.



**Scheme 3.1.** Retrosynthesis of 2-amino-5-nitro-benzene-sulfonamide derivatives.

As depicted in Scheme 3.2, synthesis first proceeded by electrophilic aromatic substitution on commercial 1-chloro-4-nitro-benzene **20** with chlorosulfonic acid, which occurred in a regioselective manner. Then, substitution of the chlorosulfonyl group of **21** was approached via two different methodologies to access the target sulfonamides. The use of aqueous ammonia afforded the primary sulfonamide **22a** in a good 48% yield. Alternatively, alkylated sulfonamides **22b-c** were achieved in good yields using methylamine or dimethylamine hydrochloride in the presence of two equivalents of triethylamine.

Finally, nucleophilic aromatic substitution with the proper alkyl amines **23a-d** occurred efficiently to afford the target compounds of type **24**.

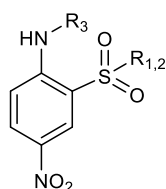


**Scheme 3.2.** Synthesis of 2-amino-5-nitro-benzene-sulfonamide derivatives of type **24**.

### 3.2.1 Testing of 2-amino-5-nitro-benzene-sulfonamide derivatives (Series A).

We then compared the inhibitory activity of the newly synthesized 2-amino-5-nitro-benzene-sulfonamide derivatives **24** with the hit compounds ARN22393 and ARN22394. For this purpose, we used the previously described Cl<sup>-</sup>-flux assay in HEK293 cells. The compounds were tested in the Cl<sup>-</sup>-flux assay at two concentrations (10 μM and 100 μM). Results are summarized in Table 3.2.





Entry	R <sub>3</sub>	R <sub>1,2</sub>	10 μM NKCC1 inhibition	100 μM NKCC1 inhibition
ARN22393 (24bb)		NHCH <sub>3</sub>	No inhibition	29.4 ± 2.8 %
ARN22394 (24bd)		NHCH <sub>3</sub>	17.7 ± 3.9 %	28.6 ± 4.3 %
24aa		NH <sub>2</sub>	11.2 ± 2.6%	No inhibition
24ab		NH <sub>2</sub>	25.4 ± 3.7 %	No inhibition
24ac		NH <sub>2</sub>	12.4 ± 2.4 %	No inhibition
24ad		NH <sub>2</sub>	5.8 ± 1.1%	No inhibition
24ba		NHCH <sub>3</sub>	No inhibition	No inhibition
24bc		NHCH <sub>3</sub>	No inhibition	No inhibition
24ca		N(CH <sub>3</sub> ) <sub>2</sub>	No inhibition	No inhibition
24cb		N(CH <sub>3</sub> ) <sub>2</sub>	16 ± 4.7%	No inhibition
24cc		N(CH <sub>3</sub> ) <sub>2</sub>	Inactive	No inhibition
24cd		N(CH <sub>3</sub> ) <sub>2</sub>	No inhibition	No inhibition

**Table 3.2.** Inhibitory activity of synthesized of 2-amino-5-nitro-benzene-sulfonamide derivatives.

Notably, only the group of compounds bearing a primary sulfonamide retained some activity compared with the hit compounds. Shortening of the chain of compound **24aa** decreased activity against NKCC1, while conservation of the *n*-hexyl chain as in **24ab** and **24cb** preserved inhibitory activity. Elongation of the chain to *n*-octyl combined with primary sulfonamide of **24ac** exhibited a slight reduction in potency. Notably, presence of *N,N*-dimethyl sulfonamide **24cb** turned out in minimal inhibitory activity compared with the parent hit ARN22393 at 10 μM. Unfortunately, other derivatives bearing alkylated sulfonamides were hampered by low solubility (Table 3.3) in the assay buffer, which affected

assay readout at both 10  $\mu\text{M}$  and 100  $\mu\text{M}$ . Nevertheless, solubility issues burdened all the series over 10  $\mu\text{M}$ . As shown in Table 3.3, compounds were characterized by low kinetic solubility in aqueous medium even below the lower test concentration. Only the presence of a primary sulfonamide (**24ab**, Table 3.3) was able to give a modest enhancement in solubility.

Entry	Kinetic solubility PBS <sup>a</sup>	$t_{1/2}$ plasma <sup>b</sup>	$t_{1/2}$ liver microsomes <sup>c</sup>
ARN22393	1 $\mu\text{M}$	>120 min	<5 min
ARN22393	3 $\mu\text{M}$	>120 min	6 min
<b>24ab</b>	6 $\mu\text{M}$	>120 min	<5 min
<b>24cb</b>	1 $\mu\text{M}$	>120 min	<5 min

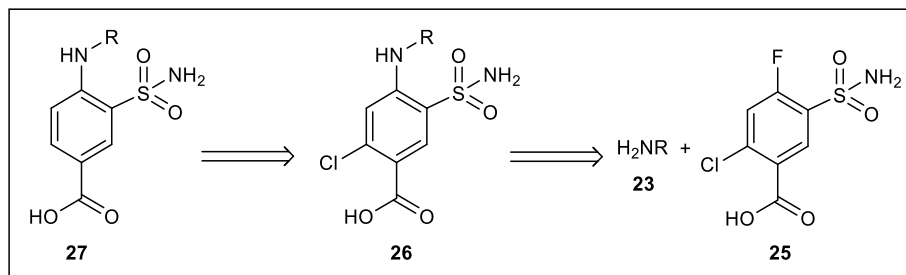
**Table 3.3. Solubility and *in vitro* drug-like properties of selected 2-amino-5-nitro-benzene-sulfonamide derivatives.** *a* Aqueous kinetic solubility of compounds from a 10mM DMSO solution in Phosphate Buffered Saline (PBS) at pH 7.4. Target concentration is 250 $\mu\text{M}$  (final DMSO 2.5%). *b* Stability in mouse plasma at 37°C. *c* Stability in mouse liver homogenates. Compounds were incubated at 5  $\mu\text{M}$  (final DMSO 0.1%).

In conclusion, by the manipulation of the substituents of this class of compounds, we were not able to obtain an acceptable boost in potency towards NKCC1 inhibition in comparison to the hit compounds ARN22393 and ARN22394. This effort did not provide highly informative structural information. In particular, low solubility issues (Table 3.3) were recurrent in this chemical class. As a further drawback, this scaffold showed also a poor profile in terms of metabolic stability *in vitro* (Table 3.3). In addition, a large body of literature proved that compounds containing nitro groups could induce severe toxicity *in vivo* (i.e. carcinogenicity, hepatotoxicity, mutagenicity, and bone marrow suppression), especially nitro aromatic compounds<sup>195</sup>. Given these limitations, we halted further synthetic efforts towards the investigation of this series.

### 3.3 Synthesis of 4-amino-3-sulfamoyl-benzoic acid derivatives (Series B).

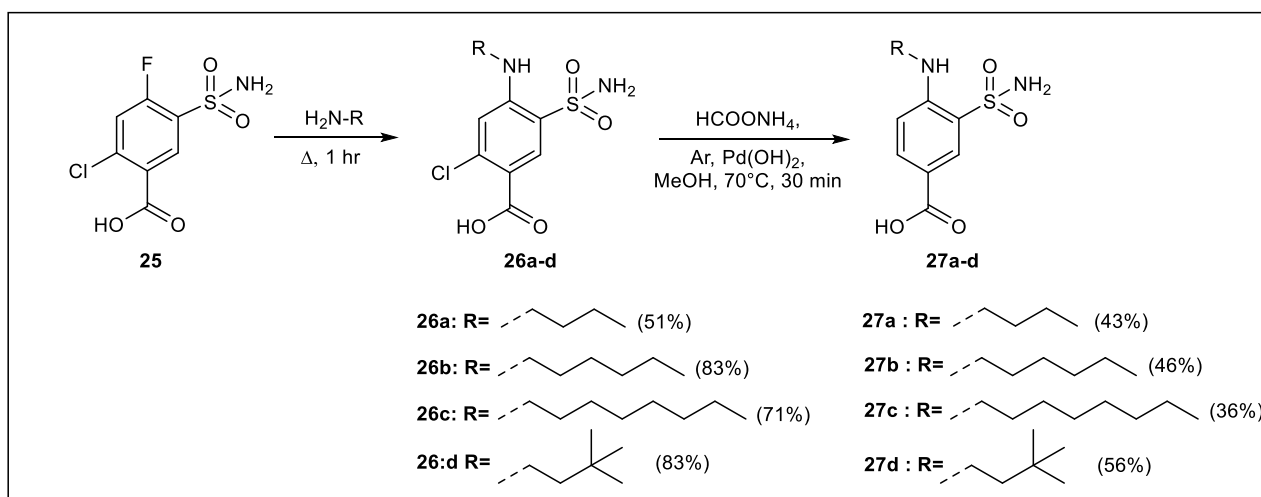
To compare the effect of a carboxylic acid moiety in position 1 on activity and solubility, we synthesized a series of 4-amino-3-sulfamoyl-benzoic acid derivatives. For the synthesis of derivatives bearing a primary sulfonamide, we used the retrosynthetic approach showed in Scheme 3.3.

Derivative **27** could be accessed by reductive dechlorination of intermediate **26**, which can be obtained by nucleophilic aromatic substitution of commercially available 2-chloro-4-fluoro-5-sulfamoylbenzoic acid **25**.



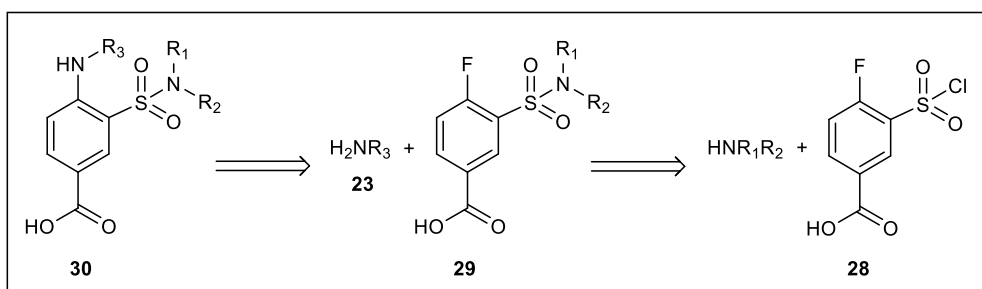
**Scheme 3.3.** Retrosynthesis of primary sulfonamide substituted 4-amino-3-sulfamoyl-benzoic acid derivatives.

Synthesis (Scheme 3.4) was achieved with a first step of nucleophilic aromatic substitution with the proper amines of commercial 2-chloro-4-fluoro-5-sulfamoylbenzoic acid **25**. The substitutions were run in neat amine in good yields (51-83%). Subsequently, dehalogenation of **26a-d** was performed via palladium-catalyzed reduction with ammonium formate as hydrogen source to afford target compounds **27a-d**.



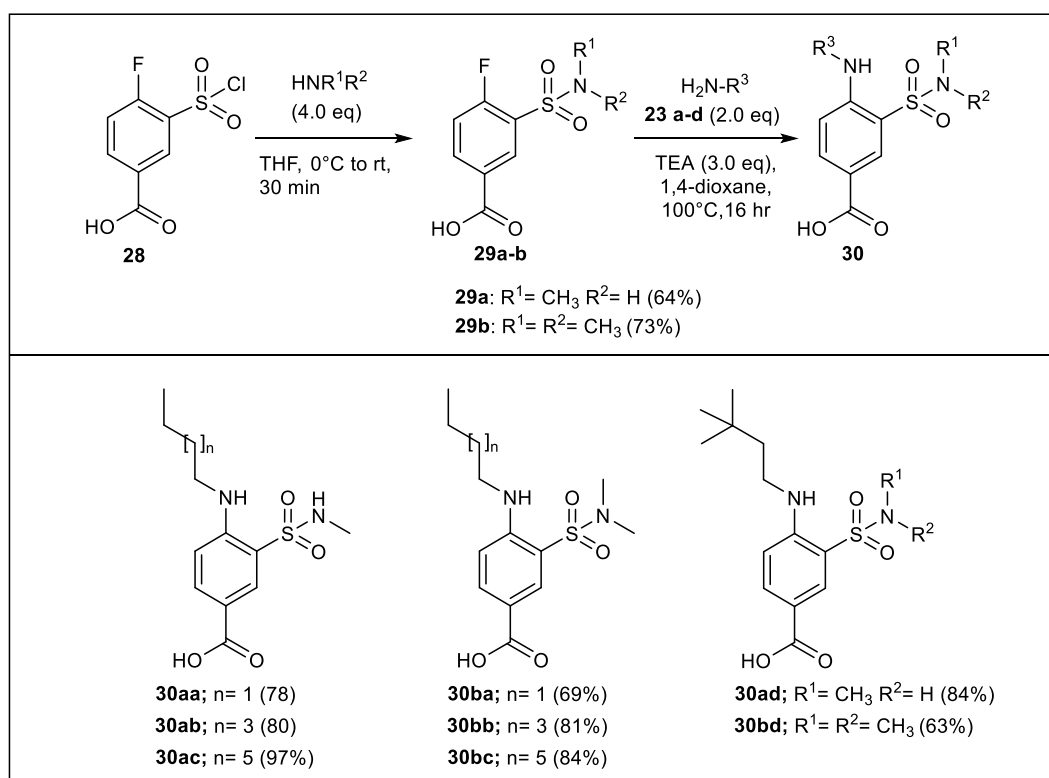
**Scheme 3.4.** Synthesis of primary sulfonamide substituted 4-amino-3-sulfamoyl-benzoic acid derivatives.

To access the alkyl sulfonamide analogues, we used a different retrosynthetic approach (Scheme 3.5). Scaffold of type **30** could be obtained by substitution of the proper 4-fluoro-*N*-alkylsulfamoyl benzoic acid derivative **29**, which in turn could be prepared by substitution of the chlorosulfonyl group of commercial 3-(chlorosulfonyl)-4-fluorobenzoic acid **28**.



**Scheme 3.5.** Retrosynthetic approach towards *N*-alkyl sulfonamide substituted 4-amino-3-sulfamoyl-benzoic acid derivatives.

As shown in Scheme 3.6, as a first synthetic step we performed the substitution of 3-(chlorosulfonyl)-4-fluorobenzoic acid **28** with an excess of methylamine or dimethylamine to access compounds **29a-b** in good yields. Finally, these intermediates were refluxed in 1,4-dioxane with suitable alkyl amines **23a-d** to afford the target compounds **30** in high yields.

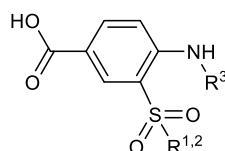


**Scheme 3.6.** Synthetic approach towards *N*-alkyl sulfonamide substituted 4-amino-3-sulfamoyl-benzoic acid derivatives.

### 3.3.1 Testing of 4-amino-3-sulfamoyl-benzoic acid derivatives (series B).

To evaluate the inhibitory activity on NKCC1 of the synthesized 4-amino-3-sulfamoyl-benzoic acid derivatives in comparison to the hit compounds and bumetanide, we used the Cl<sup>-</sup>-flux assay in HEK293 cells. The compounds were tested in the Cl<sup>-</sup>-flux assay at two concentrations (10 μM and 100 μM). Results are summarized in Table 3.4.

Notably, the insertion of the carboxylic acid generated an increase in inhibitory activity compared to Series A (Table 3.1), confirming the importance of this acid chemical group, as shown by data acquired from bumetanide analogues. Derivatives bearing the *n*-butyl chain **27a**, **30aa**, **30ba**, exhibited a decrease in potency when compared to the hit compounds, as elongation of the chain to the *n*-hexyl motif of **27b**, **30ab** and **30bb** resulted in a comparable activity at 100 μM. Interestingly, insertion of the *n*-octyl chain resulted in different effects on inhibitory activity when combined with different sulfonamides. Compound **27c** displayed a decreased activity at 100 μM compared to the shorter chain derivative, **27b** bearing a primary sulfonamide. Conversely, the methylated sulfonamide combined with the *n*-octyl chain resulted in higher potency of **30ac**, showing a two fold increase in activity at 100 μM ( $35.0 \pm 17.3$  %) compared to **27c**, suggesting a synergistic effect related with sulfonamide alkylation. The same trend was observed in derivative **30bc** compared to **30ac**. Combination with the dimethyl sulfonamide resulted in inhibitory value at 100 μM ( $70.6 \pm 9.1$  %), similar to that of bumetanide ( $71.7 \pm 7$  %). On the other end, the *N,N*-dimethyl sulfonamide **30bd** bearing the bulk 3,3-dimethylbutyl chain displayed a slight improvement in activity in relation to **27d** and **30ad**. Surprisingly, the 3,3-dimethylbutyl substituted analogues **27d** and **30ad** led to a decrease in potency compared to the corresponding structurally related hit compound ARN22394, while the presence of the dimethylated sulfonamide resulted in comparable potency of **30 bd**.



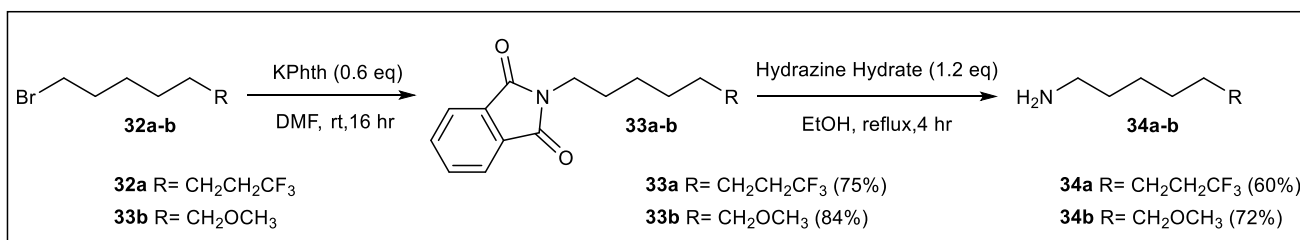
Entry	R <sup>3</sup>	R <sup>1,2</sup>	10 μM Cl <sup>-</sup> -Flux	100 μM Cl <sup>-</sup> Flux
<b>Bumetanide</b>	-	-	58.8 ± 5.6 %	71.7 ± 7 %
<b>ARN22393</b>		NHCH <sub>3</sub>	No inhibition	29.4 ± 2.8 %
<b>ARN22394</b>		NHCH <sub>3</sub>	17.7 ± 3.9 %	28.6 ± 4.3 %
<b>27a</b>		NH <sub>2</sub>	No inhibition	10.9 ± 3.7 %
<b>27b</b>		NH <sub>2</sub>	No inhibition	39.7 ± 8.5 %
<b>27c</b>		NH <sub>2</sub>	No inhibition	18.4 ± 7.6 %
<b>27d</b>		NH <sub>2</sub>	No inhibition	18.9 ± 2.5 %
<b>30aa</b>		NHCH <sub>3</sub>	8.2 ± 2.9 %	10.2 ± 2.1%
<b>30ab</b>		NHCH <sub>3</sub>	No inhibition	30.4 ± 7.3%
<b>30ac</b>		NHCH <sub>3</sub>	No inhibition	35.0 ± 17.3 %
<b>30ad</b>		NHCH <sub>3</sub>	No inhibition	16.9 ± 2.6 %
<b>30ba</b>		N(CH <sub>3</sub> ) <sub>2</sub>	10.7 ± 2.9%	12.4 ± 1.3 %
<b>30bb</b>		N(CH <sub>3</sub> ) <sub>2</sub>	11.4 ± 1.9%	26.8 ± 8.1 %
<b>30bc</b>		N(CH <sub>3</sub> ) <sub>2</sub>	No inhibition	70.6 ± 9.1 %
<b>30bd</b>		N(CH <sub>3</sub> ) <sub>2</sub>	No inhibition	29.3 ± 3.8 %

**Table 3.4.** Inhibitory activity of synthesized of 4-amino-3-sulfamoyl-benzoic acid derivatives.

These results prompted us to evaluate other derivatives of this chemical scaffold. Although the *n*-octyl chain gave the best results in term of activity, combination with the dimethyl sulfonamide of all the evaluated chains appeared to be crucial for enhancing potency. For this reason, we decided to conserve this latter motif throughout the design of novel analogues, evaluating different chain lengths.

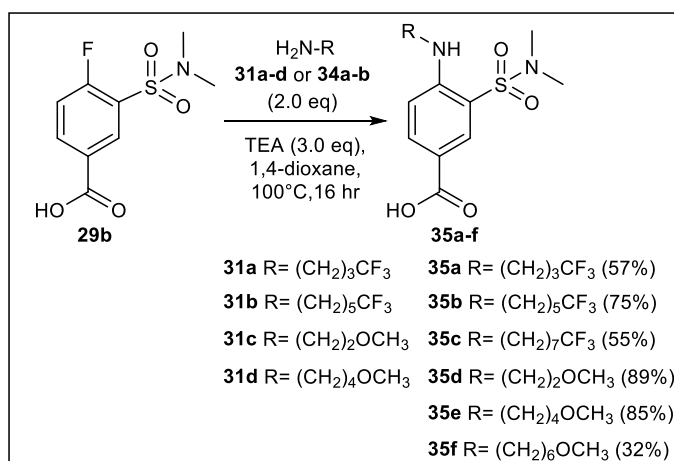
In order to improve activity and investigate the effect of the presence of a substituent at the end of the aliphatic chain, we decided to evaluate two different substitutions in the terminal point of the chain. In doing so, we conserved the dimethylated sulfonamide motif, which gave the best results in terms of inhibitory activity.

Thus, we introduced a terminal polar methyl ether and more lipophilic trifluoromethyl moiety, two groups that could also influence chemico-physical properties of our compounds. For the synthesis of *n*-butyl and *n*-hexyl derivatives, we used the corresponding commercial amines **31a-d** (Scheme 3.8). Conversely, synthesis of non-commercial substituted *n*-octyl amines **34a,b** was approached via Gabriel reaction, starting from the resulting commercial bromides **32a-b** (Scheme 3.7). *N*-alkylation of potassium phthalimide (KPhth) with alkyl bromides **32a-b** occurred efficiently to afford *N*-alkyl phthalimides **33a-b** in high yields. Amines deprotection with hydrazine hydrate led to the isolation of the pure amines **34a-b** after chromatographic purification with basic alumina.



**Scheme 3.7.** Synthesis of terminal substituted *n*-octylamines.

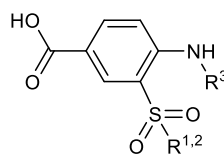
We then performed the nucleophilic aromatic substitution, using the conditions depicted in Scheme 3.7 on **29b**, to access compounds **35a-f** in good yields (Scheme 3.8).



**Scheme 3.8.** Synthesis of terminal substituted derivatives.

We then tested these new derivatives in the Cl<sup>-</sup>-flux assay at two concentrations (10 μM and 100 μM).

Results are summarized in Table 3.5.



Entry	R <sup>3</sup>	R <sup>1,2</sup>	10 μM Cl <sup>-</sup> Flux	100 μM Cl <sup>-</sup> Flux
<b>Bumetanide</b>	-	-	58.8 ± 5.6 %	71.7 ± 7 %
<b>ARN22393</b>		NHCH <sub>3</sub>	No inhibition	29.4 ± 2.8 %
<b>ARN22394</b>		NHCH <sub>3</sub>	17.7 ± 3.9 %	28.6 ± 4.3 %
<b>35a</b>		N(CH <sub>3</sub> ) <sub>2</sub>	11.0 ± 6.3 %	13.6 ± 5.8 %
<b>35b</b>		N(CH <sub>3</sub> ) <sub>2</sub>	17.3 ± 2.6 %	25.4 ± 4.2 %
<b>35c</b>		N(CH <sub>3</sub> ) <sub>2</sub>	37.1 ± 5 %	88.5 ± 11.7 %
<b>35d</b>		N(CH <sub>3</sub> ) <sub>2</sub>	No inhibition	No inhibition
<b>35e</b>		N(CH <sub>3</sub> ) <sub>2</sub>	No inhibition	17.9 ± 2.3 %
<b>35f</b>		N(CH <sub>3</sub> ) <sub>2</sub>	No inhibition	22.5 ± 6.7 %

**Table 3.5.** Inhibitory activity of synthesized terminal substituted derivatives.

We observed that the trifluoromethyl-substituted analogues **35a**, **35b** retained a similar level of activity in respect to their aliphatic counterparts. Elongation of chain length then resulted in an increase in activity, similarly to what we observed previously. Importantly, the terminal trifluoromethyl group enhanced substantially the activity of the *n*-octyl derivative **35c**. At 100 μM this compound displayed a superior inhibitory activity when compared to bumetanide, probably due to higher lipophilic interactions with the target provided by the trifluoromethyl group.

Strikingly, the insertion of the terminal methyl ether resulted in a dramatic drop in inhibitory activity, as the derivatives **35d**, **35e**, **35f** did not show any inhibition at 10 μM. Notably, also the longer chain derivative **35f** displayed a low activity even at 100 μM, suggesting that the terminal methoxy group may disrupt a key interaction established by the alkyl chain with the transporter.



### 3.4 Evaluation of the most promising compounds in calcium kinetic assay in neuronal cultures.

To confirm the activity on NKCC1 of the most active analogues, we tested their ability to revert the depolarizing GABA signaling in young neurons, indirectly measured as calcium influx into the cells with an *in vitro* calcium kinetic assay in primary neuronal cultures. For this assay, we selected the most active *n*-octyl analogues **30ac**, **30bc** and **35c**, which showed the highest activity in the Cl<sup>-</sup>-flux assay. This assay takes advantage of the physiological, endogenous, high-expression of NKCC1 in immature neurons, which causes depolarizing actions of GABA, able to activate voltage-gated Ca<sup>2+</sup> channels. Thus, in immature neurons, a compound that blocks NKCC1 is predicted to inhibit Ca<sup>2+</sup> responses upon GABA application.

Immature neurons were cultured for 3 days *in vitro* (3DIV) and loaded for 15 min with a calcium-sensitive dye (Fluo4, Invitrogen) in the extracellular solution. Then, neurons were treated with bumetanide (as a positive control) and our newly synthesized compounds (at 10 μM and 100 μM) diluted in extracellular solution for 15 min. As a functional readout, we monitored the level of fluorescence in the neuronal cultures, upon application of GABA (100 μM, for 20 sec). Results are summarized in Table 3.6.

Entry	10 μM Ca <sup>2+</sup> Flux	100 μM Ca <sup>2+</sup> Flux
<b>Bumetanide</b>	51.9 ± 2.3 %	54.7 ± 2.5 %
<b>30ac</b>	18.6 ± 5.3 %	46.3 ± 3.7 %
<b>30bc</b>	44.8 ± 4.1 %	76.0 ± 8.8 %
<b>35c</b>	45.7 ± 4.3 %	92.8 ± 1.9 %

**Table 3.6.** Inhibitory activity of the compounds evaluated in the Ca<sup>2+</sup> influx assay.

In agreement with the chloride assay, bumetanide displayed an inhibition of calcium entry of  $51.9 \pm 2.3 \%$  at  $10 \mu\text{M}$  and  $54.7 \pm 2.5 \%$  at  $100 \mu\text{M}$  and **35c** displayed the higher inhibition with values of  $45.7 \pm 4.3 \%$  at  $10 \mu\text{M}$  and  $92.8 \pm 1.9 \%$  at  $100 \mu\text{M}$ , almost 2 fold higher compared to bumetanide at  $100 \mu\text{M}$ . Surprisingly, **30ac**, **30bc** showed a significantly higher activity also at  $10 \mu\text{M}$ , **30ac** inhibited calcium entry of  $18.6 \pm 5.3\%$  at  $10 \mu\text{M}$  and  $46.3 \pm 3.7\%$  at  $100 \mu\text{M}$ , and **30bc** inhibited calcium entry of  $44.8 \pm 4.1 \%$  at  $10 \mu\text{M}$  and  $76 \pm 8.8 \%$  at  $100 \mu\text{M}$ . Thus, although the new molecular entities were able to significantly reduce the GABA depolarizing signaling in young neurons, the seeming inconsistency of the activity of furosemide, **30ac** and **30bc** between the  $\text{Cl}^-$ -flux assay and the  $\text{Ca}^{2+}$  influx assay, was furtherly investigated.

To elucidate the effect of **30ac** and **30bc** to inhibit  $\text{Ca}^{2+}$  responses upon GABA application in comparison to the moderate inhibition of NKCC1 in the  $\text{Cl}^-$ -flux assay, we decided to measure the ability of these compounds to inhibit  $\text{GABA}_A\text{R}$ . Indeed, the inhibition in  $\text{Ca}^{2+}$  responses measured in the calcium assay, could be explained by a strong NKCC1 inhibition, but also by a possible direct antagonization of  $\text{GABA}_A$  receptors. Interestingly, it is known that the loop diuretic furosemide, antagonizes the  $\text{GABA}_A$  receptor in cerebral cortex and cerebellum<sup>196-198</sup>.

Thus, the amplitude of evoked  $\text{GABA}_A$  currents were measured after application of bumetanide (as a negative control), furosemide (as a positive control), **30ac**, **30bc** and **35c**. A  $10 \mu\text{M}$  was used, to detect even small inhibitory efficacy of the compounds.

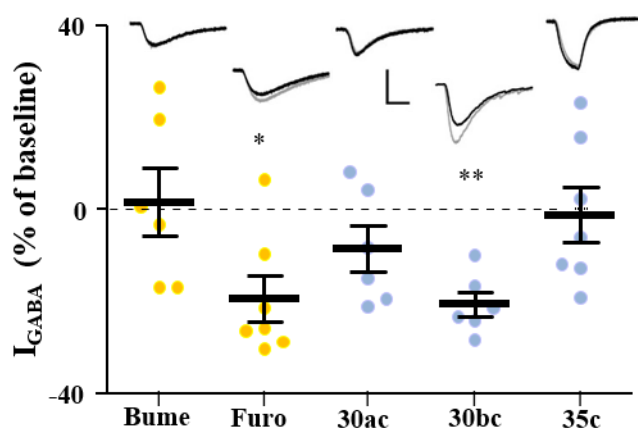


**Figure 3.2.** Amplitude change average and single cell data points of GABA-evoked currents obtained by recording 12-20 DIV neurons before (gray example recordings in the inset above) and after (black example traces) bath application of the indicated compounds ( $10 \mu\text{M}$ ). Data are presented as mean  $\pm$  SEM (Paired t-test, \* $P < 0.05$ , \*\*  $P < 0.01$ ). Scale bars: 250 pA, 250 msec

As shown in Figure 3.2, bumetanide and **35b** did not alter GABA<sub>A</sub>-current amplitude. Conversely, furosemide showed  $19.4 \pm 5$  % reduction in the GABA<sub>A</sub>-current amplitude, in agreement with the literature. Notably, **30bc** showed a significant inhibition of GABA current of a  $20.6 \pm 2.6$  % and **30ac** showed a moderate, but not significant reduction of GABA current of  $8.6 \pm 5$ .

In conclusion, via our ligand-based strategy for drug design, we were able to identify a novel scaffold able to inhibit NKCC1. Based on the hit compounds emerged from virtual screening, we synthesized and tested 12 new 2-amino-5-nitro-benzenesulfonamides (Series A). None of them exhibited enhanced potency in NKCC1 inhibition in comparison to the hit compounds (ARN22393 and ARN22394). Conversely, the 4-amino-3-sulfamoyl-benzoic acid derivatives (Series B) emerged as the best class in terms of potency when compared to nitrobenzenes. In particular, we performed numerous manipulations on this class by adding the structural motifs emerged from the screening of the bumetanide analogues (i.e. the dimethylated sulfonamide and the *n*-octyl carbon chain on the amino group). Derivatives bearing the *n*-octyl substituent showed enhanced potency when compared to the shorter chain ones. Among the tested derivatives, compound **35c** displayed the higher inhibition of NKCC1 in the chloride assay, which was confirmed in the calcium assay, and it did not show any inhibition of the GABA<sub>A</sub>R. Notably, **35c** showed a NKCC1 inhibitory activity comparable with the activity of bumetanide at 10  $\mu$ m, but displayed a higher potency than bumetanide at 100  $\mu$ m. This sharp increase in activity in comparison to bumetanide, could suggest that our compound is acting by binding NKCC1 in a cooperative manner. In this type of binding, the occupation of the binding sites by the ligand is indeed not a linear function of the ligand's concentration, and the affinity for the ligand depends on the amount of the bound ligand<sup>199</sup>.

Due to the promising activity in reverting the depolarizing GABA signalling in young neurons, we decided to further proceed with the *in vitro* characterization of compound **35c** (named **ARN23746** in our internal chemical library), toward the lead identification and optimization phase and *in vivo* evaluation.

### 3.5 Experimental section.

**Chemistry** (see Chapter 2, section 2.4 for general information):

**General procedure A for the synthesis of sulfonamides 22b-c (Scheme 3.2).** To an ice-cold solution of the proper amine hydrochloride (1.0 mmol) and triethylamine (2 mmol) in DCM (1.0 ml) was added intermediate **21** (1 mmol) solved in DCM (1.5 ml) and the reaction mixture was stirred at room temperature for 1 hour. At reaction completion, the reaction crude was diluted with DCM (20 ml) and washed with an NH<sub>4</sub>Cl saturated solution (20 ml) and the aqueous layer was extracted twice with DCM (2 x 20 ml). The combined organic layers were dried over Na<sub>2</sub>SO<sub>4</sub> and concentrated to dryness at low pressure. Purification by silica gel flash chromatography finally afforded the pure titled compounds.

**General nucleophilic aromatic substitution procedure B for the synthesis of derivatives of type 24 (Scheme 3.2).** A suspension of intermediates **22a-c** (1 mmol) and the appropriate amine (5 mmol) was stirred in dry toluene (0.7 ml) under argon atmosphere at 100°C for 1 hour. After reaction completion the mixture was evaporated to dryness at low pressure. The dry residue was treated with water (10 ml) and extracted with EtOAc (10 ml). The organic layer was dried over Na<sub>2</sub>SO<sub>4</sub> and concentrated to dryness at low pressure. Purification by silica gel flash chromatography finally afforded the pure titled compounds.

**General nucleophilic aromatic substitution procedure C for the synthesis of compounds 26a-d (Scheme 3.4).** A suspension of commercial 2-chloro-4-fluoro-5-sulfamoyl-benzoic acid **25** (1 mmol) and the appropriate amine (5 mmol) in dry toluene (0.7 ml) was stirred under argon atmosphere at 100°C for 1 hour. After reaction completion the mixture was evaporated to dryness at low pressure and the residue was treated with a saturated NH<sub>4</sub>Cl aqueous solution (15 ml) and extracted twice with EtOAc (2 x 15 ml). The combined organic layers were dried over Na<sub>2</sub>SO<sub>4</sub> and concentrated to dryness at low pressure. Trituration in cyclohexane afforded finally the pure title compounds.

**General dehalogenation procedure D for the synthesis of compounds 27a-d (Scheme 3.4).** Under argon atmosphere, to a suspension of the proper 4-amino-2-chloro-5-sulfamoyl-benzoic acid **26a-d** (1

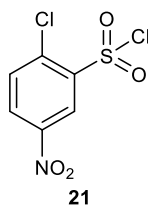
mmol) and palladium hydroxide on carbon (20 wt. %) in dry methanol (20 ml), was added ammonium formate (4 mmol) and the reaction mixture was stirred at reflux temperature for 1 hour. After reaction completion the crude was filtered through a celite coarse patch and the filtrate concentrated to dryness at low pressure. The dry residue was diluted in EtOAc (10 ml) and washed with a saturated  $\text{NH}_4\text{Cl}$  solution (10 ml). The organic layer was dried over  $\text{Na}_2\text{SO}_4$  and concentrated to dryness at low pressure. Trituration in cyclohexane afforded finally the pure title compounds.

**General procedure E for the synthesis of sulfonamides 29a-b (Scheme 3.6).** 4-Fluoro-3-chlorosulfonyl-benzoic acid **28** (1 mmol) solved in 1.5 mL of THF was added dropwise to 8 mL of an ice cold solution of the proper amine (2 mmol) in THF and stirred for 30 min at rt. At reaction completion the reaction mixture was evaporated to dryness. The dry residue was dissolved in water and treated with 2N HCl until it reached pH3. The resulting precipitated product was filtered and rinsed with water to afford the pure titled compounds.

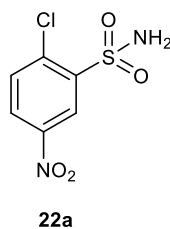
**General nucleophilic aromatic substitution procedure F for the synthesis of compounds derivatives 30, 35a-f (Schemes 3.6, 3.8).** A suspension of intermediates **29a-b** (1 mmol) and the appropriate amine (2 mmol) in dry 1,4-dioxane (3 ml) was stirred under argon atmosphere at  $100^\circ\text{C}$  for 16 hours. After reaction completion the mixture was evaporated to dryness at low pressure and the residue was treated with a saturated  $\text{NH}_4\text{Cl}$  aqueous solution (15 ml) and extracted twice with EtOAc (2x15 ml). The combined organic layers were dried over  $\text{Na}_2\text{SO}_4$  and concentrated to dryness at low pressure. Purification by silica gel flash chromatography with  $\text{CH}_2\text{Cl}_2/\text{MeOH}$  followed by trituration with a suitable solvent (cyclohexane or diethyl ether) afforded finally the pure title compounds.

**General procedure G for the synthesis of intermediates 33a-b (Scheme 3.7).** A suspension of potassium phthalimide (1 mmol) and the appropriate alkyl bromide **32a-b** (1.2 mmol) in dry *N,N*-dimethylformamide (3.5 ml) was stirred at room temperature for 16 hours. After reaction completion the mixture was diluted with water (35 ml) and extracted with EtOAc (35 ml). The organic layer was dried over  $\text{Na}_2\text{SO}_4$  and concentrated to dryness at low pressure. Purification by silica gel flash chromatography finally afforded the pure titled compounds.

**General procedure H for the synthesis of amines 34a-b (Scheme 3.7).** The corresponding intermediate **33a-b** (1 mmol) was refluxed in absolute ethanol (4 ml) with hydrazine hydrate (1.5 mmol) for 4 hours. At reaction completion the reaction mixture was cooled at room temperature and the resulting precipitated solid was filtered. The solid was washed with ethanol and the filtrate concentrated to dryness at low pressure. Purification by basic alumina flash chromatography finally afforded the pure titled amines.

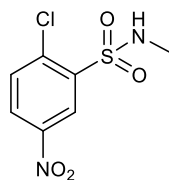


**2-chloro-5-nitro-benzenesulfonyl chloride (21).** 1-Chloro-4-nitrobenzene **20** (500 mg, 3.14 mmol) was stirred in chlorosulfonic acid (1.05 ml, 15.71 mmol) at 120° C for 16 hours. At reaction completion, the mixture was slowly poured onto ice-cold water (30 ml), and extracted twice with DCM (2x30 ml). The combined organic layers were dried over Na<sub>2</sub>SO<sub>4</sub> and concentrated to dryness at low pressure to afford **21** as brownish solid (374.1 mg, 46% yield). UPLC/MS: Rt = 2.14 min (gradient 1); MS (ESI) m/z: 253.7 [M-H]<sup>-</sup>, [M-H]<sup>-</sup> calculated: 253.9. <sup>1</sup>H NMR (400 MHz, DMSO-*d*<sub>6</sub>) δ 8.61 (d, *J* = 2.9 Hz, 1H), 8.16 (dd, *J* = 8.7, 2.9 Hz, 1H), 7.70 (d, *J* = 8.6 Hz, 1H).



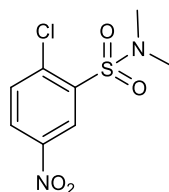
**2-chloro-5-nitro-benzenesulfonamide (22a).** To an ice-cold solution of 5 ml tetrahydrofuran and 4 ml of 20% aqueous NH<sub>4</sub>OH was added compound **21** (374.1 mg, 1.47 mmol) dissolved in THF and the reaction mixture was stirred at room temperature for 1 hour. The reaction crude was then evaporated to dryness at low pressure, and the residue suspended in water (20 ml) and extracted twice with EtOAc(2x20 ml). The combined organic layers were dried over Na<sub>2</sub>SO<sub>4</sub> and concentrated to dryness at low pressure. Purification by silica gel flash chromatography (cyclohexane/EtOAc from 90:10 to 70:30) afforded the pure **22a** (166.2 mg, 48% yield) as a brown solid. UPLC/MS: Rt = 1.42 min

(gradient 1); MS (ESI) m/z: 235.3 [M-H]<sup>-</sup>, [M-H] calculated: 235.1. <sup>1</sup>H NMR (400 MHz, DMSO-*d*<sub>6</sub>) δ 8.68 (d, *J* = 2.7 Hz, 1H), 8.42 (dd, *J* = 8.7, 2.8 Hz, 1H), 7.98 (s, 2H), 7.96 (d, *J* = 8.7 Hz, 1H).



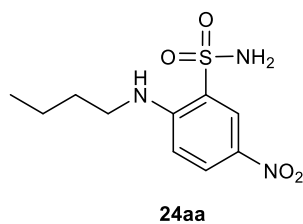
**22b**

**2-chloro-N-methyl-5-nitrobenzenesulfonamide (22b)**. Compound **22b** was synthesized following the general procedure **A** previously described using intermediate **21** (347 mg, 1.46 mmol) and methylamine hydrochloride (100.7 mg, 1.46 mmol). Purification by silica gel flash chromatography (cyclohexane/TBME 95:05) afforded the pure **22b** (204.9 mg, 56% yield) as a brown solid. UPLC/MS: Rt = 1.62 min (gradient 1); MS (ESI) m/z: 249.3 [M-H]<sup>-</sup>. [M-H]<sup>-</sup> calculated: 249.1. <sup>1</sup>H NMR (400 MHz, DMSO-*d*<sub>6</sub>) δ 8.61 (d, *J* = 2.7 Hz, 1H), 8.45 (dd, *J* = 8.7, 2.8 Hz, 1H), 8.11 (q, *J* = 4.9 Hz, 1H), 7.98 (d, *J* = 8.7 Hz, 1H), 2.53 (d, *J* = 4.7 Hz, 3H).

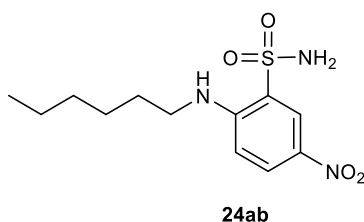


**22c**

**2-chloro-N,N-dimethyl-5-nitrobenzenesulfonamide (22c)**. Compound **22c** was synthesized following the general procedure **A** previously described using intermediate **21** (190.3 mg, 0.8 mmol) and dimethylamine hydrochloride (163.7 mg, 1.60 mmol). Purification by silica gel flash chromatography (cyclohexane/EtOAc 80:20) afforded the pure **22c** (156.32 mg, 74% yield) as a brownish solid. UPLC/MS: Rt = 1.98 min (gradient 1); MS (ESI) m/z: 265.3 [M+H]<sup>+</sup>. [M+H]<sup>+</sup> calculated: 265.0. <sup>1</sup>H NMR (400 MHz, DMSO-*d*<sub>6</sub>) δ 8.59 (d, *J* = 2.7 Hz, 1H), 8.46 (dd, *J* = 8.7, 2.8 Hz, 1H), 8.01 (d, *J* = 8.7 Hz, 1H), 2.87 (s, 6H).

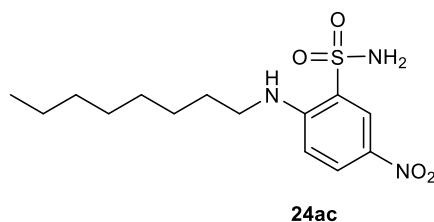


**2-(butylamino)-5-nitrobenzenesulfonamide (24aa).** Compound **24aa** was synthesized following the general procedure **B** previously described using intermediate **22a** (50 mg, 0.21 mmol) and butylamine **23a** (0.1 ml, 1.05 mmol). The compound was obtained pure as a yellow solid without silica gel purification (55.96 mg, 97% yield). UPLC/MS: Rt = 2.03 min (gradient 1); MS (ESI) m/z: 274.4 [M-H]<sup>+</sup>. [M+H]<sup>+</sup> calculated: 274.1; <sup>1</sup>H NMR (400 MHz, DMSO-*d*<sub>6</sub>) δ 8.48 (d, *J* = 2.7 Hz, 1H), 8.19 (dd, *J* = 9.4, 2.7 Hz, 1H), 6.95 (d, *J* = 9.4 Hz, 1H), 3.35 (m, 2H), 1.65 – 1.55 (m, 2H), 1.44 – 1.32 (m, 2H), 0.92 (t, *J* = 7.3 Hz, 3H). <sup>13</sup>C NMR (101 MHz, DMSO-*d*<sub>6</sub>) δ 149.37 (C), 134.57 (C), 129.04 (CH), 125.46 (CH), 124.12 (C), 111.81 (CH), 42.63 (CH<sub>2</sub>), 30.22 (CH<sub>2</sub>), 19.60 (CH<sub>2</sub>), 13.78 (CH<sub>3</sub>).

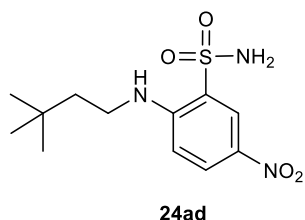


**2-(hexylamino)-5-nitrobenzenesulfonamide (24ab).** Compound **24ab** was synthesized following the general procedure **B** previously described using intermediate **22a** (50 mg, 0.21 mmol) and hexylamine **23b** (0.14 ml, 1.05 mmol). Purification by silica gel flash chromatography (cyclohexane/EtOAc from 90:10 to 70:30) afforded the pure **24ab** compound (59.81 mg, 94% yield) as a yellow solid. UPLC/MS: Rt = 2.34 min (gradient 1); MS (ESI) m/z: 302.5 [M+H]<sup>+</sup>. [M+H]<sup>+</sup> calculated: 302.1; <sup>1</sup>H NMR (400 MHz, DMSO-*d*<sub>6</sub>) δ 8.49 (d, *J* = 2.7 Hz, 1H), 8.19 (ddd, *J* = 9.4, 2.8, 0.5 Hz, 1H), 7.72 (s, 2H), 6.95 (d, *J* = 9.4 Hz, 1H), 6.85 (t, *J* = 5.6 Hz, 1H), 3.37 – 3.28 (m, 2H), 1.66 – 1.56 (m, 2H), 1.41 – 1.25 (m, 6H), 0.90 – 0.83 (m, 3H). <sup>13</sup>C NMR (101 MHz, DMSO-*d*<sub>6</sub>) δ 149.35 (C), 134.55 (C), 129.04 (CH), 125.46 (CH), 124.11 (C), 111.80 (CH), 42.92 (CH<sub>2</sub>), 31.00 (CH<sub>2</sub>), 28.08 (CH<sub>2</sub>), 26.02 (CH<sub>2</sub>), 22.15 (CH<sub>2</sub>), 14.00 (CH<sub>3</sub>).



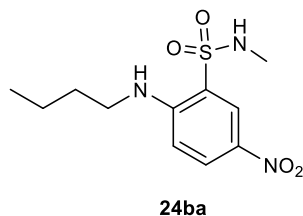


**5-nitro-2-(octylamino)benzenesulfonamide (24ac).** Compound **24ac** was synthesized following the general procedure **B** previously described using intermediate **22a** (50 mg, 0.21 mmol) and octylamine **23c** (0.175 ml, 1.05 mmol). Purification by silica gel flash chromatography (cyclohexane/EtOAc 80:20) afforded the pure **24ac** (64.27 mg, 93% yield) as a yellow solid. UPLC/MS: Rt = 2.61 min (gradient 1); MS (ESI) m/z: 330.5 [M+H]<sup>+</sup>. [M+H]<sup>+</sup> calculated: 330.1 ; <sup>1</sup>H NMR (400 MHz, DMSO-*d*<sub>6</sub>) δ 8.49 (d, *J* = 2.8 Hz, 1H), 8.20 (dd, *J* = 9.4, 2.8 Hz, 1H), 7.73 (s, 2H), 6.95 (d, *J* = 9.4 Hz, 1H), 6.86 (s, 1H), 3.34 – 3.29 (m, 2H), 1.62 (p, *J* = 7.2 Hz, 2H), 1.41 – 1.20 (m, 10H), 0.90 – 0.81 (m, 3H). <sup>13</sup>C NMR (101 MHz, DMSO-*d*<sub>6</sub>) δ 149.30 (C), 134.51 (C), 128.93 (CH), 125.38 (CH), 124.09 (C), 111.72 (CH), 42.85 (CH<sub>2</sub>), 31.23 (CH<sub>2</sub>), 28.68 (CH<sub>2</sub>), 28.65 (CH<sub>2</sub>), 28.05 (CH<sub>2</sub>), 26.28 (CH<sub>2</sub>), 22.10 (CH<sub>2</sub>), 13.98 (CH<sub>3</sub>).

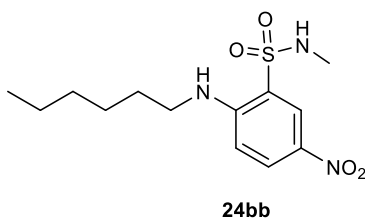


**2-(3,3-dimethylbutylamino)-5-nitrobenzenesulfonamide (24ad).** Compound **24ad** was synthesized following the general procedure **B** previously described using intermediate **22a** (50 mg, 0.21 mmol) and 3,3-dimethylbutan-1-amine **23d** (0.148 ml, 1.05 mmol). Purification by silica gel flash chromatography (cyclohexane/EtOAc from 95:05 to 75:25) afforded the pure **24ad** (55.6 mg, 88% yield) as a yellow solid. UPLC/MS: Rt = 2.29 min (gradient 1); MS (ESI) m/z: 265.3 [M+H]<sup>+</sup>. [M+H]<sup>+</sup> calculated: 265.0; <sup>1</sup>H NMR (400 MHz, DMSO-*d*<sub>6</sub>) δ 8.48 (d, *J* = 2.7 Hz, 1H), 8.21 (dd, *J* = 9.4, 2.8 Hz, 1H), 7.70 (s, 2H), 6.93 (d, *J* = 9.4 Hz, 1H), 6.78 (t, *J* = 4.7 Hz, 1H), 3.38 – 3.30 (m, 2H), 1.59 – 1.51 (m, 2H), 0.96 (s, 9H). <sup>13</sup>C NMR (101 MHz, DMSO-*d*<sub>6</sub>) δ 149.19 (C), 134.50 (C), 128.94 (CH), 125.32

(CH), 124.14 (C), 111.60 (CH), 41.69 (CH<sub>2</sub>), 39.47 (CH<sub>2</sub>, extrapolated from HSQC), 29.68 (C), 29.18 (CH<sub>3</sub>, 3C).

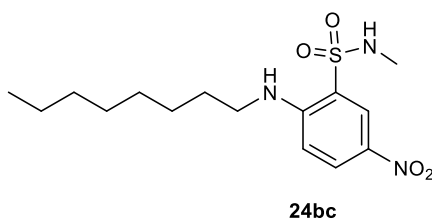


**2-(butylamino)-N-methyl-5-nitrobenzenesulfonamide (24ba).** Compound **24ba** was synthesized following the general procedure **B** previously described using intermediate **22b** (40 mg, 0.16 mmol) and butylamine **23a** (0.8 ml, 0.79 mmol). Purification by silica gel flash chromatography (cyclohexane/EtOAc 80:20) afforded the pure **24ba** (38.65 mg, 84 % yield) as a yellow solid. UPLC/MS: Rt = 2.27 min (gradient 1); MS (ESI) m/z: 288.4 [M+H]<sup>+</sup>. [M+H]<sup>+</sup> calculated: 288.1; <sup>1</sup>H NMR (400 MHz, DMSO-*d*<sub>6</sub>) δ 8.40 (d, *J* = 2.8 Hz, 1H), 8.21 (dd, *J* = 9.4, 2.7 Hz, 1H), 7.89 (s, 1H), 6.98 (d, *J* = 9.4 Hz, 1H), 6.88 (t, *J* = 5.6 Hz, 1H), 3.38 – 3.33 (m, 2H), 2.44 (s, 3H), 1.66 – 1.54 (m, 2H), 1.43 – 1.32 (m, 2H), 0.92 (t, *J* = 7.4 Hz, 3H). <sup>13</sup>C NMR (101 MHz, DMSO) δ 149.85 (C), 134.75 (C), 129.37 (CH), 126.72 (CH), 118.72 (C), 112.01 (CH), 42.50 (CH<sub>2</sub>), 30.08 (CH<sub>2</sub>), 28.18 (CH<sub>3</sub>), 19.47 (CH<sub>2</sub>), 13.62 (CH<sub>3</sub>).

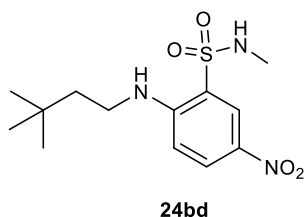


**2-(hexylamino)-N-methyl-5-nitrobenzenesulfonamide (24bb).** Title compound was synthesized following the general procedure **B** previously described using intermediate **24b** (40 mg, 0.16 mmol) and hexylamine **23b** (0.1 ml, 0.79 mmol). Purification by silica gel flash chromatography (cyclohexane/EtOAc 80:20) afforded the pure **24bb** compound (40.38 mg, 80% yield) as a yellow. UPLC/MS: Rt = 2.56 min (gradient 1); MS (ESI) m/z: 316.4 [M+H]<sup>+</sup>. [M+H]<sup>+</sup> calculated: 316.1; <sup>1</sup>H NMR (400 MHz, DMSO-*d*<sub>6</sub>) δ 8.40 (d, *J* = 2.8 Hz, 1H), 8.21 (dd, *J* = 9.4, 2.8 Hz, 1H), 7.88 (s, 1H),

6.97 (d,  $J = 9.5$  Hz, 1H), 6.92 (t,  $J = 5.6$  Hz, 1H), 3.38 – 3.27 (m, 2H), 2.44 (s, 3H), 1.66 – 1.54 (m, 2H), 1.40 – 1.24 (m, 6H), 0.90 – 0.82 (m, 3H).  $^{13}\text{C}$  NMR (101 MHz,  $\text{DMSO-}d_6$ )  $\delta$  149.89 (C), 134.71 (C), 129.29 (CH), 126.67 (CH), 112.94 (C), 111.90 (CH), 42.77 ( $\text{CH}_2$ ), 30.85 ( $\text{CH}_2$ ), 28.31 ( $\text{CH}_3$ ), 27.94 ( $\text{CH}_2$ ), 25.89 ( $\text{CH}_2$ ), 22.02 ( $\text{CH}_2$ ), 13.85 ( $\text{CH}_3$ ).

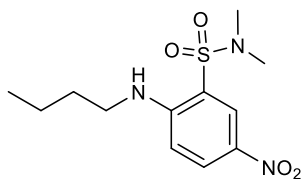


***N*-methyl-5-nitro-2-(octylamino)benzenesulfonamide (24bc)**. Title compound was synthesized following the general procedure **B** previously described using intermediate **22b** (40 mg, 0.16 mmol) and octylamine **23c** (0.13 ml, 0.79 mmol). Purification by silica gel flash chromatography (cyclohexane/EtOAc 80:20) afforded the pure **24bc** (39.56 mg, 72% yield). UPLC/MS:  $R_t = 1.99$  min (gradient 1); MS (ESI)  $m/z$ : 344.4  $[\text{M}+\text{H}]^+$ .  $[\text{M}+\text{H}]^+$  calculated: 344.1;  $^1\text{H}$  NMR (400 MHz,  $\text{DMSO-}d_6$ )  $\delta$  8.41 (d,  $J = 2.8$  Hz, 1H), 8.22 (dd,  $J = 9.4, 2.8$  Hz, 1H), 7.89 (s, 1H), 6.98 (d,  $J = 9.4$  Hz, 1H), 6.89 (t,  $J = 5.5$  Hz, 1H), 3.36 – 3.30 (m, 2H), 2.45 (s, 3H), 1.65 – 1.56 (m, 2H), 1.40 – 1.20 (m, 10H), 0.89 – 0.82 (m, 3H).  $^{13}\text{C}$  NMR (101 MHz,  $\text{DMSO-}d_6$ )  $\delta$  149.85 (C), 134.73 (C), 129.36 (CH), 126.72 (CH), 118.72 (C), 112.00 (CH), 42.78 ( $\text{CH}_2$ ), 31.17 ( $\text{CH}_2$ ), 28.61 ( $\text{CH}_2$ , 2C), 28.17 ( $\text{CH}_2$ ), 27.96 ( $\text{CH}_3$ ), 26.22 ( $\text{CH}_2$ ), 22.05 ( $\text{CH}_2$ ), 13.92 ( $\text{CH}_3$ ).



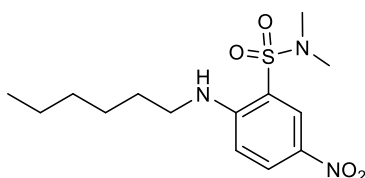
**2-(3,3-dimethylbutylamino)-*N*-methyl-5-nitrobenzenesulfonamide (24bd)**. Compound **24bd** was synthesized following the general procedure **B** previously described using intermediate **22b** (40 mg, 0.16 mmol) and 3,3-dimethylbutan-1-amine **23d** (0.11 ml, 0.79 mmol). Purification by silica gel flash chromatography (cyclohexane/EtOAc 80:20) afforded the pure title compound (42.26 mg, 84% yield)

UPLC/MS: Rt = 2.15 min (gradient 1); MS (ESI) m/z: 316.4 [M-H]<sup>+</sup>. [M+H] calculated: 316.1; <sup>1</sup>H NMR (400 MHz, DMSO-*d*<sub>6</sub>) δ 8.40 (d, *J* = 2.7 Hz, 1H), 8.23 (dd, *J* = 9.3, 2.8 Hz, 1H), 7.90 – 7.84 (m, 2H) 6.96 (d, *J* = 9.4 Hz, 1H), 6.81 (t, *J* = 5.4 Hz, 1H), 3.36 – 3.30 (m, 2H), 2.43 (s, 3H), 1.57 – 1.51 (m, 2H), 0.96 (s, 9H). <sup>13</sup>C NMR (101 MHz, DMSO-*d*<sub>6</sub>) δ 149.73 (C), 134.72 (C), 129.41 (CH), 126.69 (CH), 118.74 (C), 111.89 (CH), 41.59 (CH<sub>2</sub>), 39.57 (CH<sub>2</sub>), 29.68 (C), 29.17 (CH<sub>3</sub>, 3C), 28.19 (CH<sub>3</sub>).



**24ca**

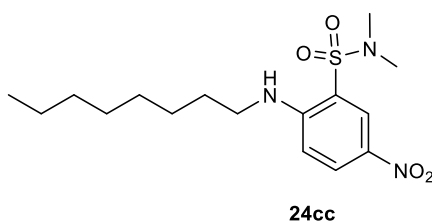
**2-(butylamino)-*N,N*-dimethyl-5-nitrobenzenesulfonamide (24ca).** Title compound was synthesized following the general procedure **B** previously described using intermediate **22c** (50 mg, 0.19 mmol) and butylamine **23a** (93 μl, 0.94 mmol). Purification by silica gel flash chromatography (cyclohexane/EtOAc 75:25) afforded the pure **24ca** (41.45 mg, 72 % yield) as a yellow solid. UPLC/MS: Rt = 2.47 min (gradient 1); MS (ESI) m/z: 302.4 [M+H]<sup>+</sup>. [M+H]<sup>+</sup> calculated: 302.1; <sup>1</sup>H NMR (400 MHz, DMSO-*d*<sub>6</sub>) δ 8.29 (d, *J* = 2.8 Hz, 1H), 8.25 (ddd, *J* = 9.4, 2.7, 0.6 Hz, 1H), 7.21 (t, *J* = 5.6 Hz, 1H), 7.03 (d, *J* = 9.5 Hz, 1H), 3.38 – 3.32 (m, 2H), 2.72 (s, 6H), 1.63 – 1.53 (m, 2H), 1.42 – 1.32 (m, 2H), 0.93 (t, *J* = 7.3 Hz, 3H). <sup>13</sup>C NMR (101 MHz, DMSO-*d*<sub>6</sub>) δ 149.95 (C), 135.05 (C), 129.55 (CH), 127.05 (CH), 118.72 (C), 112.27 (CH), 42.50 (CH<sub>2</sub>), 36.89 (CH<sub>3</sub>, 2C), 30.08 (CH<sub>2</sub>), 19.41 (CH<sub>2</sub>), 13.81 (CH<sub>3</sub>).



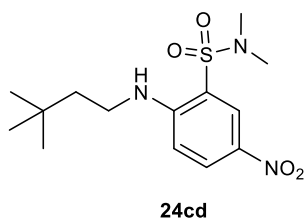
**24cb**

**2-(hexylamino)-*N,N*-dimethyl-5-nitrobenzenesulfonamide (24cb).** Compound **24cb** was synthesized following the general procedure **B** previously described using intermediate **22c** (65 mg, 0.24 mmol) and hexylamine **23b** (0.16 ml, 1.21 mmol). Purification by silica gel flash chromatography

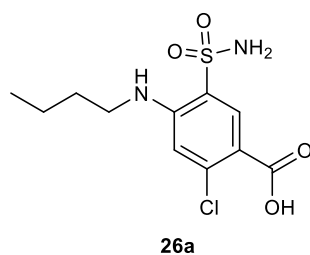
(cyclohexane/EtOAc 80:20) afforded the pure **24cb** (68.42 mg, 87% yield) as a yellow solid. UPLC/MS: Rt = 1.80 min (gradient 1); MS (ESI) m/z: 328.5 [M-H]<sup>-</sup>. [M-H]<sup>-</sup> calculated: 328.1; <sup>1</sup>H NMR (400 MHz, DMSO-*d*<sub>6</sub>) δ 8.28 (d, *J* = 2.7 Hz, 1H), 8.24 (ddd, *J* = 9.4, 2.8, 0.6 Hz, 1H), 7.21 (t, *J* = 5.6 Hz, 1H), 7.01 (d, *J* = 9.4 Hz, 1H), 3.36 – 3.30 (m, 2H), 2.71 (s, 6H), 1.62 – 1.53 (m, 2H), 1.38 – 1.24 (m, 6H), 0.90 – 0.82 (m, 3H). <sup>13</sup>C NMR (101 MHz, DMSO-*d*<sub>6</sub>) δ 149.69 (C), 134.21 (C), 129.48 (CH), 126.46 (CH), 113.24 (C), 112.22 (CH), 43.10 (CH<sub>2</sub>), 37.23 (CH<sub>3</sub>, 2C), 30.96 (CH<sub>2</sub>), 27.25 (CH<sub>2</sub>), 26.03 (CH<sub>2</sub>), 21.89 (CH<sub>2</sub>), 14.07 (CH<sub>3</sub>).



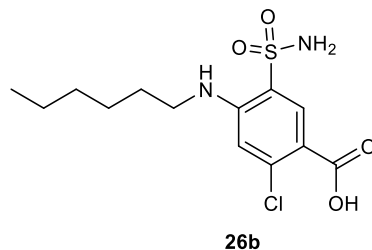
***N,N*-dimethyl-5-nitro-2-(octylamino)benzenesulfonamide (24cc)**. Compound **24cc** was synthesized following the general procedure **B** previously described using intermediate **22c** (50 mg, 0.19 mmol) and octylamine **23c** (0.15 ml, 0.94 mmol). Purification by silica gel flash chromatography (cyclohexane/EtOAc 85:15) afforded the pure **24cc** (57.52 mg, 85% yield) as a yellow solid. UPLC/MS: Rt = 2.30 min (gradient 1); MS (ESI) m/z: 358.4 [M+H]<sup>+</sup>. [M+H]<sup>+</sup> calculated: 358.2; <sup>1</sup>H NMR (400 MHz, DMSO-*d*<sub>6</sub>) δ 8.28 (d, *J* = 2.8 Hz, 1H), 8.23 (ddd, *J* = 9.4, 2.8, 0.6 Hz, 1H), 7.20 (t, *J* = 5.6 Hz, 1H), 7.01 (d, *J* = 9.5 Hz, 1H), 3.38 – 3.31 (m, 2H), 2.71 (s, 6H), 1.62 – 1.53 (m, 2H), 1.37 – 1.20 (m, 10H), 0.87 – 0.82 (m, 3H). <sup>13</sup>C NMR (101 MHz, DMSO-*d*<sub>6</sub>) δ 149.91 (C), 134.8 (C), 130.31 (CH), 127.97 (CH), 118.92 (C), 112.77 (CH), 42.56 (CH<sub>2</sub>), 27.58 (CH<sub>3</sub>, 2C), 31.17 (CH<sub>2</sub>), 28.61 (CH<sub>2</sub>, 2C), 28.36 (CH<sub>2</sub>), , 26.22 (CH<sub>2</sub>), 21.68 (CH<sub>2</sub>), 13.97 (CH<sub>3</sub>).



**2-(3,3-dimethylbutylamino)-*N,N*-dimethyl-5-nitro-benzenesulfonamide (24cd)**. Compound **24cd** was synthesized following the general procedure **B** previously described using intermediate **22c** (50 mg, 0.19 mmol) and 3,3-dimethylbutan-1-amine **23d** (0.13 ml, 0.94 mmol). Purification by silica gel flash chromatography (cyclohexane/EtOAc 85:15) afforded the pure **24cd** (51.11 mg, 82% yield). UPLC/MS: Rt = 2.70 min (gradient 1); MS (ESI) m/z: 330.4 [M+H]<sup>+</sup>. [M+H]<sup>+</sup> calculated: 330.1; <sup>1</sup>H NMR (400 MHz, DMSO-*d*<sub>6</sub>) δ 8.28 (d, *J* = 2.7 Hz, 1H), 8.25 (ddd, *J* = 9.3, 2.8, 0.6 Hz, 1H), 7.16 (t, *J* = 5.6 Hz, 1H), 6.98 (d, *J* = 9.3 Hz, 1H), 3.38 – 3.32 (m, 2H), 2.71 (s, 6H), 1.52 – 1.47 (m, 2H), 0.95 (s, 9H). <sup>13</sup>C NMR (101 MHz, DMSO-*d*<sub>6</sub>) δ 149.84 (C), 134.90 (C), 129.73 (CH), 126.82 (CH), 118.85 (C), 112.03 (CH), 41.53 (CH<sub>2</sub>), 39.08 (CH<sub>2</sub>), 37.34 (CH<sub>3</sub>, 2C). 29.58 (C). 29.07 (CH<sub>3</sub>, 3C).

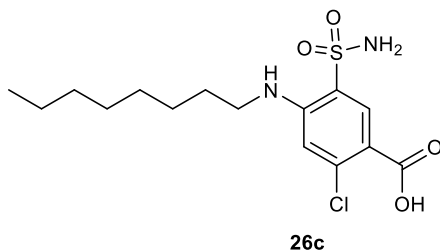


**4-(butylamino)-2-chloro-5-sulfamoyl-benzoic acid (26a)**. Compound **26a** was synthesized following the general procedure **C** previously described using intermediate **25** (70 mg, 0.26 mmol) and butylamine **23a** (0.13 ml, 1.32 mmol). Trituration with cyclohexane (1 ml) afforded the pure **26a** (40.84 mg, 51% yield) as a white solid. UPLC/MS: Rt = 1.52 min (gradient 1); MS (ESI) m/z: 305.3 [M-H]<sup>-</sup>. [M-H]<sup>-</sup> calculated: 305.04; <sup>1</sup>H NMR (400 MHz, DMSO-*d*<sub>6</sub>) δ 12.80 (bs, 1H), 8.26 (s, 1H), 7.57 (s, 2H), 6.84 (s, 1H), 6.39 (t, *J* = 5.3 Hz, 1H), 3.31 – 3.21 (m, 2H), 1.64 – 1.53 (m, 2H), 1.44 – 1.33 (m, 2H), 0.93 (t, *J* = 7.3 Hz, 3H).

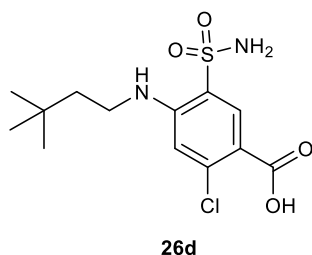


**2-chloro-4-(hexylamino)-5-sulfamoyl-benzoic acid (26b)**. Compound **26b** was synthesized following the general procedure **C** previously described using intermediate **25** (50 mg, 0.19 mmol) and

hexylamine **23b** (0.12 ml, 0.95 mmol). Trituration with cyclohexane (1 ml) afforded the pure **26b** (52.82 mg, 83% yield) as a white solid. UPLC/MS: Rt = 1.78 min (gradient 1); MS (ESI) m/z: 333.4 [M-H]<sup>-</sup>. [M-H]<sup>-</sup> calculated: 333.1. <sup>1</sup>H NMR (400 MHz, DMSO-*d*<sub>6</sub>) δ 12.77 (bs, 1H), 8.25 (s, 1H), 7.55 (s, 2H), 6.83 (s, 1H), 6.39 (t, *J* = 5.4 Hz, 1H), 3.27 – 3.20 (m, 2H), 1.59 (p, *J* = 7.1 Hz, 2H), 1.41 – 1.24 (m, 6H), 0.90 – 0.84 (m, 3H).

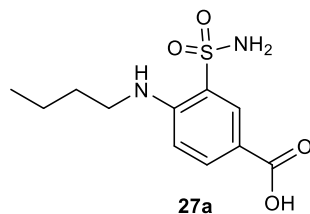


**2-chloro-4-(octylamino)-5-sulfamoylbenzoic acid (26c)**. Compound **26c** was synthesized following the general procedure **C** previously described using intermediate **25** (50 mg, 0.19 mmol) and octylamine **23c** (0.16 ml, 0.95 mmol). Trituration with cyclohexane (1 ml) afforded the pure **26c** (48.89 mg, 71% yield) as a white solid. UPLC/MS: Rt = 2.01 min (gradient 1); MS (ESI) m/z: 361.4 [M-H]<sup>-</sup>. [M-H]<sup>-</sup> calculated: 361.1. <sup>1</sup>H NMR (400 MHz, DMSO-*d*<sub>6</sub>) δ 12.78 (bs, 1H), 8.26 (s, 1H), 7.56 (s, 2H), 6.84 (s, 1H), 6.40 (t, *J* = 5.3 Hz, 1H), 3.28 – 3.21 (m, 2H), 1.65 – 1.55 (m, 2H), 1.41 – 1.20 (m, 10H), 0.90 – 0.83 (m, 3H).

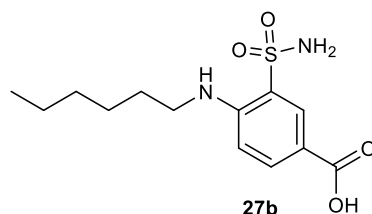


**2-chloro-4-(3,3-dimethylbutylamino)-5-sulfamoylbenzoic acid (26d)**. Compound **26d** was synthesized following the general procedure **C** previously described using intermediate **25** (50 mg, 0.19 mmol) and 3,3-dimethylbutan-1-amine **23d** (0.13 ml, 0.95 mmol). Trituration with cyclohexane (1 ml) afforded the pure **26d** (52.82 mg, 83% yield) as a white solid. UPLC/MS: Rt = 1.66 min; MS (ESI) m/z: 333.4 [M-H]<sup>-</sup>. [M-H]<sup>-</sup> calculated: 333.1; <sup>1</sup>H NMR (400 MHz, DMSO-*d*<sub>6</sub>) δ 8.25 (s, 1H),

7.54 (s, 2H), 6.83 (s, 1H), 6.29 (t,  $J = 5.1$  Hz, 1H), 3.27 – 3.20 (m, 2H), 1.56 – 1.50 (m, 2H), 0.96 (s, 9H).



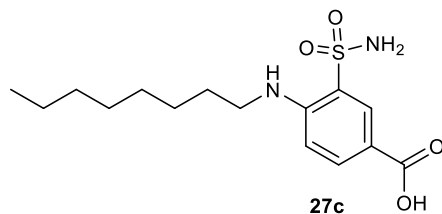
**4-(butylamino)-3-sulfamoyl-benzoic acid (27a).** Compound **27a** was synthesized following the general procedure **D** previously described using intermediate **26a** (30 mg, 0.1 mmol). Trituration with cyclohexane (1 ml) afforded the pure **27a** (11.71 mg, 43% yield) as a white solid. UPLC/MS:  $R_t = 1.53$  min (gradient 1); MS (ESI)  $m/z$ : 273.4  $[M+H]^+$ .  $[M+H]^+$  calculated: 273.1;  $^1\text{H}$  NMR (400 MHz,  $\text{DMSO-}d_6$ )  $\delta$  8.23 (d,  $J = 2.1$  Hz, 1H), 7.87 (dd,  $J = 8.8, 2.2$  Hz, 1H), 7.46 (s, 2H), 6.83 (d,  $J = 8.9$  Hz, 1H), 6.37 (t,  $J = 5.4$  Hz, 1H), 3.28 – 3.21 (m, 2H), 1.64 – 1.55 (m, 2H), 1.44 – 1.34 (m, 2H), 0.92 (t,  $J = 7.3$  Hz, 3H).  $^{13}\text{C}$  NMR (101 MHz,  $\text{DMSO-}d_6$ )  $\delta$  166.68 (CO), 148.74 (C), 134.92 (CH), 132.39 (CH), 118.85 (C), 116.54 (C), 111.68 (CH), 42.40 ( $\text{CH}_2$ ), 30.35 ( $\text{CH}_2$ ), 19.79 ( $\text{CH}_2$ ), 13.63 ( $\text{CH}_3$ ).



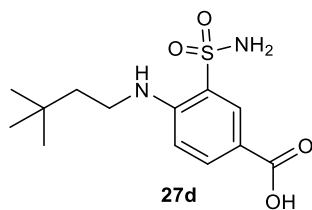
**4-(hexylamino)-3-sulfamoyl-benzoic acid (27b).** Compound **27b** was synthesized following the general procedure **D** previously described using intermediate **26b** (30.7 mg, 0.09 mmol). Trituration with cyclohexane (1 ml) afforded the pure **27b** (11.71 mg, 43% yield) as a white solid. UPLC/MS:  $R_t = 1.81$  min; MS (ESI)  $m/z$ : 301.4  $[M+H]^+$ .  $[M+H]^+$  calculated: 301.1;  $^1\text{H}$  NMR (400 MHz,  $\text{DMSO-}d_6$ )  $\delta$  12.45 (bs, 1H), 8.23 (d,  $J = 2.1$  Hz, 1H), 7.87 (dd,  $J = 8.8, 2.2$  Hz, 1H), 7.46 (s, 2H), 6.82 (d,  $J = 8.9$  Hz, 1H), 6.38 (t,  $J = 5.4$  Hz, 1H), 3.27 – 3.20 (m, 2H), 1.60 (p,  $J = 7.1$  Hz, 2H), 1.42 – 1.25 (m, 6H), 0.92 – 0.80 (m, 3H).  $^{13}\text{C}$  NMR (101 MHz,  $\text{DMSO}$ )  $\delta$  166.61 (CO), 148.73 (C), 134.92 (CH), 131.97



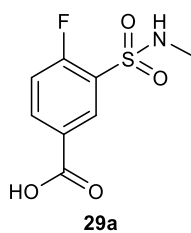
(CH), 118.65 (C), 116.43 (C), 111.48 (C), 42.64 (CH<sub>2</sub>), 31.08 (CH<sub>2</sub>), 28.32 (CH<sub>2</sub>), 26.07 (CH<sub>2</sub>), 22.19 (CH<sub>2</sub>), 14.01 (CH<sub>3</sub>).



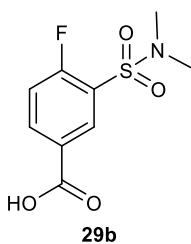
**4-(octylamino)-3-sulfamoyl-benzoic acid (27c).** Compound **27c** was synthesized following the general procedure **D** previously described using intermediate **26c** (35.7 mg, 0.1 mmol). Trituration with cyclohexane (1 ml) afforded the pure **27c** (9.68 mg, 36% yield) as a white solid. UPLC/MS: Rt = 2.16 min (gradient 1); MS (ESI) m/z: 329.4 [M+H]<sup>+</sup>. [M+H]<sup>+</sup> calculated: 329.1; <sup>1</sup>H NMR (400 MHz, DMSO-*d*<sub>6</sub>) δ 12.43 (bs, 1H), 8.23 (d, *J* = 2.1 Hz, 1H), 7.86 (dd, *J* = 8.7, 2.1 Hz, 1H), 7.46 (s, 2H), 6.82 (d, *J* = 8.9 Hz, 1H), 6.38 (t, *J* = 5.3 Hz, 1H), 3.27 – 3.19 (m, 2H), 1.65 – 1.56 (m, 2H), 1.42 – 1.15 (m, 12H), 0.92 – 0.80 (m, 3H). <sup>13</sup>C NMR (101 MHz, DMSO-*d*<sub>6</sub>) δ 166.69 (CO), 148.73 (C), 134.94 (CH), 131.99 (CH), 118.76 (C), 116.62 (C), 111.64 (C), 42.51 (CH<sub>2</sub>), 31.14 (CH<sub>2</sub>), 27.89 (CH<sub>2</sub>, 2C), 26.41 (CH<sub>2</sub>), 28.43 (CH<sub>2</sub>), 21.83 (CH<sub>2</sub>), 14.05 (CH<sub>3</sub>).



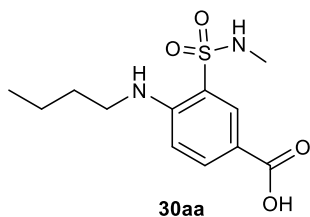
**4-(3,3-dimethylbutylamino)-3-sulfamoyl-benzoic acid (27d).** Compound **27d** was synthesized following the general procedure **D** previously described using intermediate **26d** (29.6 mg, 0.09 mmol). Trituration with cyclohexane (1 ml) afforded the pure **27d** (15.13 mg, 56% yield) as white solid. UPLC/MS: Rt = 1.80 min (gradient 1); MS (ESI) m/z: 301.4 [M+H]<sup>+</sup>. [M+H]<sup>+</sup> calculated: 301.1; <sup>1</sup>H NMR (400 MHz, DMSO-*d*<sub>6</sub>) δ 12.48 (bs, 1H), 8.24 (d, *J* = 2.1 Hz, 1H), 7.89 (dd, *J* = 8.8, 2.1 Hz, 1H), 7.46 (s, 2H), 6.83 (d, *J* = 8.9 Hz, 1H), 3.28 – 3.21 (m, 2H), 1.59 – 1.52 (m, 2H), 0.97 (s, 9H). <sup>13</sup>C NMR (101 MHz, DMSO) δ 166.54 (CO), 148.68 (C), 134.45 (CH), 129.38 (CH), 118.66 (C), 116.43 (C), 111.08 (CH), 42.04 (CH<sub>2</sub>), 39.05 (CH<sub>2</sub>), 29.68 (C), 29.05 (CH<sub>3</sub>, 3C).



**4-fluoro-3-(methylsulfamoyl)benzoic acid (29a).** Compound **29a** was synthesized following the general procedure **E** previously described using intermediate **28** (500 mg, 2.07 mmol) and a 2M methylamine solution in THF (2.07 ml, 4.15 mmol). The described workup afforded pure **29a** (313.8 mg, 64% yield) as a white solid. UPLC/MS: Rt = 1.26 min (gradient 1); MS (ESI) m/z: 232.3 [M-H]<sup>-</sup>. [M-H]<sup>-</sup> calculated: 232.02 <sup>1</sup>H NMR (400 MHz, DMSO-d<sub>6</sub>) δ 8.30 (dd, *J* = 7.0, 2.2 Hz, 1H), 8.25 – 8.19 (m, 1H), 7.89 (q, *J* = 4.8 Hz, 1H), 7.62 – 7.54 (m, 1H), 2.52 (d, *J* = 4.8 Hz, 3H).

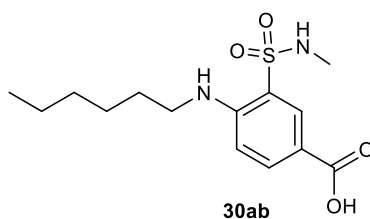


**3-(dimethylsulfamoyl)-4-fluorobenzoic acid (29b).** Compound **29** was synthesized following the general procedure **E** previously described using intermediate **28** (1 g, 4.15 mmol) and a 2M dimethylamine solution in THF (4.15 ml, 8.30 mmol). The described workup afforded pure **29b** (749 mg, 73% yield). UPLC/MS: Rt = 1.11 min (gradient 1); MS (ESI) m/z: 246.3 [M-H]<sup>-</sup>. [M-H]<sup>-</sup> calculated: 246.03. <sup>1</sup>H NMR (400 MHz, DMSO-d<sub>6</sub>) δ 8.29 – 8.24 (m, 2H), 7.67 – 7.58 (m, 1H), 2.75 (d, *J* = 1.9 Hz, 6H).

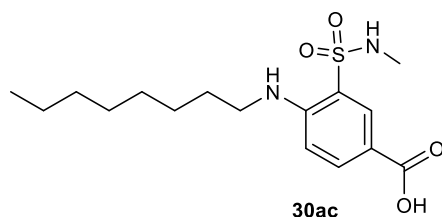


**4-(butylamino)-3-(methylsulfamoyl)benzoic acid (30aa).** Compound **30aa** was synthesized following the general procedure **F** previously described using intermediate **29a** (50 mg, 0.21 mmol)

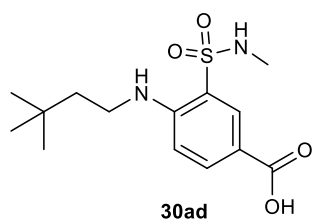
and butylamine **23a** (42  $\mu$ l, 0.42 mmol) in dry 1,4-dioxane (0.7 ml). Trituration with cyclohexane (1 ml) afforded the pure **30aa** (47.10 mg, 78% yield) as a white solid. UPLC/MS: Rt = 1.66 min (gradient 1); MS (ESI) m/z: 285.4 [M-H]<sup>-</sup>. [M-H]<sup>-</sup> calculated: 285.1. <sup>1</sup>H NMR (400 MHz, DMSO-*d*<sub>6</sub>)  $\delta$  8.15 (d, *J* = 2.1 Hz, 1H), 7.90 (dd, *J* = 8.8, 2.1 Hz, 1H), 7.66 (s, 1H), 6.86 (d, *J* = 8.9 Hz, 1H), 6.44 (t, *J* = 5.4 Hz, 1H), 3.24 (q, *J* = 6.6 Hz, 2H), 2.39 (s, 3H), 1.58 (p, *J* = 7.2 Hz, 2H), 1.43 – 1.32 (m, 2H), 0.92 (t, *J* = 7.3 Hz, 3H). <sup>13</sup>C NMR (101 MHz, DMSO-*d*<sub>6</sub>)  $\delta$  166.50 (CO), 148.58 (C), 134.92 (CH), 131.97 (CH), 118.66 (C), 116.39 (C), 111.48 (CH), 42.19 (CH<sub>2</sub>), 30.25 (CH<sub>2</sub>), 28.18 (CH<sub>3</sub>), 19.55 (CH<sub>2</sub>), 13.67 (CH<sub>3</sub>).



**4-(hexylamino)-3-(methylsulfamoyl)benzoic acid (30ab)**. Compound **30ab** was synthesized following the general procedure **F** previously described using intermediate **29a** (50 mg, 0.21 mmol) and hexylamine **23b** (57  $\mu$ l, 0.42 mmol) in dry 1,4-dioxane (0.7 ml). Trituration with cyclohexane (1 ml) afforded the pure **30ab** (51.69 mg, 78% yield) as a white solid. UPLC/MS: Rt = 2.00 min (gradient 1); MS (ESI) m/z: 313.4 [M-H]<sup>-</sup>. [M-H]<sup>-</sup> calculated: 313.1. <sup>1</sup>H NMR (400 MHz, DMSO-*d*<sub>6</sub>)  $\delta$  12.53 (bs, 1H), 8.15 (d, *J* = 2.1 Hz, 1H), 7.90 (dd, *J* = 8.8, 2.1 Hz, 1H), 7.63 (q, *J* = 5.0 Hz, 1H), 6.86 (d, *J* = 8.9 Hz, 1H), 6.44 (t, *J* = 5.3 Hz, 1H), 3.23 (q, *J* = 6.6 Hz, 2H), 2.39 (d, *J* = 4.9 Hz, 3H), 1.60 (p, *J* = 7.1 Hz, 2H), 1.40 – 1.25 (m, 6H), 0.90 – 0.83 (m, 3H). <sup>13</sup>C NMR (101 MHz, DMSO-*d*<sub>6</sub>)  $\delta$  166.52 (CO), 148.57 (C), 134.92 (CH), 131.9 (CH), 118.65 (C), 116.46 (C), 111.48 (CH), 42.49 (CH<sub>2</sub>), 30.91 (CH<sub>2</sub>), 28.19 (CH<sub>2</sub>), 28.09 (CH<sub>3</sub>), 25.99 (CH<sub>2</sub>), 22.04 (CH<sub>2</sub>), 13.86 (CH<sub>3</sub>).

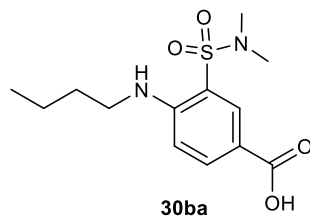


**3-(N-methylsulfamoyl)-4-(octylamino)benzoic acid (30ac).** Compound **30ac** was synthesized following the general procedure **F** previously described using intermediate **29a** (50 mg, 0.21 mmol) and octylamine **23c** (71  $\mu$ l, 0.42 mmol) in dry 1,4-dioxane (0.7 ml). Trituration with cyclohexane (1 ml) afforded the pure **30ac** (69.5 mg, 97% yield) as a white solid. UPLC/MS: Rt = 2.28 min (gradient 1); MS (ESI) m/z: 341.4 [M-H]<sup>-</sup>. [M-H] calculated: 341.2. <sup>1</sup>H NMR (400 MHz, DMSO-*d*<sub>6</sub>)  $\delta$  8.15 (d, *J* = 2.1 Hz, 1H), 7.89 (dd, *J* = 8.8, 2.1 Hz, 1H), 6.86 (d, *J* = 8.9 Hz, 1H), 6.44 (t, *J* = 5.4 Hz, 1H), 3.23 (q, *J* = 6.6 Hz, 2H), 2.38 (s, 3H), 1.59 (p, *J* = 7.1 Hz, 2H), 1.40 – 1.20 (m, 10H), 0.89 – 0.82 (m, 3H). <sup>13</sup>C NMR (101 MHz, DMSO-*d*<sub>6</sub>)  $\delta$  166.49 (CO), 148.53 (C), 134.88 (CH), 131.99 (CH), 118.64 (C), 116.42 (C), 111.44 (CH), 42.47 (CH<sub>2</sub>), 31.19 (CH<sub>2</sub>), 28.66 (CH<sub>2</sub>), 28.63 (CH<sub>2</sub>), 28.16 (CH<sub>3</sub>), 28.11 (CH<sub>2</sub>), 26.32 (CH<sub>2</sub>), 22.06 (CH<sub>2</sub>), 13.93 (CH<sub>3</sub>).

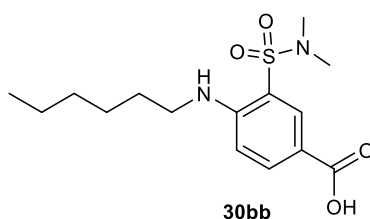


**4-(N-3,3-dimethylbutylamino)-3-(methylsulfamoyl)benzoic acid (30ad).** Compound **30ad** was synthesized following the general procedure **F** previously described using intermediate **29a** (50 mg, 0.21 mmol) and 3,3-dimethylbutan-1-amine **23d** (60  $\mu$ l, 0.42 mmol) in dry 1,4-dioxane (0.7 ml). Trituration with cyclohexane (1 ml) afforded the pure **30ad** compound (50.56 mg, 84% yield) as a white solid. UPLC/MS: Rt = 1.93 min (gradient 1); MS (ESI) m/z: 313.4 [M-H]<sup>-</sup>. [M-H] calculated: 313.1. <sup>1</sup>H NMR (400 MHz, DMSO-*d*<sub>6</sub>)  $\delta$  12.52 (s, 1H), 8.15 (d, *J* = 2.1 Hz, 1H), 7.91 (dd, *J* = 8.8, 2.1 Hz, 1H), 7.62 (q, *J* = 5.0 Hz, 1H), 6.86 (d, *J* = 8.9 Hz, 1H), 6.35 (t, *J* = 5.2 Hz, 1H), 3.27 – 3.20 (m, 2H), 2.38 (d, *J* = 5.0 Hz, 3H), 1.57 – 1.50 (m, 2H), 0.96 (s, 9H). <sup>13</sup>C NMR (101 MHz, DMSO-*d*<sub>6</sub>)  $\delta$

166.54 (CO), 148.48 (C), 134.96 (CH), 131.96 (CH), 118.66 (C), 116.38 (C), 111.41 (CH), 41.89 (CH<sub>2</sub>), 39.19 (CH<sub>2</sub>), 29.68 (C), 29.25 (CH<sub>3</sub>, 3C), 28.21 (CH<sub>3</sub>).

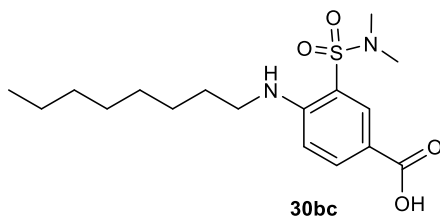


**4-(butylamino)-3-(N,N-dimethylsulfamoyl)benzoic acid (30ba).** Compound **30ba** was synthesized following the general procedure **F** previously described using intermediate **29b** (50 mg, 0.20 mmol) and butylamine **23a** (40  $\mu$ l, 0.40 mmol) in dry 1,4-dioxane (0.7 ml). Trituration with cyclohexane (1 ml) afforded the pure **30ba** (41.45 mg, 69% yield) as a white solid. UPLC/MS: Rt = 1.90 min (gradient 1); MS (ESI) m/z: 299.4 [M-H]<sup>-</sup>. [M-H]<sup>-</sup> calculated: 299.1. <sup>1</sup>H NMR (400 MHz, DMSO-*d*<sub>6</sub>)  $\delta$  12.62 (s, 1H), 8.05 (d, *J* = 2.1 Hz, 1H), 7.93 (dd, *J* = 8.9, 2.1 Hz, 1H), 6.91 (d, *J* = 9.0 Hz, 1H), 6.74 (t, *J* = 5.4 Hz, 1H), 3.29 – 3.19 (m, 2H), 2.66 (s, 6H), 1.61 – 1.52 (m, 2H), 1.42 – 1.31 (m, 2H), 0.92 (t, *J* = 7.3 Hz, 3H). <sup>13</sup>C NMR (101 MHz, DMSO-*d*<sub>6</sub>)  $\delta$  166.50 (CO), 148.58 (C), 134.98 (CH), 132.03 (CH), 118.57 (C), 116.39 (C), 111.48 (CH), 41.85 (CH<sub>2</sub>), 37.09 (CH<sub>3</sub>, 2C), 30.13 (CH<sub>2</sub>), 19.41 (CH<sub>2</sub>), 13.57 (CH<sub>3</sub>).

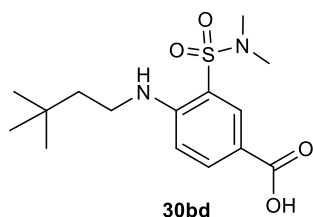


**3-(N,N-dimethylsulfamoyl)-4-(hexylamino)benzoic acid (30bb).** Titled compound was synthesized following the general procedure **F** previously described using intermediate **29b** (50 mg, 0.20 mmol) and hexylamine **23b** (53  $\mu$ l, 0.40 mmol) in dry 1,4-dioxane (0.7 ml). Trituration with cyclohexane (1 ml) afforded the pure **30bb** (53.20 mg, 81 % yield) as a white solid. UPLC/MS: Rt = 2.17 min (gradient 1); MS (ESI) m/z: 327.4 [M-H]<sup>-</sup>. [M-H]<sup>-</sup> calculated: 327.1. <sup>1</sup>H NMR (400 MHz, DMSO-*d*<sub>6</sub>)  $\delta$  12.63 (s, 1H), 8.04 (d, *J* = 2.1 Hz, 1H), 7.93 (dd, *J* = 8.8, 2.1 Hz, 1H), 6.90 (d, *J* = 9.0 Hz, 1H), 6.74 (t, *J* =

5.4 Hz, 1H), 3.28 – 3.18 (m, 2H), 2.65 (s, 6H), 1.57 (p,  $J = 7.0$  Hz, 2H), 1.39 – 1.24 (m, 6H), 0.89 – 0.84 (m, 3H).  $^{13}\text{C}$  NMR (101 MHz,  $\text{DMSO-}d_6$ )  $\delta$  166.59 (CO), 148.76 (C), 135.02 (CH), 131.90 (CH), 118.65 (C), 116.46 (C), 111.48 (CH), 42.54 ( $\text{CH}_2$ ), 37.26 ( $\text{CH}_3$ , 2C), 30.96 ( $\text{CH}_2$ ), 28.19 ( $\text{CH}_2$ ), 26.06 ( $\text{CH}_2$ ), 22.11 ( $\text{CH}_2$ ), 14.08 ( $\text{CH}_3$ ).

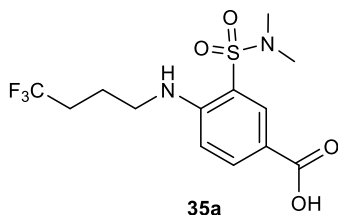


**3-(*N,N*-dimethylsulfamoyl)-4-(octylamino)benzoic acid (30bc).** Compound **30bc** was synthesized following the general procedure **D** previously described using intermediate **29b** (50 mg, 0.20 mmol) and octylamine **23c** (67  $\mu\text{l}$ , 0.40 mmol) in dry 1,4-dioxane (0.7 ml). Trituration with cyclohexane (1 ml) afforded the pure **30bc** (59.9 mg, 84% yield) as a white solid. UPLC/MS:  $R_t = 2.44$  min (gradient 1); MS (ESI)  $m/z$ : 355.4  $[\text{M-H}]^-$ .  $[\text{M-H}]^-$  calculated: 355.2.  $^1\text{H}$  NMR (400 MHz,  $\text{DMSO-}d_6$ )  $\delta$  12.62 (s, 1H), 8.04 (d,  $J = 2.1$  Hz, 1H), 7.93 (dd,  $J = 8.9, 2.1$  Hz, 1H), 6.91 (d,  $J = 9.0$  Hz, 1H), 6.75 (t,  $J = 5.4$  Hz, 1H), 3.23 (q,  $J = 6.6$  Hz, 2H), 2.65 (s, 6H), 1.57 (p,  $J = 6.9$  Hz, 2H), 1.39 – 1.19 (m, 10H), 0.90 – 0.80 (m, 3H).  $^{13}\text{C}$  NMR (101 MHz,  $\text{DMSO-}d_6$ )  $\delta$  166.79 (CO), 149.99 (C), 135.87 (CH), 132.90 (CH), 117.08 (C), 115.63 (C), 112.49 (CH), 42.76 ( $\text{CH}_2$ ), 37.76 ( $\text{CH}_3$ , 2C), 31.64 ( $\text{CH}_2$ ), 29.09 ( $\text{CH}_2$ ), 29.06 ( $\text{CH}_2$ ), 28.55 ( $\text{CH}_2$ ), 26.80 ( $\text{CH}_2$ ), 22.52 ( $\text{CH}_2$ ), 14.40 ( $\text{CH}_3$ ).

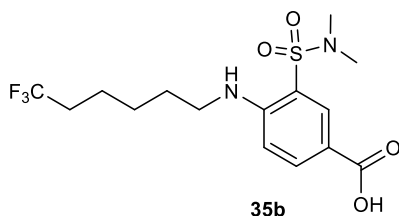


**4-(*N,N*-3,3-dimethylbutylamino)-3-(dimethylsulfamoyl)benzoic acid (30bd).** Compound **30bd** was synthesized following the general procedure **F** previously described using intermediate **29b** (50 mg, 0.20 mmol) and 3,3-dimethylbutan-1-amine **23d** (57  $\mu\text{l}$ , 0.40 mmol) in dry 1,4-dioxane (0.7 ml). Trituration with cyclohexane (1 ml) afforded the pure **30bd** (42 mg, 63% yield) as a white solid. UPLC/MS:  $R_t = 2.13$  min (gradient 1); MS (ESI)  $m/z$ : 327.4  $[\text{M-H}]^-$ .  $[\text{M-H}]^-$  calculated: 327.1.  $^1\text{H}$

NMR (400 MHz, DMSO-*d*<sub>6</sub>)  $\delta$  12.63 (s, 1H), 8.05 (d, *J* = 2.0 Hz, 1H), 7.95 (dd, *J* = 8.9, 2.1 Hz, 1H), 6.90 (d, *J* = 8.9 Hz, 1H), 6.69 (t, *J* = 5.3 Hz, 1H), 3.29 – 3.22 (m, 2H), 2.66 (s, 6H), 1.54 – 1.46 (m, 2H), 0.96 (s, 9H). <sup>13</sup>C NMR (101 MHz, DMSO-*d*<sub>6</sub>)  $\delta$  166.81(CO), 149.92 (C), 135.91 (CH), 132.89 (CH), 117.03 (C), 115.71 (C), 112.42 (CH), 42.29 (CH<sub>2</sub>), 38.95 (CH<sub>2</sub>, extrapolated from HSQC), 37.79 (CH<sub>3</sub>, 2C), 30.15 (C), 29.68 (CH<sub>3</sub>, 3C).

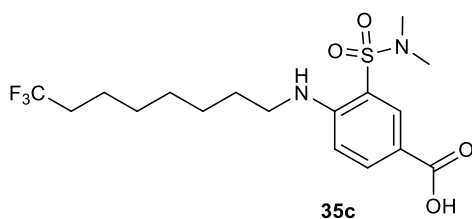


**3-(-*N,N*-dimethylsulfamoyl)-4-(4,4,4-trifluorobutylamino)benzoic acid (35a).** Titled compound was synthesized following the general procedure **F** previously described using intermediate **29b** (50 mg, 0.20 mmol) and 4,4,4-trifluorobutylamine **31a** (48  $\mu$ l, 0.40 mmol) in dry 1,4-dioxane (0.7 ml). Trituration with cyclohexane (1 ml) afforded the pure **35a** (40.13 mg, 57% yield) as a white solid. UPLC/MS: Rt = 1.78 min (gradient 1); MS (ESI) m/z: 353.4 [M-H]<sup>-</sup>. [M-H] calculated: 353.1. <sup>1</sup>H NMR (400 MHz, DMSO-*d*<sub>6</sub>)  $\delta$  12.64 (bs, 1H), 8.07 (d, *J* = 2.1 Hz, 1H), 7.95 (dd, *J* = 8.8, 2.1 Hz, 1H), 6.98 (d, *J* = 9.0 Hz, 1H), 6.88 (t, *J* = 5.9 Hz, 1H), 3.38 (q, *J* = 6.8 Hz, 2H), 2.67 (s, 6H), 2.40 – 2.25 (m, 2H), 1.83 – 1.73 (m, 2H). <sup>13</sup>C NMR (101 MHz, DMSO-*d*<sub>6</sub>)  $\delta$  166.40 (CO), 149.36 (C), 135.53 (CH), 132.60 (CH), 126.58 (CF<sub>3</sub>, q, <sup>1</sup>*J*<sub>CF</sub> = 278.6 Hz), 117.06 (C), 115.64 (C), 112.12 (CH), 41.02 (CH<sub>2</sub>), 37.35 (CH<sub>3</sub>, 2C), 30.18 (CH<sub>2</sub>, q, <sup>2</sup>*J*<sub>CF</sub> = 28.5 Hz), 20.97 (CH<sub>2</sub>).



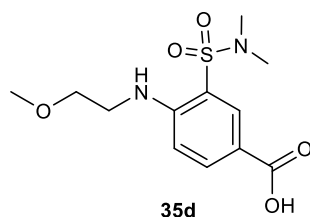
**3-(-*N,N*-dimethylsulfamoyl)-4-(6,6,6-trifluorohexylamino)benzoic acid (35b).** Compound **35b** was synthesized following the general procedure **F** previously described using intermediate **29b** (50 mg, 0.20 mmol) and 6,6,6-trifluorohexylamine **31b** (60  $\mu$ l, 0.40 mmol) in dry 1,4-dioxane (0.7 ml).

Trituration with cyclohexane (1 ml) afforded the pure **35b** (57.32 mg, 75% yield). UPLC/MS: Rt = 2.02 min (Gradient 1); MS (ESI) m/z: 381.4 [M-H]<sup>-</sup>. [M-H] calculated: 381.1. <sup>1</sup>H NMR (400 MHz, DMSO-*d*<sub>6</sub>) δ 12.64 (bs, 1H), 8.05 (d, *J* = 2.1 Hz, 1H), 7.94 (dd, *J* = 8.8, 2.1 Hz, 1H), 6.93 (d, *J* = 9.0 Hz, 1H), 6.77 (t, *J* = 5.4 Hz, 1H), 3.26 (q, *J* = 6.8 Hz, 2H), 2.66 (s, 6H), 2.32 – 2.18 (m, 2H), 1.62 (p, *J* = 7.4 Hz, 2H), 1.58 – 1.48 (m, 2H), 1.47 – 1.37 (m, 2H). <sup>13</sup>C NMR (101 MHz, DMSO-*d*<sub>6</sub>) δ 166.51 (CO), 149.36 (C), 135.62 (CH), 132.80 (CH), 126.88 (CF<sub>3</sub>, q, <sup>1</sup>*J*<sub>CF</sub> = 278.6 Hz), 116.96 (C), 115.44 (C), 112.12 (CH), 42.20 (CH<sub>2</sub>), 37.48 (CH<sub>3</sub>, 2C), 32.57 (CH<sub>2</sub>, q, <sup>2</sup>*J*<sub>CF</sub> = 27.6 Hz), 27.66 (CH<sub>2</sub>), 25.46 (CH<sub>2</sub>), 20.69 (CH<sub>2</sub>).

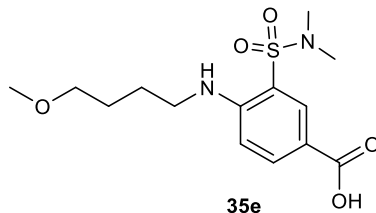


**3-(-*N,N*-dimethylsulfamoyl)-4-(8,8,8-trifluorooctylamino)benzoic acid (35c).** Compound **35c** was synthesized following the general procedure **F** previously described using intermediate **29b** (50 mg, 0.20 mmol) and amine **34a** (89 mg, 0.40 mmol) in dry 1,4-dioxane (0.7 ml). Purification by silica gel flash chromatography (CH<sub>2</sub>Cl<sub>2</sub>/MeOH from 100:0 to 98:02) followed by trituration with cyclohexane (1 ml) afforded the pure compound **35c** (44.3 mg, 54% yield) as a white solid. UPLC/MS: Rt = 2.28 min (gradient 1); MS (ESI) m/z: 409.4 [M-H]<sup>-</sup>. [M-H] calculated: 409.1. <sup>1</sup>H NMR (400 MHz, DMSO-*d*<sub>6</sub>) δ 12.62 (s, 1H), 8.05 (d, *J* = 2.1 Hz, 1H), 7.93 (dd, *J* = 8.8, 2.1 Hz, 1H), 6.91 (d, *J* = 9.0 Hz, 1H), 6.75 (t, *J* = 5.4 Hz, 1H), 3.24 (q, *J* = 6.6 Hz, 2H), 2.66 (s, 6H), 2.29 – 2.14 (m, 2H), 1.64 – 1.52 (m, 2H), 1.52 – 1.39 (m, 2H), 1.40 – 1.25 (m, 6H). <sup>13</sup>C NMR (101 MHz, DMSO-*d*<sub>6</sub>) δ 166.31 (CO), 149.50 (C), 135.38 (CH), 132.42 (CH), 127.68 (CF<sub>3</sub>, q, <sup>1</sup>*J*<sub>CF</sub> = 276.6 Hz), 116.62 (C), 115.18 (C), 112.01 (CH), 42.22 (CH<sub>2</sub>), 37.27 (CH<sub>3</sub>, 2C), 32.34 (CH<sub>2</sub>, q, <sup>2</sup>*J*<sub>CF</sub> = 26.9 Hz), 28.11 (CH<sub>2</sub>), 27.97 (CH<sub>2</sub>), 27.79 (CH<sub>2</sub>), 26.06 (CH<sub>2</sub>), 21.31 (CH<sub>2</sub>).

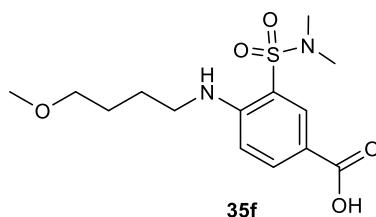




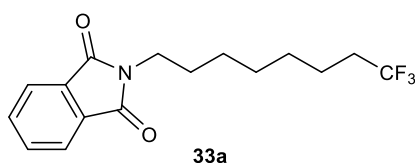
**3-(-N,N-dimethylsulfamoyl)-4-(2-methoxyethylamino)benzoic acid (35d).** Compound **35d** was synthesized following the general procedure **F** previously described using intermediate **29b** (50 mg, 0.20 mmol) and 2-methoxyethylamine **31c** (36  $\mu$ l, 0.40 mmol) in dry 1,4-dioxane (0.7 ml). Trituration with cyclohexane (1 ml) afforded the pure **35d** (53.96 mg, 89% yield). UPLC/MS: Rt = 1.40 min (gradient 1); MS (ESI) m/z: 301.4 [M-H]<sup>-</sup>. [M-H]<sup>-</sup> calculated: 301.1. <sup>1</sup>H NMR (400 MHz, DMSO-*d*<sub>6</sub>)  $\delta$  8.05 (d, *J* = 2.1 Hz, 1H), 7.93 (dd, *J* = 8.8, 2.1 Hz, 1H), 6.95 (d, *J* = 9.0 Hz, 1H), 6.89 (t, *J* = 5.3 Hz, 1H), 3.55 (t, *J* = 5.2 Hz, 2H), 3.40 (q, *J* = 5.3 Hz, 2H), 3.29 (s, 3H), 2.65 (s, 6H). <sup>13</sup>C NMR (101 MHz, DMSO)  $\delta$  166.31 (CO), 149.44 (C), 135.37 (CH), 132.36 (CH), 116.93 (C), 115.51 (C), 112.21 (CH), 69.73 (CH<sub>2</sub>), 58.02 (OCH<sub>3</sub>), 41.89 (CH<sub>2</sub>), 37.28 (CH<sub>3</sub>, 2C).



**3-(-N,N-dimethylsulfamoyl)-4-(4-methoxybutylamino)benzoic acid (35e).** Compound **35e** was synthesized following the general procedure **F** previously described using intermediate **29b** (50 mg, 0.20 mmol) and 4-methoxybutan-1-amine **31d** (51  $\mu$ l, 0.40 mmol) in dry 1,4-dioxane (0.7 ml). Trituration with cyclohexane (1 ml) afforded the pure **35e** (56.08 mg, 85% yield) as a white solid. UPLC/MS: Rt = 1.59 min (gradient 1); MS (ESI) m/z: 329.4 [M-H]<sup>-</sup>. [M-H]<sup>-</sup> calculated: 339.1. <sup>1</sup>H NMR (400 MHz, DMSO-*d*<sub>6</sub>)  $\delta$  12.63 (s, 1H), 8.05 (d, *J* = 2.1 Hz, 1H), 7.93 (dd, *J* = 8.8, 2.1 Hz, 1H), 6.91 (d, *J* = 8.9 Hz, 1H), 6.77 (t, *J* = 5.5 Hz, 1H), 3.38 – 3.32 (m, 2H), 3.26 (q, *J* = 6.5 Hz, 2H), 3.22 (s, 3H), 2.65 (s, 6H), 1.65 – 1.51 (m, 4H). <sup>13</sup>C NMR (101 MHz, DMSO-*d*<sub>6</sub>)  $\delta$  166.51 (CO), 149.40 (C), 135.67 (CH), 132.61 (CH), 117.01 (C), 115.71 (C), 112.29 (CH), 71.08 (CH<sub>2</sub>), 57.58 (OCH<sub>3</sub>), 42.08 (CH<sub>2</sub>), 37.29 (CH<sub>3</sub>, 2C), 26.55 (CH<sub>2</sub>).

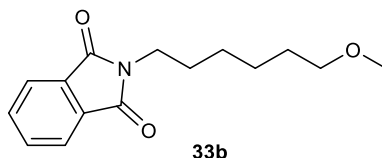


**3-(-*N,N*-dimethylsulfamoyl)-4-(6-methoxyhexylamino)benzoic acid (35f).** Compound **35f** was synthesized following the general procedure **F** previously described using intermediate **29b** (50 mg, 0.20 mmol) and 6-methoxyhexan-1-amine **34b** (53.1 mg, 0.40 mmol) in dry 1,4-dioxane (0.7 ml). Trituration with cyclohexane (1 ml) afforded the pure **35f** (23.14 mg, 32% yield) as a white solid. UPLC/MS: Rt = 1.84 min (gradient 1); MS (ESI) m/z: 357.5 [M-H]<sup>-</sup>. [M-H]<sup>-</sup> calculated: 357.2. <sup>1</sup>H NMR (400 MHz, DMSO-*d*<sub>6</sub>) δ 12.63 (s, 1H), 8.05 (d, *J* = 2.1 Hz, 1H), 7.93 (dd, *J* = 8.8, 2.1 Hz, 1H), 6.91 (d, *J* = 8.9 Hz, 1H), 6.77 (t, *J* = 5.5 Hz, 1H), 3.38 – 3.32 (m, 2H), 3.26 (q, *J* = 6.5 Hz, 2H), 3.22 (s, 3H), 2.65 (s, 6H), 1.65 – 1.51 (m, 4H). <sup>13</sup>C NMR (101 MHz, DMSO-*d*<sub>6</sub>) δ 166.77 (CO), 149.73 (C), 135.75 (CH), 132.67 (CH), 117.19 (C), 115.32 (C), 112.31 (CH), 72.02 (CH<sub>2</sub>), 58.03 (OCH<sub>3</sub>), 42.48 (CH<sub>2</sub>), 37.54 (CH<sub>3</sub>, 2C), 29.14 (CH<sub>2</sub>), , 26.37 (CH<sub>2</sub>), 25.53 (CH<sub>2</sub>). <sup>1</sup>H NMR (400 MHz, DMSO-*d*<sub>6</sub>) δ 12.63 (s, 1H), 8.05 (d, *J* = 2.1 Hz, 1H), 7.93 (dd, *J* = 8.8, 2.1 Hz, 1H), 6.91 (d, *J* = 8.9 Hz, 1H), 6.77 (t, *J* = 5.5 Hz, 1H), 3.38 – 3.32 (m, 2H), 3.26 (q, *J* = 6.5 Hz, 2H), 3.22 (s, 3H), 2.65 (s, 6H), 1.65 – 1.51 (m, 4H).

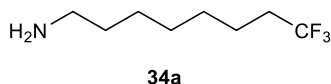


**2-(8,8,8-trifluorooctyl)isoindoline-1,3-dione (33a).** Titled compound was synthesized following the general procedure **G** previously described using potassium phthalimide (300 mg, 1.60 mmol) and intermediate 8-Bromo-1,1,1-trifluorooctane **32a** (0.4 ml, 2.08 mmol) in dry *N,N*-dimethylformamide (5.5 ml). Purification by silica gel flash chromatography (cyclohexane/EtOAc 85:15) afforded the pure **33a** (392.63 mg, 75% yield) as a colourless oil. UPLC/MS: Rt = 1.76 min (gradient 2); MS (ESI) m/z: 314.4 [M+H]<sup>+</sup>. [M+H]<sup>+</sup> calculated: 314.1. <sup>1</sup>H NMR (400 MHz, Chloroform-*d*) δ 7.86 – 7.81 (m, 2H),

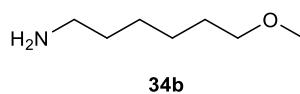
7.73 – 7.67 (m, 2H), 3.70 – 3.65 (m, 2H), 2.11 – 1.97 (m, 2H), 1.68 (p,  $J = 7.2$  Hz, 2H), 1.58 – 1.47 (m, 2H), 1.39 – 1.30 (m, 6H).



**2-(6-methoxyhexyl)isoindoline-1,3-dione (33b).** Compound **33b** was synthesized following the general procedure **G** previously described using potassium phthalimide (300 mg, 1.60 mmol) and 1-Bromo-6-methoxyhexane **32b** (0.36 ml, 2.08 mmol) in dry *N,N*-dimethylformamide (5.5 ml). Purification by silica gel flash chromatography (cyclohexane/EtOAc 70:30) afforded the pure **33b** (355.72 mg, 84% yield) as a colourless oil. UPLC/MS:  $R_t = 2.23$  min (gradient 2); MS (ESI)  $m/z$ : 262.5  $[M+H]^+$ .  $[M+H]^+$  calculated: 262.1.  $^1H$  NMR (400 MHz, Chloroform-*d*)  $\delta$  7.86 – 7.79 (m, 2H), 7.73 – 7.66 (m, 2H), 3.67 (t,  $J = 7.4$  Hz, 2H), 3.34 (t,  $J = 6.5$  Hz, 2H), 3.30 (s, 3H), 1.68 (p,  $J = 6.1$ , 5.6 Hz, 2H), 1.56 (p,  $J = 6.6$  Hz, 2H), 1.43 – 1.31 (m, 4H).



**8,8,8-trifluorooctan-1-amine (34a).** Compound **34a** was synthesized following the general procedure **H** previously described using intermediate **33a** (393 mg, 1.24 mmol) and hydrazine hydrate (0.14 ml, 1.86 mmol) in absolute ethanol (5.5 ml). Purification by basic alumina flash chromatography (dichloromethane/methanol 95:5) afforded the pure **34a** (136.31 mg, yield 60 %) as a colourless oil. UPLC/MS:  $R_t = 1.59$  min (gradient 1); MS (ESI)  $m/z$ : 184.4  $[M+H]^+$ .  $[M+H]^+$  calculated: 184.1.  $^1H$  NMR (400 MHz, DMSO-*d*<sub>6</sub>)  $\delta$  2.78 – 2.68 (m, 2H), 2.30 – 2.15 (m, 2H), 1.61 – 1.41 (m, 4H), 1.38 – 1.21 (m, 6H).



**6-methoxyhexan-1-amine (34b).** Compound **34b** was synthesized following the general procedure **H** previously described using intermediate **33b** (356 mg, 1.35 mmol) and hydrazine hydrate (0.15 ml,

2.02 mmol) in absolute ethanol (5.5 ml). Purification by basic alumina flash chromatography (dichloromethane/methanol 90:10) afforded the pure **34b** (127.55 mg, 72% yield) as a colourless oil. UPLC/MS: Rt = 1.00 min (gradient 1); MS (ESI) m/z: 132.4 [M+H]<sup>+</sup>. [M+H]<sup>+</sup> calculated: 132.1. <sup>1</sup>H NMR (400 MHz, DMSO-*d*<sub>6</sub>) δ 3.29 (t, *J* = 6.5 Hz, 2H), 3.20 (s, 3H), 1.51 – 1.43 (m, 2H), 2.68 (p, *J* = 6.2 Hz, 2H), 1.37 – 1.21 (m, 6H).

## Methods:

**Pharmacophore generation and ligand-based virtual screening.** The first pharmacophore model was built starting from bumetanide and other NKCC1 inhibitors (i.e. furosemide, azosemide, piretanide, bendroflumethiazide, benzthiazide, chlorothiazide, metolazone, quinethazone). The nine NKCC1 inhibitors were designed with Maestro (Schrödinger suite version 2015-4) and prepared with LigPrep to retrieve the most probable protonation and tautomerization states at physiological pH. Since the active conformation of NKCC1 inhibitors is unknown, we decided to use the most energetically favored conformation (i.e. the energetic minimum)<sup>200</sup> computed via MacroModel. This conformation was used for the subsequent pharmacophore modelling. For each of the nine compounds, phase software<sup>201</sup> was used to obtain the pharmacophore features, such as H-bond donor and acceptor, lipophilic and aromatic groups. The first pharmacophore model was obtained by removing from bumetanide's pharmacophore those features that were shared by the other eight compounds. The 'generate phase database' utility in Phase was used to prepare the internal and commercial molecular libraries for the ligand-based virtual screening (LBVS). Subsequently, the libraries were filtered to retain only the molecules that obey Lipinsky's rule and that do not bear reactive functional groups. The LBVS was conducted using Phase's 'find matches to hypothesis' utility. In the first run (i.e. screening of the internal database), we used default parameters. In the second run (i.e. screening of the commercial library), we customized our settings by applying a strict tolerance value (i.e. < 1 Å) for the features that strongly impacted activity towards NKCC1 (e.g. sulfonamide moiety), and by increasing the tolerance values (i.e. >1 Å) for the remaining features. After visually inspecting the resulting matches, we selected the structures with the best scores for the *in vitro* tests.

## Biology:

**Calcium kinetic assay.** Calcium kinetic assay was performed on hippocampal neurons prepared from mouse C57Bl/6J embryos on E18, and plated in a 96 well plate. At 3 DIV the neurons were loaded with a calcium-sensitive dye (Fluo4, Invitrogen) in extracellular solution (145 mM NaCl, 5 mM KCl, 10 mM HEPES, 5.55 mM Glucose, 1 mM MgCl<sub>2</sub>, 2 mM CaCl<sub>2</sub>). After 15 min neurons were treated with bumetanide (as a positive control) or each of our best compounds (10, 100 μM) in extracellular

solution for 15 min. Thus the plate was loaded onto the Victor 3V (Perkin Elmer) and the level of fluorescence upon application of GABA was monitored (100  $\mu$ M, for 20 sec). To test for neuronal viability, KCl (90 mM, for 40 sec) was applied after GABA treatment. To quantify the effect of bumetanide and the compounds on NKCC1 inhibition, the fluorescence values were normalized upon GABA application to the fluorescence levels upon KCl (90 mM) application in treated neurons.

**Electrophysiological recordings of GABA currents.** Neurons from hippocampal cell cultures (DIV12-20) were recorded at room temperature (22-24°C) in an extracellular solution containing in mM: 145 NaCl, 5 KCl, 10 HEPES, 5.55 Glucose, 1 MgCl<sub>2</sub>, 2 CaCl<sub>2</sub>. Cells were visualized with an upright microscope (Olympus BX51WI) with infrared differential interference contrast optics. Patch pipettes (3-5 M $\Omega$ ) were filled with an intracellular solution containing in mM: 100 K-Gluconate, 45 KCl, 10 HEPES, 3 MgCl<sub>2</sub>, 2 MgATP, 0.6 EGTA and 0.3 NaGTP; GABA currents were evoked by keeping the cell's membrane potential at -65 mV and puffing 20  $\mu$ M GABA (10 psi, 20-50 ms) using a Picospritzer III (Parker Instrumentation). Access resistance (Ra) was monitored during voltage-clamp recordings and traces with more than 25 M $\Omega$  Ra or a variation bigger than 20% between different sweeps were discarded. Evoked GABA-currents were obtained by averaging 5 sweeps for each experimental condition. Signals were sampled at 20 kHz and low pass filtered at 10 kHz with an Axon Multiclamp 700B (Molecular Devices).

## Chapter 4. Characterization of lead compound ARN23746.

Since ARN23746 displayed outstanding inhibition of NKCC1 in both the chloride assay and calcium assay, and it did not show any significant inhibition of the GABA<sub>A</sub>R, we decided to further proceed with an extensive *in vitro* and *in vivo* evaluation of this compound to possibly advance it as a lead compound. The experiments discussed below were designed and conducted in collaboration with the group of Dr. Laura Cancedda at IIT.

### 4.1 *In vitro* characterization of ARN23746.

#### 4.1.1 ARN23746 is able to restore the physiological chloride concentration in Ts65Dn neurons.

To test the ability of ARN23746 to modulate intracellular chloride concentration through NKCC1 modulation, we evaluated its efficacy in hippocampal Ts65Dn neurons. These cells show an increased intracellular Cl<sup>-</sup> concentration in comparison to WT littermates, caused by an increased expression of NKCC1<sup>176</sup>. Thus treatment with ARN23746 was predicted to restore physiological intracellular Cl<sup>-</sup> concentration. Experiments were performed at 15 DIV, when the GABA switch from depolarizing to hyperpolarizing has already occurred in cultures<sup>202</sup>. The intracellular Cl<sup>-</sup> concentration was measured upon treatment with DMSO (as negative control), bumetanide and furosemide (as positive controls), and ARN23746. Intracellular Cl<sup>-</sup> concentration was determined via the chloride- sensitive dye MQAE, which fluorescence is inversely correlated with the concentration of chloride. As depicted in Figure 4.1, Ts65Dn neurons are characterized by an increased intracellular Cl<sup>-</sup> level (corresponding to lower MQAE fluorescence intensity) in comparison to WT neurons. As expected, bumetanide and furosemide at 10 μM were able to significantly restore the intracellular Cl<sup>-</sup> concentration to WT levels (Figure 4.1a). Importantly, also ARN23746 at 10 μM significantly restored Cl<sup>-</sup> to physiological levels, without having any significant effect on the Cl<sup>-</sup> concentration in WT neurons.

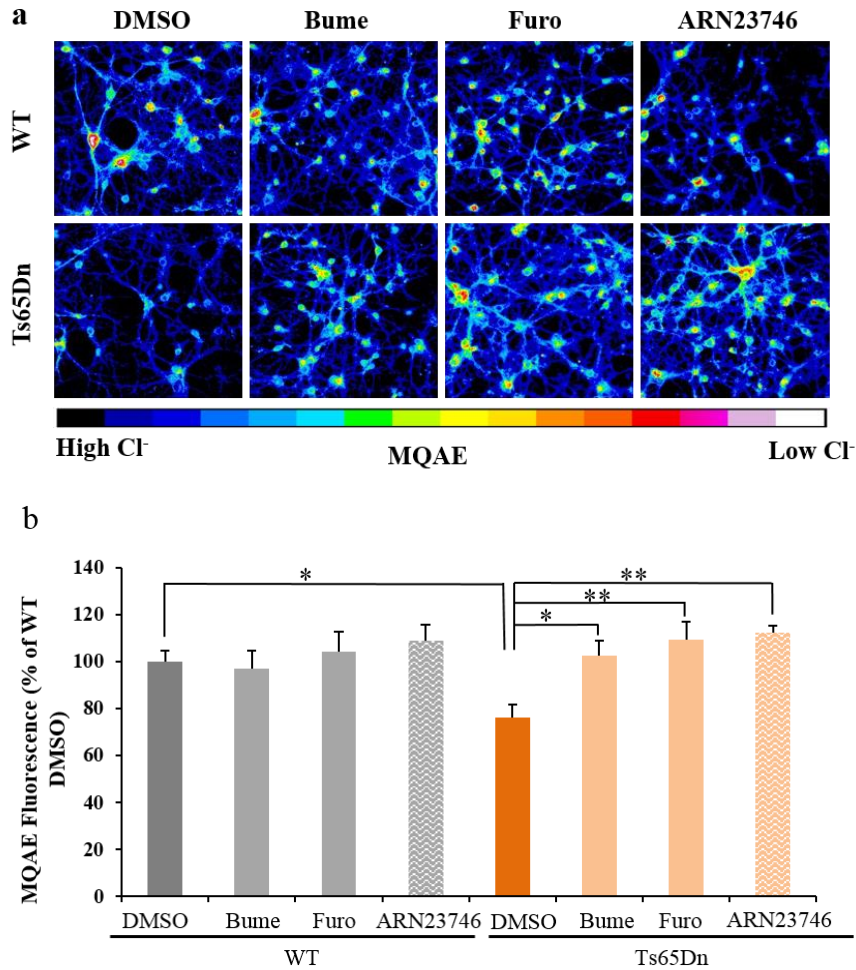


**Figure 4.1:** (a) representative pseudo-color images (coloured scale below) of the intracellular  $\text{Cl}^-$  concentration measured with the MQAE chloride dye, in WT and Ts65Dn hippocampal neurons after treatment with DMSO, bumetanide (Bume) and furosemide (Furo) and ARN23746. (b) quantification of effect of bumetanide (Bume 10  $\mu\text{M}$ ), Furosemide (Furo 10  $\mu\text{M}$ ) and ARN23746 (10  $\mu\text{M}$ ) in modulating intracellular chloride concentration at 15DIV in cultured neurons from hippocampus of WT and Ts65Dn mice. Data represents mean  $\pm$  sem from 3 independent experiments \*  $P < 0.05$ , \*\*  $P < 0.01$ ; Two Way Analysis of Variance, Tukey's *post hoc* test.

#### 4.1.2 ARN23746 does not inhibit significantly NKCC2 and KCC2.

Once we validated the efficiency of ARN23746 in inhibiting NKCC1 in multiple assays, we investigated its selectivity towards NKCC2 and KCC2. To test its activity on NKCC2, we took advantage of the previously described chloride assay on HEK293 cells transfected with NKCC2. As shown in Figure 4.2a, bumetanide at 10  $\mu\text{M}$  significantly inhibited NKCC2 to  $82.7 \pm 20.4$  %. Conversely, ARN23746 did not show a significant inhibitory activity on NKCC2 (Figure 4.2a). Then, to test the inhibitory activity of ARN23746 on KCC2 we used a different assay in HEK cells transfected with KCC2. To this aim, a thallium (Tl) influx assay based on thallium imaging by a



thallium sensitive-fluorescent dye was used<sup>102,203</sup>. The assay consists on the monitoring of the cells upon the consequent application of TlSO<sub>4</sub> (2 mM) followed by NaCl (74 mM). Upon activation of KCC2 by Cl<sup>-</sup> ions, Tl also enters the cells where binds thallium sensitive-dye, thus determining a fluorescence increase. As for the Cl<sup>-</sup>-flux assay, we validated the assay by assessing KCC2 functionality and inhibitory activity of bumetanide, furosemide and the known KCC2 inhibitor *R*-(+)-[(2-*n*-Butyl-6,7-dichloro-2-cyclopentyl-2,3-dihydro-1-oxo-1H-inden-5-yl)oxy]acetic acid (DIOA). When evaluated in this in this assay, ARN23746 (10 μM) did not show a significant inhibitory activity on KCC2 (4.6 ± 6.9 %, Figure 4.2b), compared to the inhibitory activity of DIOA (37.6 ± 6.7 %, Figure 4.2b).

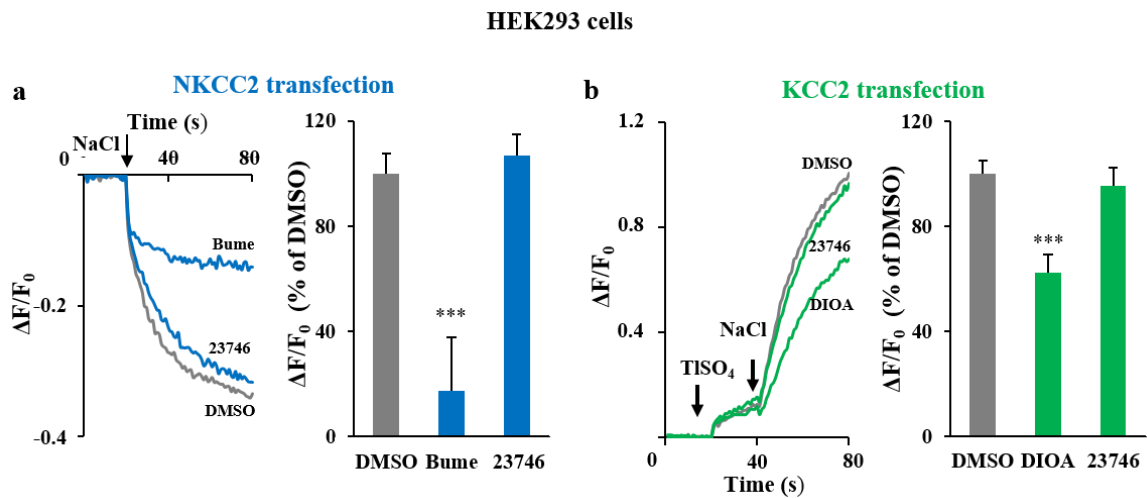


**Figure 4.2.** (a) Left, example traces obtained in the Cl<sup>-</sup> influx assay on NKCC2-transfected HEK293 cells. The arrow indicates the addition of NaCl together with each compound (10 μM). Right, quantification of the NKCC2 inhibitory activity in experiments as those on the right. Data are presented as a percentage of the respective control DMSO. Data represent mean ± SEM from 3 independent experiments (Kruskal-Wallis One Way ANOVA on Ranks, H= 16,962, DF=2, P<0.001, Dunn's *post hoc* test, \*\*\* P<0.001). (b) Left, example traces obtained in the Tl influx assay on KCC2-transfected HEK293 cells. The arrows indicates the addition of TlSO<sub>4</sub> and NaCl together with each compound (10 μM). Right, quantification of the KCC2 inhibitory activity in experiments as those on the right. Data are presented as a percentage of the respective control DMSO. Data represent mean ± SEM from 3 independent experiments (One Way ANOVA, F<sub>(2,51)</sub> = 10.676, P<0.001, Dunnett's *post hoc* test \*\*\* P<0.001).

#### 4.1.3 *In vitro* assessment of ARN23746 drug-like properties.

In view of possible *in vivo* studies via systemic administration of ARN23746, we extensively characterized its chemical, physical and drug-like properties *in vitro*. In particular, we measured the solubility of ARN23746 in PBS at pH 7.4. As reported in Table 4.1, ARN23746 exhibited an excellent kinetic solubility, reaching the target concentration of 250  $\mu\text{M}$ , and a thermodynamic solubility reaching a maximum concentration of 181  $\mu\text{M}$  in PBS. Next, we tested the plasmatic stability of ARN23746 in mouse plasma. The compound demonstrated a long plasmatic stability with a half-life of over 120 minutes and high plasmatic protein binding in this species (Table 4.1). Furthermore, to evaluate the metabolization of ARN23746, we assessed its stability in microsomes obtained from mouse and rat liver. ARN23746 displayed an extended half-life in both species (Table 4.1). Moreover, ARN23746 displayed also protracted half-life in microsomes obtained from human liver (Table 4.1).

We then, explored metabolism in rat and human more deeply by studying the formation of possible metabolites after incubation in rat and human derived liver homogenates. Two main metabolites were detected by liquid chromatography–mass spectrometry (LC-MS). In particular, one showed ARN23746 mass + 176 Dalton (Da) assignable to the glucuronic acid conjugation product, and the other one showed ARN23746 mass – 14 Da assignable to the *N*-desmethyl derivative (Figure 4.3). Interestingly, when the rate of formation of these metabolites was compared in rat vs human liver homogenates, rat metabolism resulted more prone to dealkylation (Figure 4.3) giving rise to the *N*-desmethyl derivative as the main metabolite. Conversely, in human microsomes the main metabolic route resulted to be the conjugation with glucuronic acid. Notably, ARN23746 displayed low intrinsic clearance in both species (Figure 4.3).

Finally, we performed an *in vitro* screening of a panel of 47 off-targets that comprises pharmacologically relevant receptors, transporters, ion channels and enzymes, both as agonist and as antagonist. As a result, at a 10  $\mu\text{M}$  concentration ARN23746 did not show a significant activity against any of the 47 off-targets (See Appendix). Thus, ARN23746 displayed a satisfying *in vitro* drug-like and safety profile; therefore, it was advanced for further *in vivo* evaluation.

Analysis	Species	ARN23746
Kinetic solubility PBS pH 7.4	-	> 250 $\mu\text{M}$
Thermodynamic solubility PBS pH 7.4	-	181 $\mu\text{M}$
$t_{1/2}$ plasma	mouse	> 120 min
$t_{1/2}$ liver microsomes	mouse	> 60 min
Residual liver compound	mouse	65%
$t_{1/2}$ liver microsomes	rat	189 min
$t_{1/2}$ liver microsomes	human	395 min
Intrinsic clearance	rat	0,00366 $\text{ml} \cdot \text{min}^{-1} \cdot \text{million cells}^{-1}$
Intrinsic clearance	human	0,00220 $\text{ml} \cdot \text{min}^{-1} \cdot \text{million cells}^{-1}$
Plasmatic protein binding	mouse	98.8%

**Table 4.1.** *In vitro* drug-like properties of ARN23746.

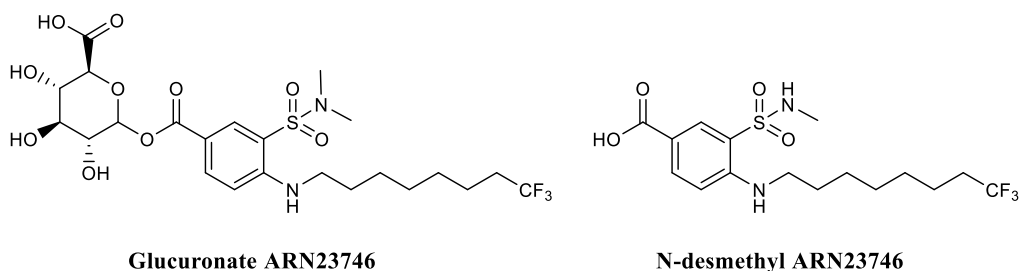


**Figure 4.3.** Proposed structures of the two main metabolites of ARN23746 identified in rat and human liver homogenates.

## 4.2 *In vivo* characterization of ARN23746.

### 4.2.1 ARN23746 displays higher brain penetration compared to bumetanide.

We then decided to evaluate ARN23746 blood-brain barrier (BBB) penetration; a crucial feature for CNS targeted compounds. For this task, we performed a pharmacokinetic analysis in WT (C57CL/6 mice) in comparison to bumetanide. Adult animals were treated with ARN23746 and bumetanide were administered intravenously (i.v) at 2 mg/kg in phosphate buffered saline (PBS).

As a result, ARN23746 displayed a significantly higher brain penetration compared to bumetanide (Figure 4.4a). In particular, ARN23746 exhibited a much more favourable brain/plasma ratio ( $> 0.04$ , Figure 4.4b). After entering the bloodstream, the compound reached a peak of concentration in the brain after 5 minutes of  $\sim 116$  ng/g (Figure 4.4a).

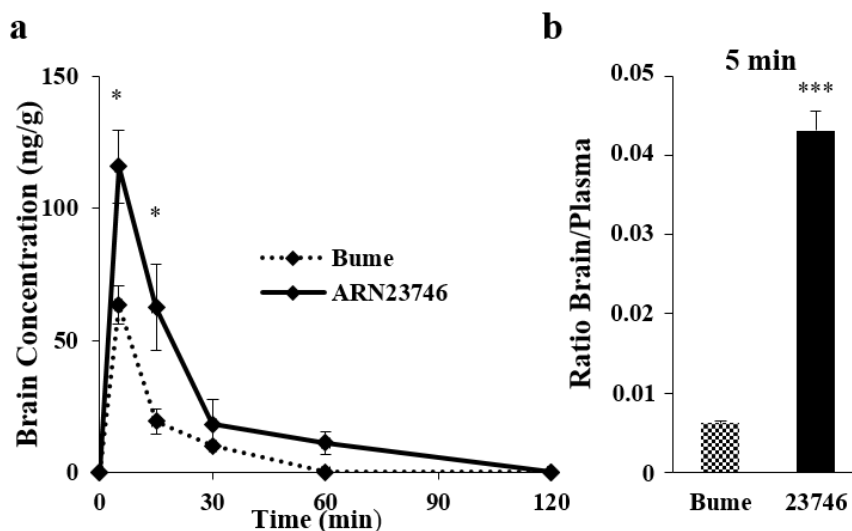


**Figure 4.4.** (a) Graph describing the pharmacokinetics of ARN23746 (black line) and bumetanide (Bume, dotted line) in the brain following 2mg/kg IV administration in WT (C57Bl/6) mice at 6 different time point (0-5-15-30-60-120 min), (two-way ANOVA, Tukey's post hoc test, \*  $P < 0.05$ ). (b) Quantification of the brain/plasma ratio at the time point of 5 mins following bumetanide or C6 administration. (Two-tailed t-test, \*\*\*  $P < 0.001$ ).

Notably, ARN23746 showed a brain permeation almost two fold higher than bumetanide ( $\sim 63$  ng/g). These results are consistent with higher predicted AlogP and a lower predicted polar surface area (PSA, Table 4.2) of ARN23746 compared to bumetanide.

Predicted property	Bumetanide	ARN23746
AlogP	2.86	3.79
PSA	127.1 Å <sup>2</sup>	95.1 Å <sup>2</sup>

**Table 4.2.** Predicted chemicoophysical properties that can affect BBB penetration of the two compounds. Values calculated with BIOVIA Draw version 16.1, Dassault systèmes.

### 4.2.3 ARN23746 does not exert significant diuretic effect *in vivo*.

Next, we assessed ARN23746 diuretic effect in WT and Ts65Dn mice. For this purpose, 2-4 month mice were treated with an intra peritoneal (ip) injection of ARN23746 dissolved in PBS at  $0.2 \text{ mg kg}^{-1}$ , which are the same route of administration and dosage used for bumetanide in the previous study from our collaborators in this project<sup>176</sup>. Bumetanide was used as a positive control at the dose of  $0.2 \text{ mg kg}^{-1}$ . After mice treatment urine was collected after 2 hrs and the volume calculated (Figure 4.5). As expected, bumetanide administration significantly increased the urine volume in both WT and Ts65Dn mice when compared with vehicle- treated mice (Figure 4.5). Conversely, ARN23746 treatment had no significant diuretic effect both in WT and in Ts65Dn mice, when compared with vehicle-treated mice (Figure 4.5b).

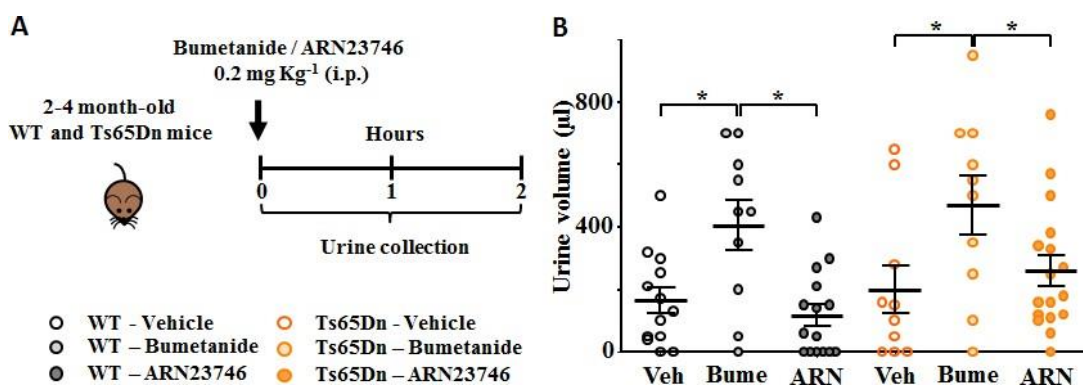


**Figure 4.5.** (A) Schematic cartoon of the experimental protocol for the treatment of WT and Ts65Dn mice with bumetanide (control) and with the compound ARN23746 for the assessment of their diuretic effect. (B) Quantification of the urine volume in mice treated with vehicle (WT,  $n = 13$ , Ts65Dn,  $n = 9$ ), bumetanide (WT,  $n = 10$ , Ts65Dn,  $n = 10$ ) or ARN23746 (WT,  $n = 12$ , Ts65Dn,  $n = 13$ ). \*  $P < 0.05$ , two-way ANOVA Tukey's *post hoc* test.

#### 4.2.2 ARN23746 is able to rescue memory deficits in Down syndrome mice.

Next, we decided to investigate ARN23746 efficacy in rescuing cognitive impairment in Ts65Dn mice, as previously assessed with bumetanide<sup>176</sup>. In particular, we evaluated both the short-term working memory and the long-term hippocampus-dependent explicit memory after a subchronic, systemic treatment with ARN23746 (0.2 mg kg<sup>-1</sup>, IP, daily; Figure 4.6).

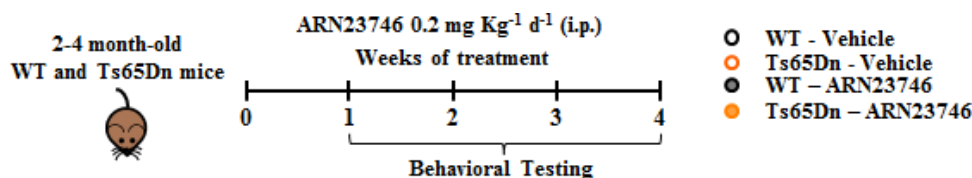


**Figure 4.6.** Schematic representation of the experimental protocol for the treatment of WT (black circle in graphs) and Ts65Dn (orange circles in graphs) mice with the compound ARN23746 for its efficacy assessment.

First, we assessed the efficacy of ARN23746 in restoring short-term memory, by testing mice in the T- maze task (spontaneous alteration protocol, 11 trial). The test was conducted similarly to what had previously described for Ts65Dn mice<sup>204</sup>. In this test, mice are started from the base of a T-shaped maze (Figure 4.7a) and they are allowed to choose one of the two arms (first choice). If they remember the previous choice, mice will choose the arm not visited in the trial before, after the first trial. The alternate choice of each arm is considered as correct, whereas the choice of the same arm as in the previous trial (reflective of a poor short-term memory) is considered as negative. The final score for each animal is calculated by the number of the correct choices over the total of 10 trials. Confirming data from previously published<sup>204</sup>, Ts65Dn showed poor short-term memory in comparison to WT littermates. ARN23746 treatment completely rescued the number of correct choices of Ts65 mice in comparison to WT animals (Figure 4.7a).

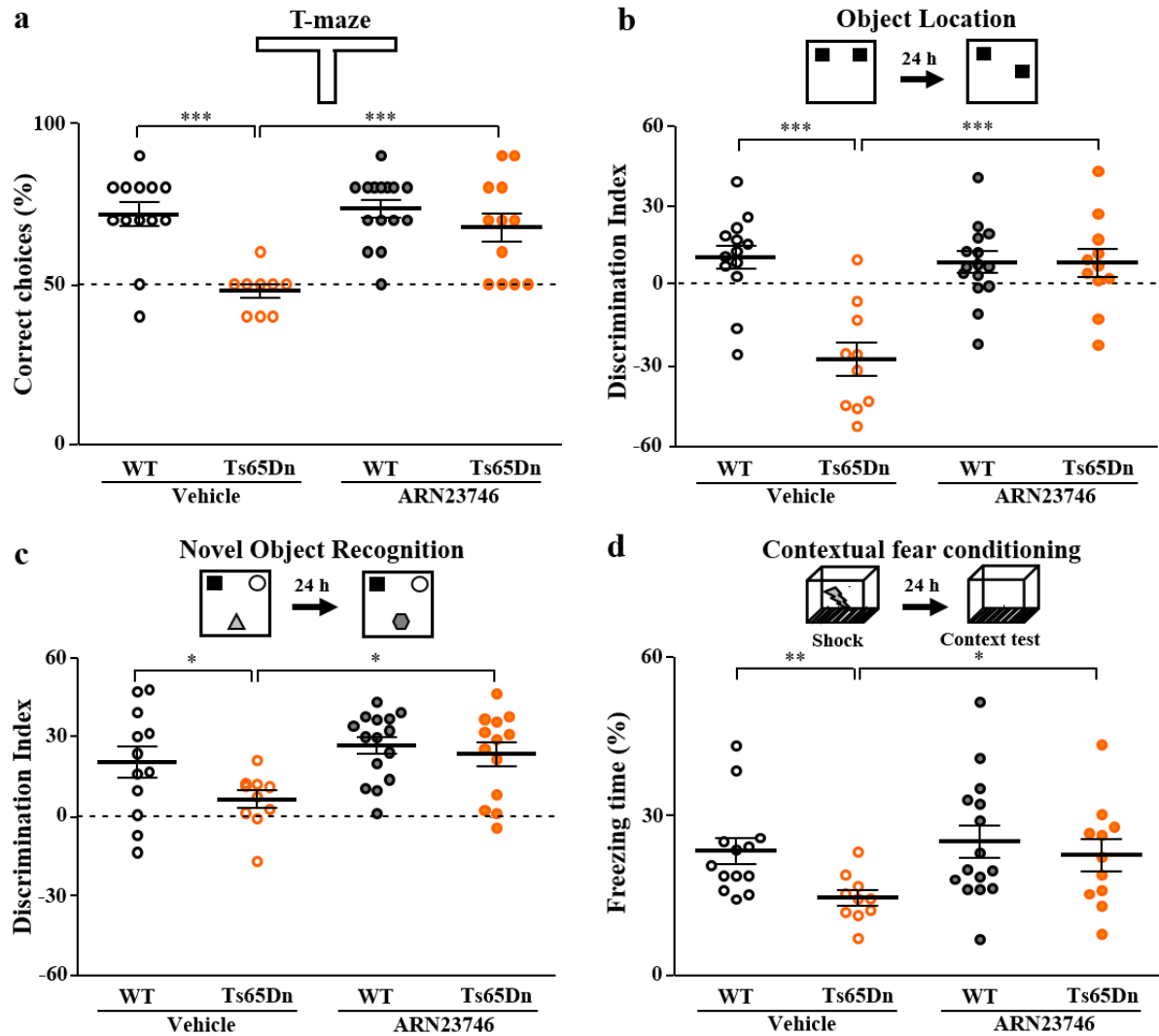


**Figure 4.7. ARN23746 rescues cognitive impairment in the Ts65Dn mouse model of Down syndrome.** (a) Top, schematic representation of the T-maze test. Bottom, quantification of the mean  $\pm$  SEM and single animal cases of correct choices in mice treated with the indicated compounds (two-way ANOVA, Finteraction (1,46)= 5.475,  $P = 0.024$ , Tukey's post hoc test, \*\*  $P < 0.01$ , \*\*\* $P < 0.001$ ). (b) Top, schematic representation of the object-location test. Bottom, quantification of the mean  $\pm$  SEM and single animal cases of discrimination index in mice treated with the indicated compounds (two-way ANOVA, Finteraction (1,45)= 15.523,  $P < 0.001$ , Tukey's post hoc test; \*\*\* $P < 0.001$ ). (c) Top, schematic representation of the novel-object recognition task. Bottom, quantification of the mean  $\pm$  SEM and single animal cases of the discrimination index in mice treated with the indicated compounds (Two-Way ANOVA, Ftreatment (1,46)= 7.154,  $P = 0.010$ , Tukey's post hoc test, \*  $P < 0.05$ , two-way). (d) Top, schematic representation of the contextual fear-conditioning test. Bottom, quantification of the mean  $\pm$  SEM and single animal cases of the freezing response in mice treated with the indicated compounds (two-way ANOVA on Ranks, Ftreatment (1,45)= 4.425,  $P = 0.041$ , Tukey's post hoc test, \*  $P < 0.05$ , \*\*  $P < 0.01$ ).

Then, the long-term memory was assessed in three independent tasks (i.e., object location, novel object recognition and contextual fear conditioning). We assessed spatial memory in the object location task (OL) (Figure 4.7b). The test measures the ability of mice to recognize the new location of a familiar object with respect spatial external cues. As previously described<sup>176</sup>, vehicle- treated Ts65Dn mice showed impaired spatial memory, as demonstrated by a poor discrimination index reflective of poor

discernment of the new object position. ARN23746 treatment restored the performance of Ts65Dn mice to the level of WT (Figure 4.7b).

We next assessed the recognition memory in the novel-object recognition (NOR) test (Figure 4.7c). This task measures the preference of mice for a novel object versus previously encountered familiar objects. As previously demonstrated<sup>176</sup>, Ts65Dn mice showed poor recognition memory in comparison to WT littermates. Interestingly, ARN23746 administration was able to completely rescue the poor novel-discrimination ability of Ts65Dn mice (Figure 4.7c). Finally, we evaluated associative memory in the contextual fear conditioning test (CFC). This task measures the freezing response that takes place after pairing of a foot shock (conditioning) with a particular context represented by the grid releasing the shock (Figure 4.7d). As previously demonstrated<sup>176</sup>, Ts65Dn mice showed poor freezing response after the re- exposure to the grid context 24h after conditioning. Notably, ARN23746 treatment fully restored the associative memory in Ts65Dn by rescuing the poor freezing response (Figure 4.7d).



#### 4.2.4 Toxicity assessment of ARN23746 after chronic treatment.

To assess any toxicity following ARN23746 systemic administration after chronic treatment, we first monitored the weight of treated animals during the four weeks of chronic treatment. As reported in Figure 4.8a, a four week-daily treatment with ARN23746 did not affect body weight, nor the general health state of the mice, as evaluated by daily eye assessment. Moreover, on the same animals we measured the visceral index (visceral weight/body weight) for the kidneys, liver, spleen, lungs, and brain. As shown in the Figure 4.8b, chronic treatment with ARN23746 did not alter the weight of internal organs.

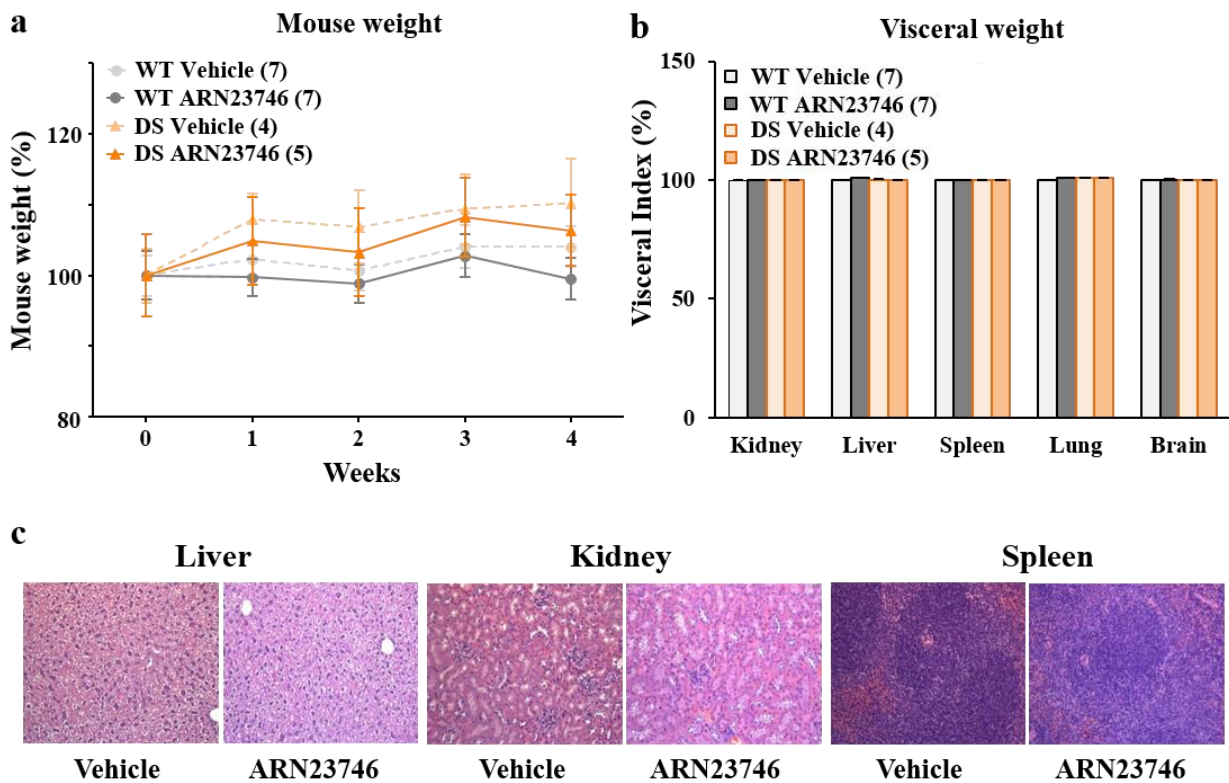


**Figure 4.8.** a), Quantification of the body weight of WT and TS65Dn mice across the four weeks of treatment with vehicle (control) and ARN23746. b), Visceral index expressed as viscera weight/body weight of 5 different organs collected from WT and TS65Dn mice after chronic treatment with vehicle (control) and ARN23746. c), Examples hematoxylin-eosin images of liver, kidney and spleen sections from mice treated with vehicle (control) or ARN23746.

<b>Tissue</b>	<b>Group</b>	<b>Physiological morphology (n.of animals)</b>	<b>Pathological morphology (n.of animals)</b>
<b>Liver</b>	WT Vehicle	5	2
	WT ARN23746	7	0
	Ts65Dn Vehicle	3	1
	Ts65Dn ARN23746	5	0
<b>Kidney</b>	WT Vehicle	6	1
	WT ARN23746	6	1
	Ts65Dn Vehicle	3	1
	Ts65Dn ARN23746	5	0
<b>Spleen</b>	WT Vehicle	6	1
	WT ARN23746	6	1
	Ts65Dn Vehicle	4	0
	Ts65Dn ARN23746	5	0

**Table 4.3.** Number of WT and Ts65Dn mice showing a physiological or pathological morphology of liver, kidney and spleen after four weeks of treatment with vehicle (control) or with ARN23746.

Moreover, we assessed the histopathological profile of liver, kidney and spleen. In particular, from each organ, we analyzed five sections stained with hematoxylin-eosin, marker of nucleus and cytoplasm respectively and gold standard of medical diagnosis. As shown in Figure 4.8c and in Table 3.4, we did not find major abnormalities following ARN23746 chronic treatment. Indeed, across the 14 WT mice (7 treated with vehicle and 7 treated with ARN23746) and the 9 Ts65Dn mice (4 treated with vehicle and 5 treated with ARN23746) we found some morphological alterations in the liver of only two WT vehicle- treated mice and one Ts65Dn vehicle-treated mouse, in one kidney of one WT vehicle-treated mouse, one WT ARN23746-treated mouse and one Ts65Dn vehicle-treated mouse, and in the spleen of one WT vehicle-treated mouse and of one Ts65Dn vehicle-treated mouse. These results are compatible with the individual variability already described in mice and cannot be ascribed at any toxic effect of ARN23746.

#### 4.2.5 ARN23746 is able to rescue social deficits and the repetitive behaviors in the valproic acid mouse model of autism with no diuretic effect.

To further corroborate ARN23746 efficacy in the treatment of neurological disorders with impaired Cl<sup>-</sup> homeostasis and depolarizing GABA transmission, we assessed its efficacy to recover behaviors related to ASD core symptoms, for which we employed the valproic-acid (VPA) mouse model of ASD. As for DS mice, firstly we evaluated the diuretic effect of ARN23746 and bumetanide (as positive control) in young adult (P40-60) VPA mice and controls by measuring the urine volume two hours following the treatment (0.2 mg kg<sup>-1</sup>, IP 6; Figure 4.9a). Similarly to the results observed in DS mice, bumetanide administration significantly increased the urine volume both in WT and VPA mice when compared to vehicle-treated mice, while ARN23746 treatment had no significant diuretic effect both in WT and VPA mice (Figure 4.9b).

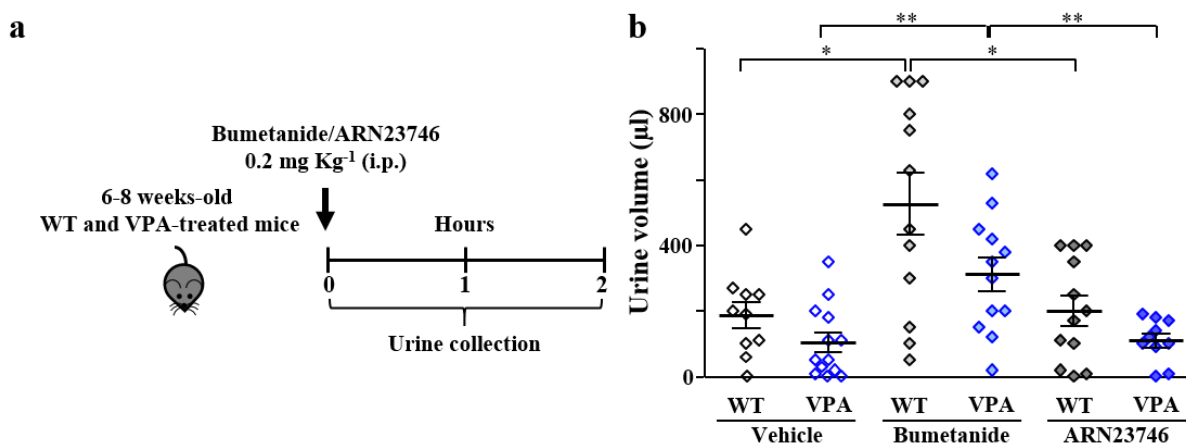


**Figure 4.9** (a) Schematic cartoon of the experimental protocol for the treatment of WT and VPA mice with bumetanide or ARN23746 for the assessment of the diuretic effect. (b) Quantification of mean  $\pm$  SEM and single animal cases of the urine volume 120 min after mice were treated with the indicated compounds (two-way ANOVA on Ranks,  $F_{\text{treatment}(2,63)} = 11.635$ ,  $P < 0.001$ , Tukey's *post hoc* test, \*  $P < 0.05$ , \*\*  $P < 0.01$ ).

Then, we evaluated the social interactions upon exposure to a stranger mouse and the repetitive behaviors (grooming and marble burying) after a chronic (7-21 days) systemic treatment with ARN23746 (0.2 mg kg<sup>-1</sup>, IP, daily) in young adult (P40 to P60) VPA mice. We found that ARN23746 administration completely rescued the poor social interaction of VPA mice. This occurred both toward a never-met-intruder vs an object (expressed as sociability index) and toward a novel mouse vs an already-met mouse (expressed as social novelty index) in the three chamber test (Figure 4.10a). Moreover, ARN23746 treatment was able to rescue poor sociability during male-female interaction (Figure.4.10b).

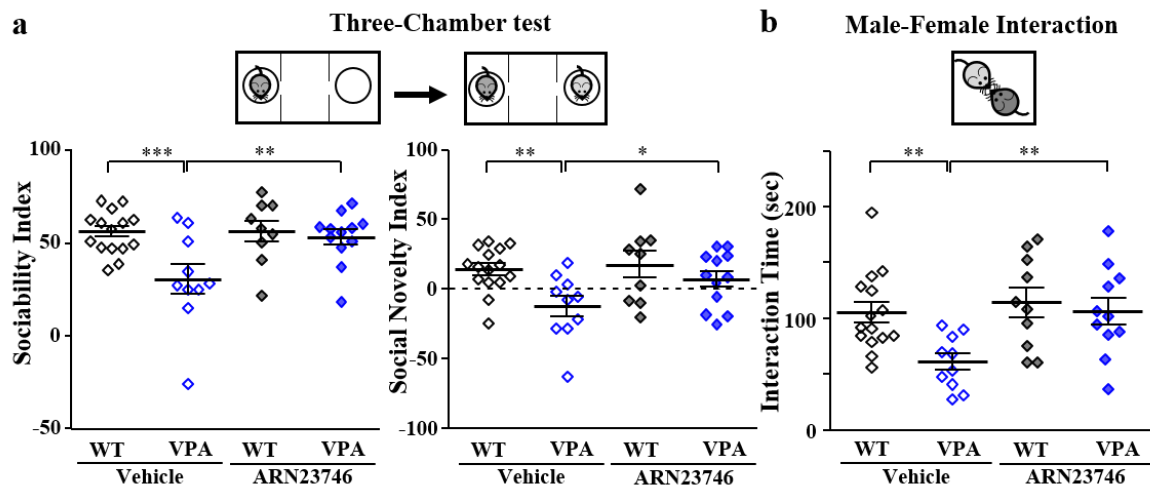


**Figure 4.10** (a) Top, schematic representation of the three-chamber test. Bottom, left, quantification of the mean  $\pm$  SEM and single animal cases of sociability index in mice treated with indicated compounds (two-way ANOVA on Ranks,  $F_{\text{interaction}(1,42)} = 4.637$ ,  $P = 0.037$ , Tukey's *post hoc* test, \*\*  $P < 0.01$ , \*\*\*  $P < 0.001$ ). Bottom, right, quantification of the mean  $\pm$  SEM and single animal cases of social novelty index in mice treated with indicated compounds (two-way ANOVA,  $F_{\text{condition}(1,42)} = 8.195$ ,  $P = 0.007$ , Tukey's *post hoc* test, \*  $P < 0.05$ , \*\*  $P < 0.01$ ). (b) Top, schematic representation of the male-female interaction test. Bottom quantification of the mean  $\pm$  SEM and single animal cases of the interaction time in mice treated with the indicated compounds (two-way ANOVA,  $F_{\text{treatment}(1,42)} = 6.351$ ,  $P = 0.016$ , Tukey's *post hoc* test, \*\*  $P < 0.01$ ).

Finally, we evaluated ARN23746 effect on repetitive behaviors in the marble burying test and in the grooming task (Figure 4.11). Notably, ARN23746 was able to restore repetitive behaviors in both the tasks (Figure 4.11a/b).

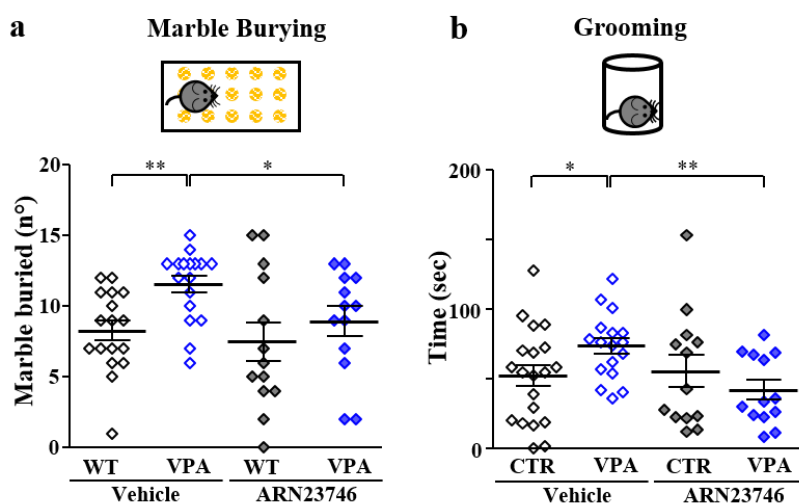


**Figure 4.11** (a) Top, schematic representation of the marble burying test. Bottom quantification of the mean  $\pm$  SEM and single animal cases of the number of marble buried in mice treated with the indicated compounds (two-way ANOVA,  $F_{\text{condition}}(1,56) = 6.727$ ,  $P = 0.012$ , Tukey's *post hoc* test, \*  $P < 0.05$ , \*\*  $P < 0.01$ ). (b) Top, schematic representation of the grooming test. Bottom quantification of the mean  $\pm$  SEM and single animal cases of the grooming time in mice treated with the indicated compounds (two-way ANOVA,  $F_{\text{interaction}}(1,59) = 4.700$ ,  $P = 0.034$ , Tukey's *post hoc* test, \*\*  $P < 0.01$ ).

### 4.3 Discussion.

Altogether our results point out that ARN23746 is able to selectively block NKCC1 without inhibiting nor NKCC2 nor KCC2 and restore the physiological  $[Cl^-]_i$  in murine DS neurons *in vitro*. Our *in vitro* studies demonstrated that ARN23746 is able to inhibit NKCC1 with a higher potency than bumetanide. Moreover, ARN23746 showed no significant inhibitory activity of NKCC2, in comparison to the significant inhibitory activity of bumetanide at 10  $\mu\text{M}$ . Conversely, at the same concentration ARN23746 was able to significantly inhibit NKCC1 at levels comparable to bumetanide. Thus, the inhibition ratio of NKCC1/NKCC2 is markedly in favor of ARN23746 when compared to bumetanide. Consistently, at the *in vivo* dosage at which bumetanide rescued cognitive impairments but it is diuretic in DS mice (0.2 mg/Kg), ARN23746 still rescued cognitive deficits but it did not show any significant diuretic effect. Possibly, at the same dosage ARN23746 does not inhibit NKCC2 expressed in endolymphatic sac and/or in vasopressinergic and oxytocinergic neurons, thus reducing, at least in part, the ototoxic effect of bumetanide and other osmotic and behavioral side effects.

In addition, administration of ARN23746 in adult animals of an ASD mouse model was able also to recover social and repetitive behaviors related to autism in four diverse tasks. Taken together, this data underlies that core symptoms in DS and ASD mice are rescued by selective pharmacological NKCC1 inhibition with a compound with a better brain/plasma ratio than bumetanide, further strengthening the notion that NKCC1 impaired function is causally linked to brain-related behaviors. Moreover, our findings rule out the possibility that bumetanide's brain-related effects are due to osmotic regulation and/or ionic imbalance through excessive NKCC2-mediated diuresis.

Taking advantage of this data, ARN23746 could open the way to new unprecedented avenues for the development of new compliant pharmacological therapies that will be potentially effective in the many other neurological disorders characterized by depolarizing GABAergic transmission.

#### 4.4 Experimental section.

**MQAE Cl<sup>-</sup> imaging in neuronal cultures.** Cl<sup>-</sup> imaging was performed with the fluorescent Cl<sup>-</sup>-sensitive indicator MQAE [*N*-(Ethoxycarbonylmethyl)-6-Methoxyquinolinium-Bromide; Molecular Probes] as previously described<sup>176</sup>. Neurons at 15 DIV were loaded with 5 mM MQAE and with bumetanide (as positive control), DMSO (as negative control), or ARN23746 at 10 μM, for 30 minutes at 37°C. Coverslips were then transferred to a holding chamber and perfused (2 mL\*min<sup>-1</sup>) with extracellular solution (NaCl 124 mM, KCl 5 mM, CaCl<sub>2</sub> 2 mM, MgCl<sub>2</sub> 1 mM, Hepes 10 mM, D-glucose 5.5 mM, pH 7.4) and with addition of the tested compound at 25°C for 5 minutes before imaging. Images were acquired with a Nikon A1 scanning confocal microscope equipped with a 20X air-objective (NA 0.75). MQAE was excited with a 405 nm diode laser and fluorescence collected with a 525/50 nm band-pass emission filter. All excitation and acquisition parameters (laser intensity, PMT offset and gain) were kept constant throughout the experiments. Image analysis was performed with NIS-Elements software (Nikon) by measuring the mean fluorescent intensity of regions of interest (ROIs) centered on the cell body of single neurons from 6 randomly-selected fields for each coverslip. For each experiment, the average fluorescent intensity of all ROIs from a coverslip was normalized to the average fluorescent intensity of control samples (WT neurons treated with DMSO) in the same experiment. Pseudo-color images were generated by ImageJ software (<http://rsbweb.nih.gov/ij/>).

**Cl<sup>-</sup>-influx assay in HEK cells transfected with NKCC2.** This experiment has been run in the same conditions described in chapter 2, Section 2.4.

**Thallium influx assay in HEK cells.** To assess KCC2 activity (Thallium influx assay), cells were transfected with 16 μg of KCC2<sup>194</sup> subcloned in PRK5 plasmid or mock control (empty vector) and 32 ul of Lipofectamin 2000. After 4 h, the cells were collected and plated in 96-well black-walled, clear-bottomed plates at a density of 2.5x10<sup>4</sup>. After 48 h, cells were used for the Cl<sup>-</sup> or Thallium influx assays. Reagents were purchased from Life Technologies, unless otherwise specified. Thallium influx assay (FluxOR Potassium Ion Channel Assay, Life Technologies), was modified from<sup>102,203</sup>. We loaded the

cell with 100  $\mu\text{l}$ /well  $\text{Cl}^-$  free-hypotonic solution (67.5 mM  $\text{Na}^+$  Gluconate, 2.5mM  $\text{K}^+$  Gluconate, 15mM HEPES pH 7.4, 50 mM Glucose, 1mM  $\text{Na}_2\text{HPO}_4$ , 1 mM  $\text{NaH}_2\text{PO}_4$ , 1 mM  $\text{MgSO}_4$ , 1 mM  $\text{CaSO}_4 \cdot 2\text{H}_2\text{O}$ ), 1:1000 TI-sensitive fluorogenic dye (Component A) and 1:100 Probenecid (Component D). After 1hr, cells were washed twice with 100  $\mu\text{l}$ /well of hypotonic solution and loaded with DIOA (Sigma, positive control) DMSO (as negative control), and ARN23746 diluted in 200  $\mu\text{l}$ /well hypotonic solution. The plate was loaded onto Tecan Spark. The dye was excited at 490 nm and detected at 520 nm. The time course was recorded over a period of 80 s. In particular for each well we performed a continuously recording fluorescence for 20 s of baseline, then for 20 s after a 2mM  $\text{TiSO}_4$  injection and for 40s after 74 mM NaCl injection.

***In vitro* mouse plasma stability.** Compounds were diluted in preheated (37 °C) mouse plasma (Rockland Immunochemicals Inc.) with 5% DMSO to favor solubilization. The final compound concentration was 2.0  $\mu\text{M}$ . At time points (0, 5, 15, 30, 60, 120 min), a 30  $\mu\text{L}$  aliquot of the incubation solution was diluted in 200  $\mu\text{L}$  of cold acetonitrile spiked with 200 nM Warfarin, as internal standard. After vortexing for 30 s, the solution was centrifuged at 3500g for 15 min at 4 °C, and the supernatant transferred for LC-MS/MS analysis on a Waters Acquity UPLC/MS TQD system. Compound stability was evaluated on the basis of the corresponding peak areas plotted *vs* time. The compounds' half-lives were calculated using a one-phase fitting decay of the peak area *vs* time profiles.

***In vitro* mouse liver microsomes stability.** 10mM DMSO stock solution of test compound was pre-incubated at 37 °C for 15 min with liver microsomes (Sekisui Xenotech, LCC), 0.1M Tris-HCl buffer (pH 7.4), and 10% DMSO. The final concentration was 4.6  $\mu\text{M}$ . After pre-incubation, the cofactors (NADPH, G6P, G6PDH,  $\text{MgCl}_2$  pre-dissolved in 0.1M Tris-HCl) were added to the incubation mixture and the incubation was continued at 37 °C for 1h. At each time point (0, 5, 15, 30, 60 min), 30 $\mu\text{L}$  of incubation mixture was diluted with 200  $\mu\text{L}$  cold acetone spiked with 200 nM of warfarin as internal standard, followed by centrifugation at 3500 g for 30 min. The supernatant was further diluted with  $\text{H}_2\text{O}$  (1:1) for analysis. An aliquot of 200  $\mu\text{l}$  of the supernatant was removed, and the concentration of the test compound was quantified by LC-MS/MS. The percentage of the test compound remaining at



each time point relative to t=0 was calculated. The half-lives ( $t_{1/2}$ ) were determined by a one-phase decay equation using a non-linear regression of compound concentration vs time.

***In vitro* rat and human liver microsomes stability.** Rat (Gibco) or human (BD Gentest) hepatocytes were thawed in Hepatocyte Plating Supplement pack (Life Technologies) and placed in  $37 \pm 1$  °C shaking water. Hepatocytes were re-suspended in Williams E medium containing Cell Maintenance Supplement Pack (Life Technologies), and counted using Trypan blue solution to a final concentration of  $0.25 \times 10^6$  cells/mL. Samples of the test compound at 10  $\mu$ M were incubated for 0, 10, 30, 60, 120, and 240 min at 37 °C. Blank samples were prepared by incubating 250  $\mu$ l of cell solution without any compound for 240 min. The incubations were quenched 1:1 with ice-cold acetonitrile spiked with 600 nM labetalol as internal standard. Samples were then centrifuged at 12000 rpm for 5 min at 4 °C. Aliquots of 200  $\mu$ l of the supernatant were removed and the concentration of the test compound was quantified by LC-MS/MS. The percentage of the test compound remaining at each time point relative to t=0 was calculated. The half-lives ( $t_{1/2}$ ) were determined by a one-phase decay equation using a non-linear regression of compound concentration vs time.

***In vitro* off-target activity profiling.** An external contractor performed the study. The activity of 10  $\mu$ M ARN23746 as agonist or antagonist for several receptors, ion channels, enzymes, and transporters was assessed using validated assays under conditions defined by the contractor (<https://www.discoverx.com/services/drug-discovery-development-services/safetyscan-profiling>). A complete list of the off-targets evaluated is provided in the Appendix.

**Pharmacokinetic analysis.** An external contractor performed the study. Additional information on the study conditions can be obtained from the contractor's website (<https://www.pharmacologydiscoveryservices.com/>). ARN23746 and bumetanide were administered i.v at 2 mg/kg in phosphate buffered saline (PBS), pH 7.4, with 2% DMSO to adult C57BL/6 mice. Blood collection was performed by cardiac puncture at 0, 5, 15, 30, 60 and 120 minutes. Blood aliquots (300-400  $\mu$ L) were collected in tubes coated with lithium heparin, mixed gently, then kept on ice and centrifuged at 2500g for 15 minutes at 4°C, within 1 hour of collection. The plasma was then harvested

and stored frozen at (-70°C) until further processing. Immediately after the blood sampling, mice were decapitated and the whole brains were quickly removed, rinsed with cold saline (0.9 % NaCl, g/mL), surface vasculature ruptured, blotted with dry gauze, weighed, and kept on ice until further processing within 1 hour of collection. Each brain was homogenized in 1.5 mL cold phosphate-buffered saline (PBS), pH 7.4, for 10 seconds on ice. The brain homogenate from each brain was then stored at -70°C until further processing. The plasma and brain samples were then processed using acetonitrile precipitation and analyzed by LC-MS/MS. Plots of plasma/ brain concentration of the compound versus time were constructed. The fundamental pharmacokinetic parameters of each compound after dosing (AUC<sub>last</sub>, AUC<sub>inf</sub>, T<sup>1/2</sup>, Cl, V<sub>z</sub>, V<sub>ss</sub>, T<sub>max</sub>, and C<sub>max</sub>) were obtained from the non-compartmental analysis (NCA) of the plasma/ brain data using WinNonlin.

**Diuresis Analysis.** Diuresis analysis was performed taking advantage of mouse metabolic cages (Tecniplast,3600m021) that are equipped with a funnel and a plastic cone enabling the separation of urine and feces, and their collection. Right after i.p. treatment with vehicle, bumetanide or ARN23746 at 0.2 mg\*kg<sup>-1</sup>, animals were placed inside the metabolic cages (one animal for each cage) where free food and water were available. After two hours, mice were returned to their home cages and the volume of the urine was measured.

**Behavioral testing.** Ts65Dn male mice (2-4 months old) and VPA male mice (6-8 weeks old) were tested after 1 week of treatment with vehicle, ARN23746 or bumetanide (0.2 mg\*kg<sup>-1</sup> i.p.) by a battery of tests over a total period of 21-28 days. During the days of battery of behavioral tests, animals were treated daily with the drug, with tests beginning right after the first hour after the injection. The tasks were video-recorded and then analyzed manually by a blind operator. After each trial or experiment, the diverse apparatus and objects were cleaned with 70% ethanol. T-Maze. The T-maze is a black, opaque, plastic apparatus composed by a starting arm and two perpendicular goal arms each equipped with a sliding door. The T-maze test (spontaneous alteration protocol, 11 trials) evaluate the short-term memory by analyzing the correct choice of the unexplored arm. The test was performed similarly to what previously conducted on Ts65Dn mice<sup>204</sup>. In each trial, a mouse was first placed in the starting chamber for 20 seconds. Then, the sliding door was removed and the animal was free to explore the

apparatus. When the mouse entered (with all four limbs) in one of the two goal arms, the opposite arm was closed with the sliding door. When the mouse -free to explore the remaining part of the apparatus- returned to the starting area, the previously closed goal arm was opened. The trial was repeated 11 times. Entry into a goal arm opposite to the one previously chosen was considered as a correct choice, while entry into the previously explored arm was defined as non-correct choice. Alternation score was calculated as the percentage of correct choice (i.e., left-right or right-left) over the total number of the 10 possible alternations. Object Location test (OL). The test evaluates the spatial memory by measuring the ability of mice to recognize the new location of a familiar object. The test was performed in a grey acrylic arena (44x44 cm). Mice were first habituated to the chamber for 15 min on the day 1. The next day, during the acquisition phase mice were exposed to 2 identical objects for 15 min. After 24 hours, during the test session, one of the two objects was moved to a novel location and the mice were tested for their ability to recognize the new location of the object for 15 min. The time spent exploring each object was calculated by measuring the second when mice show investigative behavior (i.e., head orientation, sniffing occurring within < 1.0 cm) or clear contact the object with the nose. A discrimination index was calculated as the percent time spent investigating the object in the new location *minus* the percent time spent investigating the object in the old location [Discrimination Index = (New Object Location Exploration Time/Total Exploration Time X 100) – (Old Object Location Exploration Time/Total Exploration Time X 100)]. As control, we monitored object preference during acquisition phase and exploration time both in acquisition phase and trial phase. Of note, during the trial phase, Ts65Dn mice treated with ARN23746 showed a significant increase in exploration time, possibly indicative of a more explorative interest for the objects. Nevertheless, given that the exploration of the single object was normalized on the total exploration time for each group, the increased exploration in Ts65Dn mice treated with ARN23746 did not affect the results on the discrimination index in the test. Novel Object recognition test (NOR). The test evaluates the long-term object recognition memory by measuring the ability of mice to recognize a new object respect to the familiar ones. The test was performed in a grey acrylic arena (44x44 cm). In the first day, mice were habituated to the arena by freely exploring the chamber for 15 minutes. The second day during the acquisition phase mice were free to explore 3 different objects (different in color, size, shape, and

material) for 15 min. After 24 hours, one of the objects used during the acquisition phase, was replaced with a novel object and the mice were tested for their ability to recognize the new object for 15 min. The time spent exploring each object was calculated by measuring the second when mice show investigative behavior (*i.e.*, head orientation, sniffing occurring within < 1.0 cm) or clear contact the object with the nose. The time spent exploring each object, expressed as a percentage of the total exploration time, was measured for each trial. The discrimination index was calculated as the difference between the percentages of time spent investigating the novel object and the time spent investigating the familiar objects:  $\text{discrimination index} = (\text{novel object exploration time} / \text{total exploration time} * 100) - (\text{familiar object exploration time} / \text{total exploration time} * 100)$ . As control, object preference during acquisition phase and exploration time were monitored both in acquisition phase and trial phase. *Contextual fear conditioning test (CFC)*. The test evaluates the long-term associative memory by measuring the freezing time of the animals placed in a location where 24 hours before they received an adverse stimulus (electric shock). The experiments were performed in a fear conditioning system (TSE), which is a transparent acrylic conditioning chamber (23x23 cm) equipped with a stainless-steel grid floor. Mice were placed outside the experimental room in their home cages before the test and individually transported to the TSE apparatus in standard cages. Mice were placed in the conditioning chamber and they received one electric shock (2s, 0.75mA constant electric current) through the floor grid 3 minutes later. Mice were removed 15 s after the shock. 24 hours later, mice were placed in the same chamber for 3 minutes and after 2 hours they were moved to a new context (black chamber with plastic gray floor and vanilla odor). The time spent to freeze was scored and expressed as percentage of the total time analyzed. *Three-chamber test*. The test evaluates the social approach of the tested mouse *vs* a never-met-intruder in comparison to an object (sociability) or *vs* a novel never-met-intruder in comparison to the already met intruder (social novelty), and it was performed similarly to what previously described in mouse models of ASD<sup>205,206</sup>. The three-chamber apparatus consists in a rectangle, three-chambered box of grey acrylic. The chambers are accessible by rectangle openings with sliding doors. In the first 10 minutes (habituation) the tested mouse was free to explore the apparatus containing two inverted stainless-steel wire pencil cups (one in each of the two side chambers), with a weighted plastic cup on the top of them, to prevent the mouse climbing on

the top. Then, the tested mouse was briefly confined in the center chamber while a never-met-intruder (previously habituated to the apparatus) was placed in one of the side chambers, under the pencil cup. For the following 10 minutes (sociability test), the tested mouse was allowed to explore all the three chambers. Then, the tested mouse was again briefly confined in the center chamber while a novel never-met-intruder (previously habituated to the apparatus) was placed in the other side chamber under the pencil cup. Thus, for the following 10 minutes (social novelty test) the tested mouse was allowed to explore all the three chambers. The time spent exploring the object or the intruder was calculated by measuring the second when the mice showed investigative behavior (*i.e.*, head orientation, sniffing occurring within < 1.0 cm). The sociability index was calculated as the difference between the time spent investigating the never-met-intruder and the time spent investigating the familiar object divided by the total exploration time: sociability index = (never met intruder exploration time - object exploration time) / (never met intruder exploration time + object exploration time). The social novelty index was calculated as the difference between the time spent investigating the novel never-met-intruder and the time spent investigating the already met intruder divided by the total exploration time: social novelty index = (novel never met intruder exploration time - already met intruder exploration time) / (novel never met intruder exploration time + already met intruder exploration time). *Male-female interaction test.* The test evaluates the social approach of the tested mouse vs a never-met-female mouse and it was performed similarly to what previously described in mouse models of ASD<sup>207</sup>. Briefly, the tested mouse was placed singularly in a cage (26 cm × 48 cm × 20 cm). After 5 minutes of habituation, an unfamiliar C57BL/6J female mouse was placed into the home-cage of the isolated male mouse, and behavior was recorded for a 5-min test session. The time spent interacting with the female intruder was calculated by measuring the second when the mice showed any of the following interacting behavior: anogenital sniffing, body sniffing, head sniffing, following and mounting. *Marble burying test.* The test evaluates the repetitive behavior as the tendency to dig and bury marbles in a novel environment, and it was performed as already described in ASD mice<sup>206,208</sup>. Briefly, mice were placed singularly in a cage (26 cm × 48 cm × 20 cm) filled with 4 cm fresh mouse bedding material. After 30 minutes habituation, the mouse was briefly removed and bedding surface was leveled to place 15 glass marbles equidistantly distributed in a 3 × 5 arrangement. Then, the mouse was returned to the

cage and allowed to explore for 30 min. The number of marbles covered at least two-thirds were counted as buried. Grooming. The test evaluates the repetitive behavior as the mouse grooming activity of all body parts, and it was performed as already described in ASD mice <sup>209</sup>. Self-grooming was defined as licking or scratching, head or body parts with any of the forelimbs. Briefly, mice were placed individually into a clear Plexiglass cylinder (30 cm high, 10 cm wide). After 10 minutes of habituation, the mouse was scored during 5 minutes for the time spent performing self-grooming in all body regions.

**Viscera Index and Histological Analysis.** Ts65Dn animals were analyzed after 28 days of treatment with vehicle or ARN23746 at 0.2 mg\*kg<sup>-1</sup> concentration. Liver, kidney, spleen, lungs and brain samples were excised and weighted to calculate the viscera index, which we used to evaluate hyperplasia, swelling, or atrophy of different organs potentially induced by ARN23746 treatment. Viscera Index = (Visceral weight (g) / Mouse weight (g)) \*100. Then, liver, kidney and spleen samples were fixed in 10% formalin solution and embedded in paraffin. Serial sections of 5- $\mu$ m thickness were obtained and stained with Hematoxylin&Eosin (H&E) to evaluate morphology and analyzed with a Leica DM5500 optical microscope (n=5 each group). The results were examined in blind.

## Chapter 5. Design, synthesis and characterization of ARN23746 derivatives.

### 5.1 Rationale.

In order to further explore the chemical class represented by our lead compound ARN23746, and find novel derivatives suitable for additional *in vivo* characterization, we designed and synthesized a series of analogues, obtained by manipulation of various parts of the molecule (Figure 5.1). However, since the trifluoro *n*-octyl chain resulted to be pivotal for potency and stability, we conserved this structural motif throughout the development of this chemical class.

Firstly, we explored two replacements of the carboxylic group in R<sup>1</sup>, namely the nitrile and the bioisosteric 1H-tetrazole derivatives. The nitrile derivative could produce a substantially different stereoelectronic effect compared to the carboxylic acid. In addition, this moiety can provide polar interactions with little steric demand, while suppressing an acidic function could lead to higher brain penetration. The 1H-tetrazole is a well-known bioisostere of the carboxylic acid<sup>210-212</sup>. This is a planar acidic heterocycle with similar range of pK<sub>a</sub> (tetrazole 4.5–4.9 vs carboxylic acid 4.2–4.4), size and electrostatic potential compared to the carboxylic acid. Therefore, it often undergoes very similar receptor–ligand interactions<sup>212</sup>. Importantly, this heterocycle has increased lipophilicity due to the presence of the nitrogen atoms, as 1H-tetrazoles are almost 10 times more lipophilic than the corresponding carboxylates when ionized at physiological pH (~7.4), resulting in higher membrane and, possibly, BBB permeability<sup>212</sup>.

Then, we selected the sulfonamide group in R<sup>5</sup> for additional modifications, as we designed a series of sulfonamides diversely substituted with cyclic and cycloalkylic substituents. In particular, we inserted five and six membered rings to understand the importance of the bulkiness in this position, compared to the dimethyl sulfonamide. For example, we compared pyrrolidine and piperidine, which preserve the HBA feature of the tertiary sulfonamide of ARN23746, but provide higher bulk and different ring flexibility. The cyclic sulfonamides were compared with the corresponding cycloalkylic ones to evaluate the combination between steric hindrance and the presence of the secondary sulfonamide. In addition, we evaluated the insertion of a morpholine to study the effect of a polar atom in the ring and

compared it with the corresponding tetrahydro-2H-pyran-4-amine. In addition, we prepared also the *N*-methyl sulfonamide analogue that we found to be a possible metabolite of ARN23746 *in vivo*. This was done in order to understand if the compound could retain activity after metabolization.

Finally, to investigate the presence of a supplementary substituent anchored to the central core, we decided to exploit the chemically accessible position 2 on the aromatic ring by the insertion of different moieties. In R<sup>2</sup>, we evaluated the effect of a chlorine, a hydroxyl group and different short alkyl ethers. These substituents will give us important preliminary information on the group tolerance in this position, which we could manipulate in the future to enhance chemico-physical properties while preserving or boosting potency.

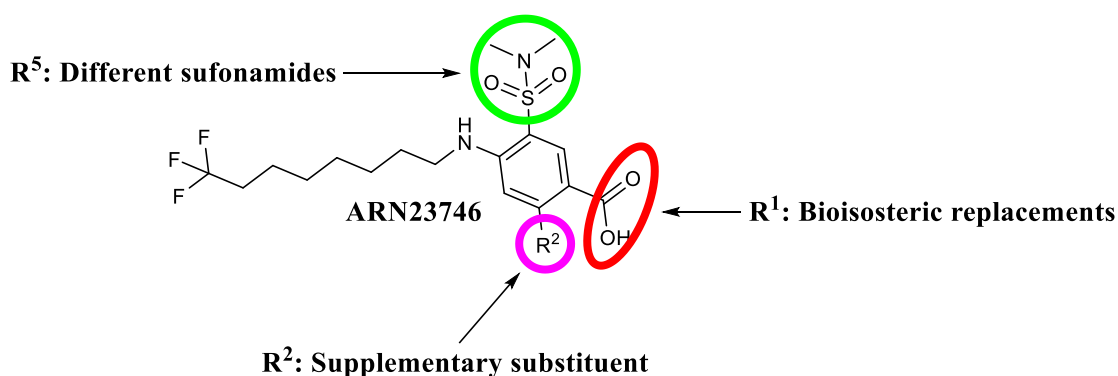
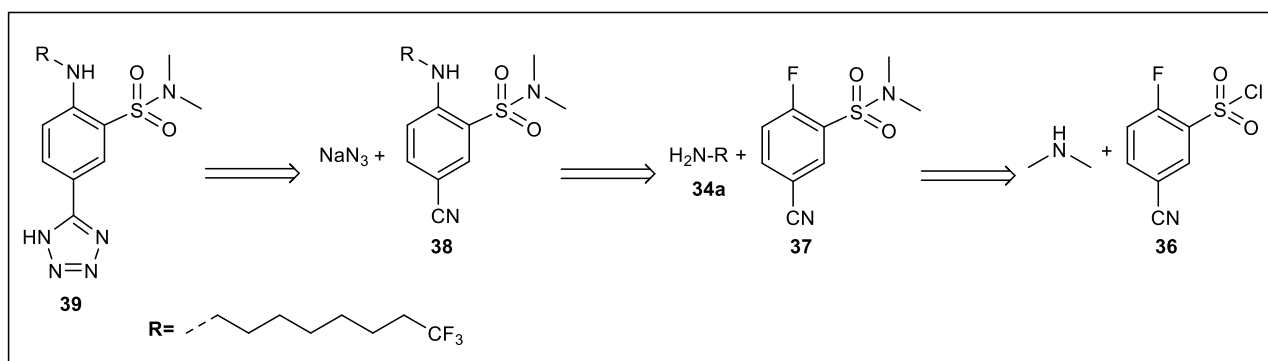


**Figure 5.1.** Schematic representation of the points subject to modification in the ARN23746 structure.

### 5.1.1 Synthesis of bioisosteric analogues of the carboxylic moiety of ARN23746.

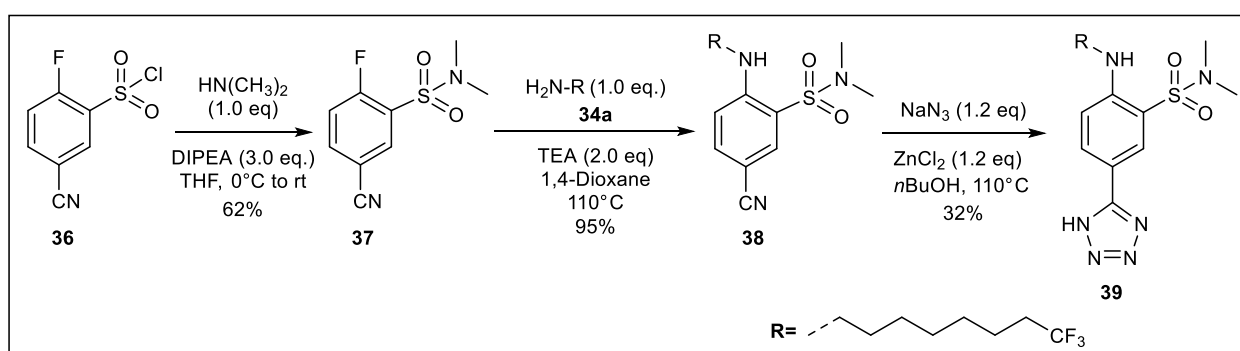
As depicted in Scheme 5.1 we retrosynthetically envisioned the target bioisosteric analogues of ARN23746 by cycloaddition of the nitrile group of intermediate **38** with an azide to obtain the 1H-tetrazole analogue **39**. Nitrile substituted analogue **38** could be assembled via nucleophilic aromatic substitution of **37** with amine **34a**. The key intermediate **37** could be generated by substitution of the chlorosulfonyl group with dimethylamine of commercial 5-cyano-2-fluoro-benzenesulfonyl chloride **36**. Notably, this retrosynthetic scheme could allow obtaining both the desired derivatives via a single linear synthetic procedure.





**Scheme 5.1.** Retrosynthetic approach towards the synthesis of the carboxylic acid bioisosteric analogue of ARN23746.

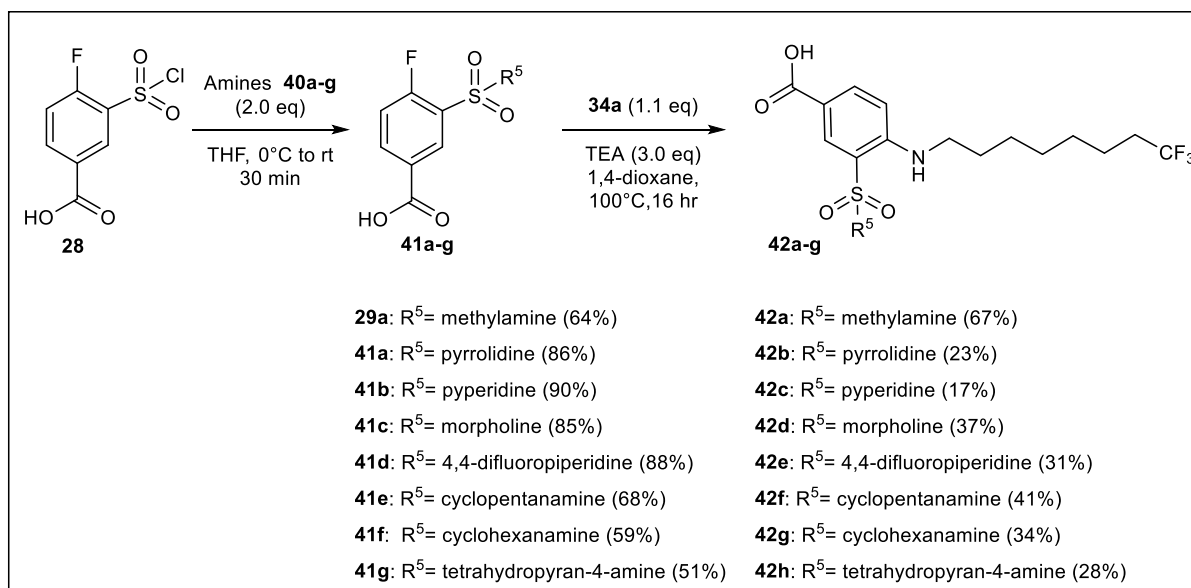
As depicted in Scheme 5.2, our synthesis started by reacting commercial **36** with 1 equivalent of dimethylamine in the presence of 3.0 equivalents of DIPEA used as additive base. Addition of DIPEA resulted to be crucial to afford **37**, as previous attempts using excess dimethylamine only the disubstituted product was generated, due to high activation of the fluorine in position 2. With this methodology **37** was obtained in a good 62% yield after chromatographic purification. Then nucleophilic aromatic substitution with amine **34a** occurred efficiently to afford compound **38** in high 95% yield. Subsequently, nitrile group of **38** was converted to 1H-tetrazole via zinc-catalyzed cycloaddition of sodium azide in *n*-butanol following a literature procedure<sup>213</sup>. Although the reaction proceeded in an efficient manner, yield turned out to be modest due to complicated workup to eliminate the zinc salts formed during the reaction.



**Scheme 5.2.** Synthesis of carboxylic acid bioisosteric analogue of ARN23746.

### 5.1.2 Synthesis of substituted sulfonamide derivatives.

We took advantage of the same synthetic procedure described in chapter 3 (Scheme 3.7) for the exploration of different sulfonamides in position R<sup>5</sup>. For the first step of substitution of chlorosulfonyl group of commercial **28**, two different methodologies were applied depending on the amine used (Scheme 5.3). Amines (**40a-c, e-g**) commercially available as free base have been used without addition of any base, while amine hydrochloride **40d** was reacted with **28** in the presence of 3.0 equivalents of DIPEA. The substitution reaction afforded the selected *N*-substituted sulfonamide **41a-g** building blocks in good yields. Interestingly, the cyclic secondary amines **40a-d** gave substantially higher yields when compared to the primary cycloalkyl amines **40e-g**, as the latter were more prone to form disubstituted by-products due to their higher reactivity. Nevertheless, the desired products were easily obtained by precipitation, a work-up that nicely removed the disubstituted by-products. Finally, nucleophilic aromatic substitution with amine **34a** yielded the target final compounds **42a-h**.

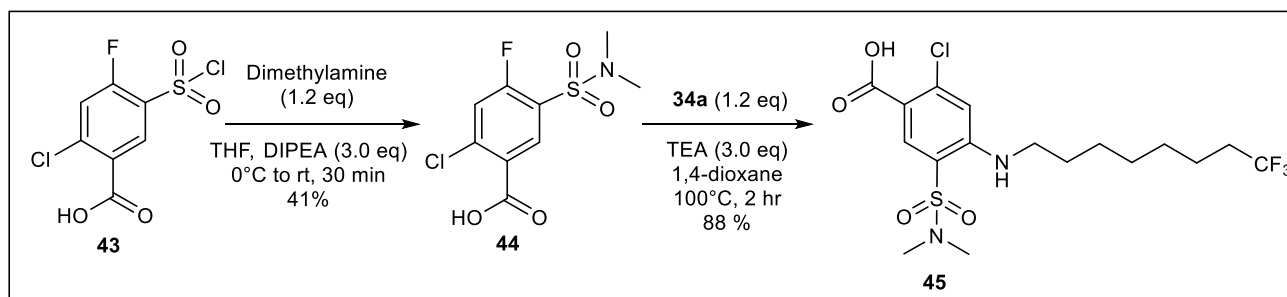


Scheme 5.3. Synthesis of substituted sulfonamide derivatives of ARN23746.

### 5.1.3 Synthesis of R<sup>2</sup> substituted analogues

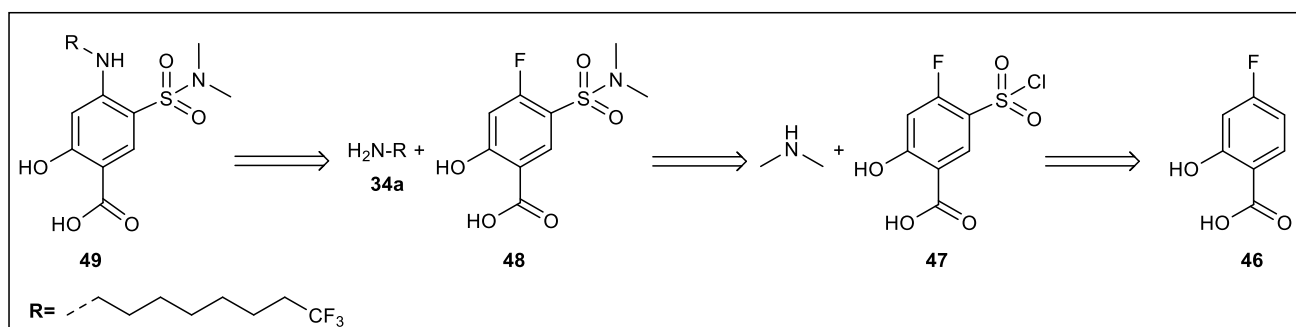
We first approached the synthesis of the 2-chloro derivative **45** (Scheme 5.4) by taking advantage of the synthetic sequence of dimethylsulfonamide generation and subsequent nucleophilic aromatic substitution (Scheme 5.4). In the first step, we reacted commercial 2-chloro-5-chlorosulfonyl-4-fluoro-

benzoic acid **43** with dimethylamine in the presence of 3.0 eq of DIPEA. Surprisingly, the addition of the base was unable to avoid the collateral substitution of the fluorine in position 4 in this case. Thus, intermediate **44** was isolated in a modest 41% yield after chromatographic purification. Consequently, the highly activated position 4 reacted efficiently in the nucleophilic aromatic substitution step with amine **34a** to afford compound **45** in high yield.



**Scheme 5.4.** Synthesis of the 2-chloro derivative of ARN23746.

For the synthesis of the 2-hydroxy and 2-alkoxy analogues we firstly approached the retrosynthesis of the hydroxyl derivative **49** (Scheme 5.5), with the aim to use it as starting point for the subsequent generation of the alkyl ethers in position 2. The target compound **49** could be prepared by nucleophilic aromatic substitution step with amine **34a** of the key intermediate **48**, which in turn could be obtained by substitution of the chlorosulfonyl group of **47** with dimethylamine. Finally, **47** could be assembled by electrophilic aromatic substitution with chlorosulfonic acid of commercial 4-fluoro-2-hydroxybenzoic acid **46**.

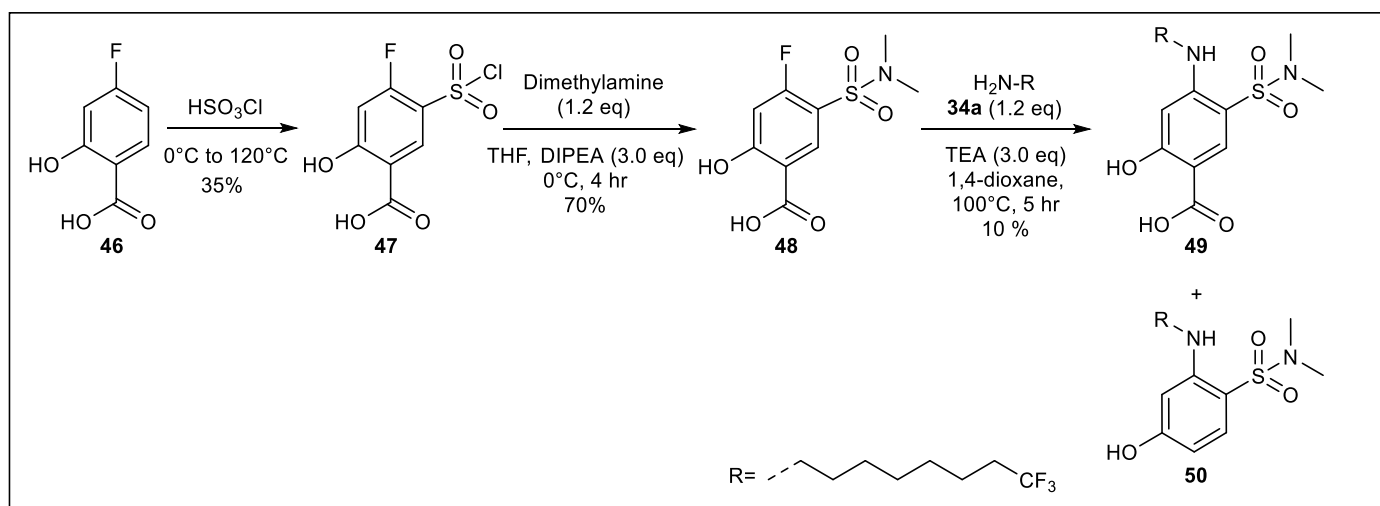


**Scheme 5.5.** Retrosynthetic approach for the preparation of 2-hydroxy analogue of ARN23746.

As shown in Scheme 5.6, synthesis started by performing the electrophilic aromatic substitution on **46** with chlorosulfonic acid. The reaction occurred in a regioselective manner, although in low yields due to decomposition of the starting material in the reaction conditions.

Subsequently, **47** was reacted with dimethylamine with the addition of 3.0 equivalent of DIPEA to afford the 5-dimethyl sulfonamide intermediate **48** in good yields. Strikingly, in the last step of nucleophilic aromatic substitution the desired product **49** was isolated in a very low 10% yield due to massive formation of decarboxylated by-product **50**. This secondary reaction probably occurred due to the high electron density of the ring caused by the insertion of the amino group in the *para* position<sup>214</sup>, combined with the presence of the hydroxyl group in *ortho*. Especially the latter one establishes an intramolecular H-bond with the carboxylic acid favouring the decarboxylation side reaction upon heating.

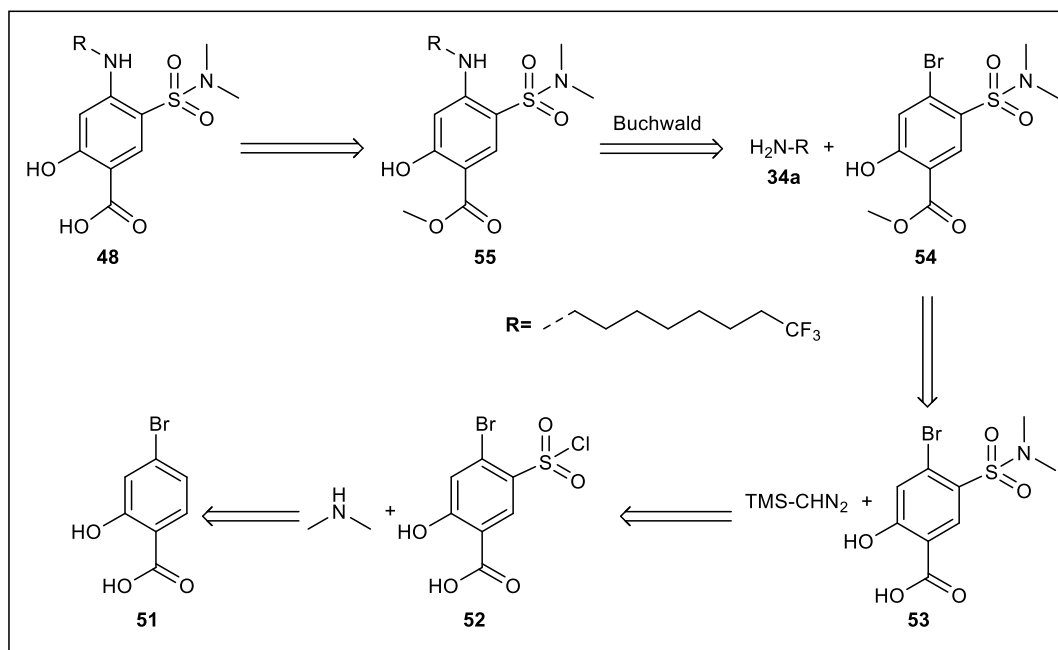
Although it was possible to isolate the target analogue, this synthetic route did not provide an acceptable yield to exploit it for the construction of further analogues bearing alkoxy substituents in position 2. Thus, we decided to move to a different synthetic strategy.



**Scheme 5.6.** Synthesis of 2-hydroxy analogue of ARN23746.

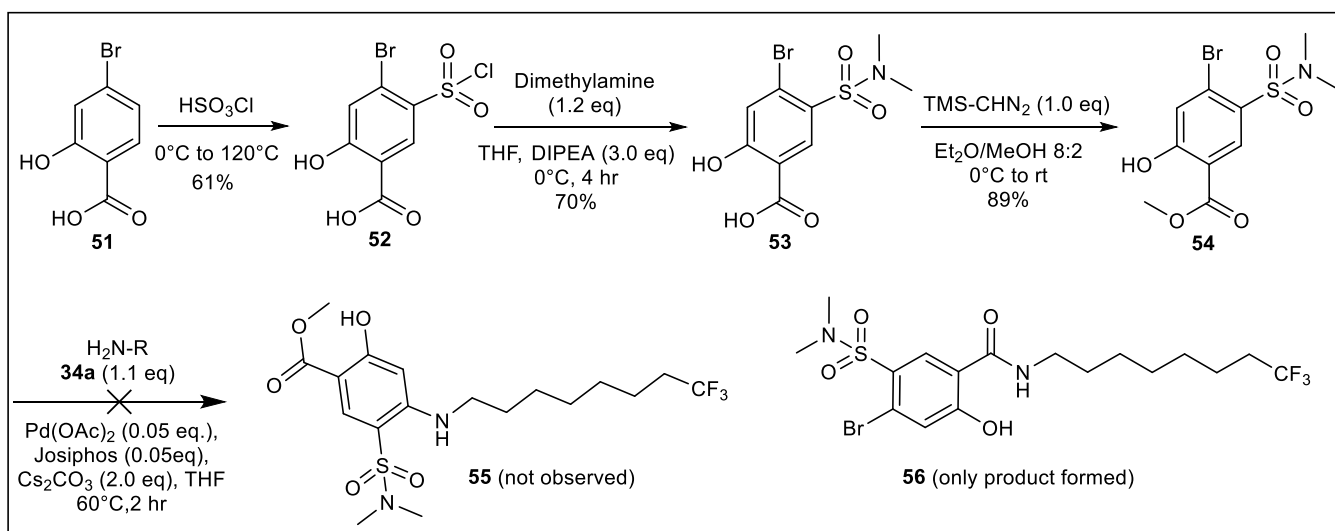
To avoid decarboxylation, we sought to mask the carboxylate formation by esterification of the carboxylic acid. Product **49** could be thus obtained by hydrolysis of methyl ester derivative **55** (Scheme 5.7), which was prepared by insertion of the amine in position 4 via palladium catalysed Buchwald-Hartwig cross coupling reaction on the corresponding 4-bromo building block **54**, as this strategy could

allow running the reaction under milder temperature conditions, compared to the nucleophilic aromatic substitution. Methyl ester **54** could be synthesized by regioselective methylation of the carboxylic acid of **53** with trimethylsilyldiazomethane (TMS-CHN<sub>2</sub>), which in turn could be obtained by substitution of the chlorosulfonyl group of **52** with dimethylamine. Finally, **52** could be prepared by electrophilic aromatic substitution with chlorosulfonic acid of commercial 4-bromo-2-hydroxy-benzoic acid **51**.



**Scheme 5.7.** Retrosynthesis of the 2-hydroxy analogue of ARN23746 via Buchwald-Hartwig cross coupling.

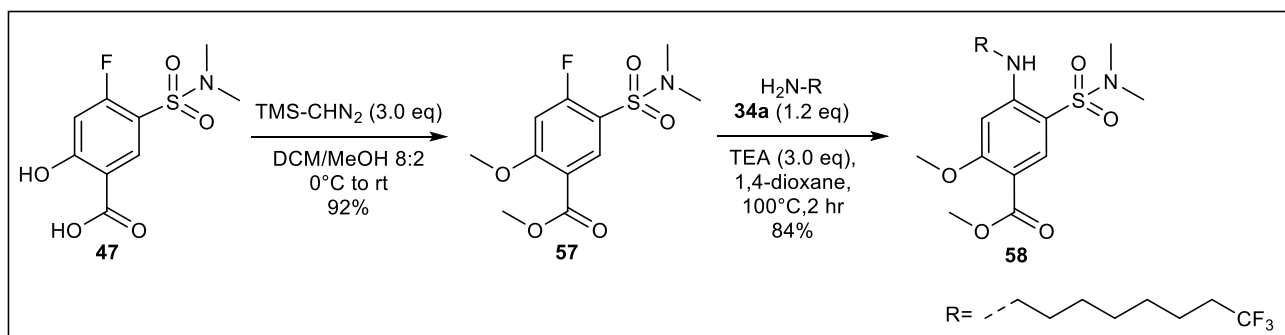
As described in Scheme 5.8 synthesis started by electrophilic aromatic substitution of commercial **51**, which afforded intermediate **52** with a good 61% yield. Subsequent substitution of the chlorosulfonyl group with dimethylamine in the presence of DIPEA gave access to intermediate **53**. Then, methylation of the carboxylic acid of **53** with TMS-CHN<sub>2</sub> efficiently yielded the methyl ester **54** in an excellent 89% yield. We then used Buchwald-Hartwig cross coupling key reaction to insert the anime in position 4, using palladium acetate and Josiphos ligand. Surprisingly, we observed only the formation of the amide by product **56** already when the reaction was ran at 60°C. This kind of reactivity may be ascribable to the presence of the free phenol, which enhanced the ester electrophilicity through an intramolecular H-bond. Thus, also this second approach was not suitable to access the desired compounds.



**Scheme 5.8.** Synthesis of the 2-hydroxy analogue of ARN23746 via Buchwald-Hartwig cross coupling.

We thus moved back to the nucleophilic aromatic substitution protocol. In this case, since both the phenol and the carboxylic acid acidity seemed to be crucial in the occurring of secondary reactions we decided to protect both the groups via methylation (Scheme 5.9). The two methyl groups can be then removed by orthogonal deprotection to access different kind of substrates, in particular compound **59** (Scheme 5.10), which is a suitable intermediate for phenol functionalization via alkylation, or Chan-Lam reaction.

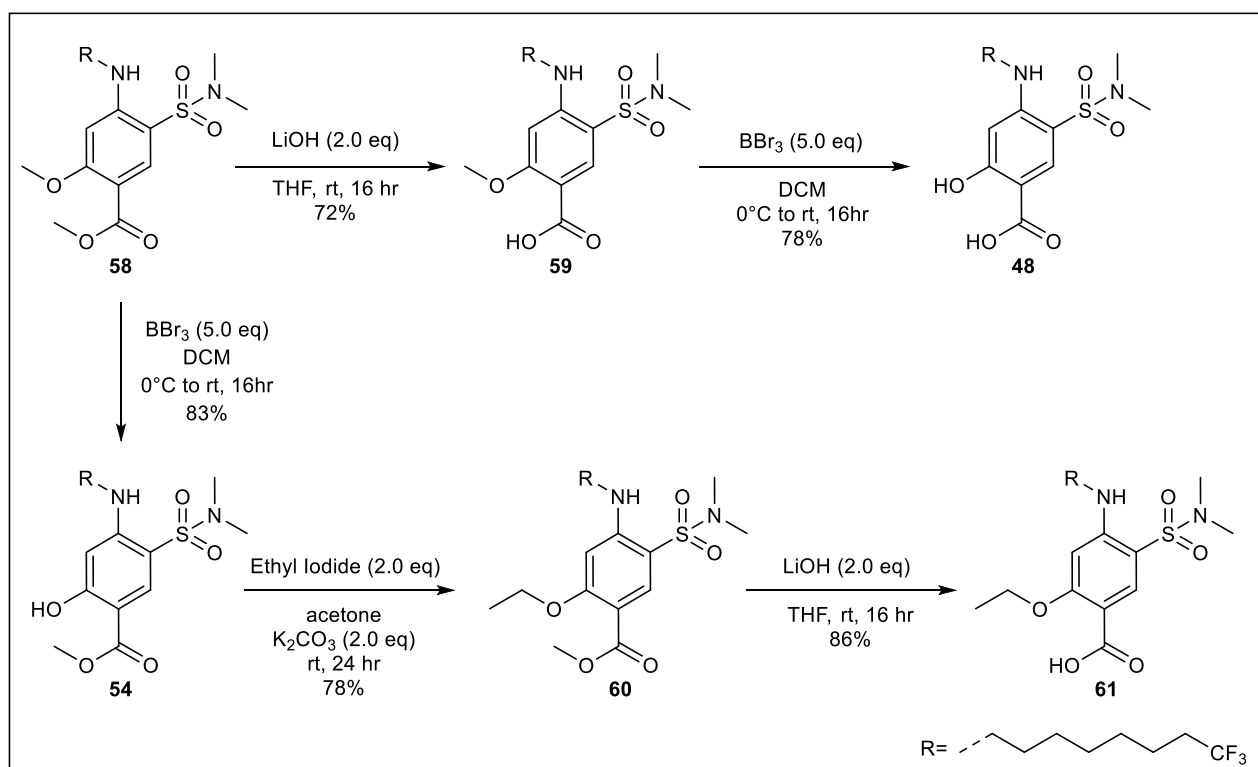
As described in Scheme 5.9, we synthesised the dimethylated intermediate **57** by reacting **47** with an excess of TMS-CHN<sub>2</sub>, which resulted in both methylation of the acid and phenol in an excellent 92% yield. Subsequent nucleophilic aromatic substitution smoothly afforded compound **58** without the formation of any by-product.



**Scheme 5.9.** Synthesis of intermediate **58**.

Intermediate **58** was then used in a first route to generate the 2-methoxy analogue **59** via ethyl ester hydrolysis with lithium hydroxide (Scheme 5.10). Then, demethylation of the phenol with an excess of boron tribromide afforded the 2-hydroxy analogue **48** in high yields.

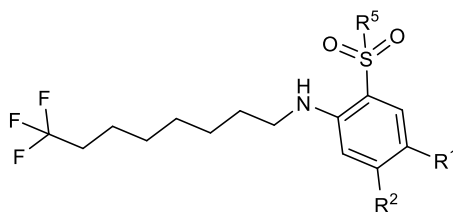
Conversely, intermediate 2-hydroxy methyl ester **54** was smoothly generated by demethylation of the methoxy group of **58** with boron tribromide. Then, the hydroxyl group of **54** was alkylated with ethyl iodide in good yields to afford **60**. Final deprotection of the acid afforded then the target 2-ethoxy derivative **61**.



**Scheme 5.10.** Synthesis of 2-alkoxy derivatives of ARN23746.

## 5.2 Results and discussion.

These new analogues were tested for their inhibitory activity at two concentrations (10  $\mu\text{M}$  and 100  $\mu\text{M}$ ) and compared to ARN23746 in the  $\text{Ca}^{2+}$  assay, in cultured immature neurons. In addition, all the compounds were characterized *in vitro* for their kinetic solubility, stability in mouse liver microsomes and plasmatic stability in mouse plasma. This allowed us to determine the effect of the substitutions on the drug-like properties of the scaffold. Results are summarized in Table 5.1.



Entry	R <sup>1</sup>	R <sup>2</sup>	R <sup>5</sup>	10 μM Ca <sup>+</sup> Flux <sup>a</sup>	100 μM Ca <sup>+</sup> Flux <sup>a</sup>	Kinetic sol. PBS <sup>b</sup>	t <sub>1/2</sub> liver <sup>c</sup>	t <sub>1/2</sub> plasma <sup>d</sup>
ARN23746	COOH	H	N(CH <sub>3</sub> ) <sub>2</sub>	45.7 ± 4.3 %	92.8 ± 1.9 %	>250 μM	>60 min	>120 min
38	CN	H	N(CH <sub>3</sub> ) <sub>2</sub>	No inhibition	No inhibition	<1 μM	<5 min	>120 min
39		H	N(CH <sub>3</sub> ) <sub>2</sub>	n.a	n.a	>250 μM	>60 min	>120 min
42a	COOH	H	HNCH <sub>3</sub>	13.8 ± 6.1 %	45.9 ± 18.8 %	242 μM	>60 min	>120 min
42b	COOH	H		39.6 ± 16.2 %	46.9 ± 17.5 %	66 μM	>60 min	>120 min
42c	COOH	H		54.8 ± 17.2 %	n.a (prec.) <sup>e</sup>	13 μM	>60 min	>120 min
42d	COOH	H		24.0 ± 14.8 %	74.3 ± 11.6 %	244 μM	>60 min	>120 min
42f	COOH	H		50.8 ± 21 %	56.5 ± 14.8 %	223 μM	>60 min	>120 min
42g	COOH	H		53.9 ± 18.5 %	n.a (prec.) <sup>e</sup>	9 μM	>60 min	>120 min
45	COOH	Cl	N(CH <sub>3</sub> ) <sub>2</sub>	25.6 ± 11.8 %	64.7 ± 22.4 %	241 μM	>60 min	>120 min
49	COOH	OH	N(CH <sub>3</sub> ) <sub>2</sub>	24 ± 8.3 %	54.5 ± 12.1 %	>250 μM	>60 min	>120 min

**Table 5.1. Inhibitory activity and drug-like properties of ARN23746 analogues.** *a*, Inhibition percentage in calcium-kinetic fluorescent assay in cultured neurons. *b*, Aqueous kinetic solubility of compounds from a 10mM DMSO solution in Phosphate Buffered Saline (PBS) at pH 7.4. Target concentration is 250μM (final DMSO 2.5%). *c*, Stability in mouse liver homogenates. *d*, Stability in mouse plasma at 37°C. Compounds were incubated at 5 μM (final DMSO 0.1%). *e*, precipitation observed in the assay buffer.

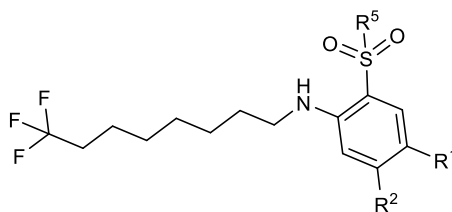


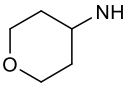
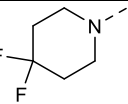
The replacement of the carboxyl moiety with a nitrile resulted in a complete loss of activity of compound **38**, further highlighting the importance of the presence of the ionizable carboxylic acid in position 1. In addition, this modification led to generally unfavourable drug like properties, decreasing both solubility and metabolic stability (Table 5.1). Instead, insertion of 1H-tetrazole of analogue **39** preserved optimal drug-like profile. However, it was not possible to test this compound as its fluorescence interfered with the assay's readout. To evaluate its activity, we are currently developing a dedicated assay through patch-clamp electrophysiological recording.

The corresponding *N*-methyl sulfonamide analogue **42a** displayed a marked decrease in inhibitory activity towards NKCC1, consistently with our previous results on the other *N*-methyl analogues (Table 3.4, Chapter 3). Remarkably, the compound **42a** retained acceptable activity, opening new avenues for its possible activity *in vivo* as an active metabolite of ARN23746. Interestingly, the insertion of a five membered cyclic sulfonamide in analogue **42b** was tolerated, but resulted in a reduction in activity at 100  $\mu$ M. We then did not observe a substantial difference in activity between the pyrrolidine **42b** and the piperidine **42c** at 10  $\mu$ M when compared to ARN23746. These results suggest that the substituted sulfonamide may interact with NKCC1 in a site where the nitrogen atom forms a key H-bond acceptor interaction orientating the group attached to the sulfonamide in a lipophilic pocket, with tolerance for bulkier groups compared to the dimethyl of ARN23746, and thus provide supplementary stacking interactions. However, the introduction of these two substituents led to a dramatic decrease in solubility of compounds **42b** and **42c**, while having no effect on the other drug-like properties screened. This drawback allowed only the testing at 10  $\mu$ M of **42c**. Unexpectedly, the polar morpholine derivative **42d** retained activity at 10  $\mu$ M, although lower than ARN23746, while showing good inhibitory activity at 100  $\mu$ M. In addition, the presence of the oxygen atom resulted in a substantially higher solubility compared to the aliphatic piperidine **42c**. Derivative **42d** showed also excellent metabolic and plasmatic stability, making it a promising analogue for further characterization. When we evaluated the two cycloalkyl derivatives **42f** and **42g**, we observed an effect comparable to the one of corresponding cyclic amines at 10  $\mu$ M, suggesting that the nitrogen atom in the secondary sulfonamide may interact in a similar manner establishing a H-bond acceptor interaction. The cyclopentane analogue **42f** did not display a substantial boost in activity at 100  $\mu$ M, while insertion

of cyclohexyl **42g** resulted in very low solubility of the compound hampering its testing at high concentrations.

The addition of a fourth substituent on the 2-substituted analogues **45** and **49** returned lower activity when compared to ARN23746. Nevertheless, these compounds retained similar activity despite the nature of the substituent inserted, as the presence of the more lipophilic chlorine atom of **45** resulted only in a slight increase in inhibitory activity compared the hydrophilic hydroxyl group of **49**, while the two displayed the same activity at 10  $\mu$ M. This suggests a wide tolerability of substituents in this position, which could lead to a better activity. In addition, these two compounds displayed favourable drug-like properties. In particular, the insertion of the chlorine atom minimally harmed the solubility of **45** compared to the target value, opening the way to the design of soluble lipophilic more brain penetrant analogues. Unfortunately, the remaining compounds **42e**, **42h**, **59**, **61** are currently pending for testing as they were lately synthesized. Structures are summarized in Table 5. 2.



Entry	R <sup>1</sup>	R <sup>2</sup>	R <sup>5</sup>
ARN23746	COOH	H	N(CH <sub>3</sub> ) <sub>2</sub>
41h	COOH	H	
41e	COOH	H	
59	COOH	OMe	N(CH <sub>3</sub> ) <sub>2</sub>
61	COOH	OEt	N(CH <sub>3</sub> ) <sub>2</sub>

**Table 5.2.** ARN23746 analogues pending for testing.

In conclusion, we synthesised 14 new analogues of ARN23746. We could test 10 of these, and the majority of these compounds retained activity on NKCC1. Overall, ARN23746 remained our best lead, with the highest potency. Nevertheless, the evaluation of these new derivatives provided us crucial information on substituents and their effect on drug-like properties. We found that cyclic and cycloalkylic sulfonamides are tolerated in terms of activity, but can have a drastic effect on solubility, which could be overcome by insertion of a morpholine in this position. We confirmed the importance of the presence of the carboxylic group in position 1 and investigated the insertion of a fourth substituent in position 2. This retained some inhibitory activity, although lower on NKCC1 compared to our lead. However, this latter position has now opened new possibilities for the design and synthesis of a number of additional analogues. Notably, all the derivatives bearing the carboxylic group displayed excellent microsomal and plasmatic stability, indicating a favourable drug-like profile of this chemical class. In addition, we identified the morpholine derivative **42d** as a suitable compound for further characterization, and backup compound generation.

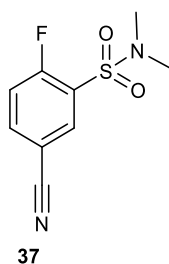
Taken together, this effort allowed us to gain a better understanding of the chemical class, suggesting additional possibilities of intervention at various points of the scaffold. Based on these results, we are currently planning the design and synthesis of additional promising derivatives, as backup and follow-up compounds of our lead compound ARN23746.

### 5.3 Experimental section.

**Chemistry** (see Chapter 2, section 2.4 for general information):

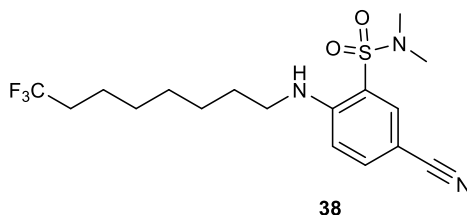
**General procedure A for the synthesis of sulfonamides 41a-g (Scheme 5.3).** 4-Fluoro-3-chlorosulfonyl-benzoic acid **28** (1 mmol) solved in 2 mL of THF was added dropwise to 8 mL of an ice cold solution of the proper amine (3 mmol) in THF and stirred for 1 hour at rt. At reaction completion the reaction mixture was evaporated to dryness and the residue treated with water and HCl. The precipitated product was filtered and rinsed with water to afford the pure titled compounds.

**General nucleophilic aromatic substitution procedure C for the synthesis of compounds derivatives 38, 42a-e, 44, 57 (Scheme 5.2, 5.3, 5.4, 5.9).** A suspension of the appropriate intermediate (1 mmol) and amine **34a** (1.1 mmol) in dry 1,4-dioxane (3 ml) was stirred under argon atmosphere at 100°C for 16 hours. After reaction completion the mixture was evaporated to dryness at low pressure and the residue was treated with a saturated NH<sub>4</sub>Cl aqueous solution (15 ml) and extracted twice with EtOAc (2 x 15 ml). The combined organic layers were dried over Na<sub>2</sub>SO<sub>4</sub> and concentrated to dryness at low pressure. Purification by silica gel flash chromatography with CH<sub>2</sub>Cl<sub>2</sub>/MeOH followed by trituration with a suitable solvent (cyclohexane or diethyl ether) afforded finally the pure title compounds.

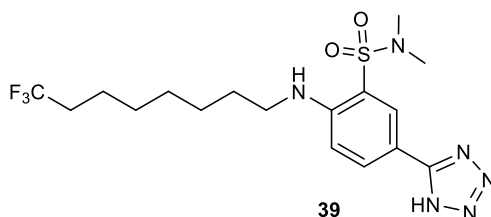


**5-cyano-2-fluoro-N,N-dimethyl-benzenesulfonamide (37).** 5-cyano-2-fluorobenzene-1-sulfonyl chloride **36** (300 mg, 1.35 mmol) solved in 3.5 mL of THF was added dropwise to an ice cold solution of 2 M dimethylamine in THF (0.74 ml, 1.49 mmol) and *N,N*-diisopropylethylamine (0.48 ml, 2.70 mmol) in 10 ml of THF and then stirred for 30 minutes at rt. At reaction completion the reaction mixture was evaporated to dryness and the residue was portioned between EtOAc (50 ml) and water (50 ml)

and the layers were separated. The organic layer was dried over Na<sub>2</sub>SO<sub>4</sub> and concentrated to dryness at low pressure. Purification by silica gel flash chromatography (cyclohexane/DCM + 1% EtOAc 70:30 to 30:70) afforded the pure **37** (194.2 mg, 63 % yield) as a white solid.: <sup>1</sup>H NMR (400 MHz, Chloroform-*d*) δ 8.20 (dd, *J* = 6.2, 2.2 Hz, 1H), 7.87 (ddd, *J* = 8.6, 4.4, 2.2 Hz, 1H), 7.36 (t, *J* = 8.9 Hz, 1H), 2.89 (d, *J* = 1.9 Hz, 6H).

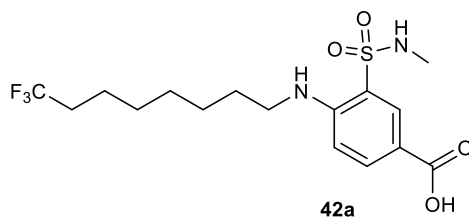


**5-cyano-*N,N*-dimethyl-2-(8,8,8-trifluorooctylamino)benzenesulfonamide (38)**. Title compound was synthesized following the general procedure **B** previously described using intermediate **37** (194 mg, 0.84 mmol) and amine **34a** (311.5 mg, 1.64 mmol) in dry 1,4-dioxane (4.2 ml). Trituration with diethyl ether (3 ml) afforded the pure **38** (317.2 mg, 97% yield) as a white solid. UPLC/MS: Rt = 1.82 min (gradient 1); MS (ESI) *m/z*: 390.3 [M-H]<sup>-</sup>. [M-H]<sup>-</sup> calculated: 390.2. <sup>1</sup>H NMR (400 MHz, chloroform-*d*) δ 7.87 (d, *J* = 2.0 Hz, 1H), 7.57 (dd, *J* = 8.8, 2.1 Hz, 1H), 6.85 (s, 1H), 6.72 (d, *J* = 8.8 Hz, 1H), 3.23 – 3.13 (m, 2H), 2.77 (s, 6H), 2.14 – 1.98 (m, 2H), 1.73 – 1.61 (m, 2H), 1.60 – 1.48 (m, 2H), 1.46 – 1.33 (m, 6H). <sup>13</sup>C NMR (101 MHz, Chloroform-*d*) δ 149.60 (C), 137.43 (CH), 135.43 (CH), 127.38 (CF<sub>3</sub>, q, <sup>1</sup>*J*<sub>CF</sub> = 279.2 Hz), 118.95 (C), 117.87 (CN), 112.51 (CH), 97.82 (C), 43.26 (CH<sub>2</sub>), 37.83 (CH<sub>3</sub>, 2C), 33.77 (CH<sub>2</sub>, q, <sup>2</sup>*J*<sub>CF</sub> = 27.5 Hz), 28.99 (CH<sub>2</sub>), 28.75 (CH<sub>2</sub>), 28.67 (CH<sub>2</sub>), 26.88 (CH<sub>2</sub>), 21.91 (CH<sub>2</sub>).



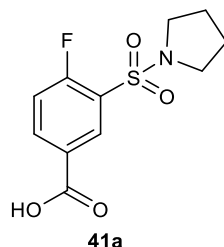
***N,N*-dimethyl-5-(1H-tetrazol-5-yl)-2-(8,8,8-trifluorooctylamino)benzenesulfonamide (39)**. A mixture of compound **38** (317.2 mg, 0.8 mmol), sodium azide (63.2 mg, 0.96 mmol) and zinc chloride

(132.6 mg, 0.96 mmol) was stirred in 4 ml of *n*-butanol at 110°C for 10 hours. At reaction completion the reaction mixture was evaporated to dryness at low pressure. Next, 5% NaOH (20 mL) was added and the mixture was stirred for 20 min. The resulting suspension was filtered, and the solid washed with a 5% NaOH aqueous solution (10 mL). The pH of the filtrate was adjusted to 1.0 with concentrated HCl and was extracted 3 times with EtOAc (3x25 ml). The combined organic layers were dried over Na<sub>2</sub>SO<sub>4</sub> and concentrated to dryness at low pressure. Purification by silica gel flash chromatography (CH<sub>2</sub>Cl<sub>2</sub>/MeOH 98:2) finally afforded the pure **39** (110.93 mg, 32% yield). UPLC/MS: Rt = 0.77min (gradient 2); MS (ESI) m/z: 433.3 [M-H]<sup>-</sup>. [M-H]<sup>-</sup> calculated: 433.2. <sup>1</sup>H NMR (400 MHz, Chloroform-*d*) δ 8.25 (d, *J* = 2.1 Hz, 1H), 8.19 (dd, *J* = 8.8, 2.2 Hz, 1H), 6.85 (d, *J* = 8.9 Hz, 1H), 6.61 (s, 1H), 3.19 (t, *J* = 7.1 Hz, 2H), 2.76 (s, 6H), 2.14 – 1.98 (m, 2H), 1.73 – 1.62 (m, 2H), 1.61 – 1.49 (m, 2H), 1.49 – 1.30 (m, 6H). <sup>13</sup>C NMR (101 MHz, Chloroform-*d*) δ 148.71 (C), 133.40 (CH), 129.73 (CH), 126.83 (CF<sub>3</sub>, q, <sup>1</sup>*J*<sub>CF</sub> = 281.4 Hz), 116.37 (C), 113.65 (C), 110.75 (CH), 42.67 (CH<sub>2</sub>), 37.85 (CH<sub>3</sub>, 2C), 32.78 (CH<sub>2</sub>, q, <sup>2</sup>*J*<sub>CF</sub> = 26.9 Hz), 28.63 (CH<sub>2</sub>), 28.48 (CH<sub>2</sub>), 28.29 (CH<sub>2</sub>), 26.58 (CH<sub>2</sub>), 21.81 (CH<sub>2</sub>).

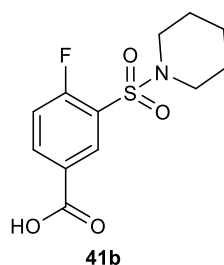


**3-(-*N,N*-methylsulfamoyl)-4-(8,8,8-trifluorooctylamino)benzoic acid (42a).** Compound **42a** was synthesized following the general procedure **B** previously described using intermediate **29a** (100 mg, 0.42 mmol) and amine **34a** (86.4 mg, 0.47 mmol) in dry 1,4-dioxane (1.4 ml). Purification by silica gel flash chromatography (CH<sub>2</sub>Cl<sub>2</sub>/MeOH from 100:0 to 98:02) followed by trituration with cyclohexane (2 ml) afforded the pure **42a** (111.5 mg, 67% yield) as a white solid. UPLC-MS: Rt = 2.11 min (gradient 1); MS (ESI) m/z: 395.2 [M-H]<sup>-</sup>. [M-H]<sup>-</sup> calculated: 395.1. <sup>1</sup>H NMR (400 MHz, DMSO-*d*<sub>6</sub>) δ 8.15 (d, *J* = 2.1 Hz, 1H), 7.90 (dd, *J* = 8.8, 2.1 Hz, 1H), 7.63 (q, *J* = 5.0 Hz, 1H), 6.86 (d, *J* = 8.9 Hz, 1H), 6.44 (t, *J* = 5.4 Hz, 1H), 3.24 (q, *J* = 6.7 Hz, 2H), 2.39 (d, *J* = 4.8 Hz, 3H), 2.28 – 2.15 (m, 2H), 1.64 – 1.55 (m, 2H), 1.51 – 1.42 (m, 2H), 1.39 – 1.30 (m, 6H). <sup>13</sup>C NMR (101 MHz, DMSO-*d*<sub>6</sub>) δ 166.14 (CO), 148.97 (C), 135.48 (CH), 132.42 (CH), 127.37 (CF<sub>3</sub>, q, <sup>1</sup>*J*<sub>CF</sub> = 277.1 Hz), 116.41

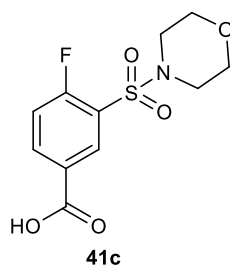
(C), 115.08 (C), 112.01 (CH), 42.22 (CH<sub>2</sub>), 32.38 (CH<sub>2</sub>, q,  $J_{CF} = 27.01$  Hz), 28.11 (CH<sub>2</sub>), 28.04 (CH<sub>2</sub>), 27.91 (CH<sub>2</sub>), 28.08 (CH<sub>3</sub>), 26.15 (CH<sub>2</sub>), 21.41 (CH<sub>2</sub>).



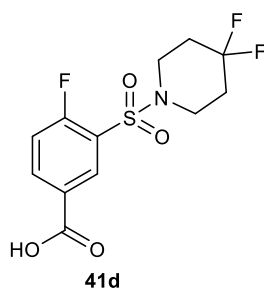
**4-fluoro-3-pyrrolidin-1-ylsulfonyl-benzoic acid (41).** Compound **41a** was synthesized following the general procedure A previously described using intermediate **28** (250 mg, 1.04 mmol) and pyrrolidine **40a** (0.26 ml, 3.11 mmol) in THF (8 ml). The described workup afforded pure **41a** (261.4 mg, 88% yield) as a white solid. UPLC/MS: Rt = 1.17 min (gradient 1); MS (ESI) m/z: 272.4 [M-H]<sup>-</sup>. [M-H]<sup>-</sup> calculated: 272.05. <sup>1</sup>H NMR (400 MHz, DMSO-*d*<sub>6</sub>) δ 8.30 (dd,  $J = 6.8, 2.3$  Hz, 1H), 8.25 (ddd,  $J = 8.6, 4.8, 2.3$  Hz, 1H), 7.62 (dd,  $J = 10.1, 8.6$  Hz, 1H), 3.28 – 3.21 (m, 4H), 1.81 – 1.73 (m, 4H).



**4-fluoro-3-(1-piperidylsulfonyl)benzoic acid (41b).** Compound **41b** was synthesized following the general procedure A previously described using intermediate **28** (250 mg, 1.04 mmol) and piperidine **40b** (0.31 ml, 3.11 mmol) in THF (8 ml). The described workup afforded pure **41b** (261.4 mg, 88 % yield) as a white solid. UPLC/MS: Rt = 1.34 min (gradient 1) ; MS (ESI) m/z: 286.4 [M-H]<sup>-</sup>. [M-H]<sup>-</sup> calculated: 286.06. <sup>1</sup>H NMR (400 MHz, DMSO-*d*<sub>6</sub>) δ 8.28 – 8.23 (m, 2H), 7.65 – 7.58 (m, 1H), 3.08 (t,  $J = 5.4$  Hz, 4H), 1.58 – 1.49 (m, 4H), 1.46 – 1.39 (m, 2H).

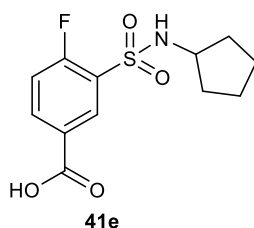


**4-fluoro-3-morpholinosulfonyl-benzoic acid (41c).** Compound **41c** was synthesized following the general procedure **A** previously described using intermediate **28** (250 mg, 1.04 mmol) and morpholine **40c** (0.27 ml, 3.11 mmol) in THF (8 ml). The described workup afforded pure **41c** (248.1 mg, 83% yield) as a white solid. UPLC/MS: Rt = 1.03 min (gradient 1); MS (ESI) m/z: 288.4 [M-H]<sup>-</sup>. [M-H]<sup>-</sup> calculated: 288.04. <sup>1</sup>H NMR (400 MHz, DMSO-*d*<sub>6</sub>) δ 8.32 – 8.24 (m, 2H), 7.64 (dd, *J* = 10.1, 8.5 Hz, 1H), 3.67 – 3.60 (m, 4H), 3.10 – 3.04 (m, 4H).

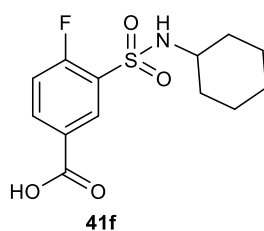


**3-((4,4-difluoropiperidin-1-yl)sulfonyl)-4-fluorobenzoic acid (41d).** To an ice-cold solution of the 4,4-difluoropiperidine hydrochloride **40d** (198.1 mg, 1.24 mmol) and DIPEA (0.33 ml, 1.87 mmol) in THF (5.0 ml) was added intermediate **28** (150 mg, 0.62 mmol) solved in THF (1.5 ml) and the reaction mixture was stirred at room temperature for 1 hour. At reaction completion the reaction mixture was evaporated to dryness. The dry residue was dissolved in water and treated with 2N HCl until it reached pH3. The resulting precipitated product was filtered and rinsed with water to afford the pure **41d** (176.4 mg, 88% yield) as a white solid. UPLC/MS: Rt = 1.38 min (gradient 1); MS (ESI) m/z: 322.0 [M-H]<sup>-</sup>. [M-H]<sup>-</sup> calculated: 322.04. <sup>1</sup>H NMR (400 MHz, DMSO-*d*<sub>6</sub>) δ 8.31 – 8.25 (m, 2H), 7.67 – 7.60 (m, 1H), 3.29 (t, *J* = 5.8 Hz, 4H), 2.07 (ddd, *J* = 19.7, 13.7, 5.8 Hz, 4H).

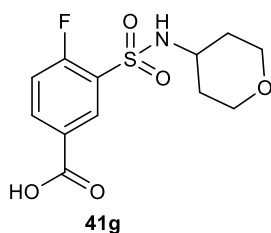




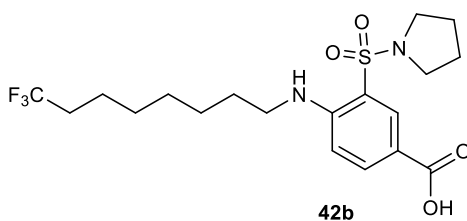
**3-(-N-cyclopentylsulfamoyl)-4-fluoro-benzoic acid (41e).** Compound **41e** was synthesized following the general procedure **A** previously described using intermediate **28** (250 mg, 1.04 mmol) and cyclopentane amine **40e** (0.21 ml, 2.07 mmol) in THF (8.5 ml). The described workup afforded the pure **41e** (203.7 mg, 68% yield) as a white solid. UPLC/MS: Rt = 1.25 min (gradient 1); MS (ESI) m/z: 286.4 [M-H]<sup>-</sup>. [M-H]<sup>-</sup> calculated: 286.06. <sup>1</sup>H NMR (400 MHz, DMSO-*d*<sub>6</sub>) δ 8.33 (dd, *J* = 7.1, 2.3 Hz, 1H), 8.21 (ddd, *J* = 8.6, 4.7, 2.3 Hz, 1H), 8.12 (d, *J* = 7.6 Hz, 1H), 7.56 (dd, *J* = 10.0, 8.6 Hz, 1H), 3.58 – 3.48 (m, 1H), 1.68 – 1.48 (m, 4H), 1.45 – 1.28 (m, 4H).



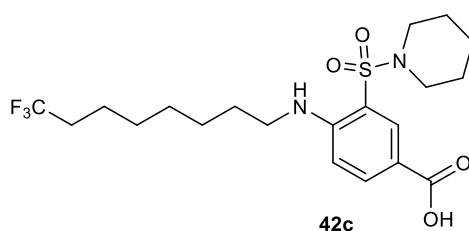
**3-(-N-cyclohexylsulfamoyl)-4-fluoro-benzoic acid (41f).** Title compound was synthesized following the general procedure **A** previously described using intermediate **28** (250 mg, 1.04 mmol) and cyclohexane amine **40f** (0.24 ml, 2.07 mmol) in THF (8.5 ml). The described workup and trituration with a cyclohexane/ethyl acetate 9:1 mixture (2 ml) afforded pure **41f** (185.6 mg, 59% yield) as a white solid. UPLC/MS: Rt = 1.37 min (gradient 1); MS (ESI) m/z: 286.4 [M-H]<sup>-</sup>. [M-H]<sup>-</sup> calculated: 286.06. <sup>1</sup>H NMR (400 MHz, DMSO-*d*<sub>6</sub>) δ 8.33 (dd, *J* = 7.1, 2.3 Hz, 1H), 8.21 (ddd, *J* = 8.6, 4.7, 2.3 Hz, 1H), 8.12 (d, *J* = 7.6 Hz, 1H), 7.56 (dd, *J* = 10.0, 8.6 Hz, 1H), 3.58 – 3.48 (m, 1H), 1.68 – 1.48 (m, 4H) 1.53 – 1.42 (m, 2H), 1.45 – 1.28 (m, 4H).



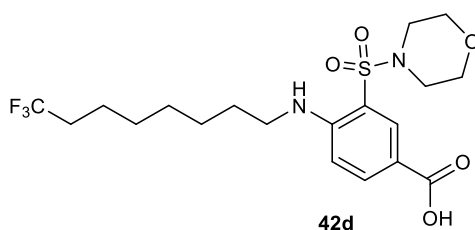
**4-fluoro-3-(N-(tetrahydro-2H-pyran-4-yl)sulfamoyl)benzoic acid (41g).** Title compound was synthesized following the general procedure **A** previously described using intermediate **28** (250 mg, 1.04 mmol) and tetrahydro-2H-pyran-4-amine **40g** (0.32 ml, 2.07 mmol) in THF (8.5 ml). The described workup afforded pure **41g** (160.9 mg, 51% yield) as a white solid. UPLC/MS: Rt = 0.93 min (gradient 1); MS (ESI) m/z: 302.1 [M-H]<sup>-</sup>. [M-H]<sup>-</sup> calculated: 302.06. <sup>1</sup>H NMR (400 MHz, DMSO-*d*<sub>6</sub>) δ 8.34 (dd, *J* = 7.1, 2.3 Hz, 1H), 8.27 (d, *J* = 7.8 Hz, 1H), 8.24 – 8.18 (m, 1H), 7.57 (t, *J* = 9.3 Hz, 1H), 3.77 – 3.68 (m, 2H), 3.27 – 3.19 (m, 3H), 1.58 – 1.49 (m, 2H), 1.49 – 1.37 (m, 2H).



**3-pyrrolidin-1-ylsulfonyl-4-(8,8,8-trifluorooctylamino)benzoic acid (42b).** Compound **42b** was synthesized following the general procedure **B** previously described using intermediate **41a** (50 mg, 0.17 mmol) and amine **34a** (34.8 mg, 0.19 mmol) in dry 1,4-dioxane (0.55 ml). Purification by silica gel flash chromatography (CH<sub>2</sub>Cl<sub>2</sub>/MeOH from 100:0 to 99:01) followed by trituration with diethyl ether (1 ml) afforded the pure **42b** (17.3 mg, 23% yield) as a white solid. UPLC/MS: Rt = 2.30 min (gradient 1); MS (ESI) m/z: 435.5 [M-H]<sup>-</sup>. [M-H]<sup>-</sup> calculated: 435.2. <sup>1</sup>H NMR (400 MHz, DMSO-*d*<sub>6</sub>) δ 8.11 (d, *J* = 2.1 Hz, 1H), 7.92 (dd, *J* = 8.8, 2.1 Hz, 1H), 6.89 (d, *J* = 8.9 Hz, 1H), 6.74 (t, *J* = 5.3 Hz, 1H), 3.24 (q, *J* = 6.7 Hz, 2H), 3.18 – 3.11 (m, 4H), 2.29 – 2.14 (m, 2H), 1.79 – 1.68 (m, 4H), 1.57 (m, 2H), 1.46 (m, 2H), 1.33 (s, 6H). <sup>13</sup>C NMR (101 MHz, DMSO-*d*<sub>6</sub>) δ 166.93 (CO), 149.84 (C), 135.81 (CH), 132.52 (CH), 126.82 (CF<sub>3</sub>, q, <sup>1</sup>J<sub>CF</sub> = 277.3 Hz), 117.33 (C), 115.18 (C), 112.45 (CH), 47.97 (CH<sub>2</sub>, 2C), 42.65 (CH<sub>2</sub>), 32.79 (CH<sub>2</sub>, q, <sup>2</sup>J<sub>CF</sub> = 27.3 Hz), 28.61 (CH<sub>2</sub>), 28.46 (CH<sub>2</sub>), 28.30 (CH<sub>2</sub>), 26.55 (CH<sub>2</sub>), 25.10 (CH<sub>2</sub>), 21.80 (CH<sub>2</sub>).

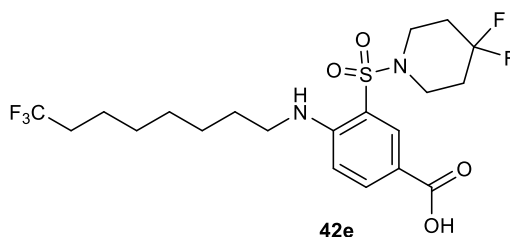


**3-(1-piperidylsulfonyl)-4-(8,8,8-trifluorooctylamino)benzoic acid (42c).** Compound **42c** was synthesized following the general procedure **B** previously described using intermediate **41b** (50 mg, 0.17 mmol) and amine **34b** (34.8 mg, 0.19 mmol) in dry 1,4-dioxane (0.55 ml). Purification by silica gel flash chromatography (CH<sub>2</sub>Cl<sub>2</sub>/MeOH from 100:0 to 99:01) followed by trituration with diethyl ether (1 ml) afforded the pure **42c** (13 mg, 17 % yield) as a white solid. UPLC/MS: Rt = 2.40 min (gradient 1); MS (ESI) m/z: 449.5 [M-H]<sup>-</sup>. [M-H]<sup>-</sup> calculated: 449.2. <sup>1</sup>H NMR (400 MHz, DMSO-*d*<sub>6</sub>) δ 8.04 (d, *J* = 2.1 Hz, 1H), 7.92 (dd, *J* = 8.8, 2.1 Hz, 1H), 6.89 (d, *J* = 9.0 Hz, 1H), 6.69 (t, *J* = 5.4 Hz, 1H), 3.24 (q, *J* = 6.7 Hz, 2H), 2.98 (t, *J* = 5.4 Hz, 4H), 2.29 – 2.15 (m, 2H), 1.62 – 1.55 (m, 2H), 1.55 – 1.43 (m, 6H), 1.42 – 1.37 (m, 2H), 1.37 – 1.30 (m, 6H). <sup>13</sup>C NMR (101 MHz, DMSO-*d*<sub>6</sub>) δ 166.93 (CO), 149.84 (C), 135.77 (CH), 132.36 (CH), 128.09 (CF<sub>3</sub>, q, <sup>1</sup>*J*<sub>CF</sub> = 278.3 Hz), 117.23 (C), 115.08 (C), 112.09 (CH), 46.19 (CH<sub>2</sub>, 2C), 38.62 (CH<sub>2</sub>), 32.23 (CH<sub>2</sub>, q, <sup>2</sup>*J*<sub>CF</sub> = 26.7 Hz), 27.77 (CH<sub>2</sub>), 24.52 (CH<sub>2</sub>, 2C), 21.33 (CH<sub>2</sub>), 23.09 (CH<sub>2</sub>), 27.91 (CH<sub>2</sub>, 2C), 26.12 (CH<sub>2</sub>).



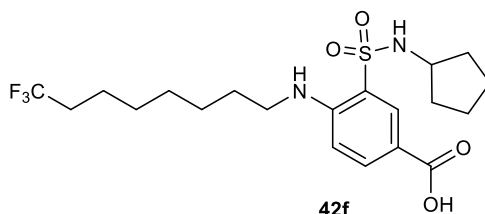
**3-morpholinosulfonyl-4-(8,8,8-trifluorooctylamino)benzoic acid (42d).** Compound **42d** was synthesized following the general procedure **B** previously described using intermediate **41c** (50 mg, 0.17 mmol) and amine **34a** (34.8 mg, 0.19 mmol) in dry 1,4-dioxane (0.55 ml). Purification by silica gel flash chromatography (CH<sub>2</sub>Cl<sub>2</sub>/MeOH from 100:0 to 98:02) followed by trituration with diethyl ether (1 ml) afforded the pure **42d** (28.4 mg, 37% yield) as a white solid. UPLC/MS: Rt = 2.21 min (gradient 1); MS (ESI) m/z: 451.2 [M-H]<sup>-</sup>. [M-H]<sup>-</sup> calculated: 451.2. <sup>1</sup>H NMR (400 MHz, Chloroform-

*d*)  $\delta$  8.33 (d,  $J = 2.1$  Hz, 1H), 8.07 (dd,  $J = 8.9, 2.1$  Hz, 1H), 6.87 (t,  $J = 5.0$  Hz, 1H), 6.74 (d,  $J = 9.0$  Hz, 1H), 3.77 – 3.70 (m, 4H), 3.21 (q,  $J = 7.0$  Hz, 2H), 3.12 – 3.06 (m, 4H), 2.14 – 1.99 (m, 2H), 1.73 – 1.63 (m, 2H), 1.61 – 1.50 (m, 2H), 1.48 – 1.32 (m, 6H).  $^{13}\text{C}$  NMR (101 MHz, Chloroform-*d*)  $\delta$  166.78 (CO), 149.96 (C), 136.14 (CH), 133.10 (CH), 127.22 (CF<sub>3</sub>, q,  $^1J_{\text{CF}} = 276.3$  Hz), 117.08 (C), 114.94 (C), 112.61 (CH), 65.71 (CH<sub>2</sub>, 2C), 46.00 (CH<sub>2</sub>, 2C), 42.69 (CH<sub>2</sub>), 32.79 (CH<sub>2</sub>, q,  $^2J_{\text{CF}} = 27.25$  Hz), 28.62 (CH<sub>2</sub>), 28.39 (CH<sub>2</sub>), 28.30 (CH<sub>2</sub>), 26.58 (CH<sub>2</sub>), 21.80 (CH<sub>2</sub>).



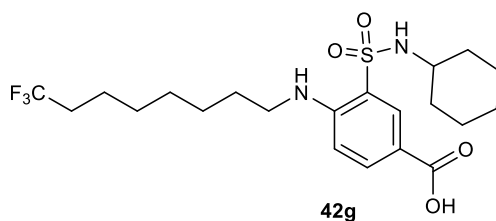
**3-((4,4-difluoropiperidin-1-yl)sulfonyl)-4-((8,8,8-trifluorooctyl)amino)benzoic acid (42e).**

Compound **42d** was synthesized following the general procedure **B** previously described using intermediate **41d** (50 mg, 0.15 mmol) and amine **34a** (34.8 mg, 0.19 mmol) in dry 1,4-dioxane (0.55 ml). Purification by silica gel flash chromatography (CH<sub>2</sub>Cl<sub>2</sub>/MeOH from 100:0 to 98:02) followed by trituration with petroleum ether (1 ml) afforded the pure **42e** (22.6 mg, 31% yield) as a white solid. UPLC/MS: *R*<sub>t</sub> = 2.39 min (gradient 1); MS (ESI) *m/z*: 485.2 [M-H]<sup>-</sup>. [M-H]<sup>-</sup> calculated: 485.2.  $^1\text{H}$  NMR (400 MHz, Chloroform-*d*)  $\delta$  8.35 (d,  $J = 2.0$  Hz, 1H), 8.08 (dd,  $J = 8.9, 2.1$  Hz, 1H), 6.78 (t,  $J = 5.0$  Hz, 1H), 6.74 (d,  $J = 9.0$  Hz, 1H), 3.31 (t,  $J = 5.8$  Hz, 4H), 3.25 – 3.18 (m, 2H), 2.14 – 2.00 (m, 6H), 1.69 (p,  $J = 7.0$  Hz, 2H), 1.62 – 1.52 (m, 2H), 1.49 – 1.35 (m, 6H).

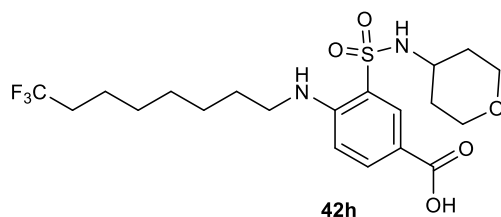


**3-(N-cyclopentylsulfamoyl)-4-(8,8,8-trifluorooctylamino)benzoic acid (42f).** Compound **42f** was synthesized following the general procedure **B** previously described using intermediate **41e** (50 mg, 0.17 mmol) and amine **34a** (35.1 mg, 0.19 mmol) in dry 1,4-dioxane (0.6 ml). Purification by silica gel

flash chromatography (CH<sub>2</sub>Cl<sub>2</sub>/MeOH from 100:0 to 98:02) followed by trituration with diethyl ether (1 ml) afforded the pure **42f** (31.7 mg, 41% yield) as a white solid. UPLC/MS: Rt = 2.33 min (gradient 1); MS (ESI) m/z: 449.5 [M-H]<sup>-</sup>. [M-H]<sup>-</sup> calculated: 449.2. <sup>1</sup>H NMR (400 MHz, Chloroform-*d*) δ 8.49 (d, *J* = 2.1 Hz, 1H), 8.08 (dd, *J* = 8.8, 2.1 Hz, 1H), 6.75 (d, *J* = 8.9 Hz, 1H), 6.53 (s, 1H), 4.63 – 4.51 (m, 1H), 3.63 – 3.53 (m, 1H), 3.25 (t, *J* = 7.1 Hz, 2H), 2.14 – 2.00 (m, 2H), 1.85 – 1.75 (m, 2H), 1.74 – 1.65 (m, 2H), 1.65 – 1.54 (m, 4H), 1.53 – 1.47 (m, 2H), 1.46 – 1.36 (m, 6H), 1.36 – 1.27 (m, 2H). <sup>13</sup>C NMR (101 MHz, Chloroform-*d*) δ 167.06 (CO), 148.73 (C), 135.28 (CH), 132.29 (CH), 127.04 (CF<sub>3</sub>, q, <sup>1</sup>*J*<sub>CF</sub> = 268.1 Hz), 121.26 (C), 116.69 (C), 111.75 (CH), 54.53 (CH), 42.85 (CH<sub>2</sub>), 32.95 (CH<sub>2</sub>, q, <sup>2</sup>*J*<sub>CF</sub> = 26.78 Hz), 32.77 (CH<sub>2</sub>, 2C), 28.74 (CH<sub>2</sub>), 28.54 (CH<sub>2</sub>), 28.34 (CH<sub>2</sub>), 26.60 (CH<sub>2</sub>), 23.21 (CH<sub>2</sub>, 2C), 21.81 (CH<sub>2</sub>).

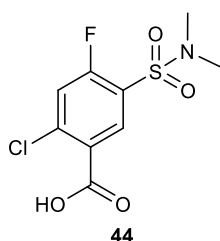


**3-(-N-cyclohexylsulfamoyl)-4-(8,8,8-trifluorooctylamino)benzoic acid (42g).** Compound **42g** was synthesized following the general procedure **B** previously described using intermediate **41f** (50 mg, 0.16 mmol) and amine **34a** (33.4 mg, 0.18 mmol) in dry 1,4-dioxane (0.55 ml). Purification by silica gel flash chromatography (CH<sub>2</sub>Cl<sub>2</sub>/MeOH from 100:0 to 98:02) followed by trituration with diethyl ether (1 ml) afforded the pure **42f** (25.3 mg, 34 % yield). UPLC/MS: Rt = 2.40 min (gradient 1); MS (ESI) m/z: 463.5 [M-H]<sup>-</sup>. [M-H]<sup>-</sup> calculated: 463.2. <sup>1</sup>H NMR (400 MHz, Chloroform-*d*) δ 8.49 (d, *J* = 2.1 Hz, 1H), 8.07 (dd, *J* = 8.8, 2.1 Hz, 1H), 6.74 (d, *J* = 8.9 Hz, 1H), 6.50 (s, 1H), 4.49 (d, *J* = 7.9 Hz, 1H), 3.25 (t, *J* = 7.1 Hz, 2H), 3.18 – 3.07 (m, 1H), 2.14 – 2.00 (m, 2H), 1.79 – 1.66 (m, 4H), 1.66 – 1.49 (m, 6H), 1.48 – 1.34 (m, 6H), 1.30 – 1.19 (m, 3H), 1.18 – 1.07 (m, 2H). <sup>13</sup>C NMR (101 MHz, Chloroform-*d*) δ 166.72 (CO), 148.26 (C), 134.86 (CH), 131.64 (CH), 127.44 (CF<sub>3</sub>, q, <sup>1</sup>*J*<sub>CF</sub> = 269.7 Hz), 121.51 (C), 116.25 (C), 111.38 (CH), 51.72 (CH), 42.50 (CH<sub>2</sub>), 33.17 (CH<sub>2</sub>, 2C), 32.33 (CH<sub>2</sub>, q, <sup>2</sup>*J*<sub>CF</sub> = 27.67 Hz), 28.40 (CH<sub>2</sub>), 28.22 (CH<sub>2</sub>), 27.99 (CH<sub>2</sub>), 26.26 (CH<sub>2</sub>), 24.91 (CH<sub>2</sub>), 24.26 (CH<sub>2</sub>, 2C), 21.48 (CH<sub>2</sub>).



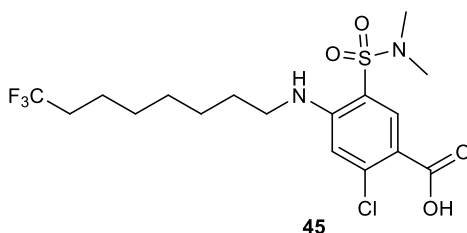
**3-(*N*-(tetrahydro-2H-pyran-4-yl)sulfamoyl)-4-((8,8,8-trifluorooctyl)amino)benzoic acid (42h).**

Compound **42h** was synthesized following the general procedure **B** previously described using intermediate **42g** (50 mg, 0.16 mmol) and intermediate **34a** (33.4 mg, 0.18 mmol) in dry 1,4-dioxane (0.55 ml). Purification by silica gel flash chromatography (CH<sub>2</sub>Cl<sub>2</sub>/MeOH from 100:0 to 98:02) followed by trituration with diethyl ether (1 ml) afforded the pure **42h** (20.9 mg, 28% yield) as a white solid. UPLC/MS: Rt = 2.40 min (gradient 1); MS (ESI) m/z: 463.5 [M-H]<sup>-</sup>. [M-H] calculated: 463.2. <sup>1</sup>H NMR (400 MHz, DMSO-*d*<sub>6</sub>) δ 8.21 (d, *J* = 2.1 Hz, 1H), 7.96 (d, *J* = 7.6 Hz, 1H), 7.88 (dd, *J* = 8.8, 2.1 Hz, 1H), 6.85 (d, *J* = 8.9 Hz, 1H), 6.35 (t, *J* = 5.6 Hz, 1H), 3.74 – 3.65 (m, 2H), 3.30 – 3.17 (m, 4H), 3.17 – 3.06 (m, 1H), 2.29 – 2.13 (m, 2H), 1.64 – 1.56 (m, 2H), 1.53 – 1.42 (m, 4H), 1.40 – 1.29 (m, 8H). <sup>13</sup>C NMR (101 MHz, DMSO-*d*<sub>6</sub>) δ 166.66 (CO), 148.20 (C), 134.95 (CH), 131.63 (CH), 127.72 (CF<sub>3</sub>, q, <sup>1</sup>*J*<sub>CF</sub> = 277.1 Hz), 121.32 (C), 116.45 (C), 111.44 (CH), 65.45 (CH<sub>2</sub>, 2C), 48.86 (CH), 42.49 (CH<sub>2</sub>), 33.24 (CH<sub>2</sub>, 2C), 32.56 (CH<sub>2</sub>, q, <sup>2</sup>*J*<sub>CF</sub> = 27.50 Hz), 28.35 (CH<sub>2</sub>), 28.19 (CH<sub>2</sub>), 27.96 (CH<sub>2</sub>), 26.24 (CH<sub>2</sub>), 21.45 (CH<sub>2</sub>).

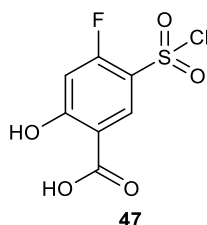


**2-chloro-5-(*N,N*-dimethylsulfamoyl)-4-fluorobenzoic acid (44).** 2-chloro-5-(chlorosulfonyl)-4-fluorobenzoic acid **43** (250 mg, 0.91 mmol) solved in 1.5 mL of THF was added dropwise to 8 mL of an ice cold solution of dimethylamine (0.45 ml, 0.91 mmol) in THF and DIPEA (0.38 ml, 2.72 mmol) and stirred for 30 hr. At reaction completion the reaction mixture was evaporated to dryness. The dry residue was dissolved in water and treated with 2N HCl till reaching pH 3. The resulting precipitated

solid was filtered and rinsed with water. Final purification by silica gel flash chromatography (CH<sub>2</sub>Cl<sub>2</sub>/MeOH from 100:0 to 98:02) afforded the pure **44** (105.1 mg, 41% yield) as a white solid. UPLC/MS: Rt = 1.04 min (gradient 1); MS (ESI) m/z: 280.0 [M-H]<sup>-</sup>. [M-H]<sup>-</sup> calculated: 280.1. <sup>1</sup>H NMR (400 MHz, DMSO-*d*<sub>6</sub>) δ 8.17 (d, *J* = 7.5 Hz, 1H), 7.91 (d, *J* = 10.1 Hz, 1H), 2.76 (d, *J* = 1.8 Hz, 6H).

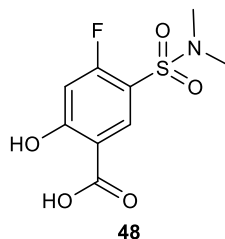


**2-chloro-5-(*N,N*-dimethylsulfamoyl)-4-((8,8,8-trifluorooctyl)amino)benzoic acid (45).** Compound **45** was synthesized following the general procedure **B** previously described using intermediate **44** (60 mg, 0.21 mmol) and amine **34a** (46.8 mg, 0.21 mmol) in dry 1,4-dioxane (0.8 ml). Purification by silica gel flash chromatography (CH<sub>2</sub>Cl<sub>2</sub>/MeOH from 100:0 to 97:03) followed by trituration with diethyl ether (1 ml) afforded the pure **45** (82.2 mg, 88% yield) as a white solid. UPLC/MS: Rt = 2.14 min (gradient 1); MS (ESI) m/z: 443.1 [M-H]<sup>-</sup>. [M-H]<sup>-</sup> calculated: 444.2. <sup>1</sup>H NMR (400 MHz, Chloroform-*d*) δ 8.37 (s, 1H), 6.88 (t, *J* = 5.0 Hz, 1H), 6.75 (s, 1H), 3.21 – 3.16 (m, 2H), 2.77 (s, 6H), 2.14 – 2.00 (m, 2H), 1.73 – 1.63 (m, 2H), 1.61 – 1.51 (m, 2H), 1.48 – 1.34 (m, 6H). <sup>13</sup>C NMR (101 MHz, chloroform-*d*) δ 168.43 (CO), 149.85 (C), 141.90 (C), 136.42 (CH), 128.12 (CF<sub>3</sub>, q, <sup>1</sup>*J*<sub>CF</sub> = 278.4 Hz), 115.68 (C), 114.04 (C), 113.62 (CH), 43.23 (CH<sub>2</sub>), 37.73 (CH<sub>3</sub>, 2C), 33.52 (CH<sub>2</sub>, q, <sup>2</sup>*J*<sub>CF</sub> = 27.89 Hz), 28.83 (CH<sub>2</sub>), 28.54 (CH<sub>2</sub>), 26.72 (CH<sub>2</sub>, 2C), 21.77 (CH<sub>2</sub>).

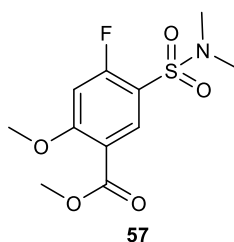


**5-(chlorosulfonyl)-4-fluoro-2-hydroxybenzoic acid (47).** 4-fluoro-2-hydroxybenzoic acid **46** (2 g, 12.81 mmol) was stirred in chlorosulfonic acid (4.30 ml, 64.06 mmol) at 120° C for 4 hr. At reaction completion, the mixture was slowly poured onto ice-cold water (50 ml) and the resulting precipitated

solid was collected by filtration to afford **47** (1.141 g, 35% yield) as a brownish solid. UPLC/MS: Rt = 1.42 min (gradient 1); MS (ESI) m/z: 253.2 [M-H]<sup>-</sup>. [M-H]<sup>-</sup> calculated: 253.0. <sup>1</sup>H NMR (400 MHz, DMSO-*d*<sub>6</sub>) δ 8.15 (d, *J* = 8.2 Hz, 1H), 7.13 – 7.03 (m, 1H).



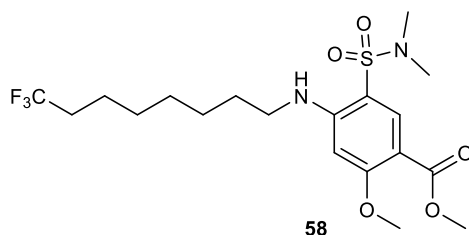
**5-(*N,N*-dimethylsulfamoyl)-4-fluoro-2-hydroxybenzoic acid (**48**)**. Intermediate **47** (1.141 g, 4.44 mmol) solved in 10 ml of THF and added dropwise to an ice-cold solution of 2M dimethylamine in THF (2.22 ml, 4.44 mmol) and DIPEA (2.34 ml, 13.31 mmol) in 35 ml tetrahydrofuran. The reaction mixture was stirred at 0°C for 8 hours. At reaction completion the mixture was evaporated to dryness at low pressure and the residue was treated with a saturated NH<sub>4</sub>Cl aqueous solution (50 ml) and extracted twice with EtOAc (2x50 ml). The combined organic layers were dried over Na<sub>2</sub>SO<sub>4</sub> and concentrated to dryness at low pressure to afford pure titled compound **48** (823.9 mg, 70% yield) UPLC/MS: Rt = 1.19 min (gradient 1); MS (ESI) m/z: 262.0 [M-H]<sup>-</sup>. [M-H]<sup>-</sup> calculated: 262.0. <sup>1</sup>H NMR (400 MHz, DMSO-*d*<sub>6</sub>) δ 8.15 (d, *J* = 8.2 Hz, 1H), 7.13 – 7.03 (m, 1H), 2.71 (d, *J* = 1.7 Hz, 6H).



**Methyl 5-(*N,N*-dimethylsulfamoyl)-4-fluoro-2-methoxybenzoate (**57**)**. To an ice cold solution of intermediate **48** (200 mg, 0.75 mmol) in DCM/MeOH 8:2 (9 ml) was carefully added trimethylsilyldiazomethane (2M in hexanes, 1.13 ml, 2.26 mmol) and the reaction mixture was stirred at room temperature for 2 hours. At reaction completion the reaction mixture was quenched with 2 ml of a 1M acetic solution in methanol and evaporated to dryness. The dry residue was suspended in a saturated NaHCO<sub>3</sub> (15 ml) aqueous solution and extracted twice with EtOAc (2 x 15 ml). Purification

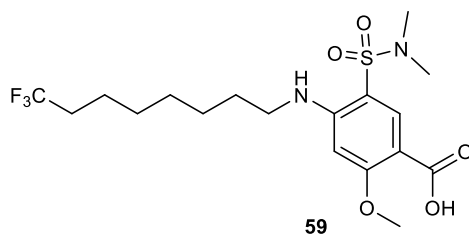


by silica gel flash chromatography (cyclohexane/EtOAc from 85:15 to 70:30) afforded the pure **57** (201 mg, 92% yield) as a white solid. UPLC/MS: Rt = 1.75 min (gradient 1); MS (ESI) m/z: 292.1 [M+H]<sup>+</sup>. [M+H]<sup>+</sup> calculated: 292.0. <sup>1</sup>H NMR (600 MHz, Chloroform-*d*) δ 8.35 (d, *J* = 5.0 Hz, 1H), 6.94 (d, *J* = 8.0 Hz, 1H), 3.85 (s, 3H), 3.79 (s, 3H), 2.72 (s, 6H).



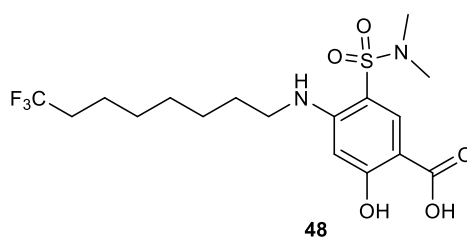
**Methyl 5-(*N,N*-dimethylsulfamoyl)-2-methoxy-4-((8,8,8-trifluorooctyl)amino)benzoate (58).**

Compound **58** was synthesized following the general procedure **B** previously described using intermediate **57** (50 mg, 0.17 mmol) and amine **34a** (75.4 mg, 0.34 mmol) in dry 1,4-dioxane (0.85 ml). Purification by silica gel flash chromatography (cyclohexane/EtOAc from 80:15 to 75:25) afforded the pure **58** (64.9 mg, 84% yield) as a white solid. UPLC/MS: Rt = 2.65 min (gradient 1); MS (ESI) m/z: 455.3 [M+H]<sup>+</sup>. [M+H]<sup>+</sup> calculated: 455.2. <sup>1</sup>H NMR (400 MHz, Chloroform-*d*) δ 8.23 (s, 1H), 6.77 (t, *J* = 4.8 Hz, 1H), 6.10 (s, 1H), 3.97 (s, 3H), 3.84 (s, 3H), 3.22 – 3.16 (m, 2H), 2.75 (s, 6H), 2.14 – 2.04 (m, 2H), 1.72 (p, *J* = 7.1 Hz, 2H), 1.60 – 1.55 (m, 4H), 1.45 (dd, *J* = 5.0, 2.0 Hz, 2H), 1.41 (dd, *J* = 3.9, 2.6 Hz, 4H).

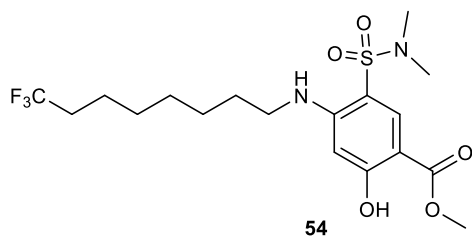


**5-(*N,N*-dimethylsulfamoyl)-2-methoxy-4-((8,8,8-trifluorooctyl)amino)benzoic acid (59).** To a solution of intermediate **58** (59 mg, 0.13 mmol) solved in tetrahydrofuran (1.3 mL) was added a 1 M LiOH aqueous solution (0.26 ml, 0.26 mmol) and the mixture was stirred at room temperature for 16 hours. At reaction completion, the crude was portioned between EtOAc (10 ml) and an NH<sub>4</sub>Cl saturated solution (10 ml) and the layers separated. The organic layer was dried over Na<sub>2</sub>SO<sub>4</sub> and concentrated

to dryness at low pressure. Trituration with cyclohexane afforded the pure **59** (41.2 mg, 72% yield) as a white solid. UPLC/MS: Rt = 1.16 min (gradient 1); MS (ESI) m/z: 439.5 [M-H]<sup>-</sup>. [M-H]<sup>-</sup> calculated: 439.2. <sup>1</sup>H NMR (400 MHz, DMSO-*d*<sub>6</sub>) δ 7.98 (s, 1H), 6.65 (t, *J* = 5.2 Hz, 1H), 6.26 (s, 1H), 3.88 (s, 3H), 3.29 – 3.22 (m, 2H), 2.61 (s, 6H), 1.65 – 1.55 (m, 2H), 1.52 – 1.42 (m, 4H), 1.39 – 1.29 (m, 6H). <sup>13</sup>C NMR (101 MHz, chloroform-*d*) δ 169.28 (CO), 160.66 (C), 149.55 (C), 137.78 (CH), 126.50 (CF<sub>3</sub>, q, <sup>1</sup>*J*<sub>CF</sub> = 266.89 Hz), 115.67 (C), 114.41 (C), 103.76 (CH), 55.85 (OCH<sub>3</sub>), 44.23 (CH<sub>2</sub>), 37.84 (CH<sub>3</sub>, 2C), 33.71 (CH<sub>2</sub>, q, <sup>2</sup>*J*<sub>CF</sub> = 26.64 Hz), 28.83 (CH<sub>2</sub>), 28.54 (CH<sub>2</sub>), 26.72 (CH<sub>2</sub>), 22.48 (CH<sub>2</sub>).

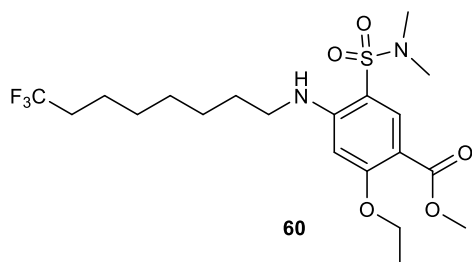


**5-(*N,N*-dimethylsulfamoyl)-2-hydroxy-4-((8,8,8-trifluorooctyl)amino)benzoic acid (48).** Under argon atmosphere, to an ice cold solution of compound **59** (50 mg, 0.12 mmol) solved in DCM (1.2 mL) was added dropwise BBr<sub>3</sub> (1 M in DCM, 0.59 ml, 0.59 mmol) and the mixture was stirred at room temperature for 16 hr. At reaction completion the reaction mixture was cooled to 0°C, quenched with 2 ml of methanol and evaporated to dryness. The dry residue crude was then portioned between EtOAc (10 ml) and an NH<sub>4</sub>Cl saturated solution (10 ml) and the layers separated. The organic layer was dried over Na<sub>2</sub>SO<sub>4</sub> and concentrated to dryness at low pressure. Trituration with cyclohexane afforded the pure **48** (39.9 mg, 78% yield) as a white solid. UPLC/MS: Rt = 1.81 min (gradient 1); MS (ESI) m/z: 425.4 [M-H]<sup>-</sup>. [M-H]<sup>-</sup> calculated: 425.1. <sup>1</sup>H NMR (400 MHz, DMSO-*d*<sub>6</sub>) δ 7.99 (s, 1H), 6.61 (t, *J* = 5.2 Hz, 1H), 6.20 (s, 1H), 3.28 – 3.21 (m, 2H), 2.61 (s, 6H), 1.67 – 1.57 (m, 2H), 1.51 – 1.43 (m, 2H), 1.37 – 1.28 (m, 6H).



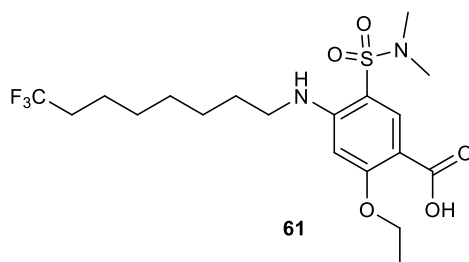
**Methyl 5-(*N,N*-dimethylsulfamoyl)-2-hydroxy-4-((8,8,8-trifluorooctyl)amino)benzoate (54).**

Under argon atmosphere, to an ice cold solution of intermediate **58** (50 mg, 0.11 mmol) solved in DCM (1.2 mL) was added dropwise BBr<sub>3</sub> (1 M in DCM, 0.55 ml, 0.55 mmol) and the mixture was stirred at room temperature for 16 hours. At reaction completion the reaction mixture was cooled to 0°C, quenched with 2 ml of methanol and evaporated to dryness. The dry residue crude was then portioned between EtOAc (10 ml) and an NH<sub>4</sub>Cl saturated solution (10 ml) and the layers separated. The organic layer was dried over Na<sub>2</sub>SO<sub>4</sub> and concentrated to dryness at low pressure. Purification by silica gel flash chromatography (cyclohexane/EtOAc 95:05) afforded the pure **54** (40.2 mg, 83% yield) as a white solid. UPLC/MS: Rt = 2.10 min (gradient 1); MS (ESI) m/z: 441.3 [M-H]<sup>+</sup>. [M+H]<sup>+</sup> calculated: 441.1. <sup>1</sup>H NMR (400 MHz, chloroform-*d*) δ 11.26 (s, 1H), 8.17 (s, 1H), 6.73 (t, *J* = 4.6 Hz, 1H), 6.16 (s, 1H), 3.92 (s, 3H), 3.16 (q, *J* = 7.1, 5.0 Hz, 2H), 2.75 (s, 6H), 2.15 – 1.99 (m, 2H), 1.74 – 1.63 (m, 2H), 1.62 – 1.54 (m, 2H), 1.48 – 1.35 (m, 6H).



**Methyl 5-(*N,N*-dimethylsulfamoyl)-2-ethoxy-4-((8,8,8-trifluorooctyl)amino)benzoate (60).** To a solution of intermediate **54** (31.8 mg, 0.07 mmol) in acetone (0.7 mL) were added ethyl iodide (10 μl, 0.11 mmol) and potassium carbonate (15 mg, 0.11 mmol) and the reaction mixture was stirred at room temperature for 24 hours. At reaction completion, the crude was portioned between EtOAc (10 ml) and an water saturated solution (10 ml) and the layers separated. The organic layer was dried over Na<sub>2</sub>SO<sub>4</sub> and concentrated to dryness at low pressure. Purification by silica gel flash chromatography (cyclohexane/EtOAc from 100:00 to 80:20) afforded the pure **54** (25.6 mg, 78% yield) as a white solid.

UPLC/MS: Rt = 1.85 min (gradient 1); MS (ESI) m/z: 469.3 [M+H]<sup>+</sup>. [M+H]<sup>+</sup> calculated: 469.2. <sup>1</sup>H NMR (400 MHz, Chloroform-*d*) δ 8.20 (s, 1H), 6.71 (t, *J* = 4.8 Hz, 1H), 6.07 (s, 1H), 4.14 (q, *J* = 7.0 Hz, 2H), 3.82 (s, 3H), 3.18 – 3.11 (m, 2H), 2.72 (s, 6H), 2.13 – 1.99 (m, 2H), 1.73 – 1.64 (m, 2H), 1.61 – 1.53 (m, 2H), 1.51 (t, *J* = 6.9 Hz, 3H), 1.48 – 1.35 (m, 6H).



**5-(*N,N*-dimethylsulfamoyl)-2-ethoxy-4-((8,8,8-trifluorooctyl)amino)benzoic acid (61).** To a solution of compound **60** (25.6 mg, 0.05 mmol) in tetrahydrofuran (0.5 mL) was added a 1 M LiOH aqueous solution (0.27 mL, 0.27 mmol) and the reaction mixture was stirred at room temperature for 16 hr. At reaction completion, the crude was portioned between EtOAc (10 mL) and an NH<sub>4</sub>Cl saturated solution (10 mL) and the layers separated. The organic layer was dried over Na<sub>2</sub>SO<sub>4</sub> and concentrated to dryness at low pressure. Trituration with cyclohexane afforded the pure **61** (19.54 mg, 86% yield) as a white solid. UPLC/MS: Rt = 1.32 min (gradient 1); MS (ESI) m/z: 453.3 [M-H]<sup>-</sup>. [M-H]<sup>-</sup> calculated: 453.2. <sup>1</sup>H NMR (400 MHz, DMSO-*d*<sub>6</sub>) δ 7.95 (s, 1H), 6.62 (t, *J* = 5.2 Hz, 1H), 6.23 (s, 1H), 4.15 (q, *J* = 6.9 Hz, 2H), 3.23 (q, *J* = 6.5 Hz, 2H), 2.60 (s, 6H), 2.29 – 2.14 (m, 2H), 1.63 – 1.52 (m, 2H), 1.51 – 1.42 (m, 2H), 1.40 – 1.25 (m, 9H). <sup>13</sup>C NMR (101 MHz, DMSO-*d*<sub>6</sub>) δ 166.08 (CO), 163.69 (C), 151.13 (C), 136.45 (CH), 128.31 (CF<sub>3</sub>, q, <sup>1</sup>*J*<sub>CF</sub> = 277.07 Hz), 107.92 (C), 107.57 (C), 95.35 (CH), 64.59 (OCH<sub>2</sub>), 42.61 (CH<sub>2</sub>), 37.77 (CH<sub>3</sub>, 2C), 32.80 (CH<sub>2</sub>, q, <sup>2</sup>*J*<sub>CF</sub> = 26.87 Hz), 28.61 (CH<sub>2</sub>), 28.37 (CH<sub>2</sub>), 28.27 (CH<sub>2</sub>), 26.59 (CH<sub>2</sub>), 21.80 (CH<sub>2</sub>), 14.83 (CH<sub>3</sub>).

## Chapter 6. Concluding Remarks.

The aim of this work was the discovery of *selective* NKCC1 inhibitors. Toward this end, we performed design, synthesis and characterization of novel *selective* NKCC1 inhibitors, with the identification of a potent lead compound, ARN23746, which is ready for preclinical development to treat neurodevelopmental disorders.

A large and fast-growing body of literature indicates that an aberrant Cl<sup>-</sup> homeostasis, due to an imbalance in NKCC1 vs KCC2 activity and/or expression, is implicated in several neurological disorders. Accordingly, several studies indicated NKCC1 inhibition by bumetanide as a valuable therapeutic strategy to ameliorate core symptoms in a number of animal models of these neurological disorders<sup>1,54</sup>. Moreover, several clinical trials and case studies indicate positive outcomes of bumetanide treatment also in patients<sup>1</sup>. Although NKCC1 inhibition is a promising target for the treatment of diverse neurodevelopmental disorders, a chronic treatment seems to be required. For this reason, the strong diuretic effect of bumetanide due to inhibition of NKCC2 in the kidney<sup>177</sup>, which leads to hypokalemia and ionic imbalance<sup>110,111</sup>, has strongly hampered its repurposing. Therefore, bumetanide is not a sustainable therapeutic approach since it may not be compatible with a lifelong treatment of several years. As another limitation, bumetanide proved to have ototoxic effect in infants. Indeed, one clinical trial for the repurposing of bumetanide for the treatment of acute neonatal encephalopathy seizures was suspended due to induced deafness in some treated subjects<sup>99</sup>. So far, diverse studies identified changes in cochlear potentials and damage in cochlear stria vascularis as the main ototoxic effect following loop-diuretic administration. Although the clear mechanisms underlying ototoxicity are still under investigation, inhibition of NKCC1 in the cochlea<sup>29</sup>, inhibition of NKCC2 expressed in endolymphatic sac at the membranous labyrinth<sup>215</sup> may possibly contribute to the inner ear damage and ototoxic effect by loop diuretics which inhibit both NKCC1 and NKCC2. For these reasons, new selective, and possibly safer NKCC1 inhibitors must be developed in order to give access to new potentially effective and sustainable pharmacological therapies for the brain disorders characterized by increased [Cl<sup>-</sup>]<sub>i</sub> and depolarizing GABAergic transmission.

In the last years, neuroscience drug discovery in the pharma industry has been often dismissed due to repeated failures in developing small molecules that typically act on target validated only in animal models, being target validation in patients extremely challenging. In this context, drug-repurposing is often used as an alternative strategy, due to lower costs of preclinical development and often established safety in humans<sup>216</sup>. However, this strategy may often result in a suboptimal care of the patient, since the repositioned drug retain secondary effects deriving from its first clinical indication. For this reason, previous studies from other groups attempted to separate the brain effect of bumetanide from its systemic effect through the synthesis of lipophilic analogs and prodrugs.<sup>185,188,190,191</sup> These derivatives rely solely on the pharmacokinetic diversification between central and systemic effects rather than direct selectivity towards NKCC1. In addition, there are no insights confirming that the activity of these derivatives is due to a mechanism of action shared with bumetanide.

Here, we have employed a rational new strategy for neuroscience drug discovery that uses at its advantage, and links together, drug repurposing as a tool to validate drug targets shared between patients and animal models, in a safe manner. We used computer-aided drug design of new molecules based on the structure and mechanism of action of the repurposed drug. As a result, with our integrated drug discovery approach, we managed to solve the drawbacks of bumetanide by developing a structurally unrelated new molecular entity. This strategy allowed us to obtain a lead compound that has optimal chemico-physical properties for a CNS targeted drug, with improved BBB penetration, as well as favorable drug-like properties as solubility and metabolic stability. The absence of NKCC2 inhibition *in vitro* and diuresis *in vivo* by ARN23746 is predicted to avoid the general ionic imbalance and reduce dangerous side effects like ototoxicity, possibly decreasing the side effects of treatment with unselective NKCC1 inhibitors. Thus, ARN23746 represents a new sustainable therapeutic option for possible lifelong treatment of NDs.

From a medicinal chemistry point of view, we combined the data generated using various approaches towards the identification of new molecules able to selectively inhibit NKCC1. The first strategy that we employed was focused on the identification and isolation of the structural features of bumetanide that could generate selective inhibition of NKCC1 by performing a structure activity relationship study.

As described in **Chapter 2**, we designed and synthesized a small library of 10 compounds modified in various parts of the molecule (See Figure 2.1). These were tested for their inhibitory activity against NKCC1 and NKCC2. As a result, we found that elongation of carbon chain of the alkyl amine in position 3 was capable to slightly direct the inhibitory activity towards NKCC1, while the benzoic acid moiety in position 1 was crucial for inhibition of both NKCC1 and NKCC2. However, none of the compounds that we evaluated showed a marked ratio in NKCC2/NKCC1 selectivity, confirming data from the literature<sup>192</sup>. In addition, the insertion of these modifications on the bumetanide core always coincided with a robust loss of potency also on NKCC1. We thus moved to the search of novel compounds, structurally unrelated to bumetanide.

In **Chapter 3**, we performed a ligand based virtual screening for the identification of novel molecular scaffolds able to selectively inhibit NKCC1. For this task, we generated a bumetanide pharmacophore model that we used as a filter for the screening of different libraries. This process led to the identification of the two moderately active 2-amino-5-nitro-benzenesulfonamide derivatives ARN22393 and ARN22394 (see Table 3.1). Two main scaffolds were generated based on the substituents in position 1 of the aromatic ring: (series A) a 2-amino-5-nitro-benzene-sulfonamide and (series B) a 4-amino-3-sulfamoyl-benzoic acid. By introducing the modifications evaluated on the bumetanide analogues, we firstly synthesized 12 derivatives of series A. Evaluation of this first series did not increase the inhibitory potency compared to the hit compounds. Moreover, low solubility issues burdened this series of compounds, and we halted their investigation. Conversely, the other 12 synthesized 4-amino-3-sulfamoyl-benzoic acid derivatives (series B) emerged as the best class in terms of potency when compared to nitrobenzenes, confirming the importance of the carboxylic acid for NKCC1 inhibition. We performed numerous manipulations on this class by adding the structural motifs emerged from the screening of the bumetanide analogues. Interestingly, benzoic acid derivatives bearing the *n*-octyl chain showed enhanced potency when compared to the shorter chain derivatives, particularly when combined with dimethylation of the sulfonamide as for compound **30bc**. Strikingly, insertion of the trifluoromethyl group in compound **35c (ARN23746)** at the terminal carbon of the *n*-octyl chain increased the potency, which was comparable to bumetanide's activity. Then, when tested in cultured immature neuron this compound, and found that it was able to potently restore GABAergic

transmission without any significant inhibition of the GABA<sub>A</sub>R. Hence, we further proceeded with the *in vitro* characterization of this lead compound, toward its optimization phase.

We proceeded in **Chapter 4** to the further characterization of ARN23746. As a first result, ARN23746 did not display any effect on NKCC2 or KCC2. Moreover, ARN23746 also had excellent drug-like properties and displayed no issues with off-target activity *in vitro*. In addition, pharmacokinetic analysis revealed that ARN23746 had a two-fold increase in brain penetration when compared to bumetanide. These results indicated a completely refined profile compared to bumetanide in terms of selectivity and preliminary pharmacokinetic properties, prompting us to the *in vivo* evaluation of ARN23746. Importantly, when administered *in vivo*, ARN23746 was able to recover cognitive deficits in the Ts65Dn mouse model of DS and social/repetitive behaviors in the VPA mouse model of ASD, with no diuretic effect and no overt toxicity upon chronic treatment in adult animals.

In view of further development and lead optimization, we also studied the chemical class represented by our lead compound ARN23746, in order to find novel derivatives suitable for additional *in vivo* characterization. We also wanted to define the effect of the trifluoro *n*-octyl chain combined with modification of the other substituents. We thus designed and synthesized a series 14 new analogues as described in **Chapter 5**. With these compounds, we further confirmed the importance of the carboxylic acid group in position 1 for activity, while nitrile derivative **38** displayed complete loss of activity compared to ARN23746. These data were used to guide the exploitation of the chemically accessible position 2 and design more brain penetrant analogues. Manipulation of position 5 preserved the compounds activity, although the introduction of cyclic and cycloalkyl sulfonamides had a detrimental effect on solubility. Finally, analogue **42d**, which bears a morpholine in this position, retained excellent drug-like properties and optimal activity, which suggest to test it *in vivo*, in the future.

Aside from DS and ASD, bumetanide has shown also to have positive effects for the treatment of core symptoms of several other brain disorders in mouse models. Most importantly, bumetanide has shown positive outcomes also in patients during clinical trials and case studies of neurodevelopmental (Fragile X, Asperger syndrome, schizophrenia), neurodegenerative (Parkinson and Huntington diseases)<sup>217,218</sup>



and neurological disorders (epilepsy). Besides suggesting a first (although not ideal) therapeutic option for many unmet medical needs, these results validated NKCC1 as a valuable target to treat patients. In addition, the investigation of NKCC1/KCC2 expression ratio also in other neurological disorders that benefit from a treatment with bumetanide, could further extend the possible application this therapeutic strategy. Therefore, these studies provide a solid foundation for the possible evaluation of ARN23746, or new derivatives of it, in animal models of other neurological diseases.

In addition, the recent resolution of the NKCC1<sup>32</sup> and, more recently, the KCC1<sup>219</sup> Cryo-EM structure, marked an important milestone in the understanding of the structure and mechanism of these cation chloride cotransporter proteins. The structural data reported in these works may open the way to structure-based drug design, towards the development of novel and more specific inhibitors. By taking advantage of this information, we will investigate bumetanide's and ARN23746 binding mode to NKCC1, which will further clarify their mechanism of action, leading also to a structure-based campaign for lead optimization.

In conclusion, the results generated by this study underlie ARN23746 as a solid candidate for advanced lead optimization and preclinical studies toward the future development of the first clinical drug for sustainable therapeutics in DS, ASD, and possibly several other neurological conditions characterized by depolarizing GABA signaling.

## References.

1. Ben-Ari, Y. NKCC1 Chloride Importer Antagonists Attenuate Many Neurological and Psychiatric Disorders. *Trends Neurosci* **40**, 536-554 (2017).
2. Kahle, K.T., *et al.* K-Cl cotransporters, cell volume homeostasis, and neurological disease. *Trends Mol Med* **21**, 513-523 (2015).
3. Ben-Ari, Y. Excitatory actions of gaba during development: the nature of the nurture. *Nat Rev Neurosci* **3**, 728-739 (2002).
4. Cellot, G. & Cherubini, E. GABAergic signaling as therapeutic target for autism spectrum disorders. *Front Pediatr* **2**, 70 (2014).
5. Leinekugel, X., Medina, I., Khalilov, I., Ben-Ari, Y. & Khazipov, R. Ca<sup>2+</sup> oscillations mediated by the synergistic excitatory actions of GABA(A) and NMDA receptors in the neonatal hippocampus. *Neuron* **18**, 243-255 (1997).
6. Takayama, C. & Inoue, Y. Developmental localization of potassium chloride co-transporter 2 (KCC2), GABA and vesicular GABA transporter (VGAT) in the postnatal mouse somatosensory cortex. *Neurosci Res* **67**, 137-148 (2010).
7. Kaila, K., Price, T.J., Payne, J.A., Puskarjov, M. & Voipio, J. Cation-chloride cotransporters in neuronal development, plasticity and disease. *Nat Rev Neurosci* **15**, 637-654 (2014).
8. Blaesse, P., Airaksinen, M.S., Rivera, C. & Kaila, K. Cation-chloride cotransporters and neuronal function. *Neuron* **61**, 820-838 (2009).
9. Li, H., Tornberg, J., Kaila, K., Airaksinen, M.S. & Rivera, C. Patterns of cation-chloride cotransporter expression during embryonic rodent CNS development. *Eur J Neurosci* **16**, 2358-2370 (2002).
10. Sipila, S.T., *et al.* Compensatory enhancement of intrinsic spiking upon NKCC1 disruption in neonatal hippocampus. *J Neurosci* **29**, 6982-6988 (2009).
11. Pfeiffer, C.K., *et al.* NKCC1-dependent GABAergic excitation drives synaptic network maturation during early hippocampal development. *J Neurosci* **29**, 3419-3430 (2009).
12. Delpire, E. & Kahle, K.T. The KCC3 cotransporter as a therapeutic target for peripheral neuropathy. *Expert Opin Ther Targets* **21**, 113-116 (2017).
13. Ben-Ari, Y. The GABA excitatory/inhibitory developmental sequence: a personal journey. *Neuroscience* **279**, 187-219 (2014).
14. Rivera, C., *et al.* The K<sup>+</sup>/Cl<sup>-</sup> co-transporter KCC2 renders GABA hyperpolarizing during neuronal maturation. *Nature* **397**, 251-255 (1999).
15. Stein, V., Hermans-Borgmeyer, I., Jentsch, T.J. & Hubner, C.A. Expression of the KCl cotransporter KCC2 parallels neuronal maturation and the emergence of low intracellular chloride. *J Comp Neurol* **468**, 57-64 (2004).
16. Wang, D.D. & Kriegstein, A.R. GABA regulates excitatory synapse formation in the neocortex via NMDA receptor activation. *J Neurosci* **28**, 5547-5558 (2008).

17. Young, S.Z., *et al.* NKCC1 knockdown decreases neuron production through GABA(A)-regulated neural progenitor proliferation and delays dendrite development. *J Neurosci* **32**, 13630-13638 (2012).
18. Nakajima, K., Miyazaki, H., Niisato, N. & Marunaka, Y. Essential role of NKCC1 in NGF-induced neurite outgrowth. *Biochem Biophys Res Commun* **359**, 604-610 (2007).
19. Nakajima, K., Niisato, N. & Marunaka, Y. Genistein enhances the NGF-induced neurite outgrowth. *Biomed Res* **32**, 351-356 (2011).
20. Nakajima, K., Niisato, N. & Marunaka, Y. Quercetin stimulates NGF-induced neurite outgrowth in PC12 cells via activation of Na(+)/K(+)/2Cl(-) cotransporter. *Cell Physiol Biochem* **28**, 147-156 (2011).
21. Nakajima, K.I. & Marunaka, Y. Intracellular chloride ion concentration in differentiating neuronal cell and its role in growing neurite. *Biochem Biophys Res Commun* **479**, 338-342 (2016).
22. Dzhala, V.I., *et al.* NKCC1 transporter facilitates seizures in the developing brain. *Nature Medicine* **11**, 1205-1213 (2005).
23. Wang, C., *et al.* Developmental changes in KCC1, KCC2, and NKCC1 mRNA expressions in the rat brain. *Brain Res Dev Brain Res* **139**, 59-66 (2002).
24. Watanabe, M. & Fukuda, A. Development and regulation of chloride homeostasis in the central nervous system. *Front Cell Neurosci* **9**, 371 (2015).
25. Sun, L., Yu, Z., Wang, W. & Liu, X. Both NKCC1 and anion exchangers contribute to Cl(-) accumulation in postnatal forebrain neuronal progenitors. *Eur J Neurosci* **35**, 661-672 (2012).
26. Blanquie, O., Liebmann, L., Hubner, C.A., Luhmann, H.J. & Sinning, A. NKCC1-Mediated GABAergic Signaling Promotes Postnatal Cell Death in Neocortical Cajal-Retzius Cells. *Cereb Cortex* **27**, 1644-1659 (2017).
27. Kanaka, C., *et al.* The differential expression patterns of messenger RNAs encoding K-Cl cotransporters (KCC1,2) and Na-K-2Cl cotransporter (NKCC1) in the rat nervous system. *Neuroscience* **104**, 933-946 (2001).
28. Steffensen, A.B., *et al.* Cotransporter-mediated water transport underlying cerebrospinal fluid formation. *Nat Commun* **9**, 2167 (2018).
29. Delpire, E., Lu, J., England, R., Dull, C. & Thorne, T. Deafness and imbalance associated with inactivation of the secretory Na-K-2Cl co-transporter. *Nat Genet* **22**, 192-195 (1999).
30. Vibat, C.R., Holland, M.J., Kang, J.J., Putney, L.K. & O'Donnell, M.E. Quantitation of Na<sup>+</sup>-K<sup>+</sup>-2Cl<sup>-</sup> cotransport splice variants in human tissues using kinetic polymerase chain reaction. *Anal Biochem* **298**, 218-230 (2001).
31. Morita, Y., *et al.* Characteristics of the cation cotransporter NKCC1 in human brain: alternate transcripts, expression in development, and potential relationships to brain function and schizophrenia. *J Neurosci* **34**, 4929-4940 (2014).
32. Chew, T.A., *et al.* Structure and mechanism of the cation-chloride cotransporter NKCC1. *Nature* **572**, 488-492 (2019).

33. Moore-Hoon, M.L. & Turner, R.J. The structural unit of the secretory Na<sup>+</sup>-K<sup>+</sup>-2Cl<sup>-</sup> cotransporter (NKCC1) is a homodimer. *Biochemistry* **39**, 3718-3724 (2000).
34. Pedersen, M., Carmosino, M. & Forbush, B. Intramolecular and intermolecular fluorescence resonance energy transfer in fluorescent protein-tagged Na-K-Cl cotransporter (NKCC1): sensitivity to regulatory conformational change and cell volume. *J Biol Chem* **283**, 2663-2674 (2008).
35. Parvin, M.N., Gerelsaikh, T. & Turner, R.J. Regions in the cytosolic C-terminus of the secretory Na<sup>(+)</sup>-K<sup>(+)</sup>-2Cl<sup>(-)</sup> cotransporter NKCC1 are required for its homodimerization. *Biochemistry* **46**, 9630-9637 (2007).
36. Nezu, A., Parvin, M.N. & Turner, R.J. A conserved hydrophobic tetrad near the C terminus of the secretory Na<sup>+</sup>-K<sup>+</sup>-2Cl<sup>-</sup> cotransporter (NKCC1) is required for its correct intracellular processing. *J Biol Chem* **284**, 6869-6876 (2009).
37. Monette, M.Y. & Forbush, B. Regulatory activation is accompanied by movement in the C terminus of the Na-K-Cl cotransporter (NKCC1). *J Biol Chem* **287**, 2210-2220 (2012).
38. Hartmann, A.M. & Nothwang, H.G. Molecular and evolutionary insights into the structural organization of cation chloride cotransporters. *Front Cell Neurosci* **8**, 470 (2014).
39. Delpire, E. & Gagnon, K.B. Na<sup>(+)</sup>-K<sup>(+)</sup>-2Cl<sup>(-)</sup> Cotransporter (NKCC) Physiological Function in Nonpolarized Cells and Transporting Epithelia. *Compr Physiol* **8**, 871-901 (2018).
40. Edwards, A., Castrop, H., Laghmani, K., Vallon, V. & Layton, A.T. Effects of NKCC2 isoform regulation on NaCl transport in thick ascending limb and macula densa: a modeling study. *Am J Physiol Renal Physiol* **307**, F137-146 (2014).
41. Simon, D.B., *et al.* Bartter's syndrome, hypokalaemic alkalosis with hypercalciuria, is caused by mutations in the Na-K-2Cl cotransporter NKCC2. *Nat Genet* **13**, 183-188 (1996).
42. Tucci, V., *et al.* Dominant beta-catenin mutations cause intellectual disability with recognizable syndromic features. *J Clin Invest* **124**, 1468-1482 (2014).
43. Pearson, M.M., Lu, J., Mount, D.B. & Delpire, E. Localization of the K<sup>(+)</sup>-Cl<sup>(-)</sup> cotransporter, KCC3, in the central and peripheral nervous systems: expression in the choroid plexus, large neurons and white matter tracts. *Neuroscience* **103**, 481-491 (2001).
44. Byun, N. & Delpire, E. Axonal and periaxonal swelling precede peripheral neurodegeneration in KCC3 knockout mice. *Neurobiol Dis* **28**, 39-51 (2007).
45. Lucas, O., Hilaire, C., Delpire, E. & Scamps, F. KCC3-dependent chloride extrusion in adult sensory neurons. *Mol Cell Neurosci* **50**, 211-220 (2012).
46. Seja, P., *et al.* Raising cytosolic Cl<sup>-</sup> in cerebellar granule cells affects their excitability and vestibulo-ocular learning. *EMBO J* **31**, 1217-1230 (2012).
47. Boettger, T., *et al.* Loss of K-Cl co-transporter KCC3 causes deafness, neurodegeneration and reduced seizure threshold. *EMBO J* **22**, 5422-5434 (2003).
48. Howard, H.C., *et al.* The K-Cl cotransporter KCC3 is mutant in a severe peripheral neuropathy associated with agenesis of the corpus callosum. *Nat Genet* **32**, 384-392 (2002).

49. Boettger, T., *et al.* Deafness and renal tubular acidosis in mice lacking the K-Cl co-transporter Kcc4. *Nature* **416**, 874-878 (2002).
50. Sedmak, G., *et al.* Developmental Expression Patterns of KCC2 and Functionally Associated Molecules in the Human Brain. *Cereb Cortex* **26**, 4574-4589 (2016).
51. Mitchell, K.J. The genetics of neurodevelopmental disease. *Curr Opin Neurobiol* **21**, 197-203 (2011).
52. Jaggi, A.S., Kaur, A., Bali, A. & Singh, N. Expanding Spectrum of Sodium Potassium Chloride Co-transporters in the Pathophysiology of Diseases. *Curr Neuropharmacol* **13**, 369-388 (2015).
53. Medina, I., *et al.* Current view on the functional regulation of the neuronal K(+)-Cl(-) cotransporter KCC2. *Front Cell Neurosci* **8**, 27 (2014).
54. Schulte, J.T., Wierenga, C.J. & Bruining, H. Chloride transporters and GABA polarity in developmental, neurological and psychiatric conditions. *Neurosci Biobehav Rev* **90**, 260-271 (2018).
55. Wu, H., *et al.* The K(+)-Cl(-) Cotransporter KCC2 and Chloride Homeostasis: Potential Therapeutic Target in Acute Central Nervous System Injury. *Mol Neurobiol* **53**, 2141-2151 (2016).
56. Kharod, S.C., Kang, S.K. & Kadam, S.D. Off-Label Use of Bumetanide for Brain Disorders: An Overview. *Front Neurosci* **13**, 310 (2019).
57. Gagnon, M., *et al.* Chloride extrusion enhancers as novel therapeutics for neurological diseases. *Nat Med* **19**, 1524-1528 (2013).
58. Cardarelli, R.A., *et al.* The small molecule CLP257 does not modify activity of the K(+)-Cl(-) co-transporter KCC2 but does potentiate GABAA receptor activity. *Nat Med* **23**, 1394-1396 (2017).
59. Gagnon, M., *et al.* Reply to The small molecule CLP257 does not modify activity of the K(+)-Cl(-) co-transporter KCC2 but does potentiate GABAA receptor activity. *Nat Med* **23**, 1396-1398 (2017).
60. Tang, X., *et al.* Pharmacological enhancement of KCC2 gene expression exerts therapeutic effects on human Rett syndrome neurons and Mecp2 mutant mice. *Sci Transl Med* **11**(2019).
61. Loscher, W., Puskarjov, M. & Kaila, K. Cation-chloride cotransporters NKCC1 and KCC2 as potential targets for novel antiepileptic and antiepileptogenic treatments. *Neuropharmacology* **69**, 62-74 (2013).
62. Di Cristo, G.A., PN; Hamidi, S; Avoli, M;. KCC2, epileptiform synchronization, and epileptic disorders. *Progress in Neurobiology* **162**, 1-16 (2018).
63. Okabe, A., *et al.* Amygdala kindling induces upregulation of mRNA for NKCC1, a Na(+), K(+)-2Cl(-) cotransporter, in the rat piriform cortex. *Neurosci Res* **44**, 225-229 (2002).
64. Li, X., *et al.* Long-term expressional changes of Na+ -K+ -Cl- co-transporter 1 (NKCC1) and K+ -Cl- co-transporter 2 (KCC2) in CA1 region of hippocampus following lithium-pilocarpine induced status epilepticus (PISE). *Brain Res* **1221**, 141-146 (2008).
65. Sivakumaran, S. & Maguire, J. Bumetanide reduces seizure progression and the development of pharmacoresistant status epilepticus. *Epilepsia* **57**, 222-232 (2016).
66. Woo, N.S., *et al.* Hyperexcitability and epilepsy associated with disruption of the mouse neuronal-specific K-Cl cotransporter gene. *Hippocampus* **12**, 258-268 (2002).

67. Cleary, R.T., *et al.* Bumetanide enhances phenobarbital efficacy in a rat model of hypoxic neonatal seizures. *PLoS One* **8**, e57148 (2013).
68. Dzhala, V.I., Brumback, A.C. & Staley, K.J. Bumetanide enhances phenobarbital efficacy in a neonatal seizure model. *Ann Neurol* **63**, 222-235 (2008).
69. Dzhala, V.I., *et al.* Progressive NKCC1-dependent neuronal chloride accumulation during neonatal seizures. *J Neurosci* **30**, 11745-11761 (2010).
70. Edwards, D.A., *et al.* Bumetanide alleviates epileptogenic and neurotoxic effects of sevoflurane in neonatal rat brain. *Anesthesiology* **112**, 567-575 (2010).
71. Eftekhari, S., *et al.* Response to Comment on "Oxytocin-mediated GABA inhibition during delivery attenuates autism pathogenesis in rodent offspring". *Science* **346**, 176 (2014).
72. Hu, J.J., *et al.* Bumetanide reduce the seizure susceptibility induced by pentylentetrazol via inhibition of aberrant hippocampal neurogenesis in neonatal rats after hypoxia-ischemia. *Brain Res Bull* **130**, 188-199 (2017).
73. Kelley, M.R., *et al.* Locally Reducing KCC2 Activity in the Hippocampus is Sufficient to Induce Temporal Lobe Epilepsy. *EBioMedicine* **32**, 62-71 (2018).
74. Koyama, R., *et al.* GABAergic excitation after febrile seizures induces ectopic granule cells and adult epilepsy. *Nat Med* **18**, 1271-1278 (2012).
75. MacKenzie, G. & Maguire, J. Chronic stress shifts the GABA reversal potential in the hippocampus and increases seizure susceptibility. *Epilepsy Res* **109**, 13-27 (2015).
76. MacKenzie, G., O'Toole, K.K., Moss, S.J. & Maguire, J. Compromised GABAergic inhibition contributes to tumor-associated epilepsy. *Epilepsy Res* **126**, 185-196 (2016).
77. Marguet, S.L., *et al.* Treatment during a vulnerable developmental period rescues a genetic epilepsy. *Nat Med* **21**, 1436-1444 (2015).
78. Mazarati, A., Shin, D. & Sankar, R. Bumetanide inhibits rapid kindling in neonatal rats. *Epilepsia* **50**, 2117-2122 (2009).
79. Nardou, R., Ben-Ari, Y. & Khalilov, I. Bumetanide, an NKCC1 antagonist, does not prevent formation of epileptogenic focus but blocks epileptic focus seizures in immature rat hippocampus. *J Neurophysiol* **101**, 2878-2888 (2009).
80. Reid, A.Y., Riazi, K., Campbell Teskey, G. & Pittman, Q.J. Increased excitability and molecular changes in adult rats after a febrile seizure. *Epilepsia* **54**, e45-48 (2013).
81. Robel, S., *et al.* Reactive astrogliosis causes the development of spontaneous seizures. *J Neurosci* **35**, 3330-3345 (2015).
82. Santos, L.E.C., *et al.* Long-term alcohol exposure elicits hippocampal nonsynaptic epileptiform activity changes associated with expression and functional changes in NKCC1, KCC2 co-transporters and Na(+)/K(+)-ATPase. *Neuroscience* **340**, 530-541 (2017).
83. Tao, K., Ichikawa, J., Matsuki, N., Ikegaya, Y. & Koyama, R. Experimental febrile seizures induce age-dependent structural plasticity and improve memory in mice. *Neuroscience* **318**, 34-44 (2016).

84. Tollner, K., Brandt, C., Erker, T. & Loscher, W. Bumetanide is not capable of terminating status epilepticus but enhances phenobarbital efficacy in different rat models. *Eur J Pharmacol* **746**, 78-88 (2015).
85. Wang, F., *et al.* NKCC1 up-regulation contributes to early post-traumatic seizures and increased post-traumatic seizure susceptibility. *Brain Struct Funct* **222**, 1543-1556 (2017).
86. Zhang, J., *et al.* Inhibition of Na(+)-K(+)-2Cl(-) cotransporter attenuates blood-brain-barrier disruption in a mouse model of traumatic brain injury. *Neurochem Int* **111**, 23-31 (2017).
87. Huberfeld, G., Blauwblomme, T. & Miles, R. Hippocampus and epilepsy: Findings from human tissues. *Rev Neurol (Paris)* **171**, 236-251 (2015).
88. Huberfeld, G., *et al.* Perturbed chloride homeostasis and GABAergic signaling in human temporal lobe epilepsy. *J Neurosci* **27**, 9866-9873 (2007).
89. Munoz, A., Mendez, P., DeFelipe, J. & Alvarez-Leefmans, F.J. Cation-chloride cotransporters and GABA-ergic innervation in the human epileptic hippocampus. *Epilepsia* **48**, 663-673 (2007).
90. Palma, E., *et al.* Anomalous levels of Cl<sup>-</sup> transporters in the hippocampal subiculum from temporal lobe epilepsy patients make GABA excitatory. *Proc Natl Acad Sci U S A* **103**, 8465-8468 (2006).
91. Sen, A., *et al.* Increased NKCC1 expression in refractory human epilepsy. *Epilepsy Res* **74**, 220-227 (2007).
92. Kim, D.Y., *et al.* GABAA receptor-mediated activation of L-type calcium channels induces neuronal excitation in surgically resected human hypothalamic hamartomas. *Epilepsia* **49**, 861-871 (2008).
93. Jansen, L.A., Peugh, L.D., Roden, W.H. & Ojemann, J.G. Impaired maturation of cortical GABA(A) receptor expression in pediatric epilepsy. *Epilepsia* **51**, 1456-1467 (2010).
94. Conti, L., *et al.* Anomalous levels of Cl<sup>-</sup> transporters cause a decrease of GABAergic inhibition in human peritumoral epileptic cortex. *Epilepsia* **52**, 1635-1644 (2011).
95. Pallud, J., *et al.* Cortical GABAergic excitation contributes to epileptic activities around human glioma. *Sci Transl Med* **6**, 244ra289 (2014).
96. Ruffolo, G., *et al.* A novel GABAergic dysfunction in human Dravet syndrome. *Epilepsia* **59**, 2106-2117 (2018).
97. Kahle, K.T., Barnett, S.M., Sassower, K.C. & Staley, K.J. Decreased seizure activity in a human neonate treated with bumetanide, an inhibitor of the Na(+)-K(+)-2Cl(-) cotransporter NKCC1. *J Child Neurol* **24**, 572-576 (2009).
98. Pressler, R.M., *et al.* Bumetanide for the treatment of seizures in newborn babies with hypoxic ischaemic encephalopathy (NEMO): an open-label, dose finding, and feasibility phase 1/2 trial. *Lancet Neurol* **14**, 469-477 (2015).
99. Ben-Ari, Y., Damier, P. & Lemonnier, E. Failure of the Nemo Trial: Bumetanide Is a Promising Agent to Treat Many Brain Disorders but Not Newborn Seizures. *Front Cell Neurosci* **10**, 90 (2016).
100. Lacivita, E., Perrone, R., Margari, L. & Leopoldo, M. Targets for Drug Therapy for Autism Spectrum Disorder: Challenges and Future Directions. *J Med Chem* **60**, 9114-9141 (2017).

101. Lewis, M.L., Kesler, M., Candy, S.A., Rho, J.M. & Pittman, Q.J. Comorbid epilepsy in autism spectrum disorder: Implications of postnatal inflammation for brain excitability. *Epilepsia* **59**, 1316-1326 (2018).
102. Delpire, E., *et al.* Small-molecule screen identifies inhibitors of the neuronal K-Cl cotransporter KCC2. *Proc Natl Acad Sci U S A* **106**, 5383-5388 (2009).
103. Lemonnier, E., *et al.* Treating Fragile X syndrome with the diuretic bumetanide: a case report. *Acta Paediatr* **102**, e288-290 (2013).
104. Kaufmann, W.E., *et al.* Autism Spectrum Disorder in Fragile X Syndrome: Cooccurring Conditions and Current Treatment. *Pediatrics* **139**, S194-S206 (2017).
105. Moss, J., Richards, C., Nelson, L. & Oliver, C. Prevalence of autism spectrum disorder symptomatology and related behavioural characteristics in individuals with Down syndrome. *Autism* **17**, 390-404 (2013).
106. Merner, N.D., *et al.* Regulatory domain or CpG site variation in SLC12A5, encoding the chloride transporter KCC2, in human autism and schizophrenia. *Front Cell Neurosci* **9**, 386 (2015).
107. Marrosu, F., Marrosu, G., Rachel, M.G. & Biggio, G. Paradoxical reactions elicited by diazepam in children with classic autism. *Funct Neurol* **2**, 355-361 (1987).
108. Bruining, H., *et al.* Paradoxical Benzodiazepine Response: A Rationale for Bumetanide in Neurodevelopmental Disorders? *Pediatrics* **136**, e539-543 (2015).
109. Lemonnier, E. & Ben-Ari, Y. The diuretic bumetanide decreases autistic behaviour in five infants treated during 3 months with no side effects. *Acta Paediatr* **99**, 1885-1888 (2010).
110. Lemonnier, E., *et al.* A randomised controlled trial of bumetanide in the treatment of autism in children. *Transl Psychiatry* **2**, e202 (2012).
111. Lemonnier, E., *et al.* Effects of bumetanide on neurobehavioral function in children and adolescents with autism spectrum disorders. *Transl Psychiatry* **7**, e1056 (2017).
112. Grandgeorge, M., Lemonnier, E., Degrez, C. & Jallot, N. The effect of bumetanide treatment on the sensory behaviours of a young girl with Asperger syndrome. *BMJ Case Rep* **2014**(2014).
113. Ehinger, Y., Matagne, V., Villard, L. & Roux, J.C. Rett syndrome from bench to bedside: recent advances. *F1000Res* **7**, 398 (2018).
114. Duarte, S.T., *et al.* Abnormal expression of cerebrospinal fluid cation chloride cotransporters in patients with Rett syndrome. *PLoS One* **8**, e68851 (2013).
115. Tang, X., *et al.* KCC2 rescues functional deficits in human neurons derived from patients with Rett syndrome. *Proc Natl Acad Sci U S A* **113**, 751-756 (2016).
116. Banerjee, A., *et al.* Jointly reduced inhibition and excitation underlies circuit-wide changes in cortical processing in Rett syndrome. *Proc Natl Acad Sci U S A* **113**, E7287-E7296 (2016).
117. Morel, A., *et al.* Overview of Social Cognitive Dysfunctions in Rare Developmental Syndromes With Psychiatric Phenotype. *Front Pediatr* **6**, 102 (2018).



118. He, Q., Nomura, T., Xu, J. & Contractor, A. The developmental switch in GABA polarity is delayed in fragile X mice. *J Neurosci* **34**, 446-450 (2014).
119. Tyzio, R., *et al.* Oxytocin-mediated GABA inhibition during delivery attenuates autism pathogenesis in rodent offspring. *Science* **343**, 675-679 (2014).
120. Owen, M.J., Sawa, A. & Mortensen, P.B. Schizophrenia. *Lancet* **388**, 86-97 (2016).
121. Dean, B., Keriakous, D., Scarr, E. & Thomas, E.A. Gene expression profiling in Brodmann's area 46 from subjects with schizophrenia. *Aust N Z J Psychiatry* **41**, 308-320 (2007).
122. Hyde, T.M., *et al.* Expression of GABA signaling molecules KCC2, NKCC1, and GAD1 in cortical development and schizophrenia. *J Neurosci* **31**, 11088-11095 (2011).
123. Arion, D. & Lewis, D.A. Altered expression of regulators of the cortical chloride transporters NKCC1 and KCC2 in schizophrenia. *Arch Gen Psychiatry* **68**, 21-31 (2011).
124. Larimore, J., *et al.* Dysbindin Deficiency Modifies the Expression of GABA Neuron and Ion Permeation Transcripts in the Developing Hippocampus. *Front Genet* **8**, 28 (2017).
125. Yang, S.S., *et al.* Effects of SPAK knockout on sensorimotor gating, novelty exploration, and brain area-dependent expressions of NKCC1 and KCC2 in a mouse model of schizophrenia. *Prog Neuropsychopharmacol Biol Psychiatry* **61**, 30-36 (2015).
126. Lemonnier, E., Lazartigues, A. & Ben-Ari, Y. Treating Schizophrenia With the Diuretic Bumetanide: A Case Report. *Clin Neuropharmacol* **39**, 115-117 (2016).
127. Rahmzadeh, R., *et al.* Effect of bumetanide, a selective NKCC1 inhibitor, on hallucinations of schizophrenic patients; a double-blind randomized clinical trial. *Schizophr Res* **184**, 145-146 (2017).
128. Rahmzadeh, R., *et al.* Lack of the effect of bumetanide, a selective NKCC1 inhibitor, in patients with schizophrenia: A double-blind randomized trial. *Psychiatry Clin Neurosci* **71**, 72-73 (2017).
129. van Slegtenhorst, M., *et al.* Identification of the tuberous sclerosis gene TSC1 on chromosome 9q34. *Science* **277**, 805-808 (1997).
130. Ghajar, J. Traumatic brain injury. *Lancet* **356**, 923-929 (2000).
131. Park, E., Bell, J.D. & Baker, A.J. Traumatic brain injury: can the consequences be stopped? *CMAJ* **178**, 1163-1170 (2008).
132. Lu, K.T., Cheng, N.C., Wu, C.Y. & Yang, Y.L. NKCC1-mediated traumatic brain injury-induced brain edema and neuron death via Raf/MEK/MAPK cascade. *Crit Care Med* **36**, 917-922 (2008).
133. Lu, K.T., Huang, T.C., Tsai, Y.H. & Yang, Y.L. Transient receptor potential vanilloid type 4 channels mediate Na-K-Cl-co-transporter-induced brain edema after traumatic brain injury. *J Neurochem* **140**, 718-727 (2017).
134. Lu, K.T., *et al.* Inhibition of the Na<sup>+</sup>-K<sup>+</sup>-2Cl<sup>-</sup>-cotransporter in choroid plexus attenuates traumatic brain injury-induced brain edema and neuronal damage. *Eur J Pharmacol* **548**, 99-105 (2006).
135. Lu, K.T., *et al.* Bumetanide administration attenuated traumatic brain injury through IL-1 overexpression. *Neurol Res* **29**, 404-409 (2007).

136. Baker, S.J., Ellison, D.W. & Gutmann, D.H. Pediatric gliomas as neurodevelopmental disorders. *Glia* **64**, 879-895 (2016).
137. Sontheimer, H. An unexpected role for ion channels in brain tumor metastasis. *Exp Biol Med (Maywood)* **233**, 779-791 (2008).
138. Haas, B.R. & Sontheimer, H. Inhibition of the Sodium-Potassium-Chloride Cotransporter Isoform-1 reduces glioma invasion. *Cancer Res* **70**, 5597-5606 (2010).
139. Garzon-Muvdi, T., *et al.* Regulation of brain tumor dispersal by NKCC1 through a novel role in focal adhesion regulation. *PLoS Biol* **10**, e1001320 (2012).
140. Schiapparelli, P., *et al.* NKCC1 Regulates Migration Ability of Glioblastoma Cells by Modulation of Actin Dynamics and Interacting with Cofilin. *EBioMedicine* **21**, 94-103 (2017).
141. Vacca, R.A., *et al.* Down syndrome: Neurobiological alterations and therapeutic targets. *Neurosci Biobehav Rev* **98**, 234-255 (2019).
142. Kazemi, M., Salehi, M. & Kheirollahi, M. Down Syndrome: Current Status, Challenges and Future Perspectives. *Int J Mol Cell Med* **5**, 125-133 (2016).
143. Reeves, R.H., *et al.* A mouse model for Down syndrome exhibits learning and behaviour deficits. *Nat Genet* **11**, 177-184 (1995).
144. Belichenko, P.V., *et al.* Synaptic structural abnormalities in the Ts65Dn mouse model of Down Syndrome. *J Comp Neurol* **480**, 281-298 (2004).
145. Chakrabarti, L., *et al.* Olig1 and Olig2 triplication causes developmental brain defects in Down syndrome. *Nat Neurosci* **13**, 927-934 (2010).
146. Chakrabarti, L., Galdzicki, Z. & Haydar, T.F. Defects in embryonic neurogenesis and initial synapse formation in the forebrain of the Ts65Dn mouse model of Down syndrome. *J. Neuroscience* **27**, 11483-11495 (2007).
147. Contestabile, A., Benfenati, F. & Gasparini, L. Communication breaks-Down: from neurodevelopment defects to cognitive disabilities in Down syndrome. *Prog Neurobiol* **91**, 1-22 (2010).
148. Contestabile, A., *et al.* Cell cycle alteration and decreased cell proliferation in the hippocampal dentate gyrus and in the neocortical germinal matrix of fetuses with Down syndrome and in Ts65Dn mice. *Hippocampus* **17**, 665-678 (2007).
149. Contestabile, A., *et al.* Lithium rescues synaptic plasticity and memory in Down syndrome mice. *J Clin Invest* **123**, 348-361 (2013).
150. Costa, A.C. & Grybko, M.J. Deficits in hippocampal CA1 LTP induced by TBS but not HFS in the Ts65Dn mouse: a model of Down syndrome. *Neurosci Lett* **382**, 317-322 (2005).
151. Kleschevnikov, A.M., *et al.* Hippocampal long-term potentiation suppressed by increased inhibition in the Ts65Dn mouse, a genetic model of Down syndrome. *J Neurosci* **24**, 8153-8160 (2004).
152. Costa, A.C., Scott-McKean, J.J. & Stasko, M.R. Acute injections of the NMDA receptor antagonist memantine rescue performance deficits of the Ts65Dn mouse model of Down syndrome on a fear conditioning test. *Neuropsychopharmacology* **33**, 1624-1632 (2008).

153. Fernandez, F., *et al.* Pharmacotherapy for cognitive impairment in a mouse model of Down syndrome. *Nat Neurosci* **10**, 411-413 (2007).
154. Escorihuela, R.M., *et al.* A behavioral assessment of Ts65Dn mice: a putative Down syndrome model. *Neurosci Lett* **199**, 143-146 (1995).
155. Sago, H., *et al.* Genetic dissection of region associated with behavioral abnormalities in mouse models for Down syndrome. *Pediatr Res* **48**, 606-613 (2000).
156. Colas, D., *et al.* Sleep and EEG features in genetic models of Down syndrome. *Neurobiol Dis* **30**, 1-7 (2008).
157. Das, D., *et al.* Increased incidence of intermittent hypoxemia in the Ts65Dn mouse model of Down syndrome. *Neurosci Lett* **604**, 91-96 (2015).
158. Stewart, L.S., Persinger, M.A., Cortez, M.A. & Snead, O.C., 3rd. Chronobiometry of behavioral activity in the Ts65Dn model of Down syndrome. *Behav Genet* **37**, 388-398 (2007).
159. Clark, S., Schwalbe, J., Stasko, M.R., Yarowsky, P.J. & Costa, A.C. Fluoxetine rescues deficient neurogenesis in hippocampus of the Ts65Dn mouse model for Down syndrome. *Exp Neurol* **200**, 256-261 (2006).
160. De la Torre, R. & Dierssen, M. Therapeutic approaches in the improvement of cognitive performance in Down syndrome: past, present, and future. *Prog Brain Res* **197**, 1-14 (2012).
161. Costa, A.C. & Scott-McKean, J.J. Prospects for improving brain function in individuals with Down syndrome. *CNS Drugs* **27**, 679-702 (2013).
162. De la Torre, R., *et al.* Epigallocatechin-3-gallate, a DYRK1A inhibitor, rescues cognitive deficits in Down syndrome mouse models and in humans. *Mol Nutr Food Res* **58**, 278-288 (2014).
163. Riediger, C., *et al.* Adverse Effects of Antidepressants for Chronic Pain: A Systematic Review and Meta-analysis. *Front Neurol* **8**, 307 (2017).
164. Hanney, M., *et al.* Memantine for dementia in adults older than 40 years with Down's syndrome (MEADOWS): a randomised, double-blind, placebo-controlled trial. *Lancet* **379**, 528-536 (2012).
165. Kishnani, P.S., *et al.* Donepezil for treatment of cognitive dysfunction in children with Down syndrome aged 10-17. *Am J Med Genet A* **152A**, 3028-3035 (2010).
166. Martinez-Cue, C., *et al.* Reducing GABAA alpha5 receptor-mediated inhibition rescues functional and neuromorphological deficits in a mouse model of down syndrome. *J Neurosci* **33**, 3953-3966 (2013).
167. ClinicalTrials.gov. A Study of RG1662 in Adults and Adolescents With Down Syndrome (CLEMATIS) - NCT02024789. (2013).
168. Engevik, L.I., Naess, K.A. & Hagtvet, B.E. Cognitive stimulation of pupils with Down syndrome: A study of inferential talk during book-sharing. *Res Dev Disabil* **55**, 287-300 (2016).
169. Martinez-Cue, C., *et al.* Behavioral, cognitive and biochemical responses to different environmental conditions in male Ts65Dn mice, a model of Down syndrome. *Behav Brain Res* **163**, 174-185 (2005).
170. Krinsky-McHale, S.J., *et al.* Vision deficits in adults with Down syndrome. *J Appl Res Intellect Disabil* **27**, 247-263 (2014).

171. Contestabile, A., Magara, S. & Cancedda, L. The GABAergic Hypothesis for Cognitive Disabilities in Down Syndrome. *Frontiers in Cellular Neurosciences* **11**(2017).
172. Perez-Cremades, D., *et al.* Alteration of inhibitory circuits in the somatosensory cortex of Ts65Dn mice, a model for Down's syndrome. *J Neural Transm (Vienna)* **117**, 445-455 (2010).
173. Bhattacharyya, A., McMillan, E., Chen, S.I., Wallace, K. & Svendsen, C.N. A critical period in cortical interneuron neurogenesis in down syndrome revealed by human neural progenitor cells. *Dev Neurosci* **31**, 497-510 (2009).
174. Kobayashi, K., *et al.* Cerebral cortical calbindin D28K and parvalbumin neurones in Down's syndrome. *Neurosci Lett* **113**, 17-22 (1990).
175. Kleschevnikov, A.M., Belichenko, P.V., Salehi, A. & Wu, C. Discoveries in Down syndrome: moving basic science to clinical care. *Prog Brain Res* **197**, 199-221 (2012).
176. Deidda, G., *et al.* Reversing excitatory GABAAR signaling restores synaptic plasticity and memory in a mouse model of Down syndrome. *Nat Med* **21**, 318-326 (2015).
177. Flamenbaum, W. & Friedman, R. Pharmacology, therapeutic efficacy, and adverse effects of bumetanide, a new "loop" diuretic. *Pharmacotherapy* **2**, 213-222 (1982).
178. Ward, A. & Heel, R.C. Bumetanide. A review of its pharmacodynamic and pharmacokinetic properties and therapeutic use. *Drugs* **28**, 426-464 (1984).
179. Arieff, A.I., Ayus, J.C. & Fraser, C.L. Hyponatraemia and death or permanent brain damage in healthy children. *BMJ* **304**, 1218-1222 (1992).
180. Donovan, M.D., O'Brien, F.E., Boylan, G.B., Cryan, J.F. & Griffin, B.T. The effect of organic anion transporter 3 inhibitor probenecid on bumetanide levels in the brain: an integrated in vivo microdialysis study in the rat. *J Pharm Pharmacol* **67**, 501-510 (2015).
181. Donovan, M.D., Schellekens, H., Boylan, G.B., Cryan, J.F. & Griffin, B.T. In vitro bidirectional permeability studies identify pharmacokinetic limitations of NKCC1 inhibitor bumetanide. *Eur J Pharmacol* **770**, 117-125 (2016).
182. Romermann, K., *et al.* Multiple blood-brain barrier transport mechanisms limit bumetanide accumulation, and therapeutic potential, in the mammalian brain. *Neuropharmacology* **117**, 182-194 (2017).
183. Tollner, K., Brandt, C., Romermann, K. & Loscher, W. The organic anion transport inhibitor probenecid increases brain concentrations of the NKCC1 inhibitor bumetanide. *Eur J Pharmacol* **746**, 167-173 (2015).
184. Wang, S., *et al.* In vivo effects of bumetanide at brain concentrations incompatible with NKCC1 inhibition on newborn DGC structure and spontaneous EEG seizures following hypoxia-induced neonatal seizures. *Neuroscience* **286**, 203-215 (2015).
185. Tollner, K., *et al.* A novel prodrug-based strategy to increase effects of bumetanide in epilepsy. *Ann Neurol* **75**, 550-562 (2014).

186. Erker, T., *et al.* The bumetanide prodrug BUM5, but not bumetanide, potentiates the antiseizure effect of phenobarbital in adult epileptic mice. *Epilepsia* **57**, 698-705 (2016).
187. Nielsen, O.B.T.F., P.W. Structure-activity relationships of aminobenzoic acid diuretics and related compounds. *Am. Chem. Soc. Symp. Ser. , Diuretic Agents* **83**, 12-23 (1978).
188. Brandt, C., *et al.* Bumepamine, a brain-permeant benzylamine derivative of bumetanide, does not inhibit NKCC1 but is more potent to enhance phenobarbital's anti-seizure efficacy. *Neuropharmacology* **143**, 186-204 (2018).
189. Hampel, P., Romermann, K., MacAulay, N. & Loscher, W. Azosemide is more potent than bumetanide and various other loop diuretics to inhibit the sodium-potassium-chloride-cotransporter human variants hNKCC1A and hNKCC1B. *Sci Rep* **8**, 9877 (2018).
190. Huang, H., *et al.* A Novel Na(+)-K(+)-Cl(-) Cotransporter 1 Inhibitor STS66\* Reduces Brain Damage in Mice After Ischemic Stroke. *Stroke* **50**, 1021-1025 (2019).
191. Auer, T., Schreppel, P., Erker, T. & Schwarzer, C. Functional characterization of novel bumetanide derivatives for epilepsy treatment. *Neuropharmacology*, 107754 (2019).
192. Lykke, K., *et al.* The search for NKCC1-selective drugs for the treatment of epilepsy: Structure-function relationship of bumetanide and various bumetanide derivatives in inhibiting the human cation-chloride cotransporter NKCC1A. *Epilepsy Behav* **59**, 42-49 (2016).
193. Watts, S.D., Suchland, K.L., Amara, S.G. & Ingram, S.L. A sensitive membrane-targeted biosensor for monitoring changes in intracellular chloride in neuronal processes. *PLoS One* **7**, e35373 (2012).
194. Cancedda, L., Fiumelli, H., Chen, K. & Poo, M.M. Excitatory GABA action is essential for morphological maturation of cortical neurons in vivo. *J Neurosci* **27**, 5224-5235 (2007).
195. Nepali, K., Lee, H.Y. & Liou, J.P. Nitro-Group-Containing Drugs. *J Med Chem* **62**, 2851-2893 (2019).
196. Korpi, E.R., Kuner, T., Seeburg, P.H. & Luddens, H. Selective antagonist for the cerebellar granule cell-specific gamma-aminobutyric acid type A receptor. *Mol Pharmacol* **47**, 283-289 (1995).
197. Korpi, E.R. & Luddens, H. Furosemide interactions with brain GABAA receptors. *Br J Pharmacol* **120**, 741-748 (1997).
198. Minier, F. & Sigel, E. Positioning of the alpha-subunit isoforms confers a functional signature to gamma-aminobutyric acid type A receptors. *Proc Natl Acad Sci U S A* **101**, 7769-7774 (2004).
199. Stefan, M.I. & Le Novere, N. Cooperative binding. *PLoS Comput Biol* **9**, e1003106 (2013).
200. Wang, Q. & Pang, Y.P. Preference of small molecules for local minimum conformations when binding to proteins. *PLoS One* **2**, e820 (2007).
201. Dixon, S.L., Smondyrev, A.M. & Rao, S.N. PHASE: a novel approach to pharmacophore modeling and 3D database searching. *Chemical biology & drug design* **67**, 370-372 (2006).
202. Ganguly, K., Schinder, A.F., Wong, S.T. & Poo, M. GABA itself promotes the developmental switch of neuronal GABAergic responses from excitation to inhibition. *Cell* **105**, 521-532 (2001).

203. Carmosino, M., Rizzo, F., Torretta, S., Procino, G. & Svelto, M. High-throughput fluorescent-based NKCC functional assay in adherent epithelial cells. *BMC Cell Biol* **14**, 16 (2013).
204. Kleschevnikov, A.M., *et al.* Deficits in cognition and synaptic plasticity in a mouse model of Down syndrome ameliorated by GABAB receptor antagonists. *J Neurosci* **32**, 9217-9227 (2012).
205. Silverman, J.L., Yang, M., Lord, C. & Crawley, J.N. Behavioural phenotyping assays for mouse models of autism. *Nature reviews. Neuroscience* **11**, 490-502 (2010).
206. Eissa, N., *et al.* The histamine H3R antagonist DL77 attenuates autistic behaviors in a prenatal valproic acid-induced mouse model of autism. *Scientific reports* **8**, 13077 (2018).
207. Drapeau, E., Riad, M., Kajiwara, Y. & Buxbaum, J.D. Behavioral Phenotyping of an Improved Mouse Model of Phelan-McDermid Syndrome with a Complete Deletion of the Shank3 Gene. *eNeuro* **5**(2018).
208. Thomas, A., *et al.* Marble burying reflects a repetitive and perseverative behavior more than novelty-induced anxiety. *Psychopharmacology* **204**, 361-373 (2009).
209. Campolongo, M., *et al.* Sociability deficits after prenatal exposure to valproic acid are rescued by early social enrichment. *Molecular autism* **9**, 36 (2018).
210. Biot, C., Bauer, H., Schirmer, R.H. & Davioud-Charvet, E. 5-substituted tetrazoles as bioisosteres of carboxylic acids. Bioisosterism and mechanistic studies on glutathione reductase inhibitors as antimalarials. *J Med Chem* **47**, 5972-5983 (2004).
211. Kraus, J.L. Isosterism and molecular modification in drug design: tetrazole analogue of GABA: effects on enzymes of the gamma-aminobutyrate system. *Pharmacol Res Commun* **15**, 183-189 (1983).
212. Neochoritis, C.G., Zhao, T. & Domling, A. Tetrazoles via Multicomponent Reactions. *Chem Rev* **119**, 1970-2042 (2019).
213. Vorona, S., Artamonova, T., Zevatskii, Y. & Myznikov, L. An Improved Protocol for the Preparation of 5-Substituted Tetrazoles from Organic Thiocyanates and Nitriles. *Synthesis* **46**, 781-786 (2014).
214. Kaeding, W.W. Oxidation of Aromatic Acids. IV. Decarboxylation of Salicylic Acids. *The Journal of Organic Chemistry* **29**, 2556-2559 (1964).
215. Kakigi, A., Nishimura, M., Takeda, T., Taguchi, D. & Nishioka, R. Expression of aquaporin1, 3, and 4, NKCC1, and NKCC2 in the human endolymphatic sac. *Auris Nasus Larynx* **36**, 135-139 (2009).
216. Pushpakom, S., *et al.* Drug repurposing: progress, challenges and recommendations. *Nat Rev Drug Discov* **18**, 41-58 (2019).
217. Lozovaya, N., *et al.* GABAergic inhibition in dual-transmission cholinergic and GABAergic striatal interneurons is abolished in Parkinson disease. *Nat Commun* **9**, 1422 (2018).
218. Dargaie, Z., *et al.* Restoring GABAergic inhibition rescues memory deficits in a Huntington's disease mouse model. *Proc Natl Acad Sci U S A* **115**, E1618-E1626 (2018).
219. Liu, S., *et al.* Cryo-EM structures of the human cation-chloride cotransporter KCC1. *Science* **366**, 505-508 (2019).

**Appendix.**

Off target profile of ARN23746 in Safety47™ Panel (Eurofins).

Gene Symbol	Assay Mode	ARN23746 10µM % of Response		
		Replicate1	Replicate2	Average
<b>GPCRs</b>				
ADORA2A	Agonist	0.0	0.0	0.0
ADORA2A	Antagonist	35.6	42.8	39.2
ADRA1A	Agonist	1.4	0.1	0.7
ADRA1A	Antagonist	2.8	5.4	4.1
ADRA2A	Agonist	13.2	12.3	12.7
ADRA2A	Antagonist	0.0	0.0	0.0
ADRB1	Agonist	0.0	0.0	0.0
ADRB1	Antagonist	67.2	83.7	75.4
ADRB2	Agonist	0.0	0.0	0.0
ADRB2	Antagonist	27.0	39.3	33.2
AVPR1A	Agonist	4.4	3.2	3.8
AVPR1A	Antagonist	4.4	0.0	2.2
CCKAR	Agonist	2.5	1.9	2.2
CCKAR	Antagonist	0.0	1.5	0.7
CHRM1	Agonist	0.0	0.0	0.0
CHRM1	Antagonist	37.9	23.1	30.5
CHRM2	Agonist	15.0	12.2	13.6
CHRM2	Antagonist	0.0	0.0	0.0
CHRM3	Agonist	0.0	0.0	0.0
CHRM3	Antagonist	11.8	14.6	13.2
CNR1	Agonist	66.7	68.9	67.8
CNR1	Antagonist	0.0	0.0	0.0
CNR2	Agonist	6.2	6.4	6.3
CNR2	Antagonist	7.8	9.4	8.6
DRD1	Agonist	0.1	0.0	0.1
DRD1	Antagonist	44.8	48.7	46.8
DRD2S	Agonist	24.6	15.0	19.8
DRD2S	Antagonist	0.0	0.0	0.0
EDNRA	Agonist	4.4	2.0	3.2
EDNRA	Antagonist	0.0	0.0	0.0

HRH1	Agonist	1.3	1.6	1.5
HRH1	Antagonist	7.0	11.3	9.2
HRH2	Agonist	0.0	0.0	0.0
HRH2	Antagonist	82.0	83.2	82.6
HTR1A	Agonist	22.3	18.2	20.2
HTR1A	Antagonist	0.0	0.0	0.0
HTR1B	Agonist	21.7	16.8	19.2
HTR1B	Antagonist	0.0	0.0	0.0
HTR2A	Agonist	5.1	3.6	4.3
HTR2A	Antagonist	49.1	52.9	51.0
HTR2B	Agonist	2.8	0.9	1.8
HTR2B	Antagonist	37.3	47.2	42.2
OPRD1	Agonist	20.6	24.5	22.6
OPRD1	Antagonist	0.0	0.0	0.0
OPRK1	Agonist	48.9	49.9	49.4
OPRK1	Antagonist	0.0	0.7	0.4
OPRM1	Agonist	37.3	47.2	42.3
OPRM1	Antagonist	0.0	0.0	0.0
<b>Nuclear Hormone Receptors</b>		<b>Replicate1</b>	<b>Replicate2</b>	<b>Average</b>
AR	Agonist	0.0	0.0	0.0
AR	Antagonist	16.1	12.0	14.1
GR	Agonist	0.0	0.0	0.0
GR	Antagonist	30.0	16.1	23.1
<b>Transporters</b>		<b>Replicate1</b>	<b>Replicate2</b>	<b>Average</b>
DAT	Blocker	7.4	0.0	3.7
NET	Blocker	0.0	1.8	0.9
SERT	Blocker	0.0	0.0	0.0
<b>Ion Channels</b>		<b>Replicate1</b>	<b>Replicate2</b>	<b>Average</b>
CAV1.2	Blocker	0.0	0.0	0.0
GABAA	Opener	0.6	1.4	1.0
GABAA	Blocker	10.2	20.0	15.1
hERG	Blocker	0.0	0.0	0.0
HTR3A	Opener	0.6	0.0	0.3
HTR3A	Blocker	10.2	17.1	13.6
KvLQT1/minK	Opener	9.5	12.9	11.2
KvLQT1/minK	Blocker	0.0	0.0	0.0
nAChR(a4/b2)	Opener	0.0	0.0	0.0
nAChR(a4/b2)	Blocker	0.0	0.0	0.0



NAV1.5	Blocker	36.1	34.6	35.4
NMDAR (1A/2B)	Opener	0.0	0.0	0.0
NMDAR (1A/2B)	Blocker	0.0	0.0	0.0

Non-Kinase Enzymes		Replicate1	Replicate2	Average
AChE	Inhibitor	2.2	1.1	1.7
COX1	Inhibitor	3.8	2.7	3.2
COX2	Inhibitor	3.5	2.7	3.1
MAOA	Inhibitor	0.0	0.0	0.0
PDE3A	Inhibitor	0.0	0.0	0.0
PDE4D2	Inhibitor	10.0	14.0	12.0
Kinases		Replicate1	Replicate2	Average
INSR	Inhibitor	9.4	7.2	8.3
LCK	Inhibitor	0.9	0.0	0.5
ROCK1	Inhibitor	14.3	0.0	7.2
VEGFR2	Inhibitor	4.9	5.4	5.2